UNIVERSITY OF Southampton

University of Southampton Research Repository
ePrints Soton

Copyright © and Moral Rights for this thesis are retained by the author and/or other copyright owners. A copy can be downloaded for personal non-commercial research or study, without prior permission or charge. This thesis cannot be reproduced or quoted extensively from without first obtaining permission in writing from the copyright holder/s. The content must not be changed in any way or sold commercially in any format or medium without the formal permission of the copyright holders.

When referring to this work, full bibliographic details including the author, title, awarding institution and date of the thesis must be given e.g.

AUTHOR (year of submission) "Full thesis title", University of Southampton, name of the University School or Department, PhD Thesis, pagination

http://eprints.soton.ac.uk

University of Southampton
Faculty of Engineering, Science and Mathematics
School of Mathematics

Knotting of Optical Vortices

Robert Paul King

Thesis for the degree of Doctor of Philosophy
September 2010

Abstract

Optical vortices form three-dimensional lines of darkness in scalar light. They are places where the phase becomes undefined and hence singular in value. We study the ability of optical vortices to form knots and links of darkness in scalar optical fields.

We describe a construction to create complex scalar fields that contain a fibred knot or link as its zero set. This procedure starts by constructing braids with strands that follow a lemniscate trajectory as they increase in height. These braids are closed using Milnor maps to form a function with a knotted or linked zero set. This braid contains a minimal amount of information rather than the minimum number of crossings, taking advantage of symmetries in the construction. The knots and links we construct exhibit patterns in their Alexander and Jones polynomial coefficients, as well as in their Conway notation as parameters in the construction are varied. We use these patterns to propose a tabulation of the knots and links we can construct.

The knots and links we can construct are examined as solutions of the paraxial equation using polynomial solutions. We show that a wide range of vortex topologies are possible and report an experimental implementation of the technique. We also consider the Helmholtz and Schrödinger equations and attempt to construct solutions to these equations with knotted phase singularities.

We conclude with a geometric approach to optical vortex control. This is used to study the initial value problem of paraxial propagation and attempts to construct a function that describes the optical vortex paths on propagation.

Contents

List of Figures

List of Tables

Declaration

I, Robert Paul King, declare that the thesis Knotting of Optical Vortices and the work presented in the thesis are both my own, and have been generated by me as the result of my original research. I confirm that :

- this work was done wholly or mainly while in candidature for a research degree at this university;
- where I have consulted the published work of others, this is always clearly attributed;
- where I have quoted from the work of others, the source is always given. With the exception of such quotations, this thesis is entirely my own work;
- I have acknowledged all main sources of help;
- where the thesis is based on work done by myself jointly with others, I have made clear what was done by others and what I have contributed myself;
- parts of this work have been published as
  - Dennis M R, King R P, Jack B, O'Holleran K and Padgett M J. *Isolated optical vortex knots*, Nature Physics, **6** (2010), 118-121

Signed :
Date :

Acknowledgements

I begin by thanking my supervisor, Mark Dennis, who has provided me with support and ideas over the last four years. I must thank Mark for thinking of research I have found so interesting to work with. He has also helped to make sure what I have written is accurate and clear.

I thank Giampaolo D'Alessandro for many proof-reads and for the printing of my submission in Southampton. Giampaolo, along with Chris Howls have made sure I keep up with all the Southampton commitments while I have been in Bristol. I have had many illuminating discussions with Michael Morgan. I'm grateful to Michael for his reading of my thesis and the resulting comments. I have also had many discussions with Anton Desyatnikov whom I thank and also thank for kindly making available data I have used in this thesis. I also thank the Leverhulme Trust and the Southampton University School of Mathematics for funding.

I must thank *everybody* at the Bristol Theory Group, staff and students, in the University of Bristol's Physics department. Everyone has made my extended stay productive, rewarding and sometimes even enjoyable! Thank you to everyone who has been on the receiving end of my constant questioning of everything.

The experimental results presented in this thesis are the work of Miles Padgett, Kevin O'Holleran and Barry Jack at the University of Glasgow. I thank them for their results and collaboration. I have made extensive use of the Mathematica packages "KnotTheory" by Dror Bar-Natan and "LinKnot" by Slavik Jablan and Radmila Sazdanović.

Southampton University Archery Club (SUAC) had the great pleasure of calling me their leader. Despite the constant piles of paper work, late nights and more arguments sat in the front of a minibus than I can count, I have made some of my best friends through SUAC. We are nearly there, EUAC will be beaten!

I must thank Alex and my parents for their constant support over the last few years. This really has meant a lot to me. Hopefully now you can ask me

something different to “Didn’t you say you’d be finished yesterday / last week /last month . . . ”

1 Introduction

Light is all around us, but so is the darkness. Threads of darkness run through light arising from destructive interference. These lines are the *optical vortices*. A remarkable feature of these dark lines is their ability to form complex topologies, linking together and becoming knotted. This thesis is the study of this dark topology.

1.1 Phase Singularities

What is the time at the North Pole? Here, all the lines of longitude converge to a point[1] and the usual notion of the twenty-four time zones does not hold. Local time defined this way is not uniquely defined here and we show this in figure 1.1. Practically the problem is : what day is it when travelling east to west? Local noon is when the Sun reaches its highest angle in the sky, but at the poles, the Sun's angle does not change during the day, hence this angle is undefinable. Elsewhere on the Earth (except the South Pole) this angle varies, cyclically around the pole. This cyclic variable, time modulo one day, has a singularity at the Earth's poles.

Generically, phase singularities arise when any cyclic variable cannot be defined at a point (two dimensions) or along a line (three dimensions). Simple functions exhibit this singular behaviour : the argument of $(x + \mathrm{i}y)$ is undefined at the origin. In a general complex scalar field, which we shall use to describe optical fields, phase singularities occur as zeroes (nodes) of the absolute value. The derivation of this representation for light is covered in section 1.5.

Physical systems containing phase singularities have been studied since the 1800s. Here we give a brief overview of the historical context, however a full

[1] We assume an 'ideal' spherical Earth and neglect the political factors in defining the time zones.

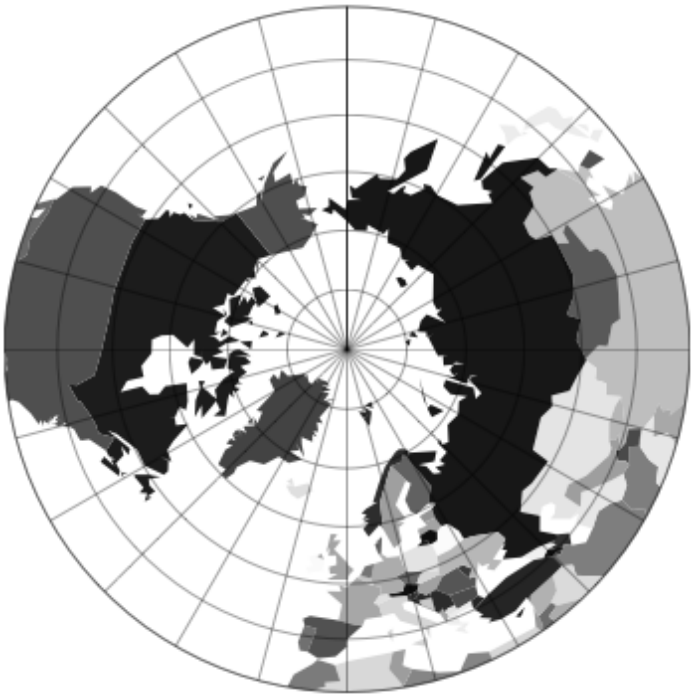

Figure 1.1: The lines of longitude radiating from the north pole. Here, the time of the day is undefined.

account can be found in the review by Dennis et al [DOP09]. The first such system discovered appears to be the existence of amphidromic points in the North Sea [Ber00]. The height of the tide has a cyclic variable : the periodic arrival time of the high tide. Whewell [Whe36] collated observations of the high tide time from many points on the coast, on both the British and continental coasts, as well as data from many other places around the world. Opposite coasts of the North Sea have the high tide arrive at very different times. These phenomena are in fact observed all around the world. Upon joining co-tidal lines (lines where the high tide arrive at the same time) they meet at two points in the North Sea. These are called *amphidromies* and there is no tidal movement at these points.

Paul Dirac in the 1930s as part of his formulation of quantum mechanics has phase singularities in the scalar quantum wavefunction of the electron [Dir31]. This work considered open ended, finite lines, the ends of which terminated by magnetic monopoles, a situation not possible in optics and not necessarily possible in quantum mechanics. The nodal lines in an optical field do not finitely end, ensuring continuity of the field.

In the field of optical physics, Wolter in 1949 [Wol50] (with English translation [Wol09]) was seemingly the first to emphasise that phase singularities occur in light. Optical vortices were found to occur in the Goos-Hänchen shift of light.

This is an effect of reflection of a finite width light beam from a dielectric material. An example of this is total internal reflection in glass at an interface with air. The centre of the reflected beam is spatially shifted from the centre of the incident beam. This example is well illustrated in [DOP09, fig. 3].

Continuing with optics, the 1950s saw Braunbek and Laukien [BL52] giving an illustration of phase singularities occurring in the diffraction of a plane wave from an infinite half-plane. Phase singularities arise on the illuminated side of the diffracting plane. This is again illustrated well in [DOP09, fig. 4] and in [BW59, fig. 11.14].

The work of Nye and Berry in 1974 [NB74] is the first work to realise the generality of phase singularities in three-dimensional wave fields. They were studying ultrasound pulse reflections in the lab to understand radio echos from the ice sheets in Antarctica. They compare the phase singularity lines observed to the dislocations found in crystals [Rea53], which we now explain.

Consider the parallel layers of atoms/molecules in a crystal. In between two layers, an additional layer can be introduced displacing the layers either side of this. This is an edge dislocation. A screw dislocation arises from a deformation of a layer (wavefront) around a point. For a crystal atomic layer, as you traverse round this point, after making a complete circuit you arrive on a different layer up or down. This displaces the layers either side and hence causes them to break and have a step in them, manifesting itself as helical wavefronts in waves. The type of dislocation can be associated with a Burgers vector. This is a vector showing the direction that is additionally needed to complete a three-dimensional circuit around the dislocation. With no dislocation present, there is a path within the layer (wavefront) that can be completed. With a dislocation present, the path cannot be closed and remain in the same layer so an additional direction and length is required to describe this circuit [Rea53]. This direction is the Burgers vector. The Burgers vector is perpendicular to the dislocation line when the dislocation is an edge dislocation. A screw dislocation has a Burgers vector in a parallel direction to the dislocation line. Example of functions with an edge and a screw type wave dislocation [NB74], are

$$\psi_{\text{edge}} = (x + \mathrm{i}y)\mathrm{e}^{\mathrm{i}y}, \quad \psi_{\text{screw}} = (x + \mathrm{i}y)\mathrm{e}^{\mathrm{i}z}, \tag{1.1}$$

respectively, where $(x, y, z) \in \mathbb{R}^3$, which are illustrated in figure 1.2. In general, optical phase singularities are of mixed edge-screw type. The Burgers vector of such a dislocation lies in between the two cases of screw and edge. An optical Burgers vector that can be defined on the singularity is found by Dennis [Den09].

Despite several observations of optical phase singularities, the term optical vortex appears not to have been used until 1989. Coullet et al [CGR89] use the

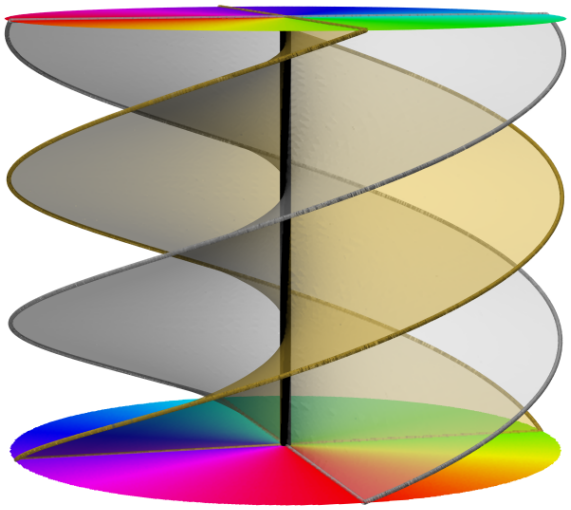

(a)

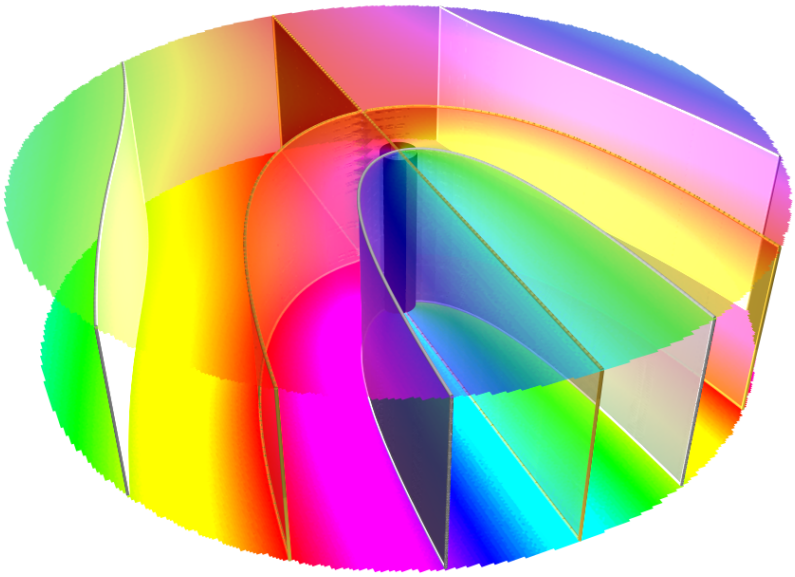

(b)

Figure 1.2: The (a) screw dislocation and (b) edge dislocation given in equation (1.1). The coloured discs are in the (x, y)-plane and the black cylinders represent the zero (vortex) line. The silver and gold surfaces represent the $\operatorname{Re}\psi =$ and $\operatorname{Im}\psi = 0$ surfaces respectively. The coloured disks represent the phase, $\arg\psi$, in their respective planes and are coloured using our stand key defined in figure 1.3.

term optical vortex to explain their observations in certain laser experiments.

Optical vortices now find themselves used in a variety of applications. The imaging technique of Westphal and Hell [WH05] uses a laser beam containing an optical vortex to super-resolve an object that has been dyed with a fluorescent dye. This technique allows for the object to be imaged with a resolution beyond the classical diffraction limit. Contrasting to microscopy, optical vortices have been applied to telescopy. A coronagraph with a vortex inducing lens instead of a conventional light stop has been developed by Foo et al [FPS05] and has been implemented [SFAM+08].

1.2 Optical Vortex Taxonomy

We represent light by a complex scalar field, ψ. These ψ will be required to satisfy certain partial differential equations which we introduce later, but the features we now describe are general. Let ψ be a smooth function $\mathbb{R}^3, \mathbb{R}^2 \to \mathbb{C}$ with domain depending on the physical situation. We are interested in the loci of the zeroes of such a function

$$\{\boldsymbol{r} \in \mathbb{R}^2, \mathbb{R}^3 : \psi(\boldsymbol{r}) = 0\}. \tag{1.2}$$

These occur when the real and imaginary parts are simultaneously zero and we can write

$$\psi(\boldsymbol{r}) = \xi(\boldsymbol{r}) + \mathrm{i}\eta(\boldsymbol{r}) = \rho(\boldsymbol{r})\mathrm{e}^{\mathrm{i}\chi(\boldsymbol{r})}, \tag{1.3}$$

where ψ can also be expressed in terms of a polar co-ordinate function with modulus ρ and argument χ. χ is single-valued modulo 2π and becomes undefinable when $\psi = 0$. With χ representing the phase of a wave (we will freely interchange the terms phase and argument), its singularities, occurring at nodes of the magnitude, are where we are interested in the function ψ. This can be observed when the intensity, $I = \rho^2$, is zero.

In general we are interested in nodal lines in three dimensions; the codimension two objects. These arise along the intersection of the $\xi = 0$ and $\eta = 0$ surfaces. On such lines, the argument χ is undefined, making them phase singularities, like at the origin of $\psi = x + \mathrm{i}y$. When ψ is a two-dimensional function, the zeroes occur as points at the intersection of the lines corresponding to $\xi = 0$ and $\eta = 0$. These points/lines where $\psi = 0$ are the features we are interested in this thesis.

For ψ, a three-dimensional function, there is another type of phase singularity that occurs naturally in optics, a surface where the argument is undefined. Motivated from optics, these arise in the simple superposition of two

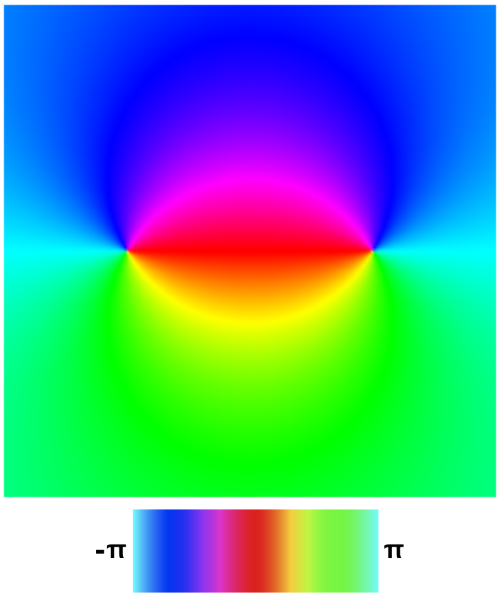

Figure 1.3: The argument of a function containing two phase singularities in the plane. The left point is negatively charged and the right positively. Both are of unit topological charge, $s = \pm 1$. At the singularities, the colour of the plot is undefined. We use the same key for all argument / phase plots in this thesis.

plane waves, waves whose wavefronts are infinite planes parallel to each other and perpendicular to $\boldsymbol{k}$,

$$\psi_{=} \exp(\mathrm{i}\boldsymbol{k}_1 \cdot \boldsymbol{r}) + \exp(\mathrm{i}\boldsymbol{k}_2 \cdot \boldsymbol{r}), \tag{1.4}$$

where $\boldsymbol{k}_1 \neq \boldsymbol{k}_2$. The phase of the function differs by π either side of such a surface. Such a singularity has been described incorrectly as an edge dislocation [SV01] which has led to some confusion in the literature. Such features also occur in Hermite-gaussian laser modes, section 1.6; however, we concentrate on the codimension two structures, the lines.

We now compare the two- and three-dimensional interpretations of optical vortex lines. In two dimensions, we can assign a topological charge to a phase singularity. This is an integer computed as the line integral

$$s = \frac{1}{2\pi} \oint_C \mathrm{d}\chi, \tag{1.5}$$

where C is a closed non-selfintersecting loop enclosing one nodal point in a right-handed sense. The integer s is positive if the phase increases in an anti-clockwise sense around C and negative otherwise. We call s the strength (or topological charge) of the singularity and it is the number of times the phase changes by 2π around C.

An example of positive and negative singularities is shown in figure 1.3; in this figure we introduce our colour scheme for plots of the phase of a function. We use the continuous colour wheel, where magenta smoothly returns to red, to represent the phase values modulo 2π. At a phase singularity, all the colours come together to manifest in a point of undefined colour. This allows their location and local properties of the phase to be easily seen [Win87].

Optical vortices form lines in three dimensions, space curves. These lines are vortices of the optical current, defined as [Jac62], notation as in [DOP09],

$$\boldsymbol{j} = \operatorname{Im} \psi^* \nabla \psi = \xi \nabla \eta - \eta \nabla \xi = I \nabla \chi. \tag{1.6}$$

The current vector points in the direction $\nabla\chi$, the direction of phase change, hence the vortex is located where this cannot be defined.

This current defines a vorticity, $\boldsymbol{\Omega}$, around the vortex line,

$$\boldsymbol{\Omega}|_{\psi=0} = \frac{1}{2} \nabla \times \boldsymbol{j} = \frac{1}{2} \nabla \psi^* \times \psi = \nabla \xi \times \nabla \eta. \tag{1.7}$$

The vorticity vector points in the direction of the vortex lines by giving the direction the current circulates in a right hand sense [BD00]. Hence this gives the tangent direction to the optical vortex line as

$$\boldsymbol{t} = \frac{\boldsymbol{\Omega}}{\Omega}. \tag{1.8}$$

The vortex line tangent does not have to have a component parallel to a given propagation direction. This means the vortex line can have regions with the vorticity in opposite directions. A hairpin shape is formed where $\boldsymbol{\Omega}$ changes sign, illustrated in figure 1.4.

At a turning point, like a hairpin, the two-dimensional view shows this as an elongated zero. This can be described in terms of the local phase structure around a vortex. Around a vortex line in three dimensions, a Taylor expansion of the wave function shows that current circulates around the vortex in a circular path [BD00]. The intensity and phase of the wavefunction is in general more complicated. Local to an optical vortex, the two-dimensional contours of constant intensity are elliptical [SS96, MTWT01, BD00]. The way the phase changes around these ellipses is such that for equal sector areas swept out there is equal phase change [Den01]. When the intensity contours are circular, the vortex is called isotropic (canonical) [MTWT01], with their elliptical counterparts being anisotropic (noncanonical). The eccentricity of these ellipses is a measure of the anisotropy of the vortex, called the *anisotropy ellipses*. Examples of both types of vortex are shown in figure 1.5

When the anisotropy ellipse is completely linear, the minor axis has zero length, the tangent of the three-dimensional line lies in the plane being observed.

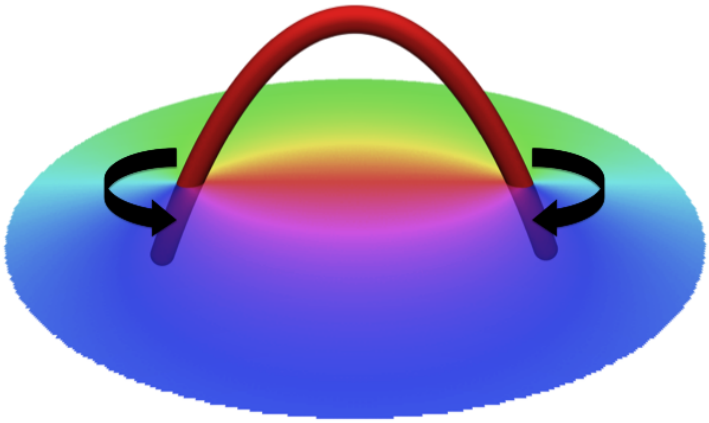

Figure 1.4: A plane containing two oppositely charged vortices. The red curve shows the propagation of the vortices in three dimensions. If this vortex pair were to be viewed in a sequence of two-dimensional planes, they would annihilate each other at the top of the curve in three dimensions.

An example of such an event is in the transverse plane containing the end of a hairpin. An isotropic vortex has local form $\psi(\boldsymbol{r}) \approx (x \pm \mathrm{i}y)$, depending on the sign of the topological charge it possesses. An anisotropic vortex locally is $\psi(\boldsymbol{r}) \approx a(x + \mathrm{i}y) + b(x - \mathrm{i}y)$ where $a, b \in \mathbb{R}$, [DOP09].

To conclude this section, we return to the vortex hairpin and consider its interpretation in three dimensions comparing it to the two-dimensional picture. In two dimensions, as z varies as a parameter, two vortices of opposite topological charge come together and annihilate each other. Further increasing z shows that there are no zeroes a small distance after this annihilation point. This manifests as a single highly anisotropic vortex at this point. What is happening is that the vortex line has its three-dimensional tangent direction lying in the (x, y)-plane. The vortex line has changed direction, preserving its topological current.

1.3 A Short Introduction to Knots

Knots arise in many areas of modern physics and science in general. The study of knots in physics goes back to at least the "vortex atom" hypothesis of Lord Kelvin [Tho67]. Section 1.7 reviews the history of knotted optical vortices and other knotted optical fields. We briefly review in this section the terminology and concepts of knot theory. Chapter 2 introduces knot theory formally and

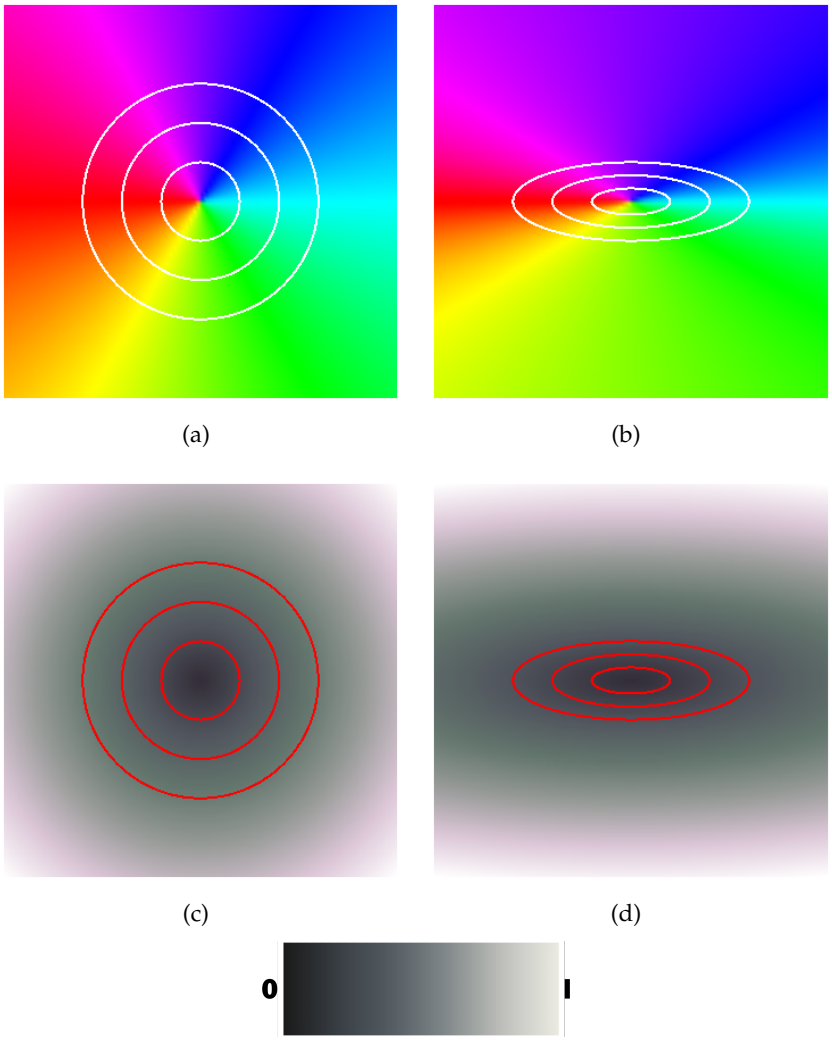

Figure 1.5: Phase (a), and intensity (c) of an isotropic vortex with contours of constant intensity shown to be circular; (b), (d) The corresponding images for an anisotropic vortex showing an elliptical contour of constant intensity and the long elongated dark section in the intensity plot. The intensity plots have scale as in the key and the phase plots use our common phase scale.

provides a more in depth review.

A knot is a closed non-selfintersecting curve in three dimensions which is homeomorphic to the circle S^1 [Rol76]. To distinguish different knot types, we must consider space minus the knotted curve K, $\mathbb{R}^3 \setminus K$. This definition is formally introduced in section 2.1 and some of the later definitions will require space to be the 3-sphere, S^3.

The fact that all knots are topologically equivalent to the circle means that techniques to distinguish knots often require the whole space to be considered in the calculation. Two curves are topologically the same knot if there exists an ambient isotopy between them. An ambient isotopy is a deformation of the whole space and preserves the topological properties of the knot. It is the actual curves we aim to create in optical fields as the optical vortex structure in $\mathbb{R}^3$.

The simplest method to distinguish between different knot-types is to create a two-dimensional projection. In this projection, information from the three-dimensional curve is kept at the projection's self-intersections to show which part of the curve is higher in the projection direction. This defines an over-arc and an under-arc of the curve at these points and gives crossing points in the projection. When the knot curve is given an orientation, this information defines the topological sign of the crossing (see figure 2.4). The self-intersections are such that only two points of the curve cross at a point. If more than two sections intersect at a crossing, the curve can be deformed by ambient isotopy (see section 2.1) to simplify.

The number of crossings in a given projection is a measure of the complexity of the knot. After performing allowed deformations, Reidemeister moves (shown later in figure 2.2), a minimum number of crossings can be calculated without destroying the topology of the knot. This number has been used historically to tabulate knots ; a history of which is in section 2.1 and this forms the basis of the standard Rolfsen table [Rol76]. We propose an alternative tabulation of a certain subset of knots as part of our knot construction in chapter 4.

The minimum crossing number turns out not to be a good way to distinguish knots. Although for knots with low minimum crossing numbers, there are only a few distinct knots with the same minimum crossing number, as this number increases the number of knot types increases (table 2.1). There are more complex knot invariants available, notably knot polynomials. A knot polynomial does not describe the curve, but encodes information about the whole space which the curve is embedded within. The Alexander polynomial [Ale28] was the first such polynomial to be discovered historically and is our polynomial of choice due to its simplicity to calculate and its connection to physics. Its simplicity does mean that it does not differentiate between all knots; different knots can have the

same Alexander polynomial. The Jones polynomial [Jon85] distinguishes more knots, yet it is not perfect, and we make use of this invariant in chapter 4. A goal of knot theory is to provide invariants that can completely determine a knot, for example the HOMFLY-PT polynomial, [FYH$^+$85, PT87] and Vassilev invariants [Vas90] attempt to address this problem but are still not perfect.

Associated to a knot are a set of two-dimensional manifolds called the Seifert surfaces. These are oriented non-selfintersecting 2-manifolds that have the knot as their boundary. Many different orientated 2-manifolds are potentially Seifert surfaces for a given knot. It is the surfaces of minimal possible genus that are those considered to be *the* Seifert surfaces (section 2.5). These surfaces are important to our optical vortex knot work because they define what class of knot we can construct in an isolated fashion. An optical vortex has surfaces of constant phase corresponding to all values of phase intersecting on the vortex curve and these surfaces do not intersect at any other point in the field. Fibred knots (section 2.5) have Seifert surfaces that do not intersect away from the knotted curve [Rol76]. The class of fibered knots have this property with their Seifert surfaces - not intersecting other surfaces in the equivalence class except at their common boundary, the knot. The Alexander polynomial of a fibered knot is monic, i.e. the first and last coefficients are equal to one. The ability to detect fibred knots is an important aspect of our work.

We conclude this section by briefly introducing braids which we formally introduced in section 2.3. Braids can be considered as a set of open curves connecting opposite points on two parallel planes. Closing a braid, by associating the start and end planes, forms a knot (or link, a set of knotted curves) [Ale23]. A braid is like a panorama picture of a knot. Chapter 4 details a construction of complex scalar functions with braided nodal lines. We use such functions in our construction of functions with knotted and linked nodal sets. It is these functions with knotted nodal sets we use to construct functions that satisfy physical differential equations such as the paraxial equation, chapters 3 and 5, and the Helmholtz and Schrödinger equation, chapter 5.

1.4 Experimentally Creating Optical Vortices

Optical vortices can be readily induced into a light beam using holography. Their positions are where the intensity of the beam is zero. We briefly cover here the scheme to create a desired optical vortex structure in a beam, experimentally, by holographic techniques. This is the method used in [DKJ$^+$10] to give the results reported in chapter 3. Further details of such an experimental approach can be found in Leach et al [LDCP05] and O'Holleran [O'H08].

A hologram does not have the prescribed optical vortex structure in the diffracted beam propagating from its surface. The hologram contains the initial conditions for a beam to propagate. The work of Leach et al [LDCP05] and O'Holleran [O'H08] show the experimental schemes used to create and view optical vortex knots. The beam can be scanned through with a camera to locate the vortices in the beam [OFDP09]. This gives a series of two-dimensional planes containing optical vortex points which can be used to reconstruct the full three-dimensional curves.

In chapter 3 we construct simple mathematical expressions with knotted nodal sets. These have non-trivial phase information to imprint in the beam. These functions underwent an optimisation algorithm, [DKJ$^+$10], to create the hologram pattern that increases the contrast between the vortices in the beam. By their nature, the optical vortices are contained in the dark regions of the beam and this can provide difficulties when trying to precisely locate them. If some brighter regions can be introduced, without effecting the overall topology of the vortices, then the location of the vortices can be determined more accurately.

1.5 The Paraxial Equation

The Helmholtz and paraxial equations are scalar equations related to the vector Maxwell's equations. It is these equations, particularly the paraxial equation, that we work with in chapters 3 and 5. In this section we give a derivation of the scalar Helmholtz equation and apply the paraxial approximation to arrive at the main equation for our work, the paraxial equation.

Maxwell's equations are a set of four coupled partial differential equations that describe the time-dependence of both the electric and magnetic fields of an electromagnetic wave. These equations are, in free space [BW59, Jac62]:

$$\nabla \cdot \boldsymbol{B} = 0, \tag{1.9a}$$

$$\nabla \times \boldsymbol{E} + \dot{\boldsymbol{B}} = 0, \tag{1.9b}$$

$$\nabla \cdot \boldsymbol{D} = 0, \tag{1.9c}$$

$$\nabla \times \boldsymbol{H} - \dot{\boldsymbol{D}} = 0, \tag{1.9d}$$

where the vectors $\boldsymbol{E}$ (electric field), $\boldsymbol{B}$ (magnetic induction), $\boldsymbol{D}$ (electric displacement field) and $\boldsymbol{H}$ (magnetic field) are three-dimensional real vector fields and $\dot{\bullet}$ are derivatives taken with respect to time t. These equations have an integral form which we do not considered here.

Although complete, when working with specific types of optical field, it is convenient to work with a reduced form or approximation to Maxwell's equations. Our interest is in light that takes the form of a coherent beam, like the

monochromatic light emitted from a laser. We now look at the assumptions required when wanting an equation to describe such a beam, which is strongly directional, and derive this equation, the paraxial equation.

When light propagates in free space, a perfect vacuum, the $\boldsymbol{B}$ field is proportional to the $\boldsymbol{H}$ field vector, and similarly for the $\boldsymbol{E}$ and $\boldsymbol{D}$ field vectors, such that

$$\boldsymbol{D} = \epsilon_0 \boldsymbol{E}, \tag{1.10a}$$

$$\boldsymbol{B} = \mu_0 \boldsymbol{H}, \tag{1.10b}$$

where ϵ_0 and μ_0 are the electric and magnetic permittivity of free space respectively. Taking the curl of (1.9b) and substituting (1.9a)

$$\begin{aligned} \nabla \times \boldsymbol{E} &= -\dot{\boldsymbol{B}} \\ -\nabla^2 \boldsymbol{E} &= -\mu_0 \nabla \times \dot{\boldsymbol{H}} \\ &= -\mu_0 \dot{\boldsymbol{D}} \\ &= -\mu_0 \epsilon_0 \ddot{\boldsymbol{E}}, \end{aligned} \tag{1.11}$$

where equations (1.10) and (1.9d) have been used. We assume that the vector functions allow the spatial and temporal derivatives to be interchanged. Similarly, taking the curl of the Maxwell equation (1.9d) and making the appropriate substitutions allows us to arrive at a similar expression for $\boldsymbol{B}$. Rearranging, we have two equations

$$\nabla^2 \boldsymbol{E} - c^2 \ddot{\boldsymbol{E}} = 0, \tag{1.12}$$

$$\nabla^2 \boldsymbol{B} - c^2 \ddot{\boldsymbol{B}} = 0, \tag{1.13}$$

where $c = (\mu_0 \epsilon_0)^{\frac{1}{2}}$ is the speed of light in a vacuum and both of these equations are the d'Alembert wave equation.

We now seek solutions to the d'Alembert equation which are monochromatic, with only one frequency present. The $\boldsymbol{E}$ field is the field we usually measure and so we choose to work with $\boldsymbol{E}$ rather than $\boldsymbol{B}$ for that reason. We observe the time-average of $\boldsymbol{E}$ and hence the structure is stationary. This allows us to write the time-dependence as a factor $\mathrm{e}^{-\mathrm{i}\omega t}$ in equation (1.14). The real vector field $\boldsymbol{E}(\boldsymbol{r}, t)$ describes the actual time-dependence of the wave. A monochromatic wave function, separable in space and time, has the form

$$\boldsymbol{E}(\boldsymbol{r}, t) = \mathrm{e}^{-\mathrm{i}\omega t} \boldsymbol{E}(\boldsymbol{r}), \tag{1.14}$$

where ω is a positive real number, the frequency of the wave.

Substituting this into equation (1.12), we are left with

$$\nabla^2 \boldsymbol{E}(\boldsymbol{r}) + k^2 \boldsymbol{E}(\boldsymbol{r}) = 0, \tag{1.15}$$

where the time-dependent exponential is dropped because it can never equal zero and $k = \frac{\omega}{c}$, a constant, which is the wavenumber defining the fundamental physical length scale. This is the Helmholtz vector wave equation.

We now choose a particular component of $\boldsymbol{E}$ to work with, which can be of arbitrary direction in the plane perpendicular to the direction of propagation. This propagation direction is usually chosen to be the z-direction and we follow this convention here. This means we only need to solve the scalar Helmholtz equation

$$\nabla^2\Psi + k^2\Psi = 0, \tag{1.16}$$

where Ψ is a complex scalar field. Ψ is required to be complex to retain the phase information of the field as its argument, although this is not directly observable and requires interferometric techniques to observe.

We finally make the paraxial approximation [LLM75]. This gives the differential equation that is used to represent beams of light such as those from a laser. Consider a scalar solution of the Helmholtz equation of the form

$$\Psi(\boldsymbol{r}) = \psi(\boldsymbol{r})\mathrm{e}^{\mathrm{i}kz}. \tag{1.17}$$

The *paraxial approximation* requires $\psi(\boldsymbol{r})$ to be such that

$$\left|\frac{\partial^2\psi}{\partial z^2}\right| \ll k\left|\frac{\partial\psi}{\partial z}\right|.$$

This is implied by the assumption that the wave vectors form only a small angle with the z-axis, which in our case is the beam axis and propagation direction.

Substituting such a function for $\Psi(\boldsymbol{r})$ into the Helmholtz equation gives

$$\left(\frac{\partial^2}{\partial x^2} + \frac{\partial^2}{\partial y^2}\right)\psi(\boldsymbol{r}) + \frac{\partial^2}{\partial z^2}\psi(\boldsymbol{r}) + 2\mathrm{i}k\frac{\partial}{\partial z}\psi(\boldsymbol{r}) = 0, \tag{1.18}$$

which, after applying the paraxial approximation, becomes

$$\boxed{\nabla_\perp^2\psi + 2\mathrm{i}k\partial_z\psi = 0} \tag{1.19}$$

where $\nabla_\perp^2 = \partial_x^2 + \partial_y^2$ is the transverse Laplacian. This is the paraxial wave equation. It is a parabolic PDE and is up to constants, the same as the $(2+1)$-dimensional Schrödinger equation, with no potentials, with t replaced with z. We consider the Schrödinger equation with potentials in $3+1$ dimensions in chapter 5, in which we generalise our knot construction to other differential equations which are not optically motivated. Later we consider waves that satisfy the paraxial or Helmholtz equations and use the notation ψ for a solution of the paraxial equation and Ψ for a solution of the Helmholtz equation.

It is interesting to note how the classification of the PDE changes at each stage of the derivation. The d'Alembert wave equation (1.12) is of hyperbolic

type while the Helmholtz equation (1.16) is an elliptic equation. Our finally derived paraxial equation (1.19) is a parabolic PDE. This takes us from a spatially isotropic, time-dependent (polychromatic) solution to a time-independent (monochromatic) solution which has a preferred propagation direction.

The complex scalar fields of Ψ and ψ, satisfying the scalar Helmholtz equation and paraxial equation respectively, do not represent the vector nature of electromagnetic waves. This means that we only have access to the phase singularities in an optical field. The full vectorial description can contain singularities in the field's polarisation. Polarisation, in two dimensions, is described by an ellipse [Jac62]. A general state of polarisation, for plane waves satisfying the d'Alembert wave equation (1.12), requires two independent plane waves of the electric field $\boldsymbol{E}$, which can be written as

$$\boldsymbol{E} = (\boldsymbol{\epsilon}_1 E_1 + \boldsymbol{\epsilon}_2 E_2) \mathrm{e}^{\mathrm{i}\boldsymbol{k}\cdot\boldsymbol{r}+\mathrm{i}\omega t} \tag{1.20}$$

where the $\boldsymbol{\epsilon}_{1,2}$ are vectors such that $\boldsymbol{\epsilon}_{1,2} \cdot \boldsymbol{k} = 0$ and $\boldsymbol{\epsilon}_2 = \boldsymbol{k} \times \boldsymbol{\epsilon}_1$ (from equations (1.9a), (1.9c) and equation (1.9b) respectively) and $E_{1,2}$ scalars. When the argument (phase) of E_1 and E_2 are the same, the wave is said to have *linear polarisation.* When the argument (phase) of E_1 and E_2 differ by 90°, the wave is said to have *circular polarisation.* The general case is elliptical polarisation, arising from the argument of the E_i giving different lengths to the vectors $\boldsymbol{\epsilon}_i$. Singular polarisation is where the two axes of this ellipse cannot be uniquely defined : circular polarisation, where both axes have the same length, and linear polarisation, where one of the axes has length zero [Den01]. Such singularities have been studied in optical fields that are not necessary monochromatic, [Nye99, and references there in]. Polarisation singularities do occur naturally in random fields [BD01c], even in the sky [BDL04] and have a three-dimensional structure akin to vortex lines [NH87, FODP08], albeit with a different mathematical structure.

1.6 Hermite- and Laguerre-gaussian Modes

Solutions of the paraxial equation represent light in a coherent laser beam. This means that some solutions are physically realisable in real beams, arising as modes of laser cavities. Here we introduce two commonly used mode families, Hermite- and Laguerre-gaussian beams [Sie86], which we use and refer to primarily in chapter 3.

In a system that is separable in Cartesian coordinates, the modes that arise are the Hermite-gaussian modes. These are solutions of the paraxial equation based on the Hermite polynomials, H_m, where m is the order of the polyno-

mial [AS64]. The Hermite-gaussian modes are [Sie86]

$$\begin{aligned} HG_{mn}(x,y,z) &= C_{m,n}\exp\left(\frac{-(x^2+y^2)}{2(w^2+\mathrm{i}\frac{z}{k})}\right)H_m\left(\frac{x}{(w^2+z^2/k^2w^2)}\right) \\ &\quad\times H_n\left(\frac{y}{(w^2+z^2/k^2w^2)}\right)GP(w,k,z), \end{aligned} \tag{1.21}$$

where

$$GP(w,k,z) = \left(\frac{w^2-\mathrm{i}\frac{z}{k}}{w^2+\mathrm{i}\frac{z}{k}}\right)^{\frac{m+n}{2}}, \tag{1.22}$$

is the Gouy phase term, $C_{m,n} = 1/\sqrt{2^{m+n}m!n!\pi}$ is a normalisation constant and w is the waist width of the beam. The Gouy phase is a term that arises from the beam being focused in the waist ($z = 0$) plane and gives an overall rotation to the phase structure upon propagation, increasing z [Sie86].

When $m = n = 0$, the beam is just a Gaussian beam, the fundamental mode. Such a beam has a circular transverse cross-section and intensity given by a Gaussian profile. There are no phase singularities in this mode, even on propagation. In higher order modes, when at least one of $m, n \neq 0$, there are surfaces of undefined phase lying on a rectangular grid. These surfaces in a single mode propagating, retain their structure and only change by a rotation induced by the Gouy phase and a scaling from the beam expanding. Examples of such modes are shown in figure 1.6.

It is possible to also construct modes based on a separable polar symmetry, giving rise to a set of paraxial solutions in cylindrical coordinates. Such solutions are based on the associated Laguerre polynomials, L_p^l, where p is the order of the polynomial and l arises from the associated Laguerre equation [AS64]. These solutions are the Laguerre-gaussian modes:

$$\begin{aligned} LG_p^l(R,\phi,z) &= C_{l,p}GP(w,k,z)\frac{1}{w^{|l|+1}}\frac{R^{|l|}\mathrm{e}^{\mathrm{i}l\phi}}{\left(w^2+\frac{\mathrm{i}z}{k}\right)^{|l|+1}} \\ &\quad\times\exp\left(-\frac{R^2}{w^2\left(1+\frac{\mathrm{i}z}{kw^2}\right)}\right)L_p^{|l|}\left(\frac{2R^2}{\left(w^2+\frac{z^2}{k^2w^2}\right)}\right), \end{aligned} \tag{1.23}$$

where $l \in \mathbb{Z}$ and $p \in \mathbb{N}$. The Gouy phase term is given by

$$GP(w,k,z) = \left(\frac{w^2-\frac{\mathrm{i}z}{k}}{w^2+\frac{\mathrm{i}z}{k}}\right)^p, \tag{1.24}$$

and the normalisation constant is given by

$$C_{l,p} = \sqrt{\frac{2^{|l|+1}p!}{\pi(|l|+p)!}}. \tag{1.25}$$

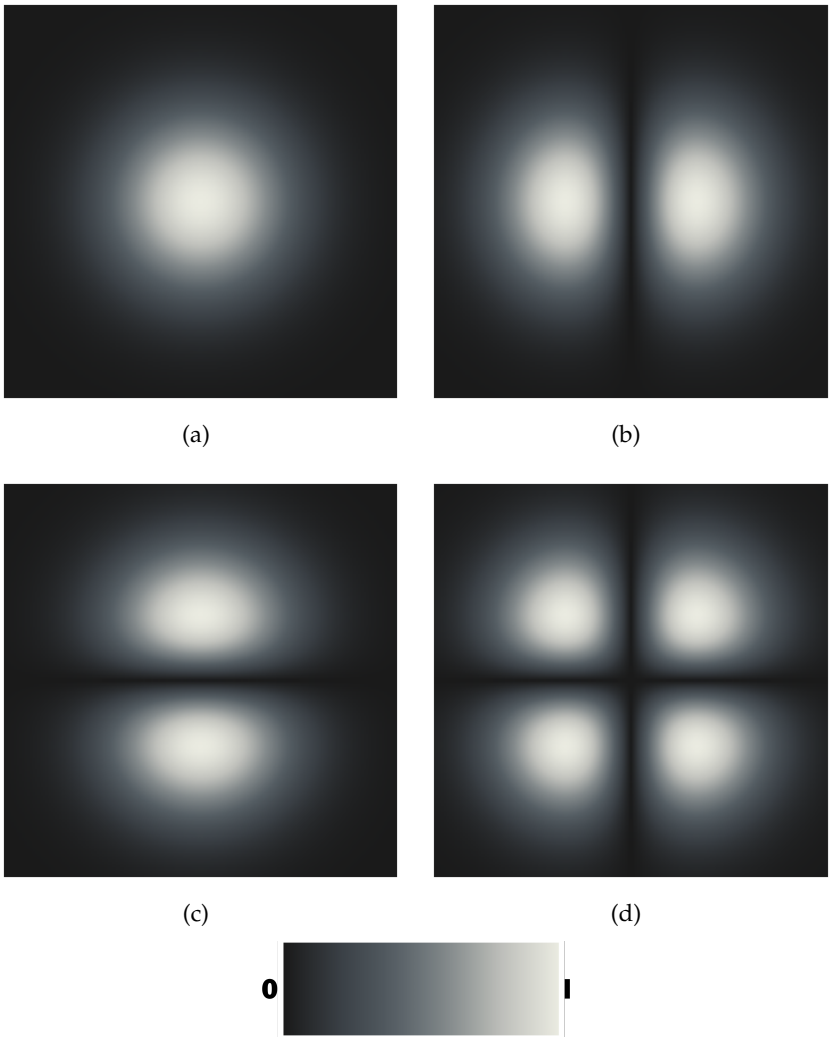

Figure 1.6: Examples of Hermite-gaussian modes. The parts (a)-(d) show the intensity pattern of the modes, written (m, n), $(0, 0)$, $(1, 0)$, $(0, 1)$ and $(1, 1)$ respectively. The dark lines, separating the bright regions, in the cases when m or n is not zero, correspond to the lines of undefined phase, although they are not optical vortices.

The $l = 0, p = 0$ mode, LG_0^0, is equivalent to the Hermite-gaussian $m = n = 0$ mode, a Gaussian beam with no phase singularities. In a Laguerre-gaussian mode there are two types of phase singularity present. When the integer $l \neq 0$, the mode possesses a phase singularity on the beam centre, $x = y = 0$. This is an optical vortex and can have both positive and negative topological charge dependent on the sign of l and can be of arbitrary magnitude. The charge of this vortex is sometimes referred to as the angular momentum of the beam or azimuthal quantum number. The non-negative integer p indicates the number of nodal rings in the beam and these coincide with the zeroes of the Laguerre polynomial, in its given argument. The rings propagate as a surface in the shape of an expanding cylinder forming a hyperboloid. The phase jumps by π across the cylinders of undefined phase. We illustrate how this happens in figure 1.7. We also give the intensity and phase in the $z = 0$ waist plane for the LG_2^1 and LG_1^2 modes in figure 1.7.

Hermite and Laguerre polynomials form a complete basis for monomials in their respective arguments. This means that for a fixed waist width, both sets of modes form a complete basis for polynomials in the $z = 0$ plane. Finite sums of a mode set, by linearity of the paraxial equation, form superpositions of modes. A simple example is the creation of an off-axis vortex in a Gaussian beam. This has superposition $\psi = LG_0^0 + \epsilon LG_0^{\pm 1}$, where ϵ is a small real parameter. Our work constructs superpositions of Laguerre-gaussian modes to experimentally realise optical vortex knots and links in chapter 3.

1.7 Knots in Optical Fields and Beams

We now review some recent results in topological optics. We concentrate on knotted and braided optical vortices, of which the former has been realised in experiments. This section concludes with a more general case of knotted field lines.

Berry and Dennis created a scheme to construct torus knots and links in optical fields satisfying the Helmholtz equation in [BD01a]. The scheme involves constructing fields that contain a pair of high order vortices. One of these is a closed loop, centred on the origin and lying in the (x, y)-plane at $z = 0$, of strength n. The second lies on the z-axis with strength m. This is an unstable system and when perturbed by a plane wave, the high order vortices unfold into a set of charge one vortices. The axial vortex of strength m splits into m separate helices. The planar ring unfolds into an (m, n)-torus knot if m and n are coprime. The appropriate torus link is formed when m and n are not coprime, with the number of components the greatest common divisor of m and n. The

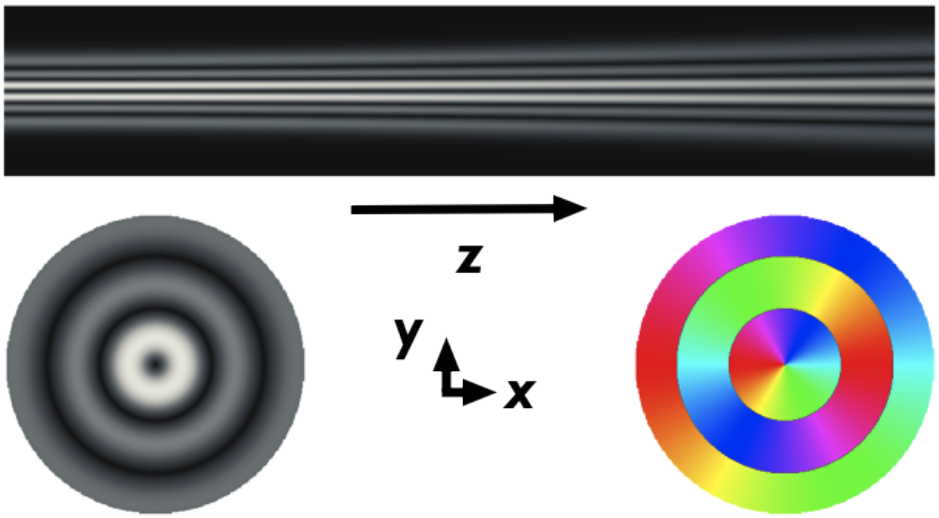

(a)

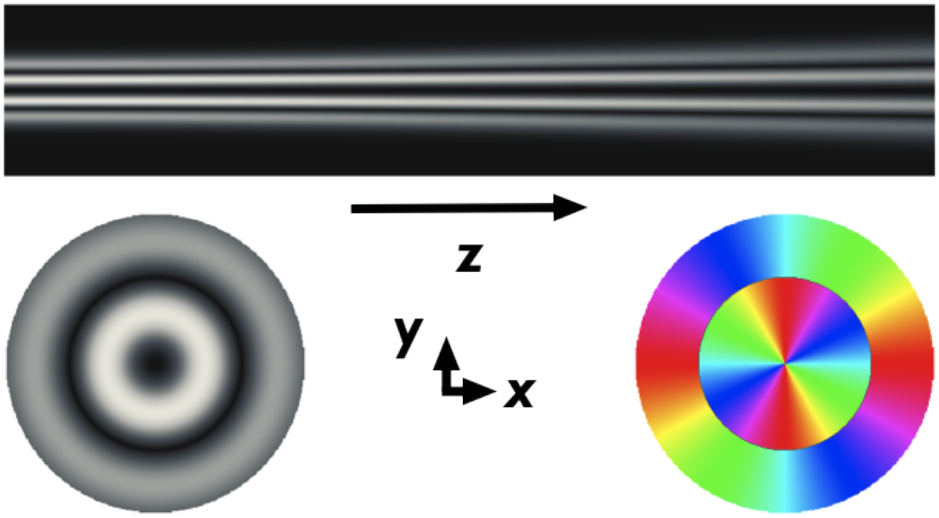

(b)

Figure 1.7: Examples of Laguerre-gaussian modes. (a) shows images of the LG_2^1 mode. The upper plot is the intensity of a cross section of the beam taken in the (y, z)-plane. The circular plots show the $z = 0$ plane of the intensity and phase. (b) shows the same plots for the LG_1^2 mode. The intensity plot has the same key as in figure 1.6.

solutions were written as superpositions of the Helmholtz Bessel beams [Dur87].

The question of the stability of the knots and links under further perturbation was addressed in a later paper [BD01b]. Functions satisfying the paraxial equation cannot have vortex loops that are of strength greater than one [BD01a]. Higher order vortices are possible, for example in an LG_0^2 Laguerre-Gaussian paraxial beam, but these are infinite open lines. Using polynomial solutions to the paraxial equation, the required solutions were able to be constructed. Polynomial solutions to the paraxial equation are introduced by us in section 3.2 and later for the Helmholtz eqution in section 5.2.

The ability to form the required optical fields paraxially, without having to create high order vortex loops, allowed for the knots to be realised in an experiment [LDCP04]. Instead of using the Bessel beam superpositions [Dur87], the required field is formed through an equivalent superposition of Laguerre-gaussian beams [LDCP05]. The Laguerre-gaussian modes all have the same frequency, hence same k value. A superposition of varying waist width modes is created that is then perturbed. This perturbation is provided by a LG_0^0 mode. Experimentally, this was implemented using a spatial light modulator (SLM) which displayed the appropriate diffraction pattern. A SLM is a computer controlled hologram [LDCP05]. A hologram that includes the intensity information in addition to the standard phase pattern was developed for this experiment, allowing for an improved control of the beam. The vortices by their nature are present in the dark regions of the beam and it can be difficult to control the behaviour of the beam in these regions. The computer controlled SLM allowed for a real-time change of the perturbation being applied to the superposition. The Hopf link and trefoil knot were both realised in the experiment as optical vortices, both threaded by helices.

Our goal with knotted optical vortices has several motivations from this earlier work. Only torus knots are possible by the Berry and Dennis construction. We wish to be able to produce non-torus knots and links out of optical vortices. We further desire to create isolated knots, those that are not threaded by other vortices. Finally, for experimental implementation, it would be desirable to be able to construct superposition of modes with all the same waist width, in contrast to the need to use a wider width mode for perturbation reasons.

Knotted topologies are not the only topology that has been considered for being constructed from optical vortex lines. Braided vortex lines have been constructed in optical fields by Dennis [Den03]. This construction begins by considering the general case of braided zero lines in general complex scalar fields. These do not in general satisfy a wave equation, Helmholtz or paraxial. The approach employed here is once again to create an unstable nodal set and apply a

perturbation.

The unperturbed function consists of two, off centre, counter-propagating Bessel beams, of order 3. This creates a vortex structure that contains a series of threaded, non-planar loops. Upon applying a perturbation with a plane wave, the vortex structure consists of a three strand braid. Transversely, these braid strands follow a lemniscate (figure of eight) trajectory. The braid is not isolated, as in the above knot construction, with some additional vortex lines around the outside of the braid.

The above papers, and our work, are focused on linear optics. This is a very good model for light propagation in free space (for standard intensities), however not all materials that light propagates through respond linearly. Some materials react in a nonlinear fashion. A beam ψ, propagating in such a nonlinear medium obeys a nonlinear Schrödinger (paraxial) equation such as

$$\nabla_{\perp}^{2}\psi + \mathrm{i}\frac{\partial\psi}{\partial z} \pm \kappa|\psi|^{2}\psi = 0, \tag{1.26}$$

which represents propagation through a Kerr-type medium [DKT05]. In equation (1.26), the sign of κ determines the type of the nonlinearity : a positive sign represents a self-focusing medium and negative a self-defocusing medium. In general any function of ψ can form the nonlinear term in equation (1.26) to represent different physical situations. The review of Desyatnikov et al [DKT05] gives an overview of optical vortices and solitons in nonlinear optics.

Knotted vortex lines have been observed in a numerical simulation of a beam propagating in a saturateable, nonlinear medium. A twisted elliptical beam, similar to that in [DBDK10], is propagated in a self-focusing medium. A bright soliton is trapped close to the optical axis, whose diffraction is contained by the self-focusing effect. The twist induces the formation of vortex rings around the soliton. Under propagation and perturbation, these vortex lines tangle and reconnect. This process can form linked and knotted optical vortex loops. An example of a Hopf link and trefoil knot in such a nonlinear system is shown in figure 1.8.

Freund [Fre00] makes the claim that torus knots, knots that can lie on the surface of a torus (section 2.1 and figure 2.6), are not possible as optical vortex knots. The above examples and our work of this thesis, show that torus knots are possible as optical vortex trajectories. Figure 1.9 shows the optical vortex trefoil knot, a torus knot, as the intersection of the $\mathrm{Re} = 0$ and $\mathrm{Im} = 0$ surfaces of the overall function containing the knot as its zero set. These surfaces are 2-hole tori which leads to some confusion because [Fre00] does not consider this case.

Away from vortices, Irvine and Bouwmeester [IB08] also consider topology

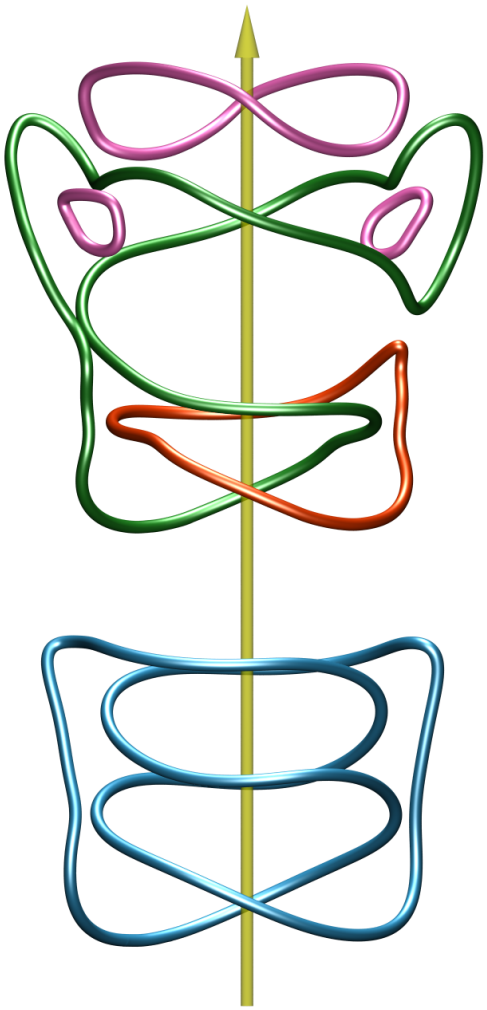

Figure 1.8: An example of vortex knotting in a saturateable, non-linear beam. The vortices are on the edge of an elliptic twisting beam in a self-focusing medium. The trefoil knot is coloured blue. The two components of the Hopf link are coloured green and orange. The beam is propagating in the direction of the yellow arrow. We are grateful to Anton Desyatnikov for use of the data to create this figure.

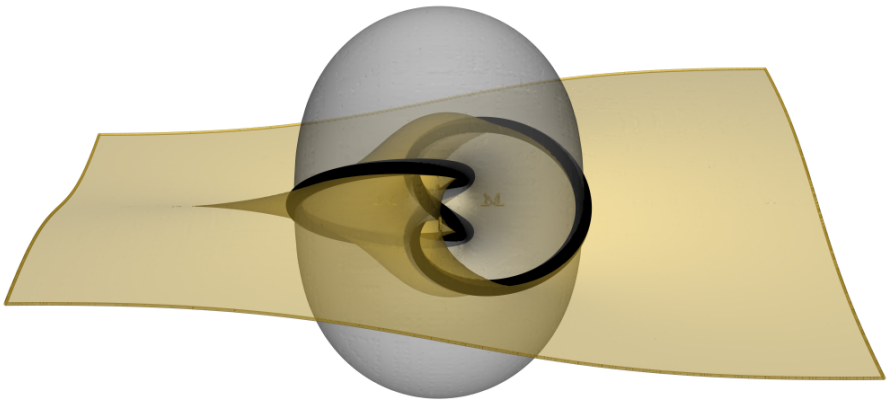

Figure 1.9: The trefoil knot, black curve, realised as the intersection of the Re $=$ 0, silver surface, and Im $=$ 0, gold surface, of a function constructed using the techniques of section 3.3.

in optical fields. This work looks at the electric and magnetic field lines in solutions of Maxwell's equation. Using the Hopf fibration, they found solutions (based on the work of Rañada [Rañ89]) in which the field lines are all mutually linked. The authors propose that such topology is realisable experimentally but viewing such features is a challenging experiment.

1.8 Random Optical Fields

Our main aim of this thesis is to study optical vortices in deterministic situations. Optical vortices also arise naturally from random processes, notably laser speckle patterns. Laser light reflected from a surface has a grainy appearance, caused by the random nature of the surface at length scales of the order of the light coherence length [Goo07]. This two-dimensional pattern has been well studied, [Ber78] through to [BD00, Goo07, DOP09].

We are interested in the three-dimensional properties of the random vortex lines. To understand the random topological features of optical vortices in a random field, we begin by using a lattice model to generate random lines. We will compare results of this lattice model to the numerical simulations made in [ODFP08] and [ODP00], which study the random speckle vortex lines in a

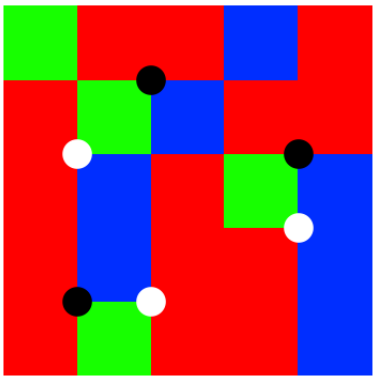

Figure 1.10: A two-dimensional version of the $\mathbb{Z}^3$ model. The coloured squares are equivalent to the corners of the cubes and are coloured red, green and blue to represent phases 0,1 and 2 respectively. The black dots represent negative faces and a vortex line coming out of the page. The white dots represent positive faces and a vortex line passing into the page.

numerical simulation of a paraxial optical field. The speckle simulations can be considered as a superposition of many plane waves. The simulation creates a finite volume by using a superposition of plane waves with k vectors confined to discrete rectangular grid. This makes the volume periodic in all three axial directions. The k-space is a grid of size 27×27, giving 729 plane wave contributions, and is only required to be two-dimensional due to the simulation being paraxial. We shall compare the fractal properties and topology of this simulation to our $\mathbb{Z}^3$ simulation results which we describe below.

The fractal properties of the vortex lines can be used to investigate the self-similarity properties of vortex lines [SAM93]. A line with a fractal dimension of two is a Brownian curve [Fal03]. We use the measures of [VV84], for example loop length spectrum, and [ODFP08], loop radius of gyration, to draw conclusions about the fractality of our vortex lines and whether they are Brownian curves.

Our model is a lattice model, discrete in real space, contrasting to the discussed optical simulation being discrete in k-space. This model is based on that presented by Vachaspati and Vilenkin in [VV84] to provide initial conditions for the modelling of cosmic string evolution. We consider a cubic lattice inside a cubic volume to model our random vortex lines. The points in the volume are represented as elements of $\mathbb{Z}^3$ and to these points a phase value is assigned. The values for phase are also discrete, taking values from $\{0, 2\pi/3, 4\pi/3\}$ which can be associated with the elements of $\{0, 1, 2\}$ respectively. We use the later representation with addition modulo three for convenience. The phase values are assigned randomly to each point with equal probability.

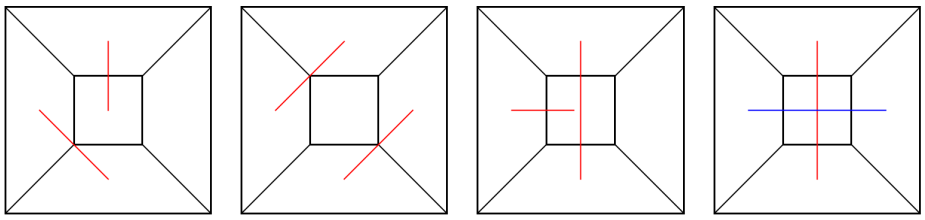

Figure 1.11: Using a planar representation of the cube, the sixth face is the region outside of the outer square. (a) - (c) show two completely avoiding vortex lines. (d) shows two vortex lines passing through opposite faces and hence the centre point of the cube. The different colours are for clarity.

A vortex line passes though a face of a cube if there is a 2π change in phase around it which we define as being the sum of differences between the values on each corner traversed in a clockwise sense. The difference is taken modulo three but the sum is taken in the standard way. When this sum is ± 3 then a vortex line passes through the face. For $+3$ we call it a positive face and the vortex line is directed into the cube. Likewise, if the sum is -3, the face is negative and the vortex line is directed out of the cube. There are only three examples of faces, up to sense and cyclic permutation, that admit a vortex line to pass through ; those with values 0012, 0112 and 0122 on their corners. The vortex lines are allowed to pass from cube to cube as the orientation of a face is reversed when considering neighbouring cubes. This gives that $24/81 \approx 30\%$ of all faces allow a vortex line to pass through; calculated from testing all combinations of the three values on the four edges of a square. Figure 1.10 shows a two-dimensional version of this model.

There are $3^8 = 6561$, three values on the eight vertices of the cube, possible configurations for the phases on each cube. Of these possible cubes we can calculate which configurations of phase admit vortex lines to pass through the cube. We can show that 1485 (22.6%) have no vortex lines passing through them. There are 4320 (65.8%) cubes that allow one vortex line to pass through; that is having only one positive and one negative face. There are 756 (11.5%) cubes that allow two vortex lines to pass through. It can be seen that once a cube has one positive face then there must be either one or two negative faces and in the case of two negative faces, there must be a second positive face. There are no combinations of phase on the cube vertices that allow three vortex lines to pass through. This leads to an average of 0.88 lines per unit cube.

The possible paths inside cubes with two vortex lines passing through are shown in figure 1.11. Three of the cases are unambiguous and the vortex lines

follow distinct paths. In the fourth case, it is possible that a reconnection occurs in the centre of the cube, where the two paths can intersect. When forming the vortex lines in our simulations we choose at random, with equal probability, which path to take when presented with a choice of two. We shall not discuss disambiguating such cases further.

In order to implement this model we use the dual lattice to the cubic lattice. The two-dimensional figure shown in figure 1.10 is dual to our description. This associates the cubes with the phase values and the cube edges with possible paths for the vortex lines. This has the advantage that all vortex line segments have the same path length, one edge unit, as apposed to two possible different values in the original lattice. In this lattice cubes that admitted two vortex lines to pass though them now correspond to points where two lines meet.

The cubic lattice is not the only lattice considered for this problem. Hindmarsh and Strobl [HS95] also use a lattice model to create initial conditions for a cosmic string model but use a different lattice. They use a tetrakaidekahedral lattice, formed from tetrahedrons. This is chosen so that the vortex line statistics are invariant to rotation. The condition for a vortex line to pass through a triangular face is simpler than the squares, with all three discrete values of phase needing to be present. No tetrahedron allows two vortex lines to pass through it, eliminating the need to make choices when faced with this scenario in the cubic lattice. The method of tracing vortex lines in [HS95] differs from our method as they start by assuming one tetrahedron has a line passing through it and calculate the phase data required as they follow the line. This has allowed for much longer lines to be studied than in [VV84], of the order that would require a 300^3 sized lattice. This method does not suffer from the finite boundary effects of the cubic lattice because the data is generated as required to form the next line segment.

It is found in [HS95] that 63.3% of the total line segments are in infinite lines. In [VV84] this is found to be 80% and our results are found to be similar to this. In this tetrahedral lattice, it is more likely that shorter loops are formed and the shortest loop length possible is $1/\sqrt{3}$ times shorter than in a cubic lattice. These factors mean that of the line segments in loops, less of the overall length is contained in the loops. The numerical optical simulation finds that approximately 73% of the total vortex line length is in the infinite lines with the remaining 23% of the total vortex length in the simulated volume contained within the closed loops.

We now give some results from the $\mathbb{Z}^3$ model which we compare to those of [ODFP08]. In the $\mathbb{Z}^3$ model there are two kinds of line : open infinite lines and closed finite loops. Obviously the definition of a line being open or closed de-

pends on how lines that end on the boundary are treated. The method of [VV84] is that any line ending on the boundary is considered to be an open infinite line, hence any closed loop is completely contained within the simulated volume. The paper of O'Holleran et al [ODFP08] employs a different method in their optical simulation, making the simulated volume have periodic boundary conditions. The computed volume is an elongated cube in the z-direction due to the scaling effects of the paraxial equation. The volume is thus topologically a 3-torus, (homeomorphic to a cube with periodic boundary conditions on the faces; not a three hole torus).

Our first result concerns the open lines of the $\mathbb{Z}^3$ model. The fractal dimension of the curve can be determined by comparing the average over all points on the line, of the Pythagorean distance between two points and the arc length along the curve between them. We consider the relationship between the Pythagorean distance between points, L, and the distance along the curve, R. This is measured for lines in a volume with periodic boundary conditions. The distance between the points along the curve is just the number of line segments separating them in the lattice model. For the line to exhibit Brownian fractality, the relationship $R \propto L^{0.5}$ must hold.

Figure 1.12 shows our results in a log-log plot. We find the fit line to be $\log R = 0.03 + 0.48 \log L$ which gives $R \propto L^{0.48}$ for our data, from 40^3 sized volumes. This relationship holds in the range $2 < L < 100$. Adjusting the lower limit does not make a significant difference to the fit. For the upper limit, increasing it does not make the fit better. Each of the black lines represents an individual line from a simulation. At the upper limit, these individual lines can be seen to diverge from the fit line. This is due to the line having to cross the periodic boundaries, potentially several times, when it is tracked. We can conclude from this measure that the $\mathbb{Z}^3$ open lines exhibit the property of being Brownian fractal.

We also studied the fractality of the closed loops and present here the results concerning the radius of gyration of the closed curves. The radius of gyration of a closed curve is the root mean square of the points from its centre of mass,

$$R_g^2 = \frac{1}{N} \sum_{k=1}^{N} (\boldsymbol{r}_k - \boldsymbol{r}_{mean})^2, \tag{1.27}$$

where $\boldsymbol{r}_{mean}$ is the average position vector of the curve and the sum is taken of the N line segments. For lattice curves, this is the mean of the vertex points. For curves that exhibit Brownian properties, the radius of gyration scales such that $R_g \propto L^{\frac{1}{2}}$ where L is the length of the loop.

In the second O'Holleran et al paper [ODP00] on three-dimensional random optical vortices, the radius of gyration is used to determine the fractal dimension

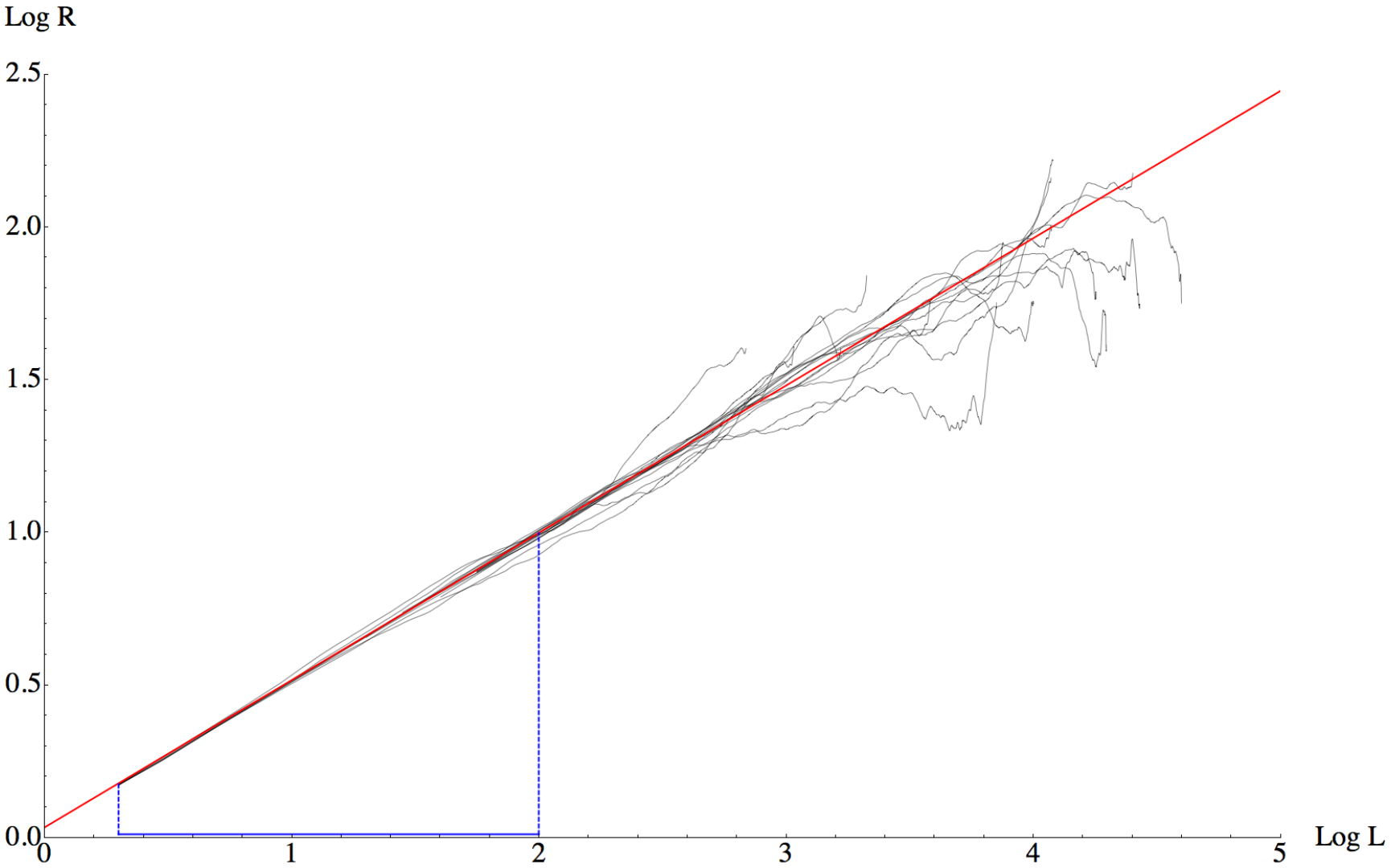

Figure 1.12: A log-log plot of the Pythagorean distance vs arc-length between points on infinite lines for $\mathbb{Z}^3$ model volumes of size 40^3. Each black line represents a line and is the average R for each L along the line. The red line is the fit, $R = 0.03 + 0.48L$, fitted in the range marked by the blue region, $2 < L < 100$.

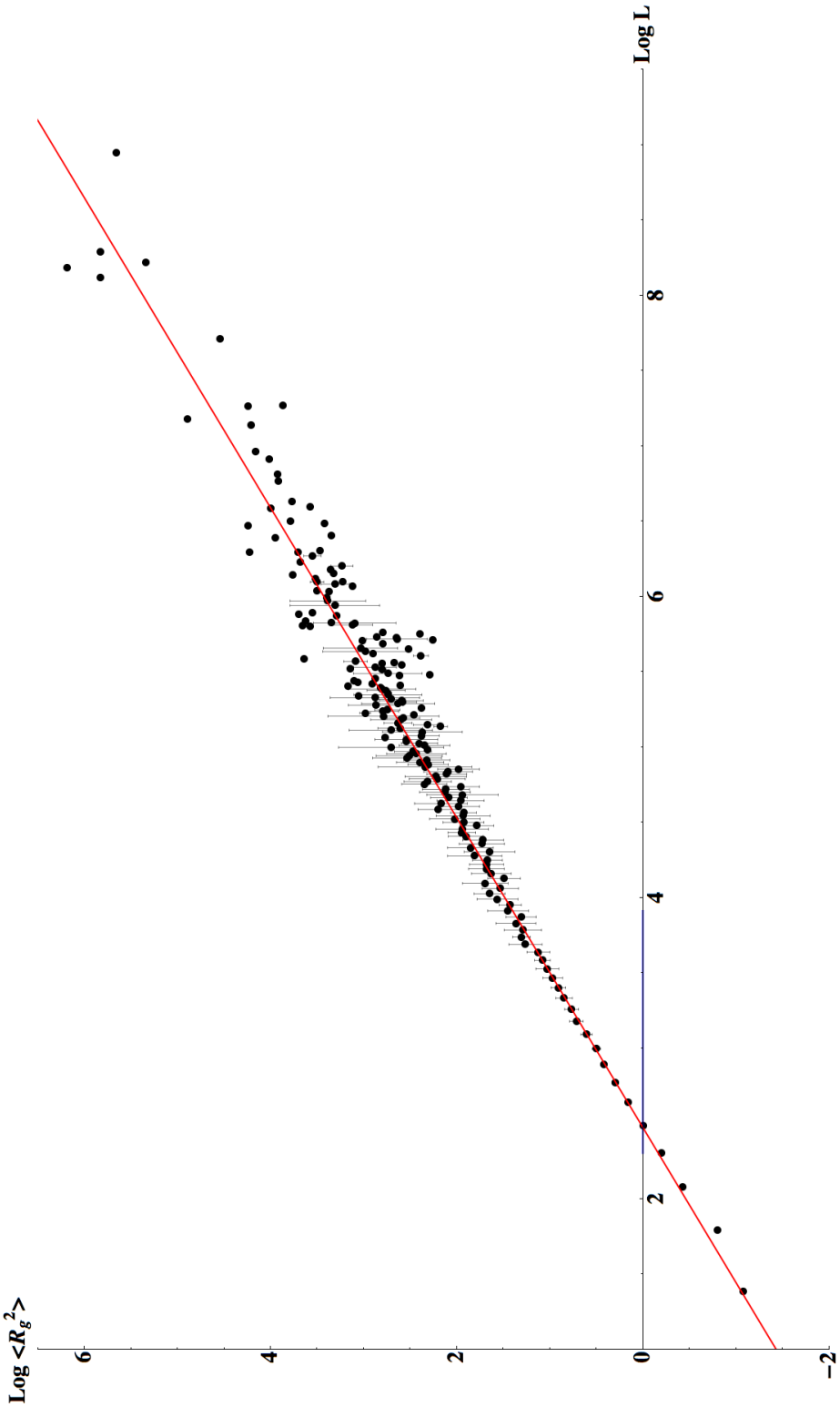

Figure 1.13: A log-log plot of radius of gyration squared against length for loops in $\mathbb{Z}^3$ volumes of size 50^3. The curves are allowed to cross the periodic boundary.

of the closed vortex loops. They find that $R_g \propto L^{0.52}$ over a range of lengths between 1.2 and 7.4 simulation units. We use our data to compare the discrete real space $\mathbb{Z}^3$ model to the speckle simulation via radius of gyration. Our data for 50^3 volumes is shown in figure 1.13, again for the simulation volume being a 3-torus.

Our plot show values for radius of gyration squared, for computational convenience. We therefore need to compute half the gradient of the fit curve. Our plot has fit line of $\log(R_g^2) = -2.40 + 0.98 \log l$. This gives for the discrete real simulation that $R_g \propto L^{0.49}$. Both simulations, the $\mathbb{Z}^3$ model and the numerical optical fields of O'Holleran, possess the similar Brownian scaling property.

Other random physical systems support the possibility of knotted structures including polymers in chemistry [OW07] (using lattice simulations), self-avoiding random walks [DDM$^+$03], DNA tangles [Sum90] and even how rope knots itself [RS07][2]. The complexity of tangled vortex lines in superfluids is also studied [BRS01].

The $\mathbb{Z}^3$ model, being based on a cubic lattice, has some interesting restrictions placed on how the closed curves can form knots. The simplest knot is the trefoil knot, used frequently through this thesis as an example. When searching for knots on a cubic lattice, the length of a trefoil knot must be at least twenty-four edge lengths, proved by Diao [Dia93]. Curves of shorter length can be discounted in a search for knots. The simplest link, the Hopf link[3], can be formed on the cubic lattice by two curves of length eight. The more complex (unique topologically) four crossing link must be formed of two curves with combined length greater than twenty-eight lattice steps [EP02]. We are yet to observe linking or knottedness with our cubic lattice simulation.

The topological features of optical vortex lines in random fields is also an interesting feature of such fields [ODP00]. The vortex topology of low numbers of plane wave in superposition is known, [OPD06, MD01], where three plane waves can give rise to parallel infinite lines and four plane waves is enough for loops, which are planar and parallel, to form. Higher numbers of plane waves in superposition give rise to more complex geometries and topologies. The topology of the superpositions in [ODP00] of up to 2025 plane waves, corresponding to a k-space grid of 45×45, is expected to be highly non-trivial. A hierarchy of threading of closed curves is studied to determine the topology of the simulation: threaded by an infinite line, threaded by another closed loop (linked) and self-threaded (knotted). Using the data from the numerical simulations, estimates on the probability of loop threading and linking are made, and

[2]This work was awarded the 2008 Ig Nobel prize for physics.
[3]The Hopf link is studied extensively later in this thesis

found to have a similar form to other random systems such as polymer modelling [OW07]. The probabilities are found to be

$$P_{\text{unthreaded}} \propto \exp\left(\frac{L-1.15}{30}\right), \tag{1.28}$$

$$P_{\text{unlinked}} \propto \exp\left(\frac{L-1.88}{185}\right), \tag{1.29}$$

where L is the length of the loop in question. Notice how these are probabilities for being not threaded and not linked respectively. These forms are similar to the forms for the probability of not being knotted given by random polymer studies [OW07]. The exponents of the probabilities can be interpreted as $\frac{-L}{TP}$ where P is the persistence length of the curves and T is a constant dependent on the model and lattice type. The persistence length [GK94] is the length along the curve before the tangent directions become uncorrelated.

No knots were observed in the simulation of [OW07]. This null result is different to saying random optical vortices cannot be knotted, just that they have not been observed, even though that of the order of half a million curves were tested for knottedness. We know that optical vortices can be knotted, section 1.7 and our work in chapter 3 and later chapters. Based on the probabilities obtained, and the likely form of the probability of a curve being unknotted, it is projected that a total simulation search volume is required to be 10^7 times that studied to provide reliable data about the knottedness of the vortex lines in numerical simulations of paraxial speckle.

1.9 Thesis Outline

This thesis now proceeds as follows :

Chapter 2 introduces the subject of knot theory, introducing the definitions we require for our later work and give our interpretations of some of the material.

Chapter 3 outlines our procedure to create knotted optical vortices in real laser beams. Our general procedure for achieving this is outlined, although some of the details are fully explained and explored in later chapters. The experimental procedure and results are reported. We also show how the paraxial equation can be transformed into the Hermite and Laguerre differential equations to generate families of polynomial solutions to the paraxial equation. We use these polynomials throughout the thesis, to examine the knots and links we create as functions satisfying the paraxial equation.

Chapter 5 explores the knots and links we can create as the nodal set of a complex scalar function. We generalise our construction based on braids to

higher lemniscates and show how some additional parameters introduced into the construction can be used to control the geometry of the knots. We outline a classification of the knots and links of our construction using knot polynomials and other knot invariants. Sequences are observed in the coefficients of the Alexander and Jones polynomials we construct, as well as trends in the Conway notation. We make use of these patterns to predict the identity of more complicated knots that are accessible to our construction.

Chapter 5 uses the knots and links that we can construct and attempts to embed them as the nodal set of functions satisfying various partial differential equations. We further examine our main example of paraxial nodal knots but also consider the Helmholtz equation and various forms of the Schrödinger equation. We construct polynomial solutions to the Helmholtz equation, analogous to our paraxial polynomials. Our look at the Schrödinger equation includes the potentials of the 3D harmonic oscillator and the hydrogen atom, and we finish with a discussion of other physical equations that could be considered.

Chapter 6 approaches the geometry of optical vortex propagation from a different perspective. Here we use the initial value problem nature of paraxial propagation to construct a function describing the locus of the vortex lines. The properties of the field we evaluate can be used as a measure of the complexity of the vortex curve and predict which vortices of opposite sign will annihilate each other given a non-trivial initial configuration.

We conclude this thesis with two appendices, the first outlining our procedure for tracking the location of phase singularities in three-dimensional fields. The second tabulates the knots and links we have been able construct.

Introduction to Knot Theory

2

The mathematical theory of knots is a rich and deep subject encompassing the description of everyday objects through to the topology of high dimensional spaces. Our motivation is to construct knots in physically realisable optical structures and hence we focus on knots which are embeddings of S^1, the circle, in $\mathbb{R}^3$ and S^3, the 3-sphere. These are the classical dimensions of knot theory. This chapter outlines the background to our knot construction and the properties of the knots we desire.

2.1 A Quick Trip Into Knot Theory

Let us begin by defining a knot.

Definition 2.1 (Knot (General))**.** *A knot, K, in classical dimensions is a subset of S^3 that is homeomorphic to S^1,*

$$S^1 \cong K \subset S^3. \tag{2.1}$$

Equivalently this is (the image of) an embedding of S^1 in S^3.

The requirement for a knot to be closed curve avoids the problem of an open string untying itself.

With all knots being homeomorphic to S^1, they are all homeomorphic to each other. This is in contrast the complements, $S^3 \setminus K$, of different knots which are not homeomorphic to each other [Rol76, p2]. This allows us, using methods described later, to distinguish between distinct knot types.

To find this topological equivalence between knot types we are required to use ambient isotopy.

Definition 2.2 (Ambient Isotopy [BZ85])**.** *Consider two embeddings of the circle into the 3-sphere, $f_1, f_2 : S^1 \to S^3$ such that $f_i(S^1) = K_i$, $i = 1, 2$, where the images, the*

K_i, are two knotted curves. Let $H : S^3 \times [0,1] \to S^3$ be a continuous function, denoted $H(u,t) \equiv H_t(u)$, such that $H_t : S^3 \to S^3$ is a homeomorphism. H is an ambient isotopy between f_1 and f_2 if $H_0 = \mathrm{id} : S^3 \to S^3$ and $H_1 \circ f_1 = f_2 : S^1 \to S^3$.

Ambient isotopy deforms the entire embedding space not just the curve. This leads us to formalise our definition of two knots being equivalent to each other.

Definition 2.3 (Knot equivalence)**.** *Two embeddings of S^1 in S^3 are equivalent, the image curves are the same knot type, if there exists an ambient isotopy between them as described in definition 2.2.*

We will relax the use of the term "knot type" to just "knot".

Despite it being mathematically desirable to work with S^3, we require for physical reasons to consider the embedding space to be $\mathbb{R}^3$. We now modify definition 2.1 to take this into account.

Definition 2.4 (Knot (for this thesis))**.** *A knot is a curve homeomorphic to S^1 embedded in $\mathbb{R}^3$.*

It is the actual knotted curves we want to work with and later in this chapter we describe techniques to distinguish knot types without having to explicitly find an ambient isotopy function, which is in general difficult. Some of our later constructions still require the use of S^3 and we now describe the concepts required.

The 3-sphere can be defined as

$$\begin{aligned} S^3 &= \left\{ x_i \in \mathbb{R}^4 : |x_0|^2 + |x_1|^2 + |x_2|^2 + |x_3|^2 = 1 \right\} \\ &= \left\{ u, v \in \mathbb{C}^2 : |u|^2 + |v|^2 = 1 \right\} \\ &\cong \mathbb{R}^3 \cup \{\infty\}. \end{aligned}$$

For our work the most useful way to think of the 3-sphere via the second definition in terms of two complex coordinates. The 3-sphere can be stereographically projected into $\mathbb{R}^3$ but what is more useful for us is the inverse stereographic projection from $\mathbb{R}^3$ to S^3 to give complex coordinates for the 3-sphere. We use

$$u = \frac{x^2 + y^2 + z^2 - 1 + 2\mathrm{i}z}{x^2 + y^2 + z^2 + 1} = \frac{R^2 + z^2 - 1 + 2\mathrm{i}z}{R^2 + z^2 + 1}, \tag{2.2}$$

$$v = \frac{2(x + \mathrm{i}y)}{x^2 + y^2 + z^2 + 1} = \frac{2R\mathrm{e}^{\mathrm{i}\phi}}{R^2 + z^2 + 1}, \tag{2.3}$$

given in both cartesian and cylindrical coordinates, the forms given explicitly in [SW03], where $R^2 = x^2 + y^2$ and $R\mathrm{e}^{\mathrm{i}\phi} = x + \mathrm{i}y$. The 3-sphere coordinates are given by $(u, v) \in \mathbb{C}^2$.

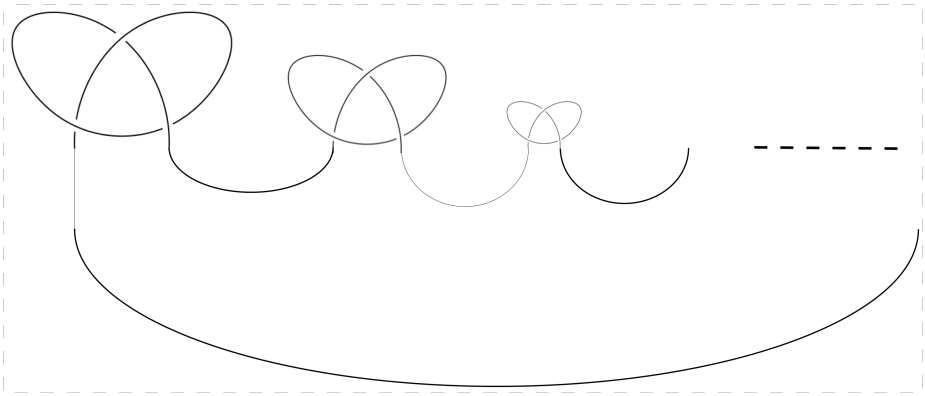

Figure 2.1: The wild knot based on the construction given in [Fox62]. Each knotted component is reducing in size, with an infinite number of copies and no lower limit on the size of each copy [CF63].

The knots that we work with are those that can be realised as a finite set of polygonal edges which are the *tame* knots ; otherwise, the knot is *wild* and can posses pathological properties. Knots that are ambient isotopic to a simple close polygon are tame. The curve given by Fox [Fox49] is simply constructed but wild and figure 2.1 shows an example of constructing a wild knot. The tame knots can be considered as smooth curves at all points [Rol76, p. 48]. All the knots we work with will be tame.

In general, it is hard to find an ambient isotopy function, therefore we need to consider other methods for determining and distinguishing the knot type of a curve. The starting point for the majority of the methods we employ involves projecting the knot into two dimensions. This gives a two-dimensional diagram in which the projected curve has potentially many self-intersections. At all of the self-intersection points, we show which part of the curve is passing over the lower section. These points, with this information given, are called *crossings* and the total number of crossings in the diagram defines the projection's *crossing number*. If a projection gives points with more than two parts of the curve self-intersecting, then the curve can be deformed through ambient isotopy or viewed from a different projection direction, to simplify the projection and make each crossing unambiguous.

The number of crossings in a projection is dependent on the projection direction and any deformation of the curve. The projection can be manipulated in three formal ways, equivalent to an ambient isotopy in three dimensions, the Reidemeister moves [Rei26]. We illustrate the Reidemeister moves in figure 2.2. The first type of move, RI, removes one crossing that is simply a twist in the curve. The second move, RII, acts on two crossings, allowing an under part of

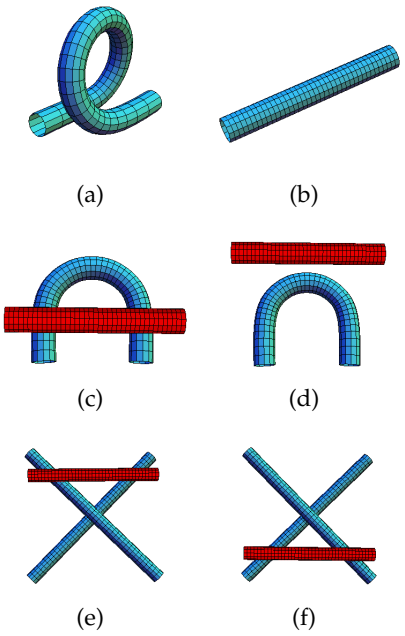

Figure 2.2: The Reidemeister moves : Type 1, RI, interchanges (a) and (b). Type 2, RII, interchanges (c) and (d). Type 3, RIII, interchanges (e) and (f).

the curve that simply returns back under the same over section, with no other crossings in between to be removed. The RII move lowers the crossing number of the projection by two. The third type of move, RIII, does not change the overall crossing number of the projection, but may reveal hidden type one and/or type two moves which are not obviously available to be made. The RIII move takes a strand from one side of a crossing to the other side.

After a repeated application of Reidemeister moves, a projection of a knot can be achieved in which no more crossings can be removed. This number of crossings is the *minimum crossing number* of the knot. This number is an invariant of the knot : it is the same whichever projection is initially taken. It is not obvious how to determine when this minimum number is reached, nor in what order to apply the required Reidemeister moves to achieve this.

The minimum crossing number has been used as a tool for the classification of knots. Historical knot tabulations have used this measure for grouping knots, for example in [Tai83a] and [Rol76, appendix C]. The unknot is a curve with minimum crossing number zero. There are no knots with minimum crossing number one or two. In such knots, the crossings can be removed by one or two applications of the RI move respectively.

From now on, unless otherwise stated, we shall assume that the number of crossings is the minimal number. With this, there is one distinct knot with three crossings and one with four, the trefoil and figure-8 knots respectively. There are

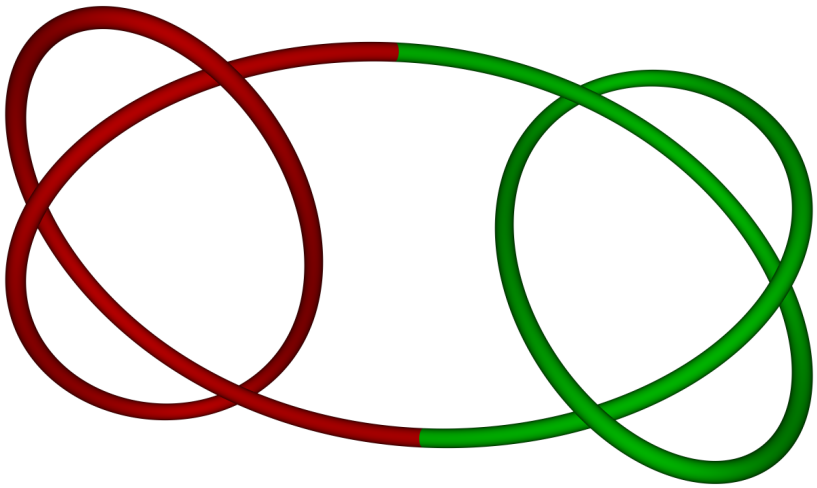

Figure 2.3: The sum of two trefoil knots. The two components are coloured red and green. This sum gives the granny knot, and is plotted from the formula given in [SKK98, ch. 18].

two knots with five crossings, the cinquefoil and the 3-twist knot.

For knots with six or more crossings there are two classifications that naturally arise : the *prime* knots and the *composite* knots, a concept similar to prime and composite numbers.[1] Two knots can be topologically joined to form their connected sum. A knot sum is formed by cutting the two knots and joining the loose ends of one knot to their respective ends in the second in such a way that no additional crossing are created. We illustrated this process in figure 2.3 for the sum of two trefoils. The sum of two knots is denoted $K_{\text{sum}} = K_1 \# K_2$.

Definition 2.5 (Prime Knot)**.** *A knot K is prime if its only decomposition into a knot sum is $K = K\#\texttt{unknot}$.*

The sum of two knots always leads to a more complicated knot and cannot become the unknot. This means that although $K\#\texttt{unknot} = K$ there is no K' such that $K\#K' = \texttt{unknot}$ unless both knots are themselves the unknot. There are no inverse knots for the knot sum operation. This result is due to the genus of a composite knot (the knot genus is discussed in section 2.5) being the sum of the genera of the component knots [Rol76, p. 119] where the unknot has genus zero. We shall assume all knots we encounter are prime.

[1] Other classifications exist at this stage, but will be introduced as required later.

The prime knots are listed by Rolfsen [Rol76] for crossing number up to ten based on Conway's tabulation [Con70]. We use the same notation for prime knots, which are the class we consider, as Rolfsen, based on the Alexander-Briggs notation [AB27] : C_i represents the i^{th} knot with crossing number C in this table. The problem of classifying knots is an ongoing process in which more knots are being classified and mistakes corrected. Rolfsen's table proliferated a mistake in the tabulation of prime knots. The knots 10_{161} and 10_{162} are actually the same but shown with differently projected diagrams. This error originates from the work of Little [Lit00] and was discovered by Perko [Per74]. Perko noted this error before the publication of Rolfsen; however when discussing the ten crossing knots care, is needed to make sure this error is not reflected in the notation.

The existence of the Perko pair illustrates the difficulties in tabulating knots. Tabulation of knots was first considered by Tait, working on the vortex atom hypothesis of Lord Kelvin [Tho67]. The work of Tait [Tai77, Tai83a, Tai83b] and Little [Lit90, Lit00] extended the tabulation, although not the concept of vortex atoms. The tabulation was increased further by Hoste et al [HTW98] reporting an extension of knot tables up to those with sixteen crossings. The title of this paper, "The First 1706936 Knots" gives an insight to the scale of the project. Recently, the work of Rankin et al [RFS04a, RFS04b, RF04] enumerated the alternating knots up to twenty two crossings. Their work gives nearly five billion distinct alternating knots with twenty two crossings, a number which does not include the non-alternating knots, nor those with lower crossing numbers! Table 2.1 shows the number of prime knots for each crossing number up to thirteen.

We have only considered the presence of one curve. It is possible for there to be multiple copies of S^1 embedded in S^3. Such situations give rise to links.

Definition 2.6 (Link)**.** *A link L_n with n components, is the disjoint union of (possibly knotted) curves such that*

$$S^3 \supset L_n = \dot{\bigcup}_{i=1}^{n} K_i, \tag{2.4}$$

where each $K_i \cong S^1$.

Linking of spheres in higher dimensions can occur when the embedding space has codimension > 2 [Rol76].

In common with knots, the curves of a link are free to be deformed by ambient isotopy whilst always remaining distinct. If a plane can be positioned between two curves of a link (after appropriate deformation) then they are not linked: they form an unlink [Ada94]. Linking can be detected by considering the link's projection into two dimensions. In such a projection, each curve is

Minimum Crossing Number	Number of Prime Knots
0	1
1	0
2	0
3	1
4	1
5	2
6	3
7	7
8	21
9	49
10	165
11	552
12	2176
13	9988

Table 2.1: The number of prime knots, up to chirality and orientation, for a given minimal crossing number up to thirteen. The tabulation up to ten crossings is popularly taken from [Rol76]. The numbers of knots with higher crossings is in [HTW98], with data on the higher crossing knots available at [BNM10] and [CL10].

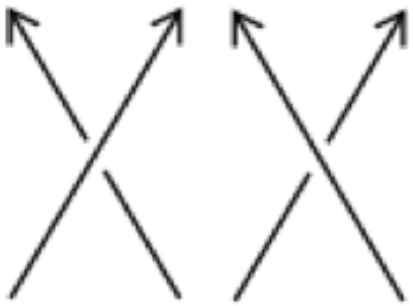

(a) (b)

Figure 2.4: (a) A positive $+1$ crossing. (b) A negative -1 crossing.

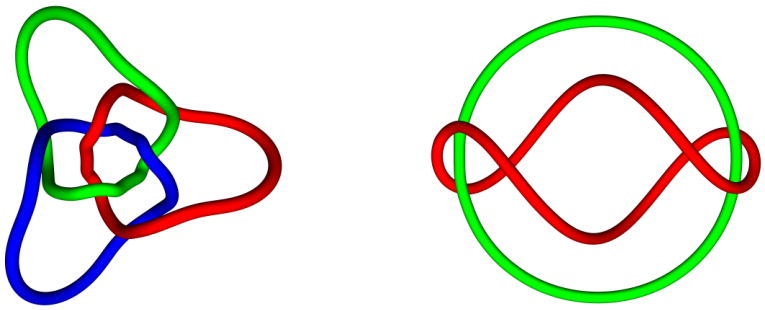

(a) (b)

Figure 2.5: (a) The three component Borromean rings in a configuration that is created with the construction of chapter 4. (b) The Whitehead link, from the form given in [PW92], given from a different projection direction to the standard projection of Rolfsen [Rol76].

given an orientation and for each crossing, a sign can be assigned as shown in figure 2.4. When disregarding self-crossing, those with another part of the same curve, half the sum of the ± 1 assigned to each crossing is the linking number, Lk. This does not detect links which have a zero linking number but are actually linked, such as the Whitehead link, $L5a1$, and the Borromean rings, $L6a4$, illustrated in figure 2.5. These kinds of linking can be detected by other measures but we do not employ them in this thesis. We use the Thistlethwaite notation for links to be consistent with [BNM10].

An important class of knots are the *torus knots* which are relatively simple to construct and are well studied. A torus knot is a closed curve that can be embedded on the surface of a torus in $\mathbb{R}^3$ or S^3. The curve wraps round the internal circle n times and the central hole m times. When m and n are coprime, then the curve is a (m, n)-torus knot, $T_{m,n}$. In cases where m and n are not coprime, then it is not possible to form such a curve on the surface of a torus. However for $\text{hcf}(m, n) = d$, it is possible to create d distinct curves that wrap round the central hole m/d times and the internal circle n/d times. This set of curves is a torus link, also denoted $T_{m,n}$. Such wrapping around the two circles of the torus can be seen by viewing the torus as a square, with periodic boundaries imposed. This is shown for the Hopf link, $T_{2,2}$, and trefoil knot, $T_{2,3}$, in figure 2.6.

In identifying torus knots, the simple projection and three-dimensional geometric form they possess has often been overlooked. The knot 8_{19} is isotopic to $T_{3,4}$ yet is presented in the historical tabulation in an overly complex projection. The calculation of knot invariants and their properties is made simpler if the calculation begins with a simpler representation. This comparison of common

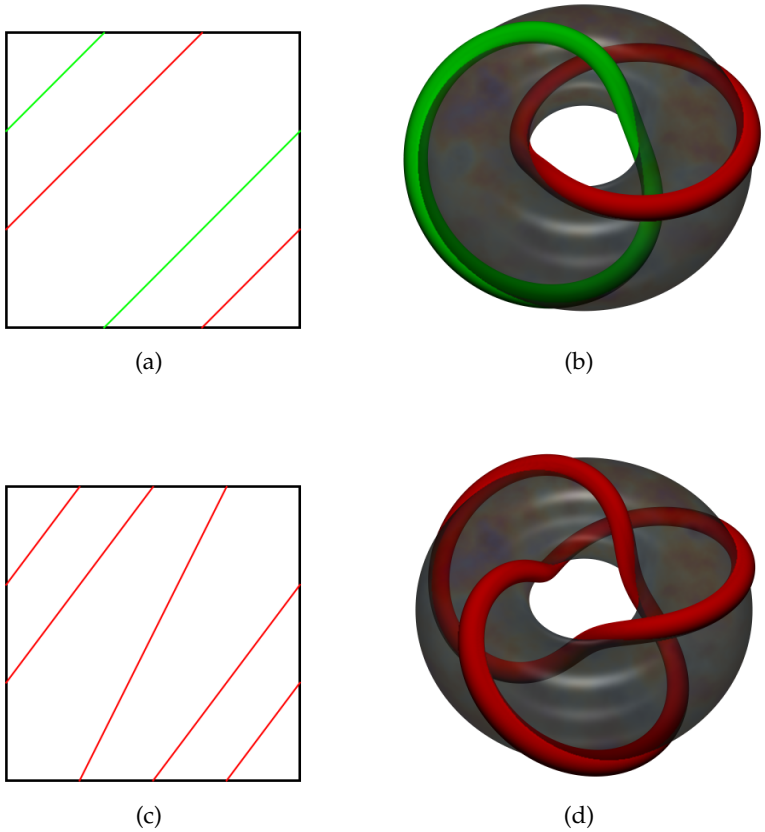

(a) (b)

(c) (d)

Figure 2.6: (a) The planar representation of the torus with the two components of the Hopf link shown in red and green with (b) showing the curves lying on the surface of a torus. (c) The trefoil knot shown on a planar torus with (d) showing the same knot on the surface of a torus.

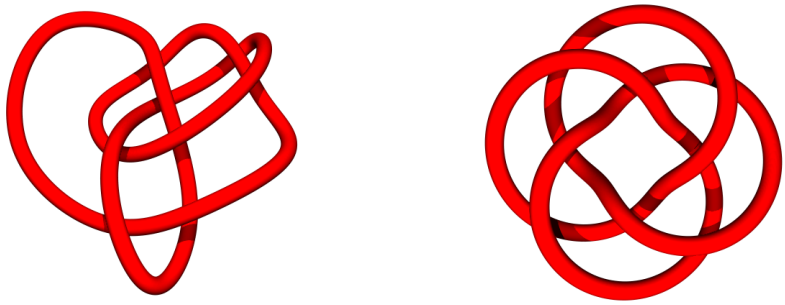

(a) (b)

Figure 2.7: Two different geometric forms of the knot 8_{19}. (a) The common form given for this knot, [Rol76] compared to (b) showing the many symmetries associated with this torus knot. The "nicer" form does not have any fewer crossings.

geometric forms for the same knot is shown in figure 2.7.

An extension of the torus knots are the cable knots. A cable knot is a form of satellite knot [BZ85] constructed in the following way : a knot, K_1 , is embedded in an unknotted torus, the torus is then treated as a curve itself and knotted to form K_2. The resulting knot is a *satellite knot*. A *cable knot* is a satellite knot formed when K_1 is itself a torus knot. These are also known as *iterated torus knots*. We consider cable knots in section 2.6.

2.2 Notations of Planar Projections

We make extensive use of the planar projections of knots and links into two dimensions to describe and identify the original three-dimensional curve. To algorithmically utilise these diagrams, we require methods to describe them. The three notations introduced in this section all possess properties that reveal different properties of the knot directly. Our preferred method in calculations is the "Planar Diagram Notation" (PD notation) [BNM10], with Conway notation [Con70] used extensively in later sections and chapters.

PD notation treats the knot projection as a graph, inheriting its planar orientation from the knot's orientation. This notation labels the edges between each crossing, the vertices of the graph, of an orientated curve. An initial crossing is chosen and one of the edges leading away from the crossing following the orientation is labelled "1". The orientation is followed and each edge is labelled consecutively as shown in figure 2.8. This procedure associates four numbers to each crossing, each representing an edge that begins/terminates there. They are listed a specific order : the first is the edge whose direction is towards the crossing and one of the two lower edges, passing under the top two edges, with the remaining three following in the order they appear travelling anti-clockwise about the crossing. The PD notation is presented as a list of X_{abcd} where the a, b, c, d are the edges in the detailed ordering.

The presence of crossings that can be removed by RI is readily seen from the PD notation. Such a crossing has an edge both start and end on the same crossing, giving a label X_{aabc} up to a cyclic permutation of $aabc$. Crossings with labels like this can be removed to make a simpler projection with the all the edge labels greater than a relabelled as one less.

It is also possible to remove crossings using RII directly from the PD notation. There are eight cases of pairs of crossings that can be removed in this fashion. The eight cases are shown in table 2.2. These cases represent the different combinations of the possible orientations of the curve segments and crossing signs.

$\{a, b+1, a+1, b\}$	$\{a+1, b+1, a+2, b+2\}$
$\{a, b+2, a+1, b+1\}$	$\{a+1, b, a+2, b+1\}$
$\{a, b+1, a+1, b+2\}$	$\{a+1, b+1, a+2, b\}$
$\{a, b, a+1, b+1\}$	$\{a+1, b+2, a+2, b+1\}$
$\{b, a, b+1, a+1\}$	$\{b+1, a+2, b+2, a+1\}$
$\{a, b+2, a+1, b+1\}$	$\{a+1, b, a+2, b+1\}$
$\{b, a+1, b+1, a+2\}$	$\{b+1, a+1, b+2, a\}$
$\{b, a+1, b+1, a\}$	$\{b+1, a+1, b+2, a+2\}$

Table 2.2: The eight pairs of crossings that can be removed by the RII move by the inspection of the PD notation.

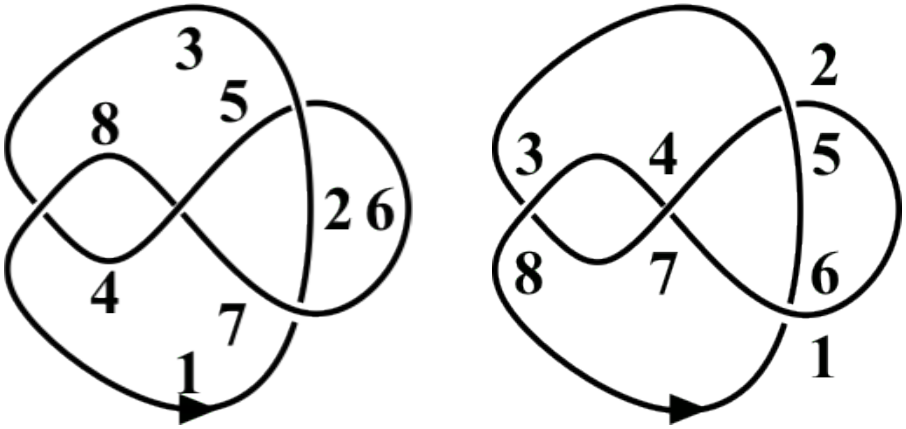

(a) (b)

Figure 2.8: (a) The figure-8 knot with the edges labelled to compute the PD notation. It can be seen that the PD notation is $X_{1627}X_{5263}X_{7584}X_{3148}$. (b) The figure-8 knot with the vertices labelled to compute the Dowker notation. From this it is $\{6284\}$.

We now introduce a second notation, Dowker notation [DT83], to compare with. This assigns two integers to each crossing, starting with 1, and following the orientation, the labels are assigned consecutively. Each crossing is therefore labelled with a pair of numbers, one odd and one even, shown in figure 2.8. In order of their appearance following the orientation, the even numbers only are kept. This list of even numbers is the *Dowker notation.*

The knot reconstructed from Dowker notation is unique if the knot is amphichiral. Amphichiral knots are equivalent to their mirror image [Ada94]. The difference between these mirror images is not usually considered when tabulating distinct knots, nor in our work on the construction of knotted nodal curves. The trefoil knot is chiral, a left-handed and right-handed version exist, but the figure-8 knot is amphichiral, not having the existence of such a mirror image.

Conway Notation

The third notation we introduce is the Conway notation [Con70]. Unlike the PD and Dowker notations, which assign a symbol to each crossing, the Conway notation builds up from elements that can represent several crossings. These individual elements are *tangles*. A section of a knot is enclosed in a 2-sphere, which becomes a circle when represented in a plane. In both cases, the knot section only intersects the bounding sphere at four distinct points. The four intersection points can be moved to fixed positions, represented by the compass directions NW, NE, SE and SW. When a projection is made, it is the interior of the circle, with the curve segments arranged as such, that we refer to as tangles. Specifically, these are 2-tangles, with only two curves terminating on the bounding circle with a not necessarily empty set of closed curves contained within the circle.

A tangle itself is not a knot or link but may contain a complete closed curve that is. To build up to a notion of a complete knot or link we begin with the simplest tangles, which contain at most one crossing in the projection. There are two tangles with no crossings, that with a curve linking the NE to NW points and a separate curve joining SE to SW, and the tangle that links NE to SE and NW to SW with no crossings. These are called the zero (0), and infinity (∞), tangles respectively. There are also two tangles that contain just one crossing, both with curves linking NE to SW and NW to SE. The sign of the crossing determines the name of such a tangle. With no orientation defined on the tangle as yet, the upper strand being the NE to SW curve leads to the tangle $+1$ and respectively the -1 tangle has this curve as the lower strand. With this orientation of the tangle, the upper stand has positive gradient; directed from the SW to the NE locations. These four basic tangles are illustrated in figure 2.9. The Reidermister moves can be used to modify a tangle to achieve one of these basic tangles, and if this is possible, then the original tangle is equivalent to the basic tangle achieved through this process.

Tangles containing more crossings are possible. The tangle 2 contains two crossings formed by the twisting of the zero tangle twice, to form two positive crossings. This tangle is shown in figure 2.9. Likewise the tangle -2 is formed in the same way by twisting in the opposite direction. Higher numbers of crossings, all with the same sign, are formed in this way.

Two arbitrary tangles, T_1 and T_2, can be combined in a number of formal ways. The first is addition, denoted $T_1 + T_2$. The sum is formed by joining the NE point of T_1 to the NW point of T_2 and the SE point of T_1 to the SW point of T_2. The new tangle formed has the NW and SW points corresponding to the respective points in T_1 and NE and SE points corresponding to the respective

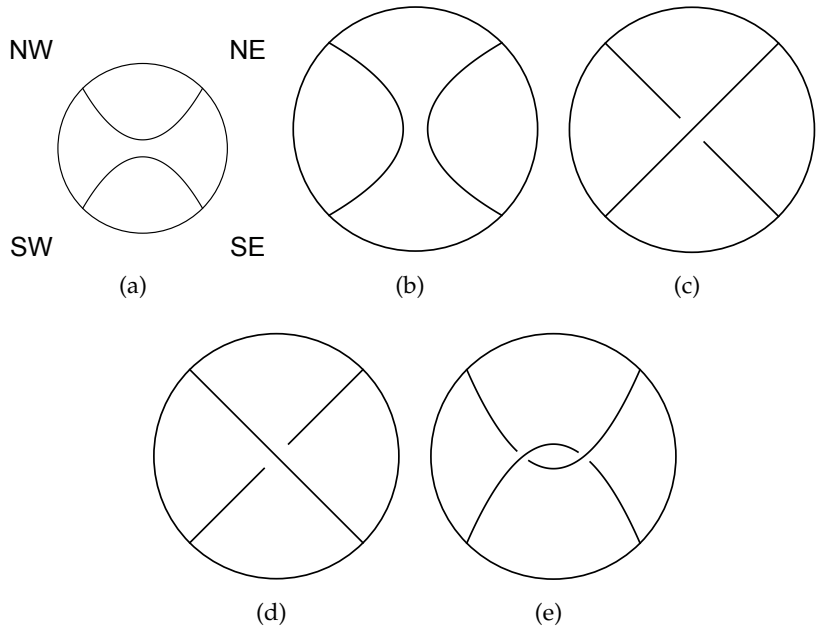

Figure 2.9: (a) The tangle 0, shown with the compass points labelled. (b)-(e) show the ∞, 1, -1 and 2 tangles respectively. This enumeration extends to higher numbers of crossings in the obvious way.

points in T_2.

The multiplication of tangles is denoted $T_1 \cdot T_2 = T_1 T_2$ which is also called the product of the two tangles. Unlike addition, multiplication requires an operation on T_1 before combining the two tangles. This operation is $T \mapsto -T$ which takes a tangle to its reflection in the line from the NW to SE points. The product of two tangles is defined as $T_1 T_2 = (-T_1) + T_2$.

The third binary operation on tangles is ramification. This is defined as $T_1, T_2 = (-T_1) + (-T_2) = -T_1 - T_2$. These three operations are illustrated in figure 2.10.

A tangle forms a knot by joining the points on the circle to each other with two curves that remain outside of the circle. The numerator closure is given by joining the northern points together and similarly the southern points. The denominator closure given by joining the two eastern points to each other as well as the two western points to each other. It is the numerator closure we assume and use through out.

It is not possible to represent every knot and link using the three operations defined so far. Conway lists a set of graphs, called polyhedra, with each vertex having valency four. The vertices, labelled $1 \ldots n$, are then replaced with n tangles $T_1 \ldots T_n$, joined as defined in Conway's paper. Each tangle is separated by . for example $6^*a.b.c.d.e.f$. The polyhedron 6^* is shown in figure 2.11. Two

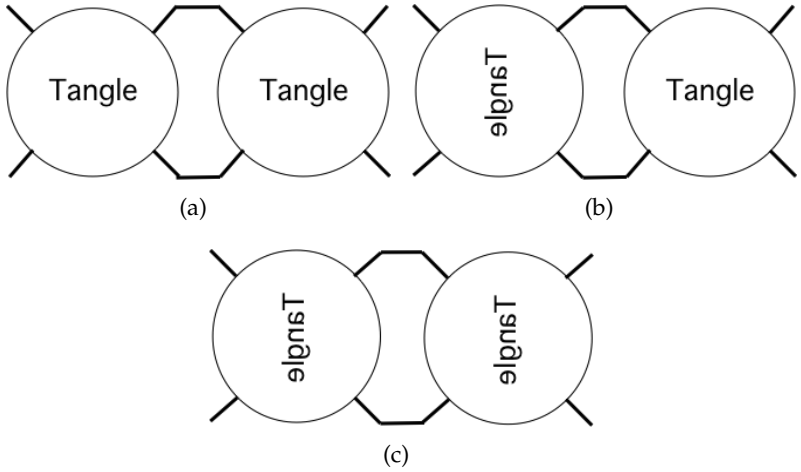

Figure 2.10: The three operations to combine tangles in Conway notation : (a) summation, (b) product and (c) ramification. The word "Tangle" shows the orientation of the tangle within each unit being combined.

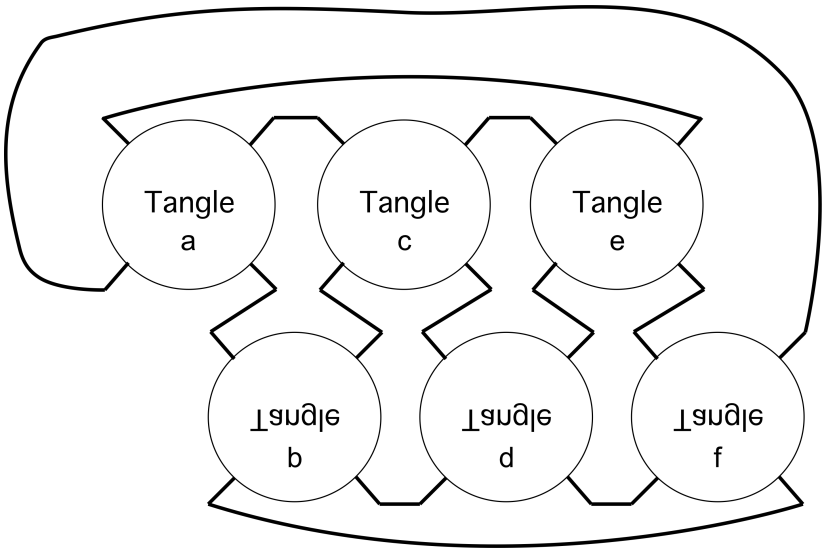

Figure 2.11: The graph of the six vertex, four-valent polyhedron represented by the symbol 6^* in Conway notation. The orientation of the tangles placed in at each vertex is shown with the word "Tangle".

distinct graphs with six vertices are required, additionally 6^{**}, along with one for both eight and nine vertices. The tabulation of knots of up to eleven crossings and links up to ten crossings, requires three graphs with ten vertices and one with eleven vertices to describe them all in Conway notation. These graphs have no unique notation outside of Conway's tabulation. The symbol : is used to contract several 1's for example $8^*2.1.3.4.1.1.5.1$, a knot on an eight vertex graph, becomes $8^*2 : 3.4 : 5 :$.

The simplest polyhedron is the 1^*, which admits just one tangle.

Definition 2.7 (Algebraic Knot (Conway))**.** *Knots and links formed by the numerator closure of a tangles formed on the simplest polyhedron, 1^*, are the algebraic knots and links in the sense of Conway. These knots are also called rational knots, explained in section 2.7 and the equivalent definition 2.14.*

We display the Conway notation of rational knots (knots algebraic in the sense of Conway) in [] brackets. These knots are formed by only combining tangles using the product operation on tangles formed on 1^* graphs. These knots and links are discussed in the later section 2.7. If a knot is not rational, the knot is called non-algebraic (in the sense of Conway) or *polyhedral*.

The figure-8 knot is a rational knot with Conway notation [2 2]; however the related Borromean rings are not rational with Conway notation 6^*. The Borromean rings are hence a polyhedral link. The Borromean rings are realised in this tangle language by placing the tangle "1" on all the vertices of the graph 6^*. This cannot represented as a sequence of products of tangles.

2.3 Braids and Complex Functions with Braided Zeroes

An important step in our work to consider functions with knotted zeroes are functions with zeroes that form braids. The abstract group definition of braids has remarkable geometric and topological interpretation which allows us to use group theoretic properties to describe a knot, yet use the simpler braided functions.

Definition 2.8 (Braid Group [Bir74])**.** *The braid group, of n strands, denoted B_n, is the group with $n-1$ generators, σ_i, with the following relations,*

$$\sigma_i\sigma_j = \sigma_j\sigma_i \quad \textit{when } |i-j| \geq 2 \tag{2.5}$$

$$\sigma_i\sigma_{i+1}\sigma_i = \sigma_{i+1}\sigma_i\sigma_{i+1} \quad \textit{when } i \leq n-2. \tag{2.6}$$

We refer to equations (2.5) and (2.6) as BR1 and BR2 respectively. A braid word, b, is a sequence of l generators and has length l. We refer to each element in a braid word as a letter.

It is the geometric interpretation of braids that makes them a powerful tool. The motion of n particles in $\mathbb{R}^3$ moving between two parallel (x, y)-planes such that z is always increasing monotonically, an example of which is given in figure 2.12, trace out as their trajectory a set of strings which forms the braid. The motion is described, without loss of generality, between the $z = 0$ and $z = 1$ plane and the motion in z is always increasing, not stationary or reversed. The strings do not intersect. The particles' initial locations are positioned with increasing x coordinate and arbitrarily in y. As z increases the particles move to a point in $z = 1$ such that it is opposite one of the starting positions in the $z = 0$ plane. This action takes the set of n points in the $z = 0$ plane $(x_i, y_i, 0)$ to the set $(x_i, y_i, 1)$. In such a motion, they remain distinct, never touching each other. The path that is taken by each particle is considered as a piece of string leading to n strands that twist around each other.

Choosing a fixed viewing direction, the braid strands pass over and under each other. These are similar to the crossings of a knot projection and map one to one to the braid group generators. At a crossing, the two strands involved are the i^{th} and $(i+1)^{th}$ position. The i^{th} strand crossing over $(i+1)^{th}$ corresponds to the generator σ_i. Crossings of the opposite sign correspond to the inverse element, σ_i^{-1}. The list of the crossings in the order they occur leads to a braid word representing the string's topology. We additionally use the notation 1 and $\bar{1}$ to represent σ_1 and σ_1^{-1} respectively.

Equivalently the particles can be replaced by the zeroes of a complex scalar function. In the (x, y)-plane, the zeroes move around, never overlapping to form a point where the multiplicity of the zero increases. The loci of the zeroes as z varies can form a braid if the conditions above are met.

We illustrate braids contained inside a cylinder. The circular faces contain the required subset of the start and end planes such that the braid intersects both of these planes in the periodic fashion described above. We represent the distance between the parallel faces by h, the height of the cylinder, and this becomes the parameter for a function describing the transverse position of each braid stand. We now use h rather than z for this coordinate to make clear in our construction the difference between the abstract braid space and real space where the knotted curve exists. An example of a braid enclosed like this is shown in figure 2.12.

To construct functions with knotted zeroes, our initial step is the construction of complex scalar fields with braided nodal lines. We construct complex functions p_h with braided zeroes as follows. For each height h, the braided functions we construct are factorisable in a formal variable u and have N distinct zeroes

Figure 2.12: The braid for the word $(\sigma_1\sigma_2^{-1})^2$. The braid is shown contained inside a cylinder with height coordinate h. The braid is given by the zeroes of equation (2.7) with $s_j = \cos h_j + \mathrm{i}\sin 2h_j$, $N = 2$ and $h_j = h - 2\pi j/3$. The strands of the braids follow the Lissajous figure, the lemniscates shown in black, as h varies.

at positions parameterised by h,

$$p_h(u) = \prod_{j=0}^{N-1}(u - s_j(h)), \tag{2.7}$$

where s_j defines the location of the N roots as a function of h. We choose to parameterise the roots trigonometrically to form Lissajous curves because of a later use of v from equation (2.3) and its proportionality to $\mathrm{e}^{\mathrm{i}h} = \cos h + \mathrm{i}\sin h$, allowing us to form Milnor maps, described below. In general, any well-behaved function can be used to construct p_h but we will only use trigonometric functions. These functions give plane curves of the form $(\cos \alpha h, \sin \beta h)$ where $\alpha, \beta \in \mathbb{N}$ give the number of "loops" in the x and y directions respectively. We choose

to set $\alpha = 1$ and hence only have, for $\beta > 1$, loops in the x direction. The case $\beta = 1$ leads to a circle, $\beta = 2$, a lemniscate and $\beta = 3$ the "double lemniscate".

We require the braids to be periodic in h. This means that for a set of starting positions at $h = 0$, $\{(x_i, y_i)\}$, the braids strands end at a point in this set when $h = 1$. In the next step, we shall be closing the braid by associating these points at $h = 0$ with their corresponding point, their opposite, at $h = 1$. A strand starting at a specific member of this set does not have to finish at the opposite point.

This means we can write equation (2.7) as

$$p_h(u) = \prod_{j=0}^{N-1} \left(u - \left(\cos h_j + \mathrm{i} \sin \beta h_j\right)\right). \tag{2.8}$$

It is now natural with this trigonometric expression to consider the braid to be formed in the region $0 \leq h \leq 2\pi$ rather than the more general normalised $0 \leq h \leq 1$. The (trigonometric) braid being periodic in h means that after each change of h by 2π, the zeroes in the complex u plane are in the same position as where they started.

Definition 2.9 (Basic Braid Word)**.** *The braid word formed in one h period of equation (2.8) is the basic braid word of the equation.*

The number of strands, N, must be chosen such that as h varies they remain distinct. For a circular trajectory this is not an issue because the curve does not self-intersect. For $\beta > 1$ the number of zeroes and their respective spacings needs to be chosen to avoid such pathological situations. This method of constructing functions with braided nodal lines we call the *Lissajous construction*. We explore the full details of the Lissajous construction are explored in chapter 4.

Geometrically a braid is a set of open ended curves. Our interest in knots requires closed curves. Alexander [Ale23] showed that any knot or link can be expressed as the closure of some braid. The closure is formed by joining each $(x_i, y_i, 0)$ to their respective $(x_i, y_i, 1)$ such that the braid encloses a fixed axis. Obviously, the stands may be in a different order in the end plane to the start plane. No strands are able to cross the fixed axis. This closure forms the knot or a link. We denote the closure of a braid word b as $\hat{b}$.

We form the closure of the braid in the following fashion. The product $p_h(u)$ has trigonometric terms, $\mathrm{e}^{\mathrm{i}h}$, which are substituted for a second formal variable, v. This leads to an expression in u, v, v^*, where v^* is the complex conjugate of v used to substitute $\mathrm{e}^{-\mathrm{i}h}$.

Definition 2.10 (Milnor Polynomial)**.** *The Milnor polynomial is the function that is formed by substituting u, v, v^* into p_h of equation (2.8).*

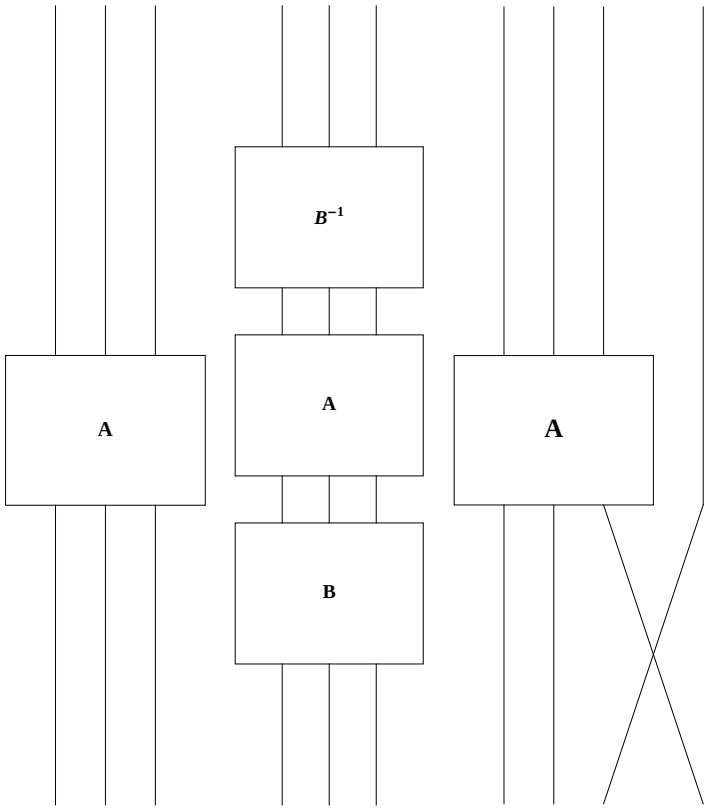

Figure 2.13: The two Markov moves. Starting with an initial braid in (a), conjugation is given by forming $B^{-1}AB$ in (b) and taking its closure. Stabilization is the addition of the extra strand and crossing shown in (c), equivalent to a Reidemeister move type one on the inner loop.

The nodal set of the Milnor polynomial corresponds to the closure of the braided nodal curves formed by taking u and v as in equations (2.2) and (2.3). The use of v^n and v^{*n} in the formation of the Milnor polynomial leads to the closure of n repeats of the basic braid word. We study the details of this closure along with the Lissajous construction in chapter 4.

In a comparable way to the Reidemeister moves, a closed braid can also be manipulated in a geometric fashion too. These are the Markov moves and there are two of them [Man04]. The first is conjugation of A with respect to B. This operation takes the closure of A and gives the closure of $B^{-1}AB$ as an isotopic pair. The second move is stabilization of A. This gives as equivalent $\hat{A}$ and the closure of $A\sigma_{n-1}$, where $A \in B_{n-2}$, the braid group of $n-2$ strands. The additional crossing can be positive or negative (by replacing σ_{n-1} with σ_{n-1}^{-1}). We make use of stabilization in our work to simplify braid word generated by our construction.

2.4 Alexander Polynomials

The problem of identifying knots is that many different knotted curves share common properties with inequivalent curves. For example, the minimum crossing number of a knot is shared with many different knots as this number increases. Knot theory aims to be able to uniquely determine the knot type of a given curve, and tell if it is topologically distinct from another curve. One kind of invariant that improves on what we have seen are knot polynomials.

A knot polynomial does not describe the curve itself; it is not a function that can be used to directly draw the knot. They encapsulate in their coefficients information about the complement of the knot and its properties. Here we introduce the *Alexander polynomial* of a knot [Ale28]. We now give a description of the Alexander polynomial and outline our algorithm for calculating it as well as discussing further knot polynomials, the Jones [Jon85] and HOMFLY-PT [FYH$^+$85, PT87] polynomials. We begin our description by requiring the notion of the group of a knot.

Definition 2.11 (Knot Group [CF63])**.** *The group of a knot is the fundamental group of the complement of the knotted curve K, $\pi_1(\mathbb{R}^3 \setminus K, p)$ where p is a fixed base point not on K.*

This could equally be defined using the complement in S^3 but we use the notations and descriptions of Crowell and Fox [CF63] and Fox [Fox62] throughout this section.

For a knot, a set of curves which can be used to define the knot group can be found by considering a projection of the knot. In between each crossing of a projection, the curve is split into arcs. Let a loop start and end at p be such that it has an arc of the projection "thread" through it. We call such a loop a *homotopy curve*. Labelling the arcs sequentially following the orientation of the knot, each arc has an associated homotopy curve x_i. Figure 2.14 shows this for the trefoil knot.

The number of required curves, labelled x_i, to define the knot group can be reduced with the following relation

$$x_j x_i x_j^{-1} = x_k, \tag{2.9}$$

which involves one crossing in the projection and where j corresponds to the j^{th} arc, the over arc, orientated such that two under arcs, the i^{th} and k^{th} are on the left and right respectively, as in figure 2.15.

Using this relation, a presentation for the knot group can be given, involving a set of relators $r_i = 1$, created by using the relation in equation (2.9). Ideally

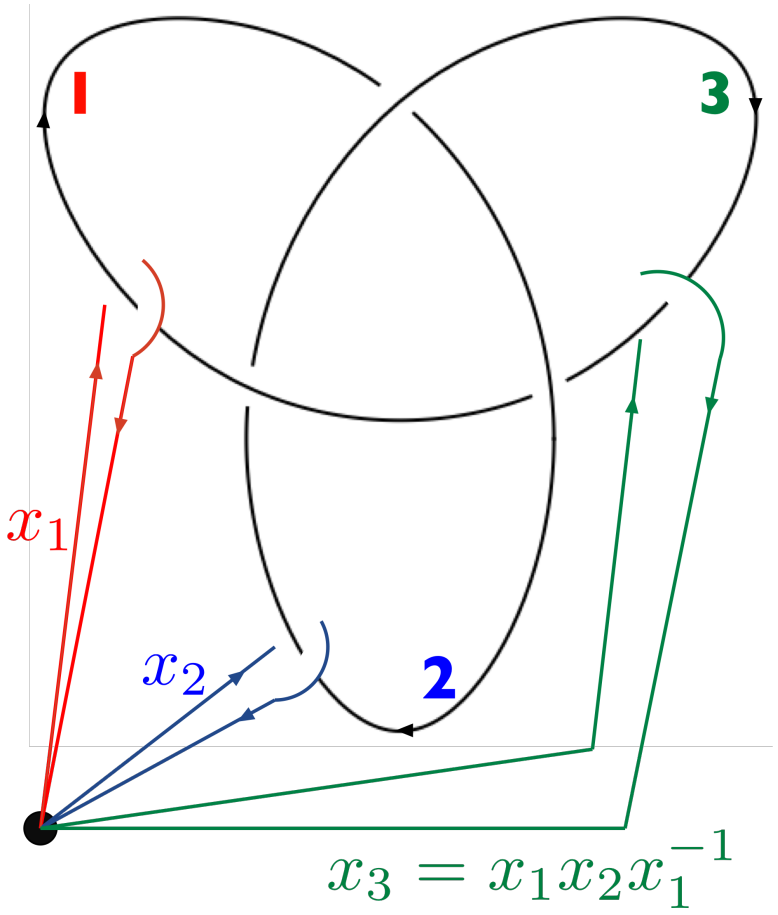

Figure 2.14: The process of constructing the Alexander polynomial for the trefoil knot. We show the three possible homotopy loops from a base point $p : x_1, x_2, x_3$. The respective arcs of the projection are also labelled $1, 2, 3$. The loop x_3 around arc 3, can be written in terms of the other two homotopy loops such that $x_3 = x_1 x_2 x_1^{-1}$.

this set of relations will be as simple as possible, eliminating as many of the x_i as possible. To arise at the Alexander polynomial, we need to introduce the *free derivative*, as used in both Crowell and Fox [CF63], and Fox [Fox62]. This is a form of calculus that acts on the elements (words) of the homotopy group π_1 and returns elements of an integral group ring of a free group, which consists of polynomials of elements of π_1 [Fox53].

Definition 2.12 (Free Derivative [Fox62]). *For a word $w = x_{j_1}^{\epsilon_1} x_{j_2}^{\epsilon_2} \ldots$, an element of the fundamental group in our case, the free derivatives are the*

$$\frac{\partial w}{\partial x_j} = \epsilon_1 \delta_{jj_1} x_{j_1}^{\frac{1}{2}(\epsilon_1 - 1)} + \epsilon_2 \delta_{jj_2} x_{j_1}^{\epsilon_1} x_{j_2}^{\frac{1}{2}(\epsilon_2 - 1)} + \ldots \tag{2.10}$$

where $\delta_{jj_i} = 0$ when $j \neq j_i$ and equals 1 when $j = j_i$.

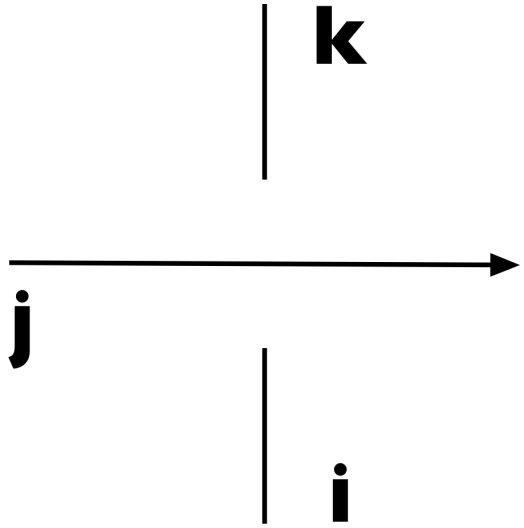

Figure 2.15: The relation for reducing the number of distinct homotopy loops required to create a presentation for the knot group. The j^{th} arc is the over-arc and it has an orientation defined on it. The i^{th} and k^{th} arcs form the under strand and their order and orientation are not required for $x_k = x_j x_i x_j^{-1}$.

We now give an example of the free derivative, with word w in a group with two generators, x_1 and x_2, where $w = x_1 x_2 x_1^{-1} x_2 x_1 x_2^{-1}$:

$$\frac{\partial w}{\partial x_1} = 1 - x_1 x_2 x_1^{-1} + x_1 x_2 x_1^{-1} x_2 \tag{2.11}$$

$$\frac{\partial w}{\partial x_2} = x_1 + x_1 x_2 x_1^{-1} - x_1 x_2 x_1^{-1} x_2 x_1 x_2^{-1} \tag{2.12}$$

The free derivatives of the knot group presentation's relations are now used to map from homotopic loops (elements of the fundamental group) to a homological loop which is an element of a homology group, which the Alexander polynomial will represent. To do this, we require a Jacobian matrix $\mathcal{J}$ of the free derivatives of the relations. This is formed as

$$\mathcal{J} = \begin{pmatrix} \frac{\partial r_1}{\partial x_1} & \cdots & \frac{\partial r_1}{\partial x_n} \\ \vdots & \ddots & \vdots \\ \frac{\partial r_m}{\partial x_1} & \cdots & \frac{\partial r_m}{\partial x_n} \end{pmatrix}. \tag{2.13}$$

This matrix $\mathcal{J}$ is next abelianized, by mapping each of the x_i to t. The variable t will form the formal variable of the Alexander polynomial. For a knot group, this final group created is the first homology group of the knot complement, H. The abelianized $\mathcal{J}$ is called the *Alexander matrix*, we denote $\mathcal{A}$. The minors of the Alexander matrix define ideals in the polynomial ring, of polynomials in formal variable t in the group H. The minors of size $n-1$ give gener-

ators for the *Alexander ideal*. Each of these generators is an *Alexander polynomial*, $\Delta(t)$, for the knot and are all the same up to a factor of $\pm t^{\lambda}$, $\lambda \in \mathbb{Z}$ a constant.

We now give a worked example from Fox [Fox62] for computing the Alexander polynomial of the trefoil knot, $\mathfrak{S}$, from its knot group. The trefoil has three crossings (minimum number) and hence it has three arcs in its projection. This gives rise to three homotopy loops, x_1, x_2 and $x_3 = x_1 x_2 x_1^{-1}$, shown in figure 2.15. The fundamental group can be written with presentation

$$\pi_1(\mathfrak{S}) = \{x_1, x_2 : x_1 x_2 x_1 - x_2 x_1 x_2 = 0\}. \tag{2.14}$$

This gives one relation which can be written as

$$r = x_1 x_2 x_1 x_2^{-1} x_1^{-1} x_2^{-1} = 1. \tag{2.15}$$

This means that the Jacobian matrix, $\mathcal{J}$, is a 2×1 matrix, two columns for the two generators x_1 and x_2, and one row for the one relation r. The Jacabian is hence

$$\begin{aligned} \mathcal{J} &= \left(\frac{\partial r}{\partial x_1}, \frac{\partial r}{\partial x_2} \right) \\ &= \left(1 - x_2 + x_1 x_2, -1 + x_1 - x_2 x_1\right), \end{aligned} \tag{2.16}$$

which when abelianized with by letting $x_i \to t$, becomes the Alexander matrix $\mathcal{A}$,

$$\mathcal{A} = \left(1 - t + t^2, -1 + t - t^2\right). \tag{2.17}$$

The Alexander polynomial is given by any minor, a 1×1 entry in this case

$$\Delta(t) = 1 - t + t^2. \tag{2.18}$$

Both minors are equivalent to equation (2.17) up to multiplication of -1.

In constructing the Alexander polynomial we have moved from working with homotopy to working with homology. The Alexander polynomial describes a homological loop that transverses different levels in the infinite cyclic cover of the knot [Rol76, p. 162]. An image of the homotopy base point exists in each level of the cover. Moving from level to level is akin to passing though the Seifert surface of the knot. Seifert surfaces are two-dimensional manifolds that have the knot as their boundary ; we introduce them in section 2.5. Within each level, a homological loop is able to move freely without affecting the parts of the curve that exist in different levels. The Alexander polynomial describes the structure of loops in the infinite cyclic cover that can be annihilated by a single curve. Each term of the Alexander polynomial, t^i, describes what level in the cyclic cover the action is occurring. The coefficients, a_i, describe how

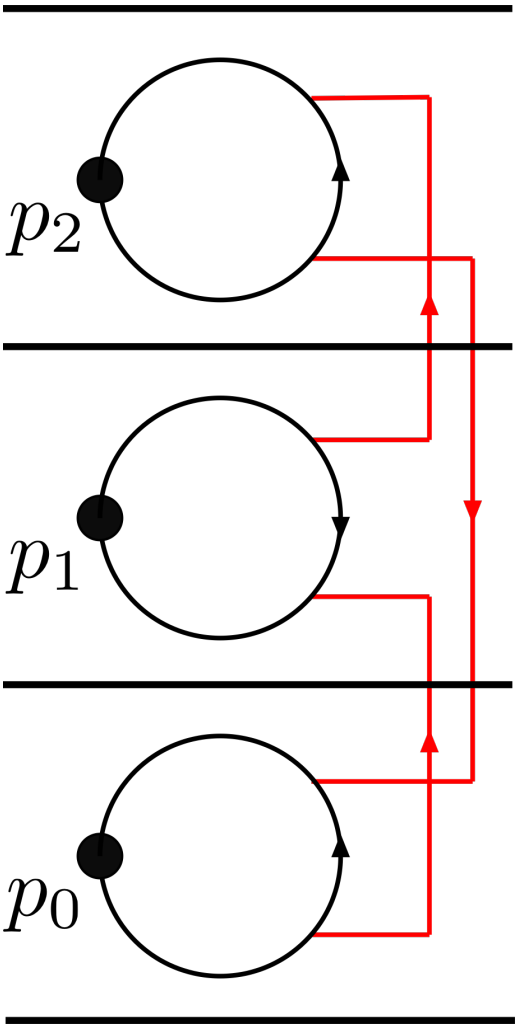

Figure 2.16: An illustration of the loops the Alexander polynomial of the trefoil knot describes and how they can be annihilated. The black loops, exist independently in the three levels of the infinite cyclic cover, at levels 0-2. The Alexander polynomial, $\Delta(t) = 1 - t + t^2$, describes that the "annihilator" loop can make trivial one positive loop in the 0^{th} level, the coefficient of the t^0 term, one loop of negative orientation in the first level and one positive orientated loop in the second. This process is shown by the red curve.

many loops, and of what sign, can be annihilated. The Alexander polynomial describes the *annihilator* of loops in the infinite cyclic cover of the knot it has been constructed for. This annihilator is shown in figure 2.16 for the trefoil knot to conclude the construction of the Alexander polynomial for that knot.

The Alexander polynomial is a symmetric polynomial. This means that for a polynomial of order n, the coefficients are such that $a_0 = a_n$, $a_1 = a_{n-1} \ldots$ Only a half list of coefficients need to be given to define the polynomial and this is often the only information tabulated, for example the tables in Rolfsen [Rol76]. Traditionally, if the Alexander polynomial is expressed fully, it is given as a symmetric Laurent polynomial, and hence the polynomial ring arising in the construction is the ring of Laurent polynomials with integer coefficients.

Jones and HOMFLY-PT Polynomials

The Alexander polynomial is not a perfect discriminator of knots. The knots 6_1 and 9_{46} share the same Alexander polynomial. For knots with eight or less crossings, the Alexander polynomial does distinguish all thirty-six cases. Clearly better methods of identifying knots are required.

The Jones polynomial $V(q)$, [Jon85], gives an improvement in knot identification over the Alexander polynomial. The difference in dates of Alexander 1928, and Jones 1985, shows the difficulty in the problem of knot identification. The Jones polynomial is in a formal variable $q^{\frac{1}{2}}$ and for knots this computes to integer powers of q. However, this polynomial faces difficulties in determining all knots. The knots 5_1 and 10_{132} share the same Jones polynomial. This is an improvement of an additional 214 knots over the Alexander polynomial before a repeat is found.

In chapter 4 we use the Jones polynomial to predict the knots and links created by our nodal knot construction of that chapter. Although a combinatoric method can be used to compute the Jones polynomial, we use the software "KnotTheory", a Mathematica program from [BNM10].

The final knot polynomial we consider is the HOMFLY-PT polynomial. This was found independently by [FYH$^+$85] and [PT87].[2] The former paper is the amalgamation of four separate papers submitted with four different methods and interpretations! The latter was sent at a similar time but sent to the different journal.

The HOMFLY-PT polynomial is a two variable polynomial, $H(a, z)$. It is related to both the Alexander and Jones polynomials. These can be recovered by $\Delta(t) = H(1, t^{\frac{1}{2}} - t^{\frac{-1}{2}})$ and $V(q) = H(q, q^{\frac{1}{2}} - q^{\frac{-1}{2}})$ respectively. This relationship

[2] HOMFLY-PT is an acronym of the authors of [FYH$^+$85], (Hoste, Ocneanu, Millett, Freyd, Lickorish, Yetter) and PT from Przytycki and Traczyk [PT87].

between the three polynomials means that although two knots may have the same Alexander *or* Jones polynomial, the HOMFLY-PT polynomial may distinguish the knots, but not necessarily. If two knots have the same Alexander and the same Jones polynomial, then the HOMFLY-PT polynomial is the same for both knots. This is the case for the 5_1 and 10_{132} knots.

Computing the Alexander Polynomial

The Alexander polynomial of a knot is computationally less involved than the equivalent Jones or HOMFLY-PT polynomials. Here we implement the method of Alexander [Ale28]. Orlandini and Whittington in [OW07] present the method used in the investigation of [ODP00] and Şimşek et al present an alternative in [ŞBY04].

Our approach is that of Alexander [Ale28] and we use the PD-notation of a knot projection as the input to the algorithm. To create the matrix required, we need the faces (or regions) of the projection to be found. This is so that their location with respect to each vertex can be correctly assigned. This is done by considering adjacent edges at a crossing that form a corner of the face, represented by the ordered pair $\{a, b\}$. This can be any consecutive edge labels from one crossing, such that you turn right when going from edge a to edge b. The algorithm looks for what the next possible corner is, that continues to make a right turn. Unless a crossing is removable by a Reidemeister type one move, which is normally pre-removed from the input, there are two possibilities for the next edge on the face boundary.

The next edge is chosen to continue round the face so that the edge chosen does not relate to the crossing it has just passed through. This process continues until an edge is found that is related to the first crossing considered. A look up table is formed of the location of the face with respect to each crossing as they are found. Once the maximum number of faces is found, number of crossing plus two, the algorithm halts its search process and this avoids double counting.

The matrix from which we compute the Alexander polynomial, the incidence matrix, is constructed by placing the values $\pm 1, \pm t$ as appropriate. The look-up table is used to remove columns from the incidence matrix that relate to adjacent faces. As a check, the algorithm will not remove faces bounded by a single edge, even though it can be assumed that crossings that lead to this situation have already been removed.

The determinant of the modified incidence matrix is computed. It is for this reason that we desire as many crossings that can be removed prior to entering the algorithm are removed as computing determinants is expensive computationally. The result is returned as a list of integers, representing the coefficients

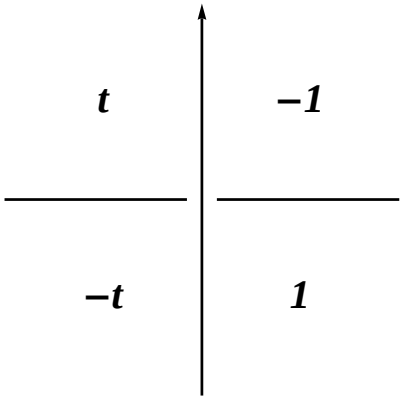

Figure 2.17: The designation of the terms $\pm t$ and ± 1 in constructing the Alexander polynomial from a projection. The orientation of the under arc is not important in the calculation. This is comparable to constructing a presentation for the knot group, see figure 2.15.

of the Alexander polynomial. This list is checked to ensure the central element is positive, and the list multiplied by -1 if necessary. The Alexander polynomial is symmetric, hence only the need for the coefficient list to be returned. This also removes the need for the correct power of $\pm t$ to be found by which to divide the determinant.

2.5 Fibred Knots

Now we have a method for constructing knotted zeroes in functions, we ask can these knots be realised as optical vortices? Or is there a prohibition from a property of the knot that restricts this physical realisation? We now look at such a property of a knot, the Seifert surfaces and relate this to optical situations.

A knotted curve has codimension two in its embedding space. To introduce fibred knots, we first consider the properties of the codimension one objects. These are two-dimensional manifolds and have the knot as their boundary. Such a manifold is a candidate to be a Seifert surface for the knot. If a manifold $M^2 \subset S^3$ such that $\partial M^2 = K$ is connected, orientable and compact, then it is a Seifert surface for the knot [Rol76, p. 118]. The surfaces normally considered have the lowest possible genus. The genus of an oriented surface is the maximum number of closed curves that can be removed from the surface, such that the remaining surface is still connected. The genus of a sphere is zero and that of a torus is one. The minimal genus of a Seifert surface is the genus of the knot and is a knot invariant. The genus of the Seifert surface of a torus knot $T_{m,n}$, is given by $\frac{1}{2}(m-1)(n-1)$ [Rol76, p. 122].

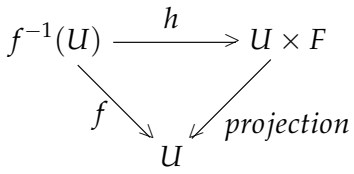

Figure 2.18: The properties of a fibration require that this diagram commutes, the functions and spaces are defined in the text.

We are now interested in a class of knots that have certain properties of their Seifert surfaces. Let f be a map between two topological spaces, $f : E \to B$ where E is known as the total space and B as the base space. There is also an associated space, F, the fibre. For all points $b \in B$, assign a neighbourhood U such that $h : f^{-1}(U) \to U \times F$ as in figure 2.18. If given U and h, a homeomorphism exists for each b and the diagram in figure 2.18 commutes, then f is a fibration [Rol76, p. 323], where the projection map is $(u, x) \mapsto u$. The sets $f^{-1}(b)$ are the fibres of the map f and are each homeomorphic to F.

Definition 2.13 (Fibred Knot [Rol76])**.** *If a fibration, f, can be found for $E = S^3 \setminus K$ and $B = S^1$, then K is a fibred knot. It is also required that f when restricted to a tubular neighbourhood of the knot $S^1 \times D^2 \setminus 0$ is the map to S^1 given by $(x, y) \mapsto \frac{y}{|y|}$ where $y \in D^2 \setminus 0$ which is a punctured disk. A fibred link has the same definition but with K replaced by L a link.*

If K is a fibred knot, then for $x \in B$ the base space, each of the $f^{-1}(x) \cup K$ is a 2-manifold with the knot as its boundary. This is a Seifert surface for the knot. In this case, they do not intersect except on the knot and they fill all space. Each Seifert surface can be parameterised by an angle in $[0, 2\pi)$ arising from such a description of S^1.

It is this property that interests us in seeking optical fields with knotted nodal lines. Optical fields have two-dimensional surfaces that are orientable and represent all phase labels in $[0, 2\pi)$. These are the surfaces of constant phase, or wavefronts. The wavefronts only intersect on vortex lines and hence have any knotted (or otherwise) vortex line as their boundary. For this reason, it is the *fibred knots* that we consider to create as optical phase singularities.

Fibred knots arise in singularity theory. The case for classical dimensions is explored here, although it can be to n-dimensional spaces. Let $f(u, v)$ be a polynomial with u and v being complex variables, that is not constant. The nodal set (the zero set) of this polynomial is $V = \{(u, v) : f(u, v) = 0\} = f^{-1}(0)$ and is a complex hypersurface. Around a critical point of f, where $\frac{\partial f}{\partial u} = \frac{\partial f}{\partial v} = 0$,

a small 3-sphere, denoted S_ϵ, is centred about the point. The intersection formed $V \cap S_\epsilon$ is a fibred knot [Mil68].

Fibred knots are detectable from the coefficients of their Alexander polynomial. The Alexander polynomial of a fibred knot is monic [Rol76, p. 326]. A monic polynomial has first and last (non-zero) coefficients equal to ± 1. This property gives the Alexander polynomial an advantage over the other knot polynomials in our work because it detects an important property in our work.

Not every knot is a fibred knot. All of the torus knots are fibred, as well as the figure-8 knot. It is however early on in the knot tabulation that examples of non-fibred knots are found. The knot 5_2 is not fibred.

The braid representation of a knot can be used to detect whether a knot is fibred or not. A homogeneous braid of n strands is one in which each of the $n-1$ generators appears in the braid word, each time at the same power, ± 1. The braid $\sigma_1\sigma_2^{-1}$ is homogeneous. By *Stalling's theorem* [Sta78], the closure of a homogeneous braid is a fibred knot.

2.6 Knots which are Algebraic in the sense of Milnor

In complex scalar fields, linked nodal lines are readily obtainable when the components themselves are unknotted. A single zero ring can be created as $\psi = u(\boldsymbol{r})$ where u is defined in equation (2.2). The location of the ring can be moved arbitrarily while maintaining the topology of the ring. Two rings can be placed by forming $\psi = (u+v)(u-v) = u^2 - v^2$, where v is as in equation (2.3). This forms the Hopf link. Chains of linked zeroes can be formed using this method by a simple extension. These chains are fibred links as the unknotted curve of each component is fibred; links consisting of components that are all fibred, are fibred links [Sta78].

The above polynomial in u and v generalises to the form $u^m - v^n$ which has a (m,n)-torus knot (or link) as its nodal set. Brauner [Bra28] gives this as a knot in S^3 arising from the intersection of the pre-images of zero with a small 3-sphere. This intersection lies in the torus of all points (u,v) where $|u| = \xi$ and $|v| = \eta$ where both ξ and η are constants [Mil68]. The knot is then the set $K = \left\{ (\xi \mathrm{e}^{\mathrm{i}n\theta}, \eta \mathrm{e}^{\mathrm{i}(m\theta + \frac{\pi}{n})}) : 0 \leq \theta < 2\pi \right\}$. Functions such as $u^m - v^n$ are algebraic $\mathbb{C}^2 \to \mathbb{C}$ functions. The torus and cable knots can be constructed from mappings of this form.

We therefore need to consider polynomials of a more general form to create a more varied range of knots. The case of functions $\mathbb{C}^2 \to \mathbb{C}$ are not the only way knots can arise. Functions that are algebraic $\mathbb{R}^4 \to \mathbb{R}^2$ functions, not requiring the complex structure of above, can also realise knots in their zero set.

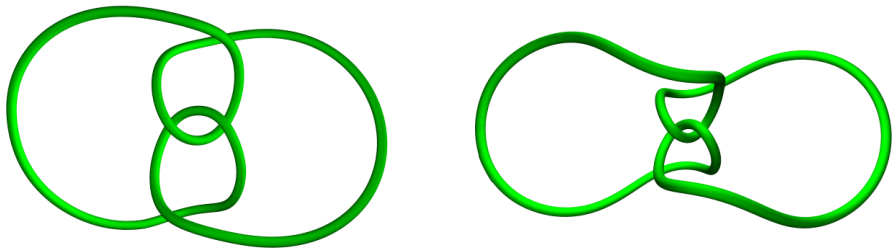

(a) (b)

Figure 2.19: (a) The figure-8 knot of Perron, given in equation (2.19). Here, $\rho^2 = \sqrt{2}$ as in [Per82]. (b) The figure-8 knot of Rudolph, given in equation (2.20). Both plotted curves are the zero (nodal) set of their respective functions.

Looijenga [Loo71] gives that a fibred knot arising from an isolated polynomial singularity of a function of the type $\mathbb{R}^4 \to \mathbb{R}^2$ cannot be homeomorphic to a fibred knot arising from an isolated holomorphic singularity of a $\mathbb{C}^2 \to \mathbb{C}$ function. Grothendieck's[3] work in this area gives that the Alexander polynomial of a fibred knot arising from an isolated holomorphic singularity of a function $\mathbb{C}^2 \to \mathbb{C}$ is always cyclotomic. The roots of a cyclotomic polynomial are roots of unity. In this case the Alexander polynomial is multiplied by the appropriate power of t to remove negative powers of t.

This is another reason for using the Alexander polynomial instead of other knot polynomials and invariants; it detects what type of function realises the knot. The figure-8 knot is fibred with Alexander polynomial (multiplied by t), $t\Delta(t) = t^2 - 3t + 1$. This is not cyclotomic, however the trefoil knot ($(2,3)$-torus knot) has $t\Delta(t) = t^2 - t + 1$ which is cyclotomic. This is consistent with our polynomial $u^2 - v^3$ being a function $\mathbb{C}^2 \to \mathbb{C}$.

Perron [Per82], gives an explicit form for the figure-8 knot, as a function $\mathbb{R}^4 \to \mathbb{R}^2$:

$$F(x,y,z,t) = (z\rho^2 + x(8x^2 - 2\rho^2, \sqrt{2}tx + y(8x^2 - \rho^2)) \tag{2.19}$$

where $\rho^2 = x^2 + y^2 + z^2 + t^2$. The set $V = F(x,y,z^2 - t^2, 2zt) \cap S^3_\epsilon$, where S^3_ϵ is a 3-sphere in $\mathbb{R}^4$ with a small radius centred on the origin in $\mathbb{R}^4$, gives rise to the knotted curve. The expression requires replacing z and t with the real and imaginary parts of the complex variable v^2 where $v = z + it$. Using v^2 allows for the figure-8 knot to be realise; the cube, v^3, gives rise to the Borromean rings. This

[3]We believe this result to be in Grothendieck's Séminaire de Géométrie Algébrique du Bois Marie.

comes from the underlying braid being generated by equation (2.19); we study this braid in sections 3.3 and 4.2. Writing solely in coordinates of $\mathbb{C}^2$, with additionally $u = x + \mathrm{i}y$, this becomes a complex function in $\mathbb{R}^3$ once equations (2.2) and (2.3) are substituted for u and v respectively. The higher powers of the braid word have the z and t expressions substituted for $\mathrm{Re}(z + \mathrm{i}t)^n$ and $\mathrm{Im}(z + \mathrm{i}t)^n$ respectively. The figure-8 knot curve formed is shown in figure 2.19(a).

Akbulut and King [AK81] prove that every knot arises from considering such intersection of algebraic sets in $\mathbb{R}^4$. The algebraic sets can be taken as the intersection of a small sphere around a singularity of a function $\mathbb{R}^4 \to \mathbb{R}^2$. Hence all knots are algebraic in a real sense. This does not provide a restriction on the knots that are accessible to us.

A further class of functions are those of type $\mathbb{C} \times \mathbb{R}^2 \to \mathbb{C}$. Rudolph in [Rud87] gives an expression for the figure-8 knot (and other multiples of its basic braid word) as

$$q_{\text{rudolph}}(u, v, v^*) = u^3 - 3(vv^*)^2(1 + v - v^*)u - 2(v + v^*). \tag{2.20}$$

When v is taken as v^2 the zeroes of this function are the figure-8 knot, with v^n giving the higher powers of the basic braid word. The curve is shown in figure 2.19(b).

We believe that the type of function required to realise knots in the above fashion, allows us to think of knots existing in three categories, detailed in table 2.3. This classification is based on the type of braid word that the knot allows to describe it. Knots that admit a strictly positive braid word, all letters in the word with positive power, are the torus and cable knots. Fibred knots allow a braid word of homogeneous type, each occurrence of a specific word σ_i always occurs raised to a power of the same sign. Outside of these two classes are the non-fibred knots, which do not have any such restrictions on a specific form of braid word being admissible to represent them. This classification is ordered. A torus knot can be given a non-strictly positive braid representation and a inhomogeneous braid word. Hence, if a knot is in the set of torus and cable knots, then the knot is in the set of fibred knots and in the set of all (including non-fibred) knots. The figure-8 knot is in the homogeneous and inhomogeneous braid word sets but is not a torus or cable knot and cannot be given a braid word that is strictly positive. It is knots with Milnor-like maps of type $\mathbb{C} \times \mathbb{R}^2 \to \mathbb{C}$ that we believe are accessible to us via the constructions we present in later chapters.

Braid representation admitted by knot	Knot Class	Milnor-like Map
Strictly Positive	Torus and Cable Knots	$\mathbb{C}^2 \to \mathbb{C}$
Homogeneous	Fibred Knots	$\mathbb{C} \times \mathbb{R}^2 \to \mathbb{C}$
Inhomogeneous	Non-fibred knots	$\mathbb{R}^4 \to \mathbb{R}^2$

Table 2.3: Our classification of knots via the braid representation they admit. The classifications are as described in the main text.

2.7 Knots which are Algebraic in the sense of Conway

The Conway notation [Con70] of a knot is sufficient to determine if a knot or link is algebraic by Conway's definition, given by us in definition 2.7.

Definition 2.14 (Algebraic in the sense of Conway)**.** *A Knot is algebraic in the sense of Conway if its Conway notation is made of products of the n-crossing tangles. Such Conway notation is of the form* $[t_1 t_2 \dots t_n]$ *where the* t_i *are basic tangles defined on page 44 and explained in figure 2.9.*

Such knots are also called *rational knots*. Knots of this form have an invariant that is calculated from the list of tangles, the *rational fraction* of the knot. Hence, algebraic knots are also called rational knots.

The rational fraction is a continued fraction

$$R(\text{knot}) = a_n + \cfrac{1}{a_{n-1} + \cfrac{1}{a_{n-2} + \cfrac{1}{a_{n-3} + \dots}}} \tag{2.21}$$

where $[a_1, a_2, \dots, a_n]$ is the Conway notation for the tangle.

Theorem 2.15 (Equivalence of rational knots with the same rational fraction value [Con70])**.** *If two rational knots (or links) formed by the closure of different rational tangles have the same rational fraction, then they are equivalent by ambient isotopy.*

Proof. Conway in [Con70] admits a proof of his theorem. A proof can be found in Goldman and Kauffman [GK97]. □

Rational knots coincide exactly with the class of 2-bridge knots. We now discuss bridge numbers of knots to understand some results about 2-bridge knots. Normally, a knot is considered completely projected onto a plane, but here consider a plane that the knot intersects several times, but in which a projection of the knot either side of the plane can be formed. The intersection points of the knot and the plane are called vertices with arcs the part of the knot between vertices. The knot is manipulated, by ambient isotopy, such that if all the arcs

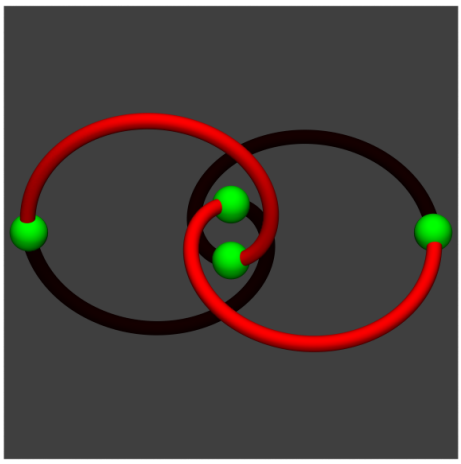

Figure 2.20: The trefoil knot in a projection showing that it is a 2-bridge knot because of the two over arcs above the grey plane.

above the plane are projected onto it, they are unknotted and do not intersect. Similarly for the arcs below the plane. This coincides with an arc above the plane crossing the maximal number of arcs below the plane before intersecting the plane. Any further crossings of the arcs would have to be on the same side of the plane but this is not allowed. The number of arcs which can achieve this in the given projection is the bridge number of the projection.

Definition 2.16 (Bridge Number)**.** *The bridge number, $b(K)$, of the knot is the least value possible for the number of bridges, over all projections, and is equal to half the number of intersections of the plane in such a projection. A knot is said to be an n-bridge knot when $n = b(K)$.*

Figure 2.20 shows the trefoil knot projected such that it can be seen that it is a 2-bridge knot.

Knots that are algebraic in the sense of Conway arise in our tabulation of knots that have been successfully created as nodal sets of paraxial functions. In chapter 4 we use the Conway notation of these rational knots and links, and patterns within a list of knots, to create families of knots based on similar notations. It is these families that our constructions seek to generalise with the Lissajous construction.

3 Vortex Knots in Gaussian Beams

We now apply the theory of the previous chapter to construct a variety of functions that contain as their nodal set a desired knot or link. Following the outline of [DKJ+10], we introduce a scheme to construct solutions of the paraxial equation which are used to construct functions that contain the desired nodal topology and satisfy the paraxial equation. We construct explicit Milnor polynomials from the Lissajous construction before introducing a scheme to embed the Milnor polynomial's nodal topology into solutions of the paraxial equation. We construct a family of polynomial solutions to the paraxial equation, *paraxial polynomials*. These polynomials are used to construct functions with our knotted nodal set as solutions of the paraxial equation. These paraxial polynomials are finally expressed as superpositions of Laguerre-gaussian laser modes which have been experimentally implemented. This chapter introduces several concepts which we study in detail in later chapters, both in the construction of functions with knotted nodal sets and the implications for the nodal topology when embedded as a solution of the paraxial equation.

3.1 Milnor Polynomials

In chapter 2 we constructed functions with their pre-image of zero a periodic braid. We now construct braids where the trajectory of the strands follows first a circle, and secondly a lemniscate. The two products formed with these zero sets are

$$p_{\text{circle}}(u) = \prod_{j=0}^{1} \left[u - \left(\cos\left(h + \pi j\right) + \mathrm{i}\sin\left(h + \pi j\right)\right)\right], \tag{3.1}$$

and

$$p_{\text{lemniscate}}(u) = \prod_{j=0}^{2} \left[u - \left(\cos\left(h + \frac{2\pi j}{3}\right) + \mathrm{i}\sin\left(2\left(h + \frac{2\pi j}{3}\right)\right)/a\right)\right]. \tag{3.2}$$

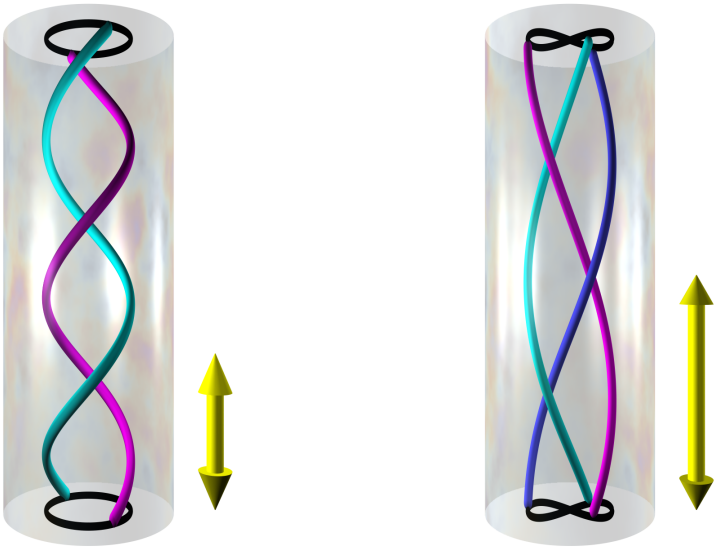

(a) (b)

Figure 3.1: The braids generated from equations (3.1) and (3.2) shown in (a) for the circular trajectories and (b) for the lemniscate trajectory respectively. The h direction is vertical, in the direction of the arrow points (both ways) and the black trajectories show the two dimensional projection of the braid strands in the u plane. The arrow's length indicates the basic braid word, σ_1, which is repeated three times for the circular trajectory and $\sigma_1\sigma_2^{-1}$, repeated twice for the lemniscate trajectory. These braid words represent the trefoil and figure-8 knots respectively.

We set $a = 2$ in this chapter and the effects of this real parameter a are studied in chapter 4. The circular braids with two strands have a basic braid word σ_1 and the lemniscate based braids with three strands have basic braid word $\sigma_1\sigma_2^{-1}$. These braids are shown in figure 3.1, for three repeats of the circular trajectory and two repeats of the lemniscate trajectory. The closure of these braids, σ_1^3 and $(\sigma_1\sigma_2^{-1})^2$, are the trefoil and figure-8 knot respectively.

These products can be written in terms of exponentials, and letting $v = \mathrm{e}^{\mathrm{i}h}$, we form functions in formal variables u and v. The number of repeats of the basic braid word depends on the power of v and hence v is replaced with v^n where n is the number of repeats of the basic braid word. This gives rise to

$$q_{\text{circle}}(u,v) = u^2 - v^n \tag{3.3}$$

$$\begin{aligned} q_{\text{lemniscate}}(u,v) &= 64u^3 - 12u(2v^n + 2v^{*n} + 3) \\ &\quad -(14v^n + 14v^{*n} + v^{2n} - v^{*2n}). \end{aligned} \tag{3.4}$$

We now take the Milnor map of the respective q functions in equations (3.3)

and (3.4). This procedure is performed by setting u and v to the functions in equations (2.2) and (2.3). The height coordinate of the braid cylinder is smoothly mapped to the azimuthal coordinate of the torus in the closure of the braid. This creates a complex function of position $\boldsymbol{r}$. We take this complex function over a common denominator which gives a polynomial in x, y, z. This polynomial is the Milnor polynomial, definition 2.10. We require a polynomial function, not a rational function, to enable us to re-write the function at $z = 0$ in terms of another basis, then apply its z-dependence to let this newly formed function satisfy the paraxial equation (and in later chapters other PDEs).

The Milnor maps of equations (3.3) and (3.4) give rise to their respective Milnor polynomials

$$\begin{aligned} f_{\text{trefoil}}(\boldsymbol{r}) &= \{(R^4-1)(R^2-1) - 8R^3\mathrm{e}^{3\mathrm{i}\phi}\} + 4\mathrm{i}z(R^4-1) \\ &\quad + z^2(3R^4 - 6R^2 - 5) + 8\mathrm{i}z^3R^2 + z^4(3R^2-5) + 4\mathrm{i}z^5 + z^6, \end{aligned} \tag{3.5}$$

and

$$\begin{aligned} f_{\text{figure-8}}(\boldsymbol{r}) &= \{28R^8 - 8(19\mathrm{e}^{2\mathrm{i}\phi} + 19\mathrm{e}^{-2\mathrm{i}\phi} + 25)R^6 \\ &\quad -(7\mathrm{e}^{2\mathrm{i}\phi} + 19\mathrm{e}^{-2\mathrm{i}\phi} + \mathrm{e}^{4\mathrm{i}\phi} - \mathrm{e}^{-4\mathrm{i}\phi})R^4 \\ &\quad +8(5\mathrm{e}^{2\mathrm{i}\phi} - 19\mathrm{e}^{2\mathrm{i}\phi} + 25)R^2 - 28\} \\ &\quad +24\mathrm{i}(13 - 25R^2 - 8\mathrm{e}^{2\mathrm{i}\phi}R^2 - 25R^4 - 8\mathrm{e}^{2\mathrm{i}\phi}R^4 + 13)z \\ &\quad +(121 - 14\mathrm{e}^{2\mathrm{i}\phi}R^2 - 38\mathrm{e}^{-2\mathrm{i}\phi}R^2 - 171R^4 - 38\mathrm{e}^{2\mathrm{i}\phi}R^4 \\ &\quad -38\mathrm{e}^{-2\mathrm{i}\phi}R^4 + 14R^6)z^2 \\ &\quad -8\mathrm{i}(139 + 214R^2 + 24\mathrm{e}^{2\mathrm{i}\phi}R^2 - 117)z^3 \\ &\quad -8(267R^2 + 19\mathrm{e}^{2\mathrm{i}\phi}R^2 + 19\mathrm{e}^{-2\mathrm{i}\phi}R^2 - 21R^4)z^4 \\ &\quad -8\mathrm{i}(139 - 117R^2)z^5 - 8(121 - 14R^2)z^6 + 312\mathrm{i}z^7 + 28z^8, \end{aligned} \tag{3.6}$$

where the numerator of the Milnor map is taken from the function over a common denominator. The $\{\bullet\}$ emphasises the part of the Milnor polynomial that is not z-dependent and remains upon setting $z = 0$ and hence defines f in the $z = 0$ plane. This plane is used later in this chapter to build functions that satisfy the paraxial equation and in chapter 5, the Helmholtz equation. The nodal sets of the respective f are the trefoil and figure-8 knots. In the (R, z)-plane as ϕ varies, the geometry of the braid trajectories is not necessary the same as before taking the Milnor map, although topologically they are equivalent. The lemniscate of the figure-8 knot can be seen to have lost the symmetry in the size of the loops in figure 3.2(b) (the black curve). (R, z)-plane projections are considered

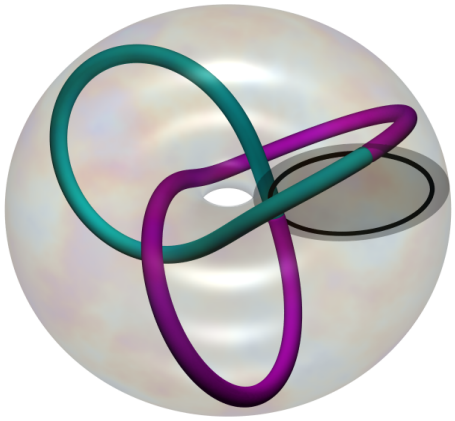

(a)

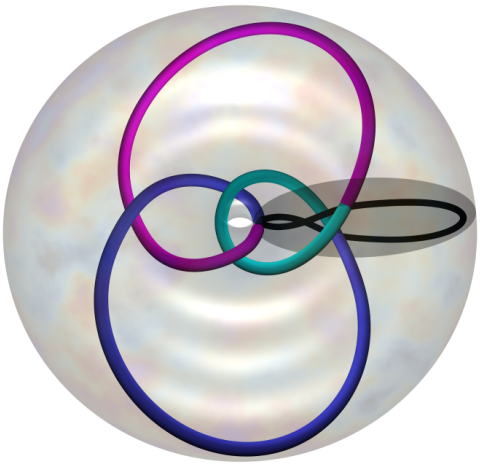

(b)

Figure 3.2: The closure of the braids in figure 3.1 formed by taking the Milnor maps of the respective braid functions corresponding to equations (3.5) and (3.6). The cylinder enclosing the braids in figure 3.1 is mapped to the torus and the knots are contained within the solid torus (not on the surface like a torus knots). The disks show the join of the ends of the cylinders under closure and the black curves show the image of the braid trajectories in the u-plane under the Milnor map. The strand colours are the same as in figure 3.1 and (a) shows the trefoil knot and (b) shows the figure-8 knot. The z-axis is the central torus axis and the $z = 0$ plane intersects the equatorial plane of the tori.

further in chapter 4 on the study of constructing Milnor polynomials for more general Lissajous figures.

3.2 Paraxial Polynomials

Milnor polynomials do not satisfy the paraxial equation (1.19). We require a method of constructing functions that satisfy the paraxial equation that also inherit the nodal topology of the Milnor polynomials. As an intermediate step we now construct a specific set of solutions, the paraxial polynomials, which we use to achieve this topological embedding.

The Laguerre-gaussian modes, introduced in chapter 1, are solutions of the paraxial equation. Properties of these solutions make the initial investigation into paraxial nodal knots difficult. The Gouy phase term and the overall Gaussian factor contribute to additional zeroes in the field away from the vortex knot in question being introduced. Ultimately we desire our knots to be embedded in such physical solutions but we begin this chapter with the construction of solutions which do not introduce these effects. These are the *paraxial polynomials*. Linear combinations of these polynomials are created in the next section, based on Milnor polynomials, to obtain solutions of the paraxial equation that contain a knotted nodal set.

Polynomial solutions to wave equations have been considered before, although not directly for the study of optical vortex topology. The case of polynomials satisfying the Helmholtz equation has been used by Nye [Nye98] and Berry [Ber98]. Both papers use the polynomials to consider properties local to singularities of wave fields. Both Dennis [Den01] and Berry and Dennis [BD01b] have used expansions of non-polynomial solutions to the Helmholtz and paraxial equation to generate the respective polynomial families. We now derive for the paraxial equation, polynomial families based on both the cylindrical-polar and Cartesian coordinate systems. These coincide with the results of expanding known solutions to the paraxial equation [Den01].

We begin by deriving the Laguerre differential equation [AS64] from the paraxial equation. Beginning with the paraxial equation (1.19), in cylindrical coordinates

$$\psi_{RR} + \frac{1}{R}\psi_R + \frac{1}{R^2}\psi_{\phi\phi} + 2\mathrm{i}k\psi_z = 0, \tag{3.7}$$

where subscripts represent derivatives, we consider solutions of the form

$$\psi(R, z, \phi) = R^l \mathrm{e}^{\mathrm{i}l\phi} f(R, z), \tag{3.8}$$

where $l > 0$ is an integer. Substituting this into equation (3.7) we get

$$R^2 f_{RR} + (2l+1) R f_R + 2\mathrm{i}k R^2 f_z = 0. \tag{3.9}$$

We now make a change of variables

$$R \to \rho = R^2, \quad z \to \zeta = \tfrac{-2\mathrm{i}z}{k},$$

and let $f(R,z) = F(\rho,\zeta)$, which after taking out a common factor of 4ρ allows us to write,

$$\rho F_{\rho\rho} + (l+1)F_\rho + F_\zeta = 0. \tag{3.10}$$

The final step is to assume that F is a homogeneous function that has the form $F(\rho,\zeta) = \zeta^p G(\frac{\rho}{\zeta})$ and letting $\frac{\rho}{\zeta} = X$, equation (3.10) is finally expressed as

$$XG'' + (l+1-X)G' + pG = 0, \tag{3.11}$$

where $\bullet'$ is the derivative with respect to X and the differential equation (3.11) is the Laguerre differential equation.

We also derive polynomials based on the Cartesian coordianate system. Expressed in Cartesian coordinates the paraxial equation is

$$\psi_{xx} + \psi_{yy} + 2\mathrm{i}k\psi_k = 0, \tag{3.12}$$

and we seek a separable solution, in x,z and y,z, of the form

$$\psi(x,y,z) = F(x,z)G(y,z). \tag{3.13}$$

With this substituted into the paraxial equation, we arrive at the equation

$$F_{xx}(x,z) + 2\mathrm{i}kF_z(x,z) = 0, \tag{3.14}$$

for x, which is the same equation for y but with x exchanged for y. We make the substitution, only needed for one of the variables in this case,

$$z \to \zeta = \frac{-2\mathrm{i}z}{k}, \tag{3.15}$$

which transforms equation (3.14) into

$$\psi_{xx} + 4\psi_\zeta = 0. \tag{3.16}$$

We seek a solution of the form

$$\psi(x,z) = \zeta^{\frac{n}{2}} H\left(\frac{x}{\sqrt{\zeta}}\right), \tag{3.17}$$

which when substituted into equation (3.16), we get, up to a multiple of $\zeta^{\frac{n-2}{2}}$, and letting $X = \frac{x}{\sqrt{\zeta}}$,

$$H_{XX} - 2XH_X + 2nH = 0, \tag{3.18}$$

which is the Hermite differential equation. Hence the Cartesian paraxial polynomials are of the form

$$\psi_{m,n}(x,y,z) = \zeta^{\frac{m+n}{2}} H_n\left(\frac{x}{\sqrt{\zeta}}\right) H_m\left(\frac{y}{\sqrt{\zeta}}\right), \tag{3.19}$$

where H_m is the m^{th} Hermite polynomial.

Such polynomial solutions have also been considered before as solutions of parabolic partial differential equations like the paraxial equation. The heat equation, in one space and one time dimension, is

$$\frac{\partial^2 u}{\partial x^2} = \frac{\partial u}{\partial t}, \tag{3.20}$$

which can be seen to be of the same form as the paraxial equation with $iz \to t$, and is a real equation. The heat equation has a particular solution of the form given in Cannon [Can84]

$$p_n(x,t) = n! \sum_{k=0}^{\left[\frac{n}{2}\right]} \frac{t^k}{k!} \frac{x^{n-2k}}{(n-2k)!}, \tag{3.21}$$

where $\left[\frac{n}{2}\right]$ is the greatest integer less than $\frac{n}{2}$. Such polynomials in equation (3.21) are the heat, or caloric polynomials. When $t = -1$, these are of the form of the Hermite polynomials [PŠ08], where Poláčik and Šverák are also similarly interested in nodal sets of differential equations. This suggests that it is possible to also transform the heat equation into Hermite's equation.

The paraxial polynomials can be constructed from other solutions of the paraxial equation. These are used as a generating function and expanded about a parameter not dependent on the paraxial equation. The beginning for this construction, of [Den01], are the Bessel beams [Dur87] and have the form

$$\psi_{\text{paraxial}} = e^{im\phi} e^{-iz^2 \frac{\kappa}{2}} J_m\left(\sqrt{\kappa} R\right). \tag{3.22}$$

This is a solution for all κ but it is physically only valid for small κ [Den01]. We Taylor expand equation (3.22) about $\kappa = 0$ and consider the coefficients of the powers of κ. These are functions in R, ϕ, z with m as a parameter. Each coefficient is itself a solution of the paraxial equation. These functions are normalised to form the set of functions shown in the tables of appendix 3.A to this chapter. For each power of R, the z-dependence is the unique function that allows R^n to satisfy the paraxial equation.

The physically realisable solutions formed by superpositions of Laguerre-gaussian modes constructed later in this chapter can also be used to create the paraxial polynomials. Here, expanding in $\frac{1}{w}$, the Laguerre-gaussian modes act as a generating function for the cylindrical paraxial polynomials. An example of this is shown for the Hopf link in appendix 3.C to this chapter.

3.3 Constructing Paraxial Knots

The functions of section 3.1 with braided zeroes lines and their respective Milnor polynomials are used now to create solutions of the paraxial equation which contain the same knotted nodal topology. Using the Milnor polynomials for the Hopf link and cinquefoil knots, in addition to that of the trefoil equation (3.5) and the figure-8 knot of equation (3.6), we now construct their paraxial counterparts and examine their nodal topology.

The Milnor polynomial of a knot has a symmetry plane at $z = 0$. There exists a unique function, that coincides at $z = 0$ with the Milnor polynomial, and satisfies the paraxial equation. We construct this function using the paraxial polynomials. The constructed polynomial is endowed with the paraxial propagation dependence in z and in general the z-dependent terms are different to that of the Milnor polynomial. For each term of the form $R^m e^{in\phi}$ in the Milnor polynomial, it is substituted with $R^m e^{in\phi} + g(\boldsymbol{r})$ where $g(\boldsymbol{r})$ is as constructed in section 3.2. This leads to a function, ψ, for which $\psi|_{z=0} = f|_{z=0}$. Hence for a given Milnor polynomial at $z = 0$, the $R^m e^{in\phi}$ terms are replaced with the corresponding paraxial polynomial. In the case of $m = n$, terms have the form $R^m e^{\pm im\phi}$ and satisfy the paraxial equation themselves and do not require z-dependent terms to do this. This leaves the R- and ϕ-dependence in this plane unchanged but all z-dependent terms change. We now construct such functions ψ and examine the associated nodal topology.

We have the following procedure to follow:

- Construct the Milnor polynomial and set $z = 0$
- Collect the $R^m e^{in\phi}$ terms
- Construct, using paraxial polynomials, the function that coincides with this at $z = 0$ and satisfies the paraxial equation.

$(2, n)$-torus Knots

The Hopf link has a Milnor polynomial of

$$\begin{aligned} f_{\text{Hopf}}(\boldsymbol{r}) &= \{1 - 2R^2 - 4R^2 e^{2i\phi} + R^4\} \\ &\quad -4iz + 4iR^2 z - 6z^2 + 2R^2 z^2 + 4iz^3 + z^4, \end{aligned} \tag{3.23}$$

arising from $q_{\text{Hopf}} = u^2 - v^2$, with terms that are not z-dependent placed in the $\{\bullet\}$ brackets. This comes from taking the Milnor map of equation (3.1) and setting $n = 2$. At $z = 0$ there are four terms that remain. For each remaining

term in equation (3.23) at $z = 0$, we construct ψ_{Hopf} by replacing each term $R^m e^{in\phi}$ with its corresponding paraxial polynomial, defined in section 3.2. The paraxial polynomial that corresponds at $z = 0$ is, with $k = 1$,

$$\begin{aligned}\psi_{\text{Hopf}} &= 1 + 8\left(\frac{1}{4}R^2 + \frac{1}{2}iz\right) + (4e^{2i\phi}R^2) + (R^4 + 8iR^2z - 8z^2) \\ &= \{1 - 2R^2 - 4e^{2i\phi}R^2 + R^4\} - 4iz + 8iR^2z - 8z^2. \end{aligned} \tag{3.24}$$

We set $k = 1$ throughout this chapter.

In both the Milnor and paraxial forms, the terms in the $\{\bullet\}$ brackets are identical. However, the z-dependent terms are very different with ψ_{Hopf}, since the highest degree in the z terms have only half the degree in z of f_{Hopf}. Despite this difference, the nodal lines of both equations form the Hopf link. This difference in z-dependence can be seen by plotting the curves in the (R, z)-plane. Figure 3.3 shows the curves formed in this plane as ϕ varies. The paraxial function has a more complicated geometry of the curves compared to that of the Milnor polynomial. The (R, z)-plane shows the mapping of the braid trajectories in ϕ which are first mapped from braid space to $\mathbb{R}^3$ by the Milnor map, and second time by constructing the function that satisfies the paraxial equation.

The (R, z)-plane plots are an important tool in determining the success of this procedure. The two curves, of the Milnor polynomial and paraxial function, can be compared to ensure they both are equivalent to the lemniscate the braid was constructed on. In the paraxial case, the geometry of the paraxial case, as in figure 3.3, is more complicated than the Milnor polynomial's case. This can be used to understand differences in crossing numbers of the two cases, even if they have the same projection directions.

The same procedure is now applied to the Milnor polynomial of the trefoil knot in equation (3.5). Similar to the Hopf link, the $z = 0$ part of the polynomial is used to construct a function that satisfies the paraxial equation. After the paraxial polynomial substitution, we arrive at

$$\begin{aligned}\psi_{\text{trefoil}} &= \{1 - R^2 - 8R^3e^{3i\phi} - R^4 + R^6\} \\ &\quad + i(-2 - 8R^2 + 18R^4)z + (8 - 72R^2)z^2 - 48iz^3, \end{aligned} \tag{3.25}$$

which as before matches the Milnor map at $z = 0$ with both functions coinciding in the $\{\bullet\}$ terms. The nodal line of ψ_{trefoil} forms the trefoil knot as in the Milnor map.

The nodal line of the paraxial trefoil knot is shown in figure 3.4. The geometric form of the nodal line of the paraxial function is again different to that of the Milnor map.

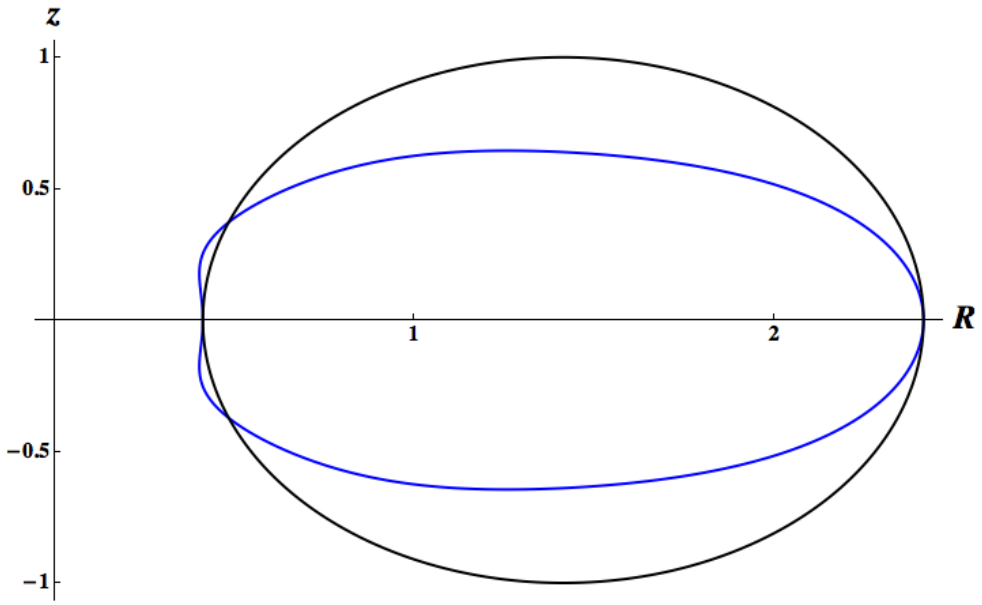

Figure 3.3: The (R, z)-plane of the Hopf link for the Milnor polynomial, black, and the paraxial function, blue. The difference in z range is clear and the geometry of the trajectories can be seen to be different. These curves are the maps from the circular braid trajectories.

The cinquefoil knot has a Milnor polynomial constructed from $q_{\text{cinq}} = u^2 - v^5$, which arises from two braid strands following a circular trajectory with five repeats of the basic braid word. This polynomial has corresponding paraxial function

$$\begin{aligned}\psi_{\text{cinq}}(\boldsymbol{r}) \quad = \quad & \{1 + R^2 - 2R^4 - 32\mathrm{e}^{5\mathrm{i}\phi}R^5 - 2R^6 + R^8 + R^{10}\} \\ & +2\mathrm{i}(1 - 8R^2 - 18R^4 + 16R^6 + 25R^8)z \\ & +16(1 + 9R^2 - 18R^4 - 50R^6)z^2 \\ & +96\mathrm{i}(1 - 8R^2 - 50R^4)z^3 + 384(1 + 25R^2)z^4 + 3840\mathrm{i}z^5.\end{aligned} \tag{3.26}$$

This contains only one term of the form $R^m\mathrm{e}^{\mathrm{i}m\phi}$, where $m = 5$. This arises from the v^m term in construction the function of u and v. The trefoil knot similarly exhibits this for $m = 3$ and the Hopf link for $m = 2$.

This function contains the cinquefoil knot in its nodal set in the geometric form of the $(2, 5)$-torus knot. A Milnor polynomial constructed for the $(5, 2)$-form, a five strand braid $(\sigma_1\sigma_2\sigma_3\sigma_4)^2$, can also be entered into this procedure. In this case the resulting paraxial function does not contain the cinquefoil knot as its nodal set. The $(3, 2)$-form of the trefoil knot exists in its place. This failure to embed the topology is examined in chapter 5 where a procedure to successfully

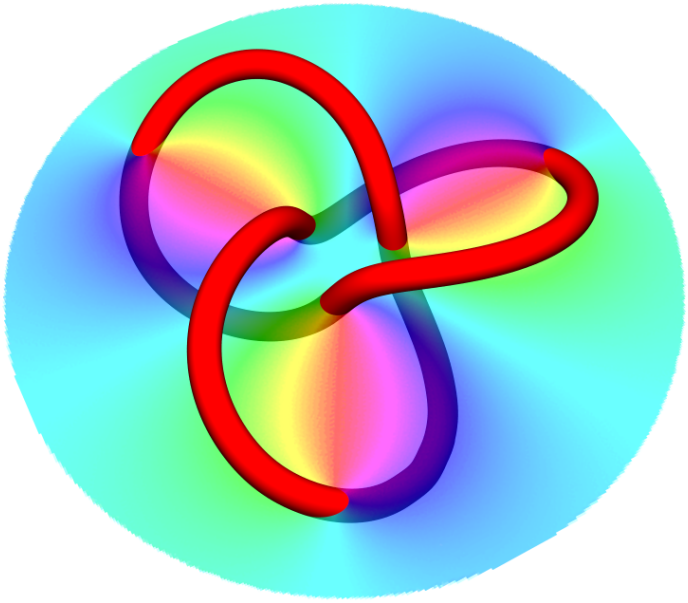

Figure 3.4: The trefoil knot formed in the nodal set of the paraxial function equation (3.25). The coloured, semi-transparent plane is the circular region about the origin at $z = 0$. The colouring represents the phase of the function with our standard colour key for phase.

embed it is discussed. Our given examples do not prove the general case of all knots constructed in this fashion will be successfully transferred into solutions of the paraxial equation.

This difference in the geometric appearance of the paraxial polynomial nodal curve and that of the Milnor polynomial, can be attributed to the paraxial function have a different z-dependence. The order in z of the paraxial polynomials is half that of the corresponding terms in the Milnor polynomial. This difference in order arises from the paraxial equation treating the transverse and z derivatives differently. This procedure has been used to create all the $(2, n)$-torus knots and links for $n \leq 10$. There does not appear to be any restriction that would place an upper bound on n; however the range in z where the nodal knot exists, decreases as n increases.

The Figure-8 Knot Family

The figure-8 knot has Milnor polynomial equation (3.6). We now construct the function that satisfies the paraxial equation and coincides with this Milnor polynomial in the $z = 0$ plane. To do this, we follow the same procedure as before

and arrive at

$$\begin{aligned}\psi_{\text{figure-8}}(\boldsymbol{r}) \;=\; & \{28R^8 - 8(19\mathrm{e}^{2\mathrm{i}\phi} + 19\mathrm{e}^{-2\mathrm{i}\phi} + 25)R^6 \\ & -(7\mathrm{e}^{2\mathrm{i}\phi} + 19\mathrm{e}^{-2\mathrm{i}\phi} + \mathrm{e}^{4\mathrm{i}\phi} - \mathrm{e}^{-4\mathrm{i}\phi})R^4 \\ & +8(5\mathrm{e}^{2\mathrm{i}\phi} - 19\mathrm{e}^{2\mathrm{i}\phi} + 25)R^2 - 28\} \\ & +16\mathrm{i}(25 - 42\mathrm{e}^{2\mathrm{i}\phi}R^2 - 114\mathrm{e}^{-2\mathrm{i}\phi}R^2 - 225R^4 \\ & -152\mathrm{e}^{2\mathrm{i}\phi}R^4 - 152\mathrm{e}^{-2\mathrm{i}\phi}R^4 + 56R^6)z \\ & +192R^2(75 + 38\mathrm{e}^{2\mathrm{i}\phi} + 38\mathrm{e}^{-2\mathrm{i}\phi} - 42R^2)z^2 \\ & +384\mathrm{i}(25 - 56R^2)z^3 + 10752z^4. \end{aligned} \tag{3.27}$$

The paraxial nodal figure-8 knot is shown in figure 3.5 along with the phase of the $z = 0$ plane.

The higher repeats of the basic braid word, $n = 3$ and $n = 4$, give rise to the Borromean rings and Turk's head knot respectively. These curves, constructed with the above method, give rise to a three-fold and four-fold symmetric geometry of the same basic azimuthal braid structure. The figure-8 knot has a two-fold symmetry. A paraxial function for the Borromean rings, constructed from its Milnor polynomial, successfully inherits the link as its nodal set. Again, due to the difference in z-dependence, the lemniscate of the braids, mapped into the respective (R, z)-planes, show these differences. Figure 3.6 shows this projection for the Milnor polynomial and the paraxial function for the Borromean rings. Similarly, figure 3.7 shows these images for the Turk's head knot. Higher repeats of the basic braid word give rise to an interesting family of knots and links that include, when $n \equiv 0 \mod 3$, a set of generalised three component Brunnian links, [Jab99] and section 4.2. This family is considered further in chapter 4. In chapter 4 the Lissajous construction is generalised and additional parameters, such as a of equation (3.2), are discussed.

3.4 Laguerre-gaussian Knots

The paraxial polynomials used throughout this chapter are not physically realisable solutions to the paraxial equation. Their absolute value tends to infinity as R tends to infinity. Solutions with an overall Gaussian factor, such as the Hermite-gaussian and Laguerre-gaussian laser modes introduced in section 1.6, do converge as R increases.

We use the cylindrical coordinate system to construct the Milnor polynomials. It is natural therefore to use the cylindrically symmetric Laguerre-gaussian modes in this section to construct realisable optical fields with a prescribed knot in its vortex structure. The Hermite-gaussian modes could equally be used, and

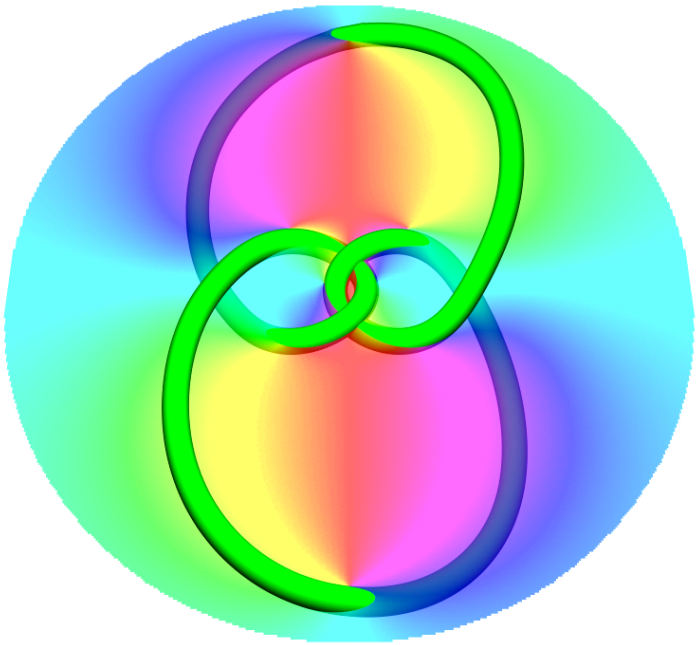

Figure 3.5: The nodal curve of the paraxial function equation (3.27) which is the figure-8 knot. The circular disk is as in figure 3.4. This plane is identical in both the Milnor polynomial and paraxial function.

Cartesian coordinate functions can be used. Cylindrical coordinate are natural for us because $v(\boldsymbol{r})^n \propto LG_0^n$ at $z = 0$, this allows simpler superpositions, with less modes required, to be constructed.

Our methodology for creating the mode superpositions is similar to that used to create the paraxial polynomial solutions. The $z = 0$ plane of the Milnor polynomial forms the focal plane of the superposition. Laguerre-gaussian modes have a parameter w giving the beam's Gaussian width. We show later that this width acts as a parameter controlling the success of the nodal topology transferring from the Milnor polynomial to the superposition. The width is thus kept as a parameter in the following integrations and the results shall be w-dependent. For a fixed width w, the Laguerre-gaussian modes form a basis for functions of R and ϕ in the $z = 0$ plane. The use of all modes having the same width contrasts to the approach of [LDCP04].

We form the superposition as a sum of weighted modes,

$$\psi_{\mathrm{LG}_{\mathrm{knot}}} = \sum_{l,p} c_{l,p} LG_p^l(\boldsymbol{r}, w), \tag{3.28}$$

where the sum taken over all modes where $c_{l,p} \neq 0$, each term satisfying the linear paraxial equation (1.19). The coefficient weighting to each mode, $c_{l,p}$, is

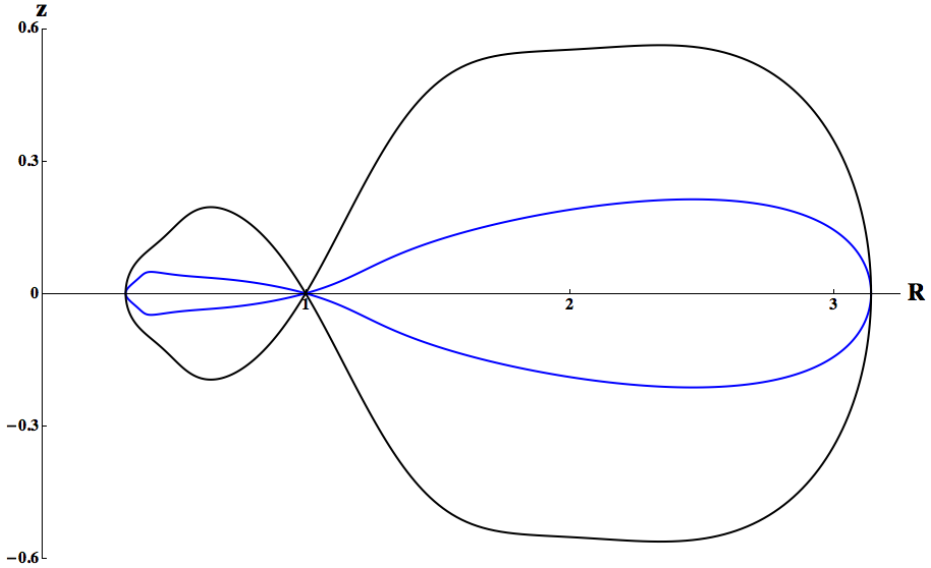

(a)

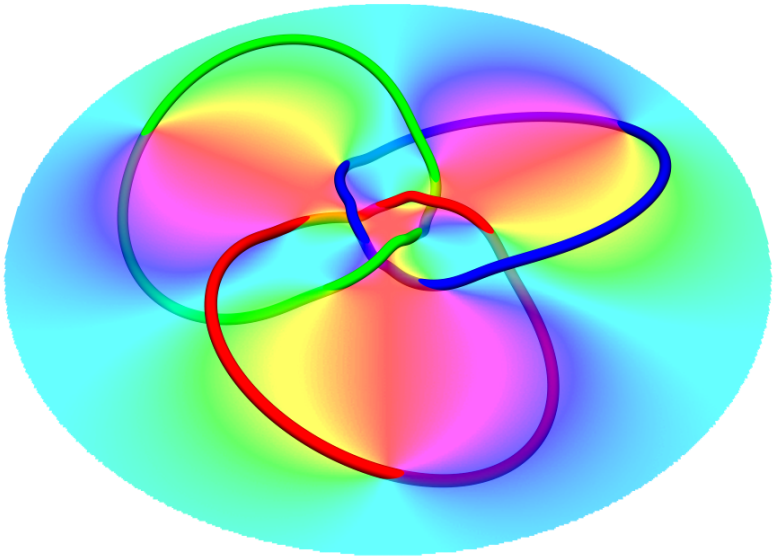

(b)

Figure 3.6: Paraxial and Milnor Borromean rings. (a) The (R, z)-plane trajectories of the Borromean rings for the Milnor polynomial in black and the paraxial function in blue. (b) The paraxially propagating Borromean rings, with the phase of the $z = 0$ plane shown. The three-fold symmetry of the knot constructed from the braid $(\sigma_1\sigma_2^{-1})^3$ can be seen, especially in the $z = 0$ plane vortex constellation. Each of the three components is coloured distinctly in red, green and blue.

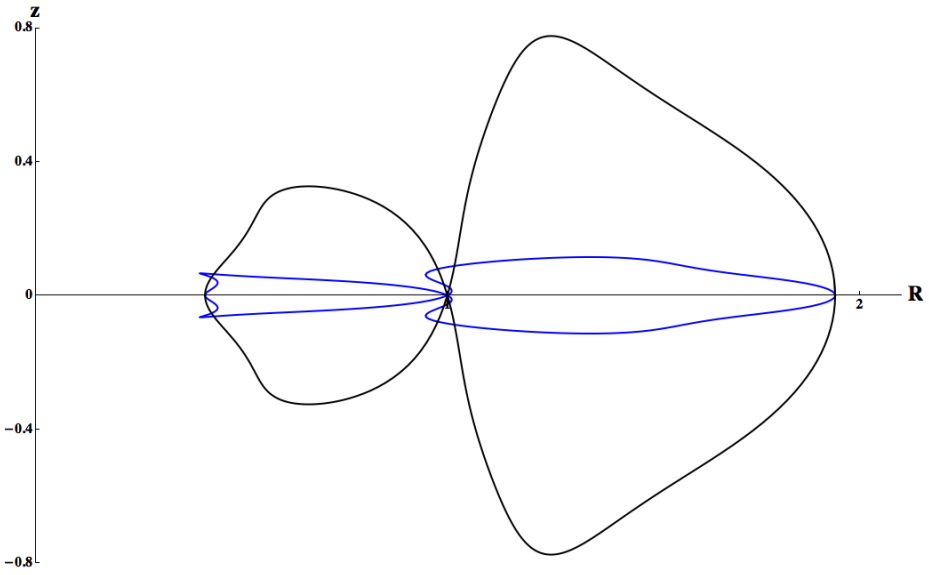

(a)

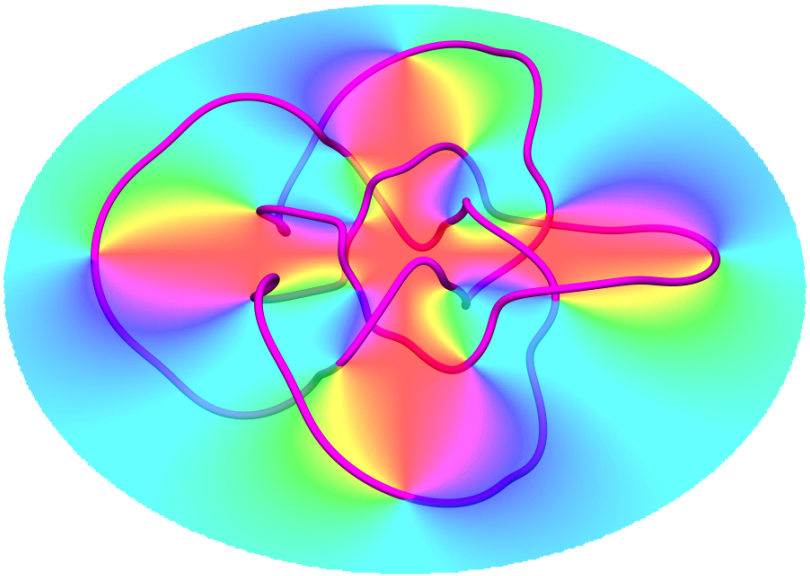

(b)

Figure 3.7: Paraxial and Milnor Turk's head knot, also denoted 8_{18}. (a) The (R, z)-plane of the Turk's head knot for the Milnor polynomial in Black and the paraxial function in blue. (b) The paraxially propagating Turk's head knot, with the phase of the $z = 0$ plane shown. The four-fold symmetry of the knot constructed from the braid $(\sigma_1\sigma_2^{-1})^4$ can be seen, especially in the $z = 0$ plane vortex constellation, the opaque disk. The contortions in the knot in (b) are represented by the "bat's ears" in (a).

calculated from a Fourier-like integral

$$c_{l,p} = \iint_{\mathbb{R}^2} \mathrm{d}^2\boldsymbol{R} \quad LG_p^{-l}(R,0,\phi) LG_0^0(R,0,\phi) f_{\mathrm{knot}}(R,0,\phi), \tag{3.29}$$

where $f_{\mathrm{knot}}(R,0,\phi)$ is the Milnor polynomial at $z=0$ and the $c_{l,p}$ are the coefficients of the respective LG_p^l.

The $LG_0^0(R,0,\phi)$ term in equation (3.29) means that we are integrating a function of the form polynomial times Gaussian. This is a non-zero factor which does not effect the phase at $z=0$, which means we are examining the paraxial propagation of

$$F(R,0,\phi) = \mathrm{e}^{-\frac{R^2}{w^2}} f_{\mathrm{knot}}(R,0,\phi), \tag{3.30}$$

but we shall refer to just the function f when necessary. The Gaussian width w is kept in the $c_{l,p}$ but assumed to be constant. In the Milnor polynomial, additional parameters such as a and further parameters discussed in later chapters, can be kept in the integration to give coefficients, the set of all non-zero $c_{l,p}$ of equation (3.29), dependent on them in addition to w. This allows the superposition to be fine tuned experimentally, as well as the geometric effects on the superposition to studied. The coefficients should really be written $c_{l,p}(a,w)$.

In appendix 3.B to this chapter, we give the Laguerre-gaussian mode superpositions for the Hopf link, trefoil, cinquefoil and figure-8 knots. The topology of the vortex lines is successfully transferred to the superposition and as expected it has a different geometric form to the Milnor map. We now explore the effect of the Gaussian width w on the superposition's vortex topology and its isolation.

Unlike the paraxial polynomials, the Laguerre-gaussian superpositions have an additional vortex structure to them away from the knot. The rest of this section is concerned with studying these additional vortices. These additional nodal lines arise from the Gouy phase terms of the mode that have different p values. This additional structure is evident in the far-field of the beam. The far-field, the plane formed in the limit as $z \to \infty$, is given by the Fourier transform of the $z=0$ plane, where the length scale of the propagation direction z moves the beam from the Fresnel diffraction region into the Fraunhofer regime [BW59, p. 421]. The Laguerre-gaussian modes at $z=0$ can be written

$$LG_p^l \,|_{z=0} = \sqrt{\frac{p!}{\pi(p+l)!}} w^{-1-l} R^l \mathrm{e}^{\mathrm{i}l\phi} \mathrm{e}^{\frac{-R^2}{2w^2}} L_p^l\left(\frac{R^2}{w^2}\right). \tag{3.31}$$

The Fourier transform of a circularly symmetric function can be written

$$\mathcal{F}(\rho,\theta) = \iint_{\mathbb{R}^2} \mathrm{d}^2\boldsymbol{R}\ f(R,\phi)\mathrm{e}^{\mathrm{i}R\rho\cos(\phi)}. \tag{3.32}$$

For the Laguerre-gaussian modes, the ϕ integral is

$$\int_0^{2\pi} \mathrm{d}\phi\ \ \mathrm{e}^{\mathrm{i}l(\phi+\theta)}\mathrm{e}^{\mathrm{i}R\rho\cos(\phi+\theta)} = 2\pi\mathrm{i}^l J_l(\rho R), \tag{3.33}$$

which is of the form of Bessel's first integral. The remaining R integration is now in the form a Hankel transform of l^{th} order, and using [GR00],

$$\begin{aligned}\int_0^\infty \mathrm{d}R\ f(R)J_l(\rho R) &= C(l,p,w)\int_0^\infty \mathrm{d}R\ R^{l+1}\mathrm{e}^{\frac{-R^2}{2w^2}}L_p^l\left(\frac{R^2}{w^2}\right)J_l(\rho R)\\ &= K(l,p,w)\rho^l\mathrm{e}^{\frac{-\rho^2w^2}{2}}L_p^l\left(\frac{w^2\rho^2}{4}\right),\end{aligned} \tag{3.34}$$

where C is a mode and width dependent constant encompassing all such terms and the final constant is

$$K(l,p,w) = \mathrm{i}^l\frac{2\sqrt{2^{l+1}p!}\pi^{\frac{2}{3}}}{\sqrt{(l+p)!}w^{2(l+2p+1)}}. \tag{3.35}$$

This shows that the Laguerre-gaussian modes are eigenfunctions of the Hankel transform integral operator. Hence up to constants, the Fourier transform of a Laguerre-gaussian mode is the same Laguerre-gaussian mode, with a factor i^l and a substitution of $w \mapsto \frac{1}{w}$.

In the limit $w \to \infty$, the Laguerre-gaussian mode superpositions generate the paraxial polynomial of the Milnor polynomial. This is because the Laguerre-gaussian modes are generators for the paraxial polynomials when expanded in $\frac{1}{w}$. We now explore the effect of varying w in superposition and observe critical values for w which are topology-changing.

The Hopf link far-field plane, in polar coordinates, is given by

$$\widetilde{\psi}_{\mathrm{Hopf}} = \frac{1}{\sqrt{\pi}}\mathrm{e}^{\frac{-w^2(\rho^2)}{2}}(w - 4w^3 + 2w^5(4+\rho^2+2\rho^2\mathrm{e}^{2\mathrm{i}\theta}) - 8w^7\rho + w^9\rho^2) \tag{3.36}$$

where ρ and θ are the Fourier variables for R and ϕ respectively. As w varies, a quantitative change in the vortex constellation occurs. A numerical search, by counting the number of zeroes in a given plane for a fixed z, finds the transitional value at $w \sim 1.41421$, to five decimal places, where greater than this value, there are eight zeroes in the far field and less than, there are four zeroes. At the critical value there are six zeroes, with two of them being higher order zeroes with a topological charge of two. This transition is shown in figure 3.8 with values of w above and below the critical value.

However, this critical value of w is not the same Gaussian width value for which the vortex link becomes isolated. Except in the limit $w \to \infty$ in the case of Gaussian beams, the vortex knot is not the only vortex structure present. The knot can be isolated by a region of space in the z direction from the additional structures present.

The transition from the link actually existing and being destroyed by the vortices persistent to infinity exhibits intricate geometric and topological features.

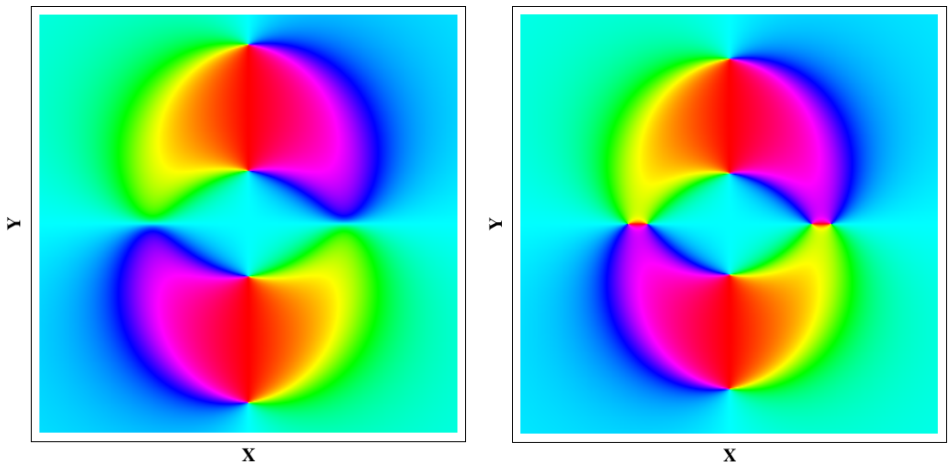

(a) (b)

Figure 3.8: The far-field of the Laguerre-gaussian superpositon for the Hopf link for (a) $w = 1.35$ and (b) $w = 1.45$. The former has a vortex constellation with four vortices and the latter with eight, representing the vortex lines that persist from the near-field region to the far-field.

As the Gaussian beam width decreases, the vortices persisting to the far-field reconnect with the vortex link and the topology undergoes an interesting transition from isolation to four infinite lines. For values of w where there are eight vortices in the far field, the vortex link exists and is isolated from the additional vortex structure of the beam. Decreasing w, the far-field plane loses four of its vortices, creating vortex lines which now have hairpin like bends in them, creating four distinct vortex lines away from the link instead of the eight (counting both cases as $z \to \pm\infty$) before. With further reductions in the value of w, to $w = 1.378$, a reconnection occurs creating four vortex lines that persist from $-\infty$ to $+\infty$. The vortex lines passing through the outer vortices in the $z = 0$ plane do not undergo any further topological change and remain distinct from the rest of the vortex structure as the Gaussian width further decreases. The inner pair of lines still possess the hairpin geometry created when the number of vortices present in the far-field decreases. This structure now creates a self-reconnection, that destroys the structure of the hairpins that have remained after the far-field has lost four of its vortices, and creates four vortex rings. These rings are formed at $w = 1.352$ and shrink in size until they annihilate at $w = 1.347$. These topology changing events are shown in figure 3.9.

The remaining four infinite vortex lines remain in this form as $w \to 0$ although they move towards each other and develop very sharp turns close to $z = 0$, in order to pass through the prescribed points in this plane.

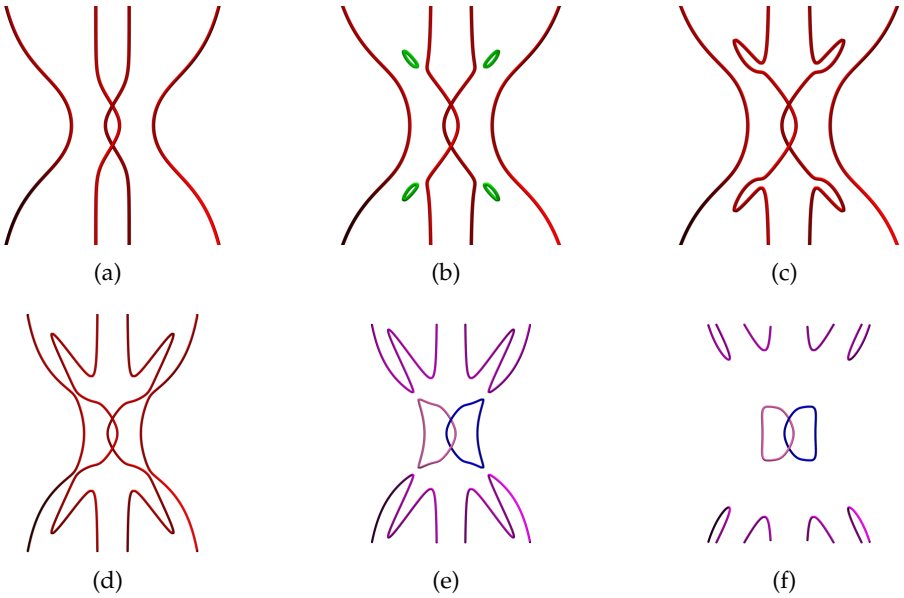

Figure 3.9: The vortex curves formed by the Laguerre-gaussian superposition for the Hopf link as the Gaussian width is increased, for values of w : (a) $w = 1.301$, (b) $w = 1.349$, (c) $w = 1.353$, (d) $w = 1.376$, (e) $w = 1.381$ and (f) $w = 1.440$, numerically found. The infinite lines in (a) reconnect with the loops nucleated shown in (b) which reconnect with the infinite lines to form the geometry in (c). The layout of the Hopf link can be forming in (d) which has formed in (e). The infinite lines that return to the same far-field plane are eight distinct lines in (f) where the far-field has eight vortices persisting to it. Persisting lines are shown in red, loops which are not linked are green, linked loops are shown in pink and blue, identifying the components and lines that start and return to the same far-field plane are magenta. The z-direction is vertical. The view point is on the positive y-axis looking at the origin and we have plotted the range $-10 \leq z \leq 10$.

3.5 Experimental Realisation

The methods of this chapter were used to create real optical fields with knotted phase singularities. The experiments and optimisation algorithms were carried out by Miles Padgett, Kevin O'Holleran and Barry Jack, at the University of Glasgow. These take the form of superpositions of Laguerre-gaussian laser modes with weightings created using the method of the previous section. Such Laguerre-gaussian mode superpositions have been implemented successfully in several cases. In contrast to previous experimental investigations [LDCP05], which by necessity of the construction were threaded, these knots are isolated. This isolation persists up to the Gaussian beam width decreasing below the critical value as described above. Based on functions described here, the Hopf link, trefoil and cinquefoil knots have been successfully created in the vortex struc-

ture of real optical systems. The full details of the experimental setup can be found in [DKJ+10, O'H08], with the vortex line positions obtained using the methods of [OFDP09]. We now describe the procedure and present the results.

The beam from a standard Helium Neon (HeNe) laser is manipulated using a spatial light modulator (SLM). A SLM is a computer controlled pixelised liquid crystal device which imposed an optical delay to light incident on its surface. The different phase values imprinted depend on the brightness of each pixel which can be given one of 256 (8-bit) values. A pattern is formed on the SLM that represents the superposition of Laguerre-gaussian modes requires to create the desired vortex knot. This pattern normally only contains phase information but this experimental setup also uses a technique to include the intensity information, as in [LDCP04]. Finally, the SLM has a blazed diffraction grating applied to put the desired reflection in the first order diffracted component. This allows the zero ordered reflection to be blocked out from entering the imaging part of the system but at the cost of making the intensity of the used component lower.

The beam containing the imprinted phase pattern then propagates and the interference pattern evolves with distance along the beam. A CCD camera is used to image the beam in planes transverse to the propagation direction. Each plane is imaged separately with a set of mirrors on a motorised stage moved to lengthen the beam path to the desired length. Approximately one hundred separate planes are measured for each knot. The intensity can be measured directly and the phase obtained by a series of interferometric measurements.

The theoretically created superpositions of Laguerre-gaussian modes do contain the desired vortex knot but they often do not provide a sufficient contrast between individual vortices to accurately image their location. The vortices are located in regions of the beam that have a low intensity because the intensity must be zero at the vortex. To overcome this, the superposition is subject to an optimisation algorithm to modify the superposition so that the required vortex topology remains but an area of higher intensity persists between vortices. This also creates a superposition where the additional vortex hairpins at high z are moved away from the structure to be viewed. A cost function is used to determine if one superposition is better experimentally than another. The sum of the inverse intensity at a set of points in each transverse plane, in a cylindrical volume containing the vortex knot, is minimised with the constraint that the vortex topology remains unchanged. A coefficient of one mode is randomly changed by a small amount and

$$f_{\text{cost}} = \sum_{\boldsymbol{r} \text{ in the prescribed volume}} \left(\min(I_0, I(\boldsymbol{r}))\right)^{-1}, \tag{3.37}$$

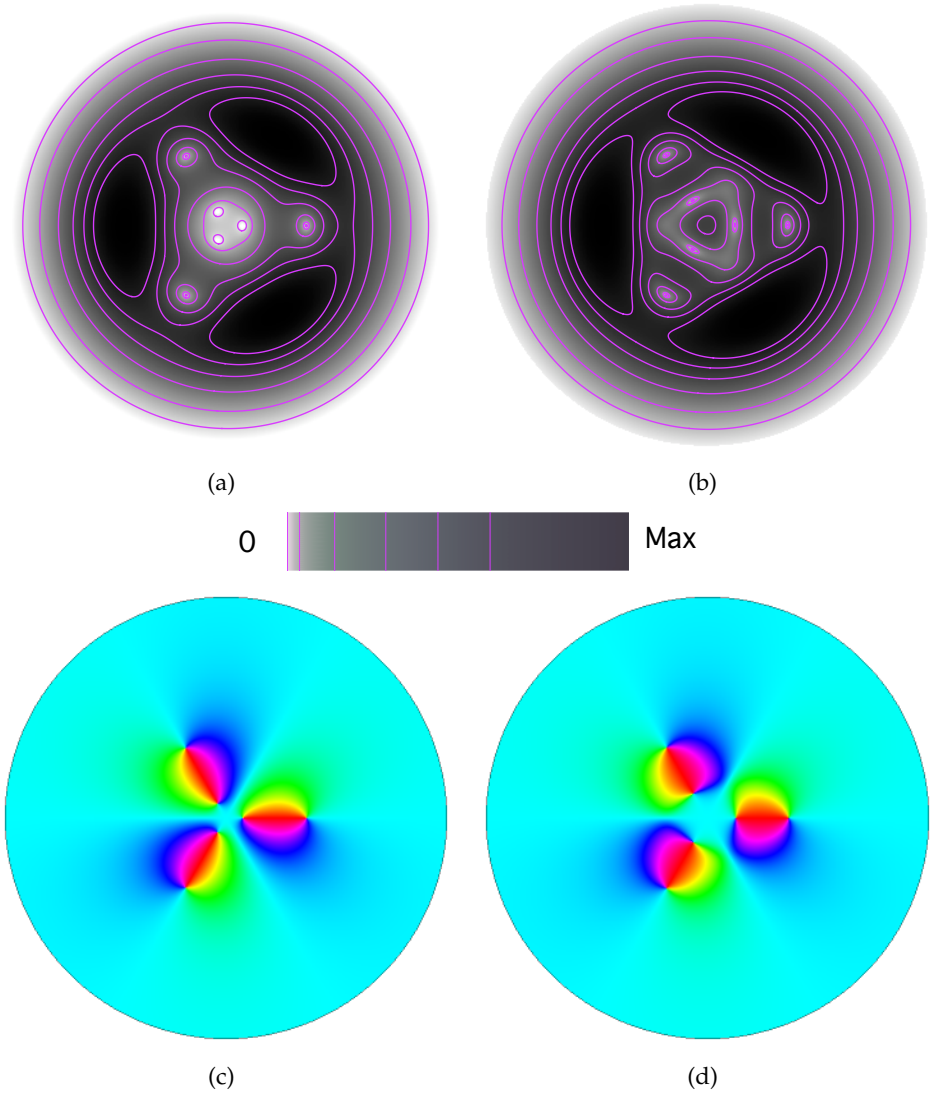

Figure 3.10: The effect of optimising the Laguerre-gaussian superposition of the trefoil knot for the experiment. The unoptimised $z = 0$ plane is shown in (a) and (c) for the intensity and phase respectively. The optimised superposition is shown in (b) and (d). The intensity is shown as "inverse intensity" where the lighter the colour, the lower the intensity as per the key (this is different to other intensity plots throughout this thesis) where the contours match those contour values in the planes shown. The increased areas of darkness in the optimised plane between the vortices can be seen in the intensity plots.

is calculated, where I_0 is a saturating intensity and $I(\boldsymbol{r})$ is the intensity at the position $\boldsymbol{r}$. If this value is lower and the vortex topology is correct then the new coefficient set is kept and the process is repeated, creating an iterative process, which converges on the same set of values after several runs of a few hundred iterations.

The effect of this optimisation is shown in figure 3.10. Overall, the vortices remain approximately parallel to the beam axis over a larger distance, only beginning to approach another vortex close to where they annihilate. This is shown in figure 3.11.

The fact that the optimised superposition has, for some of the modes, a large variation over the initial theoretical values demonstrates the stability of knotted vortices in superposition space.

The theoretical construction has been used to create the Hopf link, and the trefoil and cinquefoil knots. A superposition of Laguerre-gassian modes is created which is then acted on by the optimisation algorithm. The locations of the vortices in each transverse plane can be combined to give the full three dimension vortex lines. We do this in figure 3.13 which are constructed from the experimental data. The Hopf link was realised with an unoptimised superposition; however attempting this with the cinquefoil led to the $T_{2,4}$ link being formed [O'H08] which we plot in figure 3.12.

In order to avoid the target knot reconnecting with the additional vortex structure of the Laguerre-gaussian superpositions, different beam widths were required for each knot. The Hopf link, trefoil and cinquefoil knots were formed in beams with Gaussian widths $w = 1.40, 1.20, 0.93$ respectively. Figure 3.14 additionally shows the experimental trefoil knot with the measured phase from the symmetry plane.

To date, the figure-8 knot has not successfully been experimentally realised. At the time the experiments were being carried out, the technique to create the figure-8 knot from the Lissajous construction had not been fully developed. A Hermite-gaussian superposition was created based on the equation (2.20) of Rudolph. In the $z = 0$ plane, the range in R in which vortices occur is very large compared to those of the successfully created knots. An experimental attempt using a Laguerre-gaussian superposition, with appropriate choice of a and θ introduced in chapter 4, based on the Lissajous construction we believe would be successful.

3.6 Discussion

This chapter has described the method we use to construct optical fields that contain knotted optical vortex lines. The knots constructed go beyond the torus knots of the existing construction of Berry and Dennis [BD01a, BD01b] and we have presented knots and links based on the figure-8 knot. Knots and links, constructed from braids following lemniscate trajectories are fully introduced in the next chapter. These vortex knots have been implemented successfully for a

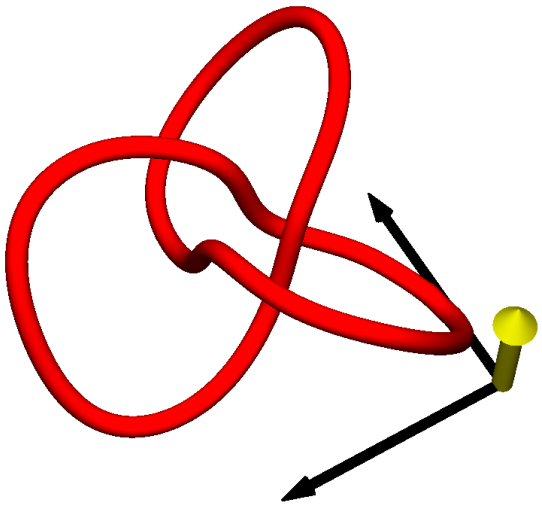

(a)

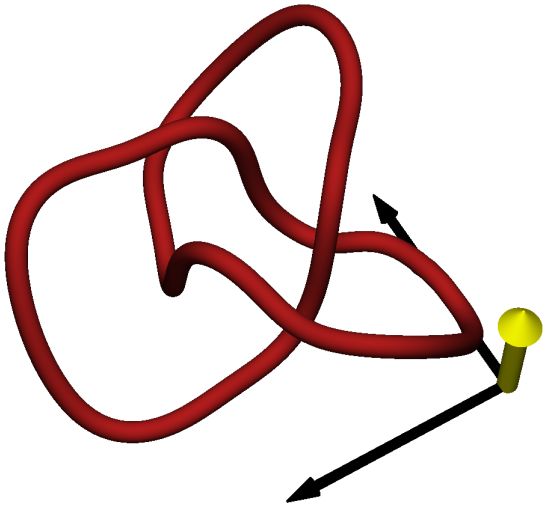

(b)

Figure 3.11: (a) The simulated three-dimensional form of the trefoil knot from the theoretically created Laguerre-gaussian superposition and (b) for the optimised superposition. The black arrows represent the waist width, $w = 1.2$, with both arrows pointing in the x and y directions respectively. The yellow arrows show a Rayleigh range in the propagation z-direction.

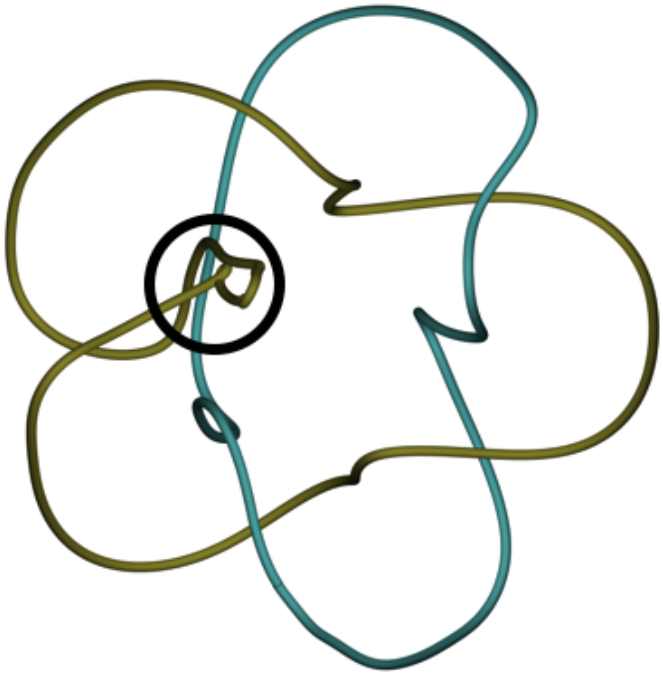

Figure 3.12: The experimentally formed vortex curves for the unoptimised cinquefoil Laguerre-gaussian superposition. There are two components, coloured yellow and blue, which form the $T_{2,4}$ link. The circled crossing shows where the "error" occurs. The cinquefoil knot is formed after the appropriate superposition optimisation and this vortex curve is shown in figure 3.13(c).

number of cases, figure 3.13.

The paraxial polynomials of section 3.2 provide an ideal basis for exploring the nodal topology permitted by the paraxial equation. They are free from factors that induce additional vortex structure, such as those arising from the interference of the Gouy phase terms different Laguerre- or Hermite- gaussian modes contain. In Gaussian beams, the topology of the vortex lines is dependent on the width of the Gaussian. The width of the beam that allows the knot to be successfully formed needs to be found which is not the case for the polynomial solutions. We have seen (section 3.4) that the vortex topology in a Laguerre-gaussian superposition is beam width w-dependent. We introduce additional parameters into our knot construction in the next chapter which could effect the required beam width for successful realisation.

The superpositions of Laguerre-gaussian modes provide a physically realisable solution set. The Hopf link, trefoil and cinquefoil knots have been experimentally realised as such superpositions. These results give a vortex knot that is not threaded, and constructed using knot theory as its basis. In principle,

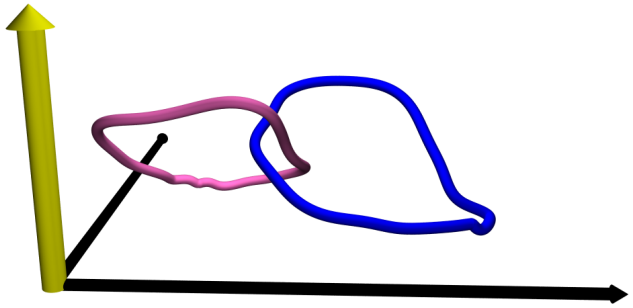

(a)

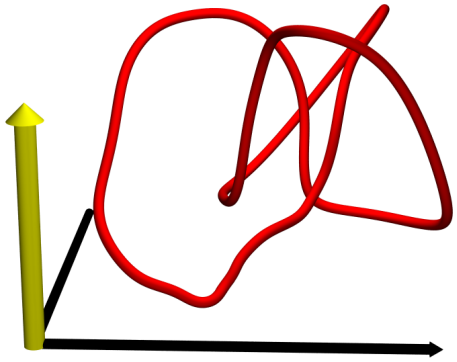

(b)

(c)

Figure 3.13: The experimentally realised (a) Hopf link, with the two components coloured distinctly in pink and blue, (b) trefoil knot and (c) cinquefoil knot. The arrows are the same as in figure 3.11.

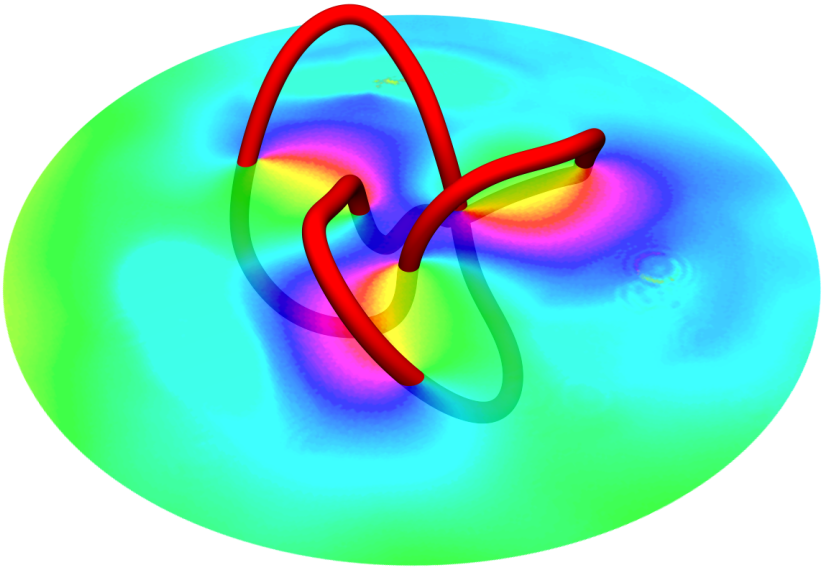

Figure 3.14: The experimental trefoil knot with the measured phase of the symmetry plane shown. The Newton rings formed from reflection of the light from dust can be seen. The measurement of the phase was only accurately measured in the dark regions of the beam, hence the patchy nature of the colouring away from vortices, where the intensity had reached a saturating value.

the figure-8 family of knots could be implemented experimentally, as well as the families of knots and links we explore in chapter 4. This would provide an interesting demonstration of more complex knots beyond the torus knots normally encounted in physics.

These physically realisable superpositions introduce additional vortex lines as illustrated in figure 3.9. This additional structure is dependent on the waist width, w, of the beam. The presence of these additional structures means that the vortex knots we desire to create are not truly isolated. However, the vortex knot in the neighbourhood of $z = 0$, is isolated for a range of w, with a vortex free region around the knot.

We have seen that the Hopf link superposition actually exhibits a range of topology types as w varies, from multiple infinite lines and unlinked loops, in addition to the desired linked loops. For small w, we observe the vortex lines persist from the $z = 0$ plane through to the far-field. Finding the critical values of w for when the link is destroyed is in general difficult. It is also not clear when the vortex lines are infinite or not. This is a question of algebraic geometry, section 6.7, finding solutions of multi-variable polynomials, in our case three-

dimensional polynomials parametrised by w.

We seek to address the questions that arise from the knot construct in chapters 4 and 5.

3.A The Paraxial Polynomials

$n = 0$	1
$n = 1$	$R^2 + 2\mathrm{i}(1+m)z$
$n = 2$	$R^4 + 4\mathrm{i}(2+m)R^2z + 4(1+m)(2+m)z^2$
$n = 3$	$R^6 + 6\mathrm{i}(3+m)R^4z - 12(2+m)(3+m)R^2z^2$ $-8\mathrm{i}(1+m)(2+m)(3+m)z^3$
$n = 4$	$R^8 + 8\mathrm{i}(4+m)R^6z - 24(3+m)(4+m)R^4z^2$ $-32\mathrm{i}(2+m)(3+m)(4+m)R^2z^3$ $+16(1+m)(2+m)(3+m)(4+m)z^4$
$n = 5$	$R^{10} + 10\mathrm{i}(5+m)R^8z - 40(4+m)(5+m)R^6z^2$ $-80\mathrm{i}(3+m)(4+m)(5+m)R^4z^3$ $+80(2+m)(3+m)(4+m)(5+m)R^2z^4$ $+32\mathrm{i}(1+m)(2+m)(3+m)(4+m)(5+m)z^5$

Table 3.1: The paraxial polynomials, explained in the text of this appendix.

Table 3.1 shows the function $f_{m,n}(R,z)$ such that $\psi = R^m \mathrm{e}^{\mathrm{i}m\phi} f_{m,n}(R,z)$ satisfies the paraxial equation. These are the Laguerre polynomial based cylindrical coordinate functions. The table is constructed from the techniques of section 3.2.

3.B Laguerre-gaussian Mode Coefficients

The following tables list the Laguerre-gaussian mode superpositions with their w dependent coefficients for the Hopf link, trefoil, cinquefoil and figure-8 knots.

mode (l,p)	$(0,0)$	$(0,1)$	$(0,2)$	$(2,0)$
Coefficient	$1 - 2w^2 + 2w^4$	$2w^2 - 4w^4$	$2w^4$	$4\sqrt{2}w^2$

Table 3.2: Laguerre-gaussian mode coefficients for the Hopf link.

mode (l,p)	$(0,0)$	$(0,1)$	$(0,2)$
Coefficient	$1 - w^2 - 2w^4 + 6w^6$	$w^2 + 4w^4 - 18w^6$	$2w^4(-1 + 9w^2)$
	$(0,3)$	$(3,0)$	
	$-6w^6$	$8\sqrt{6}w^3$	

Table 3.3: Laguerre-gaussian mode coefficients for the trefoil knot.

mode (l,p)	Coefficient
$(0,0)$	$1+w^2-4w^4-12w^6+24w^8+120w^{10}$
$(0,1)$	$-w^2(1-8w^2-36w^4+96w^6+600w^8)$
$(0,2)$	$4w^4(-1-9w^2+36w^4+300w^6)$
$(0,3)$	$-12w^6(-1+8w^2+100w^4)$
$(0,4)$	$24w^8(1+25w^2)$
$(0,5)$	$-120w^{10}$
$(5,0)$	$64\sqrt{30}w^5$

Table 3.4: Laguerre-gaussian mode coefficients for the cinquefoil knot.

mode (l,p)	Coefficient
$(0,0)$	$\frac{1}{16}\left(168w^8-300w^6+50w^2-7\right)$
$(-2,0)$	$\frac{w^2\left(-19-42w^2+60w^4\right)}{4\sqrt{2}}$
$(0,1)$	$-(1/8)w^2(25-450w^4+336w^6)$
$(2,0)$	$-\frac{w^2\left(-5+42w^2+228w^4\right)}{4\sqrt{2}}$
$(-4,0)$	$\sqrt{\frac{3}{2}}w^4$
$(-2,1)$	$\frac{1}{2}\sqrt{\frac{3}{2}}w^4\left(7-20w^2\right)$
$(0,2)$	$\frac{9}{4}w^6\left(-25+28w^2\right)$
$(2,1)$	$\frac{1}{2}\sqrt{\frac{3}{2}}w^4\left(7+76w^2\right)$
$(4,0)$	$-\sqrt{\frac{3}{2}}w^4$
$(-2,2)$	$\frac{5\sqrt{3}w^6}{2}$
$(0,3)$	$\frac{75w^6}{4}-42w^8$
$(2,2)$	$-\frac{19}{2}\sqrt{3}w^6$
$(0,4)$	$\frac{21w^8}{2}$

Table 3.5: Laguerre-gaussian mode coefficients for the figure-8 knot.

3.C Laguerre-gaussian Superpositions as Generating functions for Paraxial Polynomials

We now show that from the Laguerre-gaussian superposition of table 3.2 we can extract the paraxial polynomial solution for the Hopf link. This is the analogous calculation to one given in the supplementary information of [DKJ+10] for the trefoil knot. We can write the Laguerre-gaussian modes, equation (1.23), in

terms of the Rayleigh range [Sie86]

$$\begin{aligned} LG_p^l(R,\phi,z) &= \sqrt{\frac{p!}{\pi(|l|+p)!}}\frac{R^{|l|}\mathrm{e}^{\mathrm{i}l\phi}}{w^{|l|+1}\left(1+\frac{\mathrm{i}z}{z_R}\right)^{|l|+1}}\left(\frac{1-\frac{\mathrm{i}z}{z_R}}{1+\frac{\mathrm{i}z}{z_R}}\right)^p \\ &\quad\times\exp\left(-\frac{R^2}{2w^2\left(1+\frac{\mathrm{i}z}{z_R}\right)}\right)L_p^{|l|}\left(\frac{R^2}{w^2\left(1+\frac{z^2}{z_R^2}\right)}\right), \end{aligned} \tag{3.38}$$

which allows us to look at the w dependence in a clearer fashion, with $z_R = kw^2$ and we will set $k = 1$. Using the coefficients of table (3.2), and collecting the $\frac{z}{z_R}$ terms, we get, after dropping the non-zero terms which include the Gaussian factor,

$$\begin{aligned} \psi &= \{1-2R^2-4\mathrm{e}^{2\mathrm{i}\phi}R^2+R^4\} \\ &\quad+\frac{4\mathrm{i}\left(-1+R^2-2\mathrm{e}^{2\mathrm{i}\phi}R^2+w^2+2R^2w^2\right)z}{w^2} \\ &\quad+\frac{2\left(3-R^2+2\mathrm{e}^{2\mathrm{i}\phi}R^2-6w^2+4R^2w^2-4w^4\right)z^2}{w^4} \\ &\quad+\frac{4\mathrm{i}\left(1-3w^2+4w^4\right)z^3}{w^6} \\ &\quad+\frac{\left(-1+4w^2-8w^4\right)z^4}{w^8}, \end{aligned} \tag{3.39}$$

which in the limit $w \to \infty$, gives

$$\psi = \{1-2R^2-4\mathrm{e}^{2\mathrm{i}\phi}R^2+R^4\} - 4\mathrm{i}z + 8\mathrm{i}R^2z - 8z^2, \tag{3.40}$$

which is the paraxial polynomial for the Hopf link given in equation (3.24).

Lissajous Constructed Knots

4

In the previous chapter we constructed several knots and links as the nodal sets of functions. Such knots were shown to be able to be embedded in solutions of the paraxial wave equation and ultimately produced in real light beams. We now explore the construction of the knots and links and in chapter 5 go on to investigate the physics of the construction.

The knots and links we construct exhibit patterns in their Conway notation and the coefficients of their Alexander and Jones polynomials. These patterns manifest themselves when the knot formed is from a square of a braid word constructed by the Lissajous construction. The patterns can be used to predict the knot or link created by increasing the number of strands in the braid while keeping the trajectory they follow fixed. Different trajectories give rise to different patterns.

Our knot/link construction naturally forms a three-dimensional set of fibred knots and links. Although our analysis is restricted to lemniscates, a form of Lissajous curve, this classification can be extended to include more general closed Lissajous figures for the braid strand trajectories.

We create functions with knotted nodal lines from functions with zeroes forming a periodic braid. The Lissajous construction, chapter 2, creates braids that are formed with the strands transversely following a Lissajous curve. We have explored simple torus knots and generalisations to knots and links that are related to the figure-8 knot in chapter 3, along with their ability to arise as solutions of the paraxial equation. This chapter explores the extent of the knots and links that can be created by the closure of braids formed by the Lissajous construction. We develop relations between the knot polynomials of the knots and links that are created from the same braid trajectories and use this to give predictions of how the families extend. In this chapter, we begin by studying

specific lemniscates and the knots generated from such braid trajectories before introducing some intricacies of our construction. Recall from chapter 2 that the equation for a function with a braided nodal set b is:

$$p(h) = \prod_{j=0}^{N-1} \left[u - \left\{ \cos\left(h - \frac{2\pi j}{N} \right) + \mathrm{i} \sin\left(\beta \left(h - \frac{2\pi j}{N} \right) \right) \right\} \right], \qquad (4.1)$$

where $\beta \in \mathbb{N}$ is the type of lemniscate (a specific type of Lissajous figure) the strands follow and $b \in B_N$, the group of all braid words with N strands.

4.1 Torus Knots

The torus knots have braid words of the form b^n where $b = \sigma_1 \sigma_2 \ldots \sigma_{N-1}$ is the basic braid word, see definition 2.9 and section 3.1, and N is the number of strands [Lic97]. The closure of this braid word is a $(N-1, n)$-torus knot. We have constructed Milnor polynomials based on braids following a circular trajectory with two strands in chapter 3, with braid word σ_1^n. These are the $(2, n)$-torus knots. We now increase the number of strands in the construction to obtain Milnor polynomials for these higher torus knots.

The torus knots are such that $T_{m,n} \cong T_{n,m}$ giving a symmetry we expect to be preserved by our construction. We now construct the Milnor polynomial for the $(3, 2)$ form of the trefoil knot. The function with the appropriate braid as its nodal set takes equation (4.1) to

$$p(h) = \prod_{j=0}^{2} \left[u - \left\{ \cos\left(h - \frac{2\pi j}{3} \right) + \mathrm{i} \sin\left(h - \frac{2\pi j}{3} \right) \right\} \right]. \qquad (4.2)$$

The Milnor polynomial, see section 3.1, has the form

$$q_{T_{3,2}}(u, v) = u^3 - v^2 \qquad (4.3)$$

$$\begin{aligned} f_{T_{3,2}}(\boldsymbol{r}) = {} & \{1 - 3R^2 + R^2 \mathrm{e}^{2\mathrm{i}\phi} + 3R^4 + 4R^4 \mathrm{e}^{2\mathrm{i}\phi} - R^6\} \\ & - 6\mathrm{i}z + 12\mathrm{i}R^2 z - 6\mathrm{i}R^4 z - 15z^2 + 18R^2 z^2 + 4R^2 \mathrm{e}^{2\mathrm{i}\phi} z^2 - 3R^4 z^2 \\ & + 20\mathrm{i}z^3 - 12\mathrm{i}R^2 z^3 + 15z^4 - 3R^2 z^4 - 6\mathrm{i}z^5 - z^6, \end{aligned} \qquad (4.4)$$

where $\{\bullet\}$ is the z-independent part. The nodal set of this function is the trefoil knot, formed with the curve having a different symmetry to the $(2, 3)$-form of chapter 3 ambient isotopic to it. It is this $(3, 2)$-form of the trefoil knot that shows that it is a 2-bridge knot, as shown in figure 2.20.

Higher torus knots, both $(3, n)$-, and in general (m, n)-, can be constructed in this fashion. The higher torus knots do not however always transfer their nodal topology to a paraxial function using the methods described. Section 4.6 shows how the paraxial function can be built with a modified approach and the knot or link inherited successfully.

Repeats n	2	3	4	5	6
Name	Figure-8 4_1	Borromean Rings $L6a4$	Turk's Head 8_{18}	10_{123}	12 Crossing Brunnian Link

Table 4.1: The knots and links formed by the closure of n repeats of the braid word $\sigma_1\sigma_2^{-1}$. Their common name is given where it exists and the Rolfsen [Rol76] or Dowker/Thistlethwaite notation is given where known.

4.2 Lemniscate Knots

When $\beta = 2$ in equation (4.1) the zero points in the u plane follow a lemniscate (figure of eight, 2-lemniscate, ∞-shape) trajectory. Hence the braided function takes the form

$$p(h) = \prod_{j=0}^{N-1} \left[u - \left\{ \cos\left(h - \frac{2\pi j}{N}\right) + \mathrm{i}\sin\left(2\left(h - \frac{2\pi j}{N}\right)\right)/a \right\} \right], \tag{4.5}$$

where $a \in \mathbb{R}^+$ is discussed later in this section. Given that the lemniscate curve self-intersects, the number of strands becomes critical; we desire that the stands remain distinct. For the lemniscate, N is required to be odd, so the first non-trivial case is $N = 3$. This gives rise to the figure-8 knot family of knots and links, seen in chapter 3. The basic braid word in this case is $b = \sigma_1\sigma_2^{-1}$, which has closures $\widehat{b^n}$, shown in table 4.1.

For $n \geq 6$ with $n \equiv 0 \mod 3$, the closure of the braid gives rise to a Brunnian link [Jab99]. A Brunnian link is a link that becomes trivial (unlinked) when one component is removed. In our three strand braids, $(\sigma_1\sigma_2^{-1})^n$, this is equivalent to removing one strand, which represents one component.

The real, positive definite parameter a in equation (4.5) is now investigated. The effect of increasing a is to reduce the range of the lemniscate curve in y in the u-plane. As a parametric curve, $(\cos h, \frac{\sin 2h}{a})$, the maximum value of y reached is $\frac{1}{a}$. In the closure of the braid, the geometric form of the knot varies as a varies. This is shown in figure 4.1, for $a = 1, 2, 3$ as well as showing how the lemniscate of the strand trajectories varies with a. Figure 4.1 also shows, for various a, the lemniscate of the braid trajectories. In this case of the lemniscate, $a = 2$, forms the "lemniscate of Gerono" [Law72] as the trajectory of the braid strands.

As a increases, the $z = 0$ plane of the Milnor polynomial retains the same zero constellation but the spacing of the zeroes increases as a increases. The effect this has on the three-dimensional curve is shown in figure 4.1. This allows the zeroes in the $z = 0$ plane to be positioned closer to each other, providing for a narrower Gaussian width, to enclose all the zeroes, in Laguerre-gaussian superpositions. Along with a parameter introduced in section 4.5, we give the

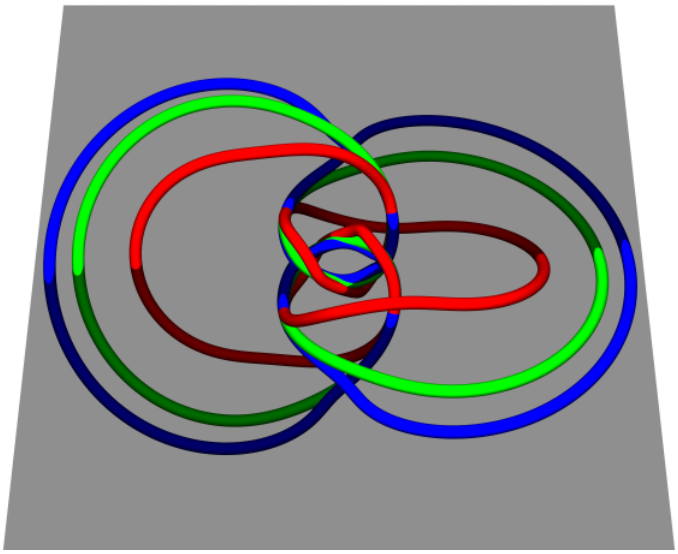

(a)

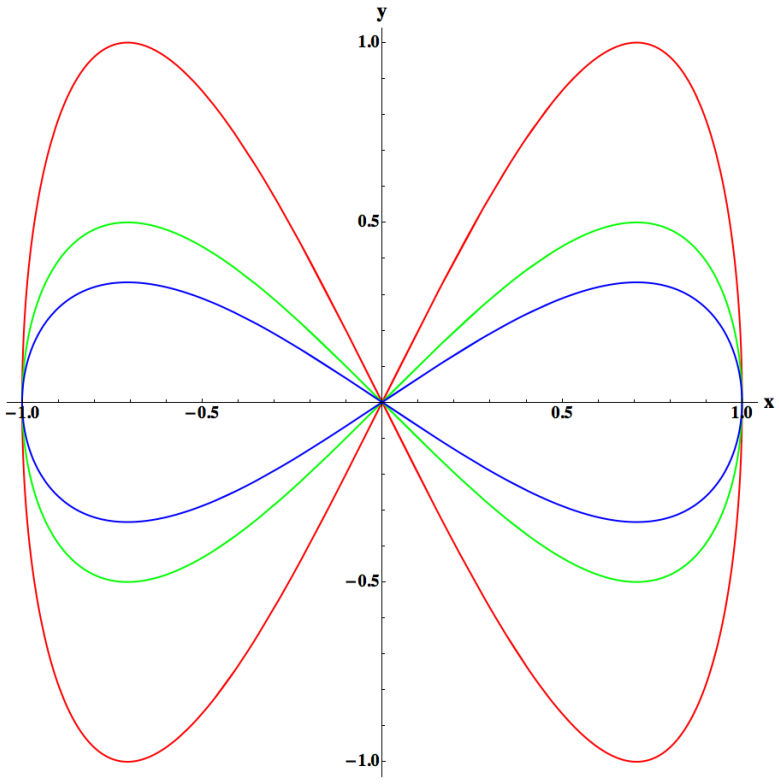

(b)

Figure 4.1: The figure-8 knot formed from closing the braid of equation (4.5) with different values of a. (a) The 3-dimensional curves formed for $a = 1, 2, 3$, shown by the red, green, blue curves respectively. The $z = 0$ plane is shown for orientation, with the origin at the centre. Although similar near the origin, the three curves differ substantially as $\boldsymbol{r}$ increases. (b) The actual lemniscates for $a = 1, 2, 3$ coloured as in (a).

$1\bar{3}2\bar{4}1\bar{3}2\bar{4}$	Starting word from Lissajous construction
$\bar{3}121\bar{4}\bar{3}2\bar{4}$	Use of $\sigma_i\sigma_j = \sigma_i\sigma_j$ when $\lvert i-j\rvert \geq 2$
$\bar{3}212\bar{4}\bar{3}2\bar{4}$	$121 = 212$
$\bar{3}22\bar{4}\bar{3}2\bar{4}$	Stabilisation
$\bar{3}22\bar{4}\bar{3}\bar{4}2$	Use of $\sigma_i\sigma_j = \sigma_i\sigma_j$ when $\lvert i-j\rvert \geq 2$
$\bar{3}22\bar{3}\bar{4}\bar{3}2$	$\bar{4}\bar{3}\bar{4} = \bar{3}\bar{4}\bar{3}$
$\bar{3}22\bar{3}\bar{3}2$	Stabilisation
$\bar{2}11\bar{2}\bar{2}1$	Relabelling of the strands
$11\bar{2}1\bar{2}\bar{2}$	Cyclic permutation

Table 4.2: The steps to the braid word from the Lissajous construction, a lemniscate with five strands, to the form given by Gittings [Git08].

Strands	3	5	7	9	11
Knot / Link	Figure-8	6_3	8_9	10_{17}	$12a1273$
Conway Notation	[22]	[2112]	[3113]	[4114]	[5115]

Table 4.3: The knots formed in the closure of the square of a the basic braid word of the braid stands following a lemniscate trajectory with N strands. The Conway notation for the knots is also shown.

Laguerre-gaussian superposition for the figure-8 knot in appendix 4.A to this chapter, to complement the superposition given in table 3.5.

We now increase the number of strands in the braid, which must be odd to avoid the braid strands intersecting each other. Increasing the number of strands creates a generalised family of knots which we now construct. For $N = 5$ the basic braid word formed is, now dropping the symbol σ and using overbars for inverses for brevity, $1\bar{3}2\bar{4}$, whose square represents the knot 6_3. This has eight letters and is obviously not the minimum length of word for 6_3. The use of the Markov move of stabilisation, section 2.3, is required to reduce the number of strands down to three. These steps are shown in table 4.2. The final word is the form given by Gittings [Git08] where the minimal braid representations for knots are tabulated.

This family continues with the closure of the cube representing the knot $12n706$.[1] Beyond twelve crossings it becomes difficult to uniquely identify knots and links from the common sources. Obviously these higher crossing knots are accessible via the Lissajous construction. We will next concentrate on increasing the number of strands following the lemniscate trajectories.

Table 4.3 shows the knot / link formed by the closure of lemniscate based braids with various numbers of strands. Also shown is the Conway notation for the knot, which apparently forms a pattern as N increases. The pattern in

[1] The notation we use for knots of eleven and higher minimum crossing number is from Knot Atlas [BNM10] and KnotInfo [CL10].

the Conway notation is $[(N-1)/2\ 1\ 1\ (N-1)/2]$, where N is the number of strands in the Lissajous construction which suggests that these knots and links are related in other ways. The basic braid words for the lemniscate knots, b_{strands} (also called b_s), have the form of the ordered product

$$b_s = \prod_{i=1}^{M} i\ \overline{(M+i)}, \tag{4.6}$$

where $M = (N-1)/2$ and N is the number of strands. Given this form, and the ability of the knot 6_3 to simplify as above, this leads us to the following proposition.

Proposition 4.1. *The knot formed by the closure of b_s^2, as in equation (4.6) for a 2-lemniscate braid, can be written in the form of $(1\ \bar{N}\ 2\ \overline{(N+1)} \ldots N\ \overline{(2N+1)})^2$, arising from the Lissajous construction on the lemniscate trajectory. This can then be written in the form $1^N\bar{2}1\bar{2}^N$, to be consistent with the minimal forms given by Gittings [Git08].*

Proof. The case of three strings is trivial and for five strands is shown in table 4.2. For higher numbers of strands, the same procedure as presented in table 4.2 needs to be followed :

- Use the braid relation $\sigma_i\sigma_j = \sigma_i\sigma_j$ when $|i-j| \geq 2$ (BR1, equation (2.5)) to rearrange the braid word to form a sequence of letters $\overline{(M+1)}\bar{M}\overline{(M+1)}$. This can occur only once and be rearranged to $\bar{M}\overline{(M+1)}\bar{M}$ by the other braid group relation, (BR2, equation (2.6)). This leaves only one occurrence of $\overline{(M+1)}$ which can be removed by the Markov move stabilisation (figure 2.13).

- A similar procedure is applied to the element 1 and it is removed. It may be necessary to make use of the fact the braid word is closed, so any cyclic permutation of the elements still represents the same knot. This leaves a braid word with two less strands than the constructed word.

- These two steps are repeated, cyclically permuting the word as necessary, reducing the number of strands the word needs. This will ultimately create a word with only two uniquely labelled elements which are relabelled 1 and 2. There are $N+1$ occurrences of each and 2 occurs as $\bar{2}$.

- The string of N 1's is written 1^N; similarly for the string of $\bar{2}$'s. In general this requires the use of cyclic permutation. This leaves a braid word of the form $1^N\bar{2}1\bar{2}^N$.

□

Knot	Alexander Polynomial Coefficients
Figure-8	1 -3
6_3	1 -3 5
8_9	1 -3 5 -7
10_{17}	1 -3 5 -7 9
$12a1273$	1 -3 5 -7 9 -11

Table 4.4: The Alexander polynomial coefficients for the given knots, which are the closure of the square of a basic braid word where the strands follow a lemniscate trajectory. Only the non-repeated coefficients are shown, in order, because of the symmetry of the Alexander polynomial coefficients.

The Conway notation is not the only knot invariant that exhibits a pattern for the squared lemniscate braids. The coefficients of the Alexander polynomials of the knots also form a pattern. Table 4.4 shows the Alexander polynomial coefficients for the knots in table 4.3. This set of coefficients have the form $-1^{i+1}(2i-1)$ where $i \in \mathbb{N}$. The alternating sign is due to the fact the coefficients of the Alexander polynomial of a 2-bridge (rational) knot must alternate; Hartley has a proof of this [Har79].

This relationship between the Alexander polynomial and the Conway notation form has been observed by Jablan [Jab01]. This reference uses Conway notation to group knots by relationships between their knot polynomials and other invariants. The closest family given to our construction is the knots with Conway notation $[p11q]$ where $p \equiv q \mod 2$. When $p = q$, this is the family of knots we generate from the squares of basic braid words following a lemniscate trajectory. We now look for similar relationships between the knots and links generated from braids following higher lemniscates.

4.3 3-Lemniscate Knots

Higher order lemniscates are those with more loops and they can also be used in the Lissajous construction. The case of $\beta = 3$ in equation (4.1) gives rise to the double lemniscate with two self-intersections, we call this a *3-lemniscate*. The braid strands are initially positioned with equal spacing between them on the 3-lemniscate. In order to avoid the strands intersecting as h varies, the number of strands must not be $N \equiv 0 \mod 3$.

Definition 4.2 (Trivial Lemniscate Knot / Link)**.** *If a knot or link can be formed by the Lissajous construction using a m-lemniscate and a n-lemniscate such that $m < n$, we call it a trivial knot or link on the n-lemniscate.*

The $(2, n)$-torus knots and links are trivial on the 3-lemniscate. They can be formed on the 1-lemniscate (the circle).

The lowest non-trivial number is four strands and has basic braid word $13\bar{2}$ which has the link $L6a1$ as the closure of its square. This braid, $(13\bar{2})^2$ is illustrated in figure 4.2 with the link $L6a1$ shown as its closure. This braid is the same word given by Gittings but shorter than the word given by the online resource "Knot Atlas" [BNM10]. Like in the case of the 2-lemniscates, the basic braid word can be taken to higher powers before the braid is closed. Let $b = 13\bar{2}$, then $\widehat{b^3}$ is the knot 9_{40} and $\widehat{b^4}$ forms a twelve crossing four component link. There are no common names for this twelve crossing link or the higher crossing number knots and links formed in this fashion.

We now increase the number of strands and look at the relationship between the square of the basic braid word and its Conway notation. On five strands, the basic braid word is $b = 1\bar{3}\bar{2}4$ and $\hat{b}^2$ is the knot 7_7. This braid trajectory gives rise to both knots and links for $\widehat{b^2}$, contrasting to only knots for the 2-lemniscate trajectories. The minimal crossing number of the knots increases by one for each additional strand in the construction and hence there is a jump of two when missing the case of $N \equiv 0 \mod 3$. These knots and links are shown in table 4.5.

The Conway notation for the knots and links exhibits a pattern as the number of strands increase in $\widehat{b^2}$. This notation exhibits a relationship between adjacent knots in the table. When increasing the number strands in the braid by one, the central element increases by one. In the case where the number of strands increases by two, when missing out a multiple of three, the outer two elements both increase by one. This sequence begins when the number of strands is seven and can be seen in table 4.5.

The 3-lemniscate braid trajectory gives rise to both knots and links as the square of the basic braid words. This means that the Alexander polynomial is not a good invariant to find patterns and sequences. We will use the Jones polynomial for these knots and links we look at the Jones polynomial. The Jones polynomial, section 2.4, is only used as a tool in the chapter and we do not consider its construction or more general properties here. The Jones polynomial is defined for links, where for links with an even number of components it is a Laurent polynomial in the variable $q^{\frac{1}{2}}$ [Jon85], otherwise only in q. We now consider just the coefficients of the Jones polynomial as an ordered list created by multiplying the polynomial by the appropriate factor q^m such that we create a polynomial with a constant term and the remaining terms have positive integer powers. The order of the coefficient list is reversed for links in table 4.5, mirroring the polynomial by taking $q \to q^{-1}$.

As the number of strands in the basic braid word increases, the number of

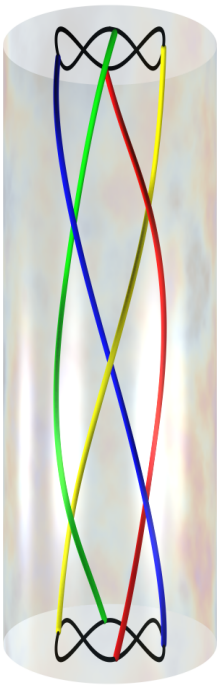

(a)

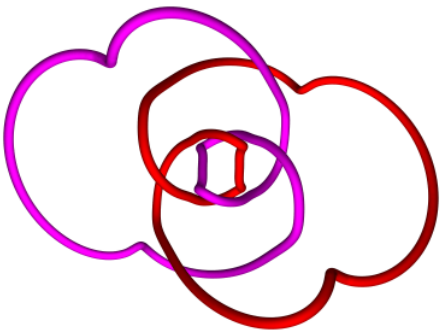

(b)

Figure 4.2: (a) The braid word $(13\bar{2})^2$ on the 3-lemniscate in B_4. This has basic braid word, $13\bar{2}$. (b) The two component link $L6a1$ formed by the closure of the braid word $(13\bar{2})^2$.

Strands	Conway Notation	Knot or Link	Jones Polynomial Coefficients
4	[2 2 2]	$L6a1$	1 2 2 2 3 1 1
5	[2 1 1 1 2]	7_7	1 2 3 4 4 3 3 1
7	[2 1 1 1 1 1 2]	9_{31}	1 4 6 8 10 9 8 5 3 1
8	[2 1 1 2 1 1 2]	$L10a91$	1 4 7 10 13 13 9 3 1
10	[3 1 1 2 1 1 3]	Two component 12 crossing Link	1 4 9 14 20 23 24 21 17 11 6 3 1
11	[3 1 1 3 1 1 3]	$13a4296$	1 4 9 15 22 28 30 29 25 18 12 6 3 1
13	[4 1 1 3 1 1 4]	$K15a75986$	1 4 9 17 26 36 43 45 44 37 29 20 12 6 3 1

Table 4.5: The knots and links constructed from the squares of the basic braid words created from braids following a 3-lemniscate trajectory. The Conway notation and the coefficients of the Jones polynomials are given.

terms in the Jones polynomial increases. Unlike the Alexander polynomial, the coefficients of the Jones polynomial are not symmetric. We find the Jones polynomial exhibits two sequences, one starting at either end of the list. For the first few 3-lemniscate knots, we list their Jones polynomial, $V(q)$, and highlight the terms forming the two sequences with underlining:

$$\begin{aligned}
[2112112] \quad & V(q) = -q^{\frac{7}{2}}(\underline{1 - 3q + 6q^2} - 9q^3 + 13q^4 - 13q^5 + 13q^6 - 10q^7 \\
& +7q^8 - \underline{4q^9 + q^{10}}) \\
[3112113] \quad & V(q) = -q^{\frac{-5}{2}}(\underline{1 - 3q + 6q^2} - 11q^3 + 17q^4 - 21q^5 + 24q^6 - 23q^7 \\
& +20q^8 - 14q^9 + \underline{9q^{10} - 4q^{11} + q^{12}})
\end{aligned}$$

The coefficients of the successive Jones polynomial, as the number of strands increases, tend to these sequences; the central coefficients are not members of the sequence. These sequences are

$$1, 4, 9, 17, 29, 65, 89, 117, 149, 185, 225, 269, 317, 369, 425 \ldots$$
$$1, 3, 6, 12, 21, 33, 49, 69, 93, 121, 153, 189, 229, 273, 321, 373 \ldots$$

which are the appropriate 31 terms of the 53 term Jones polynomial for the link with Conway notation [16 1 1 16 1 1 16]. Neither of these sequences appear on the Online Encyclopaedia Integer of Sequences database [OEI10]. This is an online database of common integer sequences and using this we have not been able to determine if there is a known pattern or meaning to the sequence. This does not mean that there is not a known meaning to the sequence. The existence of these sequences shows that the 3-lemniscate knots and links have related properties between them beyond the braid construction.

Strands	Conway Notation	Knot / Link
3	[2 2]	Figure-8
5	[2 2 2 2]	8_{12}
7	[2 1 1 1 1 1 1 2]	10_{45}
9	[2 1 1 1 1 1 1 1 1 2]	$12a499$
11	[2 1 1 2 1 1 2 1 1 2]	$14a10074$
13	[3 1 1 2 1 1 2 1 1 3]	A 16 crossing knot
15	[3 1 1 3 1 1 3 1 1 3]	An 18 crossing knot

Table 4.6: The knots constructed from the squares of the basic braid words created from braids following a 4-lemniscate trajectory. The Conway notation is given and the common name shown where it exists.

4.4 Higher Lemniscate Knots

The Lissajous construction can be extended to use general n-lemniscate braid trajectories, for any $\beta \in \mathbb{N}$. The 4-lemniscate is the next set of knots and links we can construct. The closure of the basic braid words formed, squared, exhibit a relation in their Conway notations as the number of strands in the braid is increased. The number of strands N must be odd to ensure that they remain distinct. Table 4.6 shows the knots formed by the closure of the square of the basic braid word with its Conway notation.

We list the 5-lemniscate knots we have studied in the tables of Appendix B. There are a number of trivial knots on this lemniscate and we expect for these-higher lemniscates, the knots and links formed by the closure of the basic braid word squared, duplicate those that can be formed more simply from lower values of β before non-trivial knots are formed and patterns can be observed. This means that the patterns in the Conway notation and knot polynomial coefficients potentially begin at a high number of braid strands. In the case of $\beta = 5$ the Conway notation pattern begins at braids with eleven stands, which corresponds to a fifteen crossing knot. This leads us to believe that a knot or link with a low number of crossings, if it cannot be created by a lemniscate with a low β, then it cannot be created with a higher order lemniscate. We expect, as the number of loops in the lemniscate increases, the number of unique knots and links created will increase for a high enough number of braid strands.

4.5 The $z = 0$ Plane

The paraxial functions of chapter 3 and their later analysis in this thesis, require the $z = 0$ plane of the Milnor polynomial in their formation. The nodal knot or link in these functions is formed from the closure of a braid. We are however free

to choose the location of this axis in braid space. This axis forms the z-axis in real space. The topology of the nodal set of the Milnor polynomial is isotopic to any other axis choice, but the geometric shape of the curve is in general different. We now introduce a further parameter into the Lissajous construction to position the closure axis.

Our illustrations of braids are shown contained inside a cylinder. The closure axis is located at the mid-point in the braid's height h. It touches the cylinder tangentially and such that it is perpendicular to the h direction. This gives a full 2π possible positions for the location of the axis. We label this angle θ. This angle is that which the closure axis makes with the $y = 0$ line in a transverse u plane.

Under closure, the axis, in braid space, forms the z-axis passing through the origin of $\mathbb{R}^3$ and hence the $z = 0$ plane in $\mathbb{R}^3$ is the plane that intersects the enclosing torus, the image of the cylinder under the Milnor map, through the equator. This is the plane parallel to the h direction and perpendicular to the closing axis. Geometrically, the nodal curve is unique up to the value of θ modulo π. An illustration of placing the closure axis and the value of θ is shown in figure 4.3.

The value of θ is built into the Milnor map by letting $u \to \mathrm{e}^{\mathrm{i}\theta}u$. The 3-sphere inverse stereographic projection is preserved : $|\mathrm{e}^{\mathrm{i}\theta}u|^2 + |v|^2 = 1$. The Milnor maps taken so far have closed the braid with $\theta = 0$ and we call this the *standard* closure and view of the knot.

We now explicitly construct the Milnor polynomial for the figure-8 knot with the parameter θ included. The process is shown in figure 4.4. When $\theta = 0$, the standard view, the braid strands pass through the $z = 0$ plane eight times. This persists under the Milnor map to keep eight zeroes in the Milnor polynomial at $z = 0$. The other extreme value for the angle is $\theta = \frac{\pi}{2}$, equivalent to $u \to \mathrm{i}u$. Here the same braid only passes through the $z = 0$ plane four times. This leads to two very different curves of the nodal figure-8 knot but they remain ambient isotopic to each other. In the $z = 0$ plane, we get a θ-dependent Milnor polynomial

$$\begin{aligned} f_{\text{fig-8}}(\boldsymbol{r}, \phi, \theta) \;=\; & \mathrm{e}^{3\mathrm{i}\theta} - 2\mathrm{e}^{3\mathrm{i}\theta}R^2 + 3\mathrm{e}^{\mathrm{i}\theta}R^2\mathrm{e}^{-2\mathrm{i}\phi} - 3\mathrm{e}^{\mathrm{i}\theta}R^2\mathrm{e}^{2\mathrm{i}\phi} + 2R^2\mathrm{e}^{-2\mathrm{i}\phi} + 2R^2\mathrm{e}^{2\mathrm{i}\phi} \\ & + 4R^4\mathrm{e}^{-2\mathrm{i}\phi} + 4R^4\mathrm{e}^{2\mathrm{i}\phi} - 2R^4\mathrm{e}^{-4\mathrm{i}\phi} + 2R^4\mathrm{e}^{4\mathrm{i}\phi} \\ & + 2\mathrm{e}^{3\mathrm{i}\theta}R^6 - 3\mathrm{e}^{i\theta}R^6\mathrm{e}^{-2\mathrm{i}\phi} + 3e^{\mathrm{i}\theta}R^6\mathrm{e}^{2\mathrm{i}\phi} + 2R^6\mathrm{e}^{-2\mathrm{i}\phi} + 2R^6\mathrm{e}^{2\mathrm{i}\phi} \\ & - \mathrm{e}^{3\mathrm{i}\theta}R^8. \end{aligned} \tag{4.7}$$

This Milnor polynomial can be made into a function satisfying the paraxial equation using the techniques of chapter 3. We give the Laguerre-gaussian superposition for the figure-8 knot, with the mode coefficients containing the θ- and a-dependence, in appendix 4.A to this chapter.

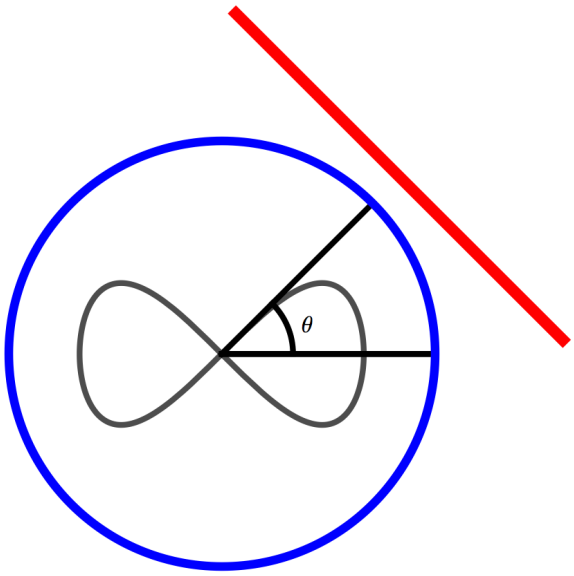

(a)

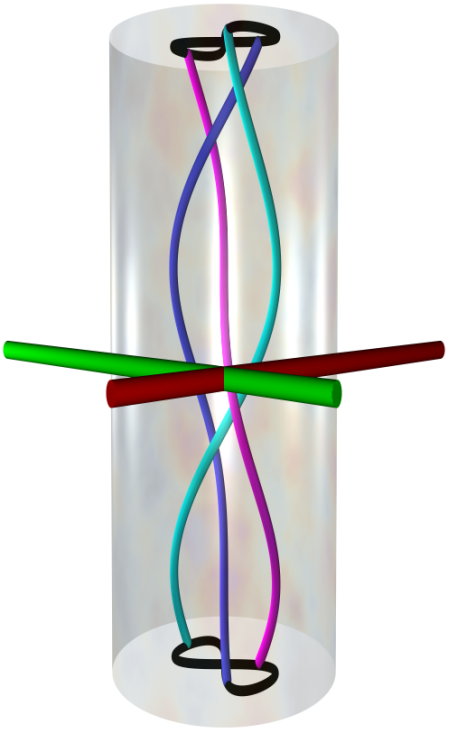

(b)

Figure 4.3: The location of the axis around which the braid is closed. (a) In a u-plane, an example braid trajectory lemniscate is shown. The blue circle represents the enclosing cylinder and the positive x-axis is drawn in black, from which the angle θ is measured. The example angle shown is $\theta = \frac{\pi}{4}$ with the corresponding axis shown as the thick red line. (b) A three-dimensional plot of two possible axes for closing the shown braid. They are in a tangential direction to the enclosing cylinder, lying in the u-plane at half the total height of the braid.

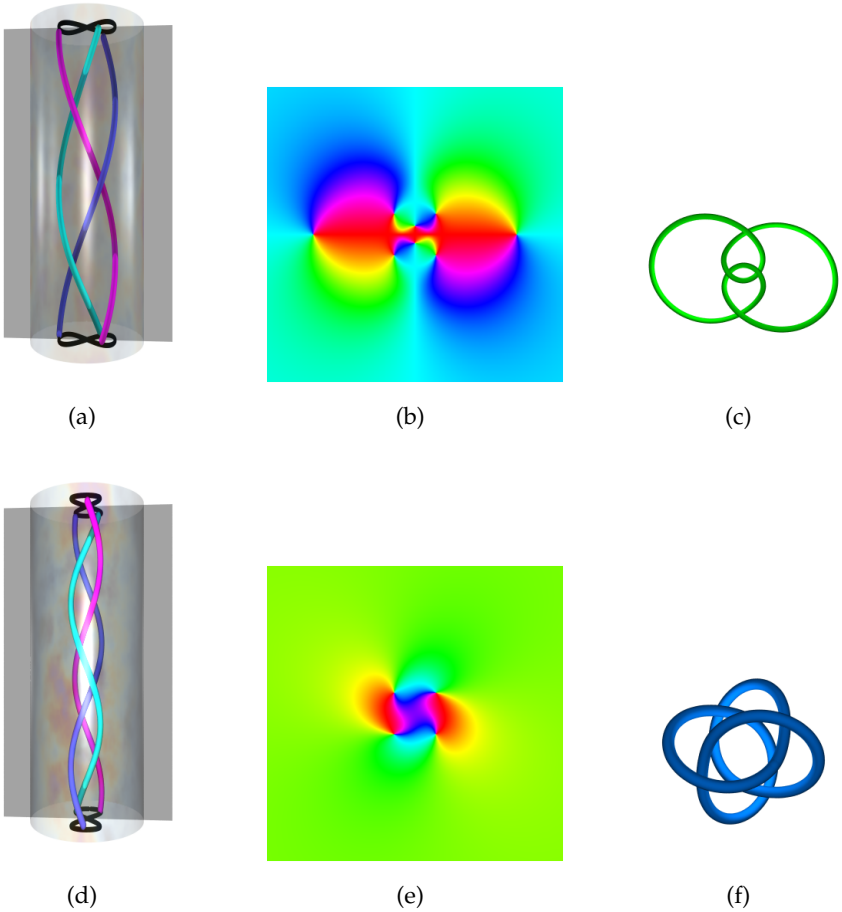

(a) (b) (c)

(d) (e) (f)

Figure 4.4: The effect of varying θ when using $e^{i\theta}u$ in the Milnor map for the figure-8 knot. The $z = 0$ plane shown intersecting the braid (a) eight times for $\theta = 0$ and (d) four times for $\theta = \pi/2$. The $z = 0$ plane of the Milnor map (b) with eight corresponding zeroes and (e) with four zeroes for $\theta = 0, \pi/2$ respectively. The geometric form of the nodal lines show in (c) the standard view for $\theta = 0$ and (f) the form generated with $\theta = \pi/2$.

The link $L6a1$ undergoes a similar change in its geometric form when different positions for the closure axis are chosen. The $z = 0$ plane for this link is shown in figure 4.2 for $\theta = 0$ and for $\theta = \frac{\pi}{2}$.

The torus knots constructed from a circular trajectory do not undergo a geometric change with a variation with θ. The circle does not have an orientation direction definable like the lemniscates do. Hence the number of zeroes in the $z = 0$ plane is constant and the constellation also remains fixed up to rotation.

The parameter θ provides a method of controlling the geometric form of the knot or link being constructed. This means that a continuous set of curves can be formed and solutions of the paraxial equation created and tested to see if all the forms of the curve are supported. Different values of θ in general lead to

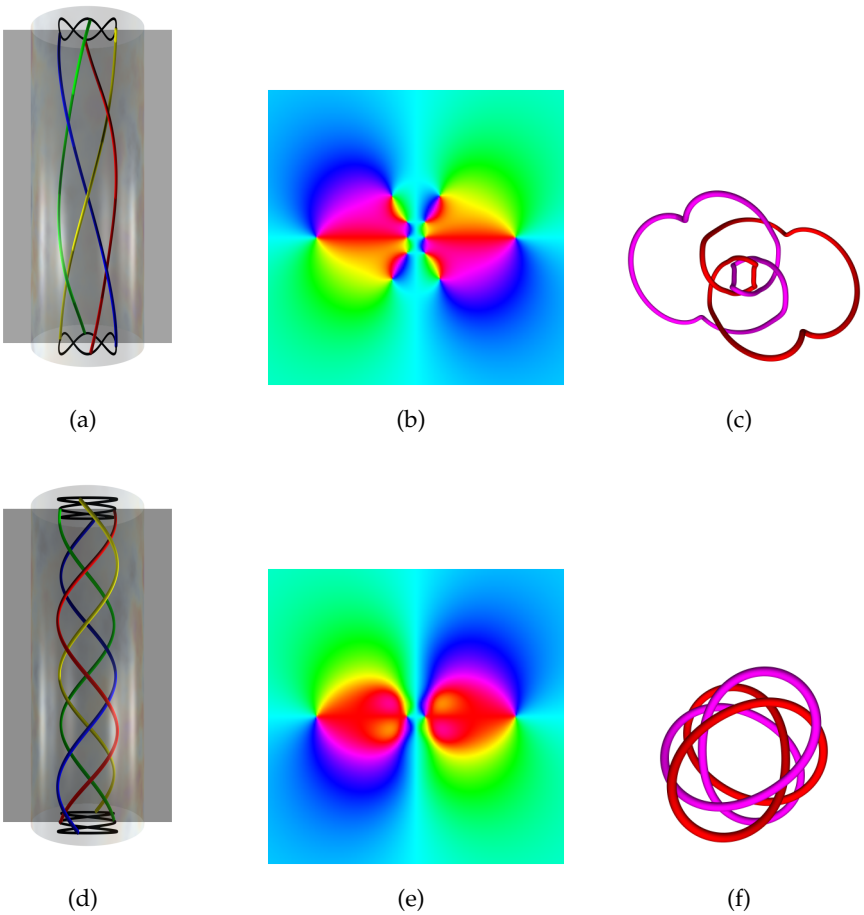

(a) (b) (c)

(d) (e) (f)

Figure 4.5: The link $L6a1$ with $\theta = \frac{\pi}{2}$. The braid now only intersects the $z = 0$ plane four times, (d) in braid space ((a) $\theta = 0$) and in the expected two-fold symmetric way in (e) showing the phase of the $z = 0$ plane of the Milnor polynomial ((b) $\theta = 0$). The two components of the link are coloured distinctly in (f) and although geometrically different to the curves in (c) where $\theta = 0$ they are equivalent topologically.

different zero constellations in the $z = 0$ plane. These different constellations could lead to successful experimental implementations when the default $\theta = 0$ value leads to a more complex layout, for example the figure-8 knot which becomes a lot simpler, figure 4.4, when $\theta = \frac{\pi}{2}$.

4.6 Over Homogenisation

We have remarked that some knots do not successfully occur in a paraxial function using the methods we have developed so far. This section examines one such knot and introduces a method that can be used to aid this topology transfer.

In taking the Milnor map of a braided function to form the Milnor polynomial, the functions u and v are rational functions of position with a common denominator, $1 + R^2 + z^2$. Our Milnor maps have consisted of the numerator of the complex function formed once the function is placed over a common denominator to each term. This is achieved by making all terms in u, v, v^* homogenous by multiplying by a function $w(\boldsymbol{r}) = 1 + R^2 + z^2$ such that there is no overall factor of w in the expression. When a function satisfying the paraxial equation is constructed from such a Milnor polynomial, we have already noted that some knots, for example the $T_{5,2}$ form of the cinquefoil knot, do not successfully inherit the desired nodal topology. We now investigate the effect of introducing an overall factor of w (and multiple factors of w) on the nodal set of the corresponding paraxial function.

The homogenisation with w above is the minimal power of w to be able to take the numerator of the expression to form the Milnor polynomial. A Milnor polynomial can be formed with a different power of w such that the polynomial in u, v, v^*, w is still homogeneous but with an overall factor of w present. This leads to a equation form of the Milnor map

$$q'_s = w^s q(u, v, v^*, w), \tag{4.8}$$

where q is the Milnor map created by the Lissajous construction and $s \in \mathbb{N}$ is the *level of over homogenisation.* The case of $s = 0$ corresponds to the unchanged Milnor map which we call the *standard homogenisation*.

We now illustrate over homogenisation by example using the $T_{5,2}$ cinquefoil knot and how this affects the topology of the nodal set in the formed function that satisfies the paraxial equation. This knot can be given the following levels of homogenisation

$$q_0 = u^5 - v^2 w^3, \tag{4.9}$$

$$q_1 = wu^5 - v^2 w^4, \tag{4.10}$$

$$q_2 = w^2 u^5 - v^2 w^5, \tag{4.11}$$

where s in q_s is the level of homogenisation. All three levels of homogenisation contain the cinquefoil knot in their respective Milnor polynomial's nodal set and they are almost identical in their geometric appearance. The paraxial functions they create are very different in their nodal sets.

The standard homogenisation, q_0, when made to satisfy the paraxial equation does not form the cinquefoil knot in its nodal set. For almost all values of ϕ, only three zeroes are present in the (R, z)-plane. This is in contrast to the five in the Milnor polynomial arising from the five braid strands. Figure 4.6 shows the

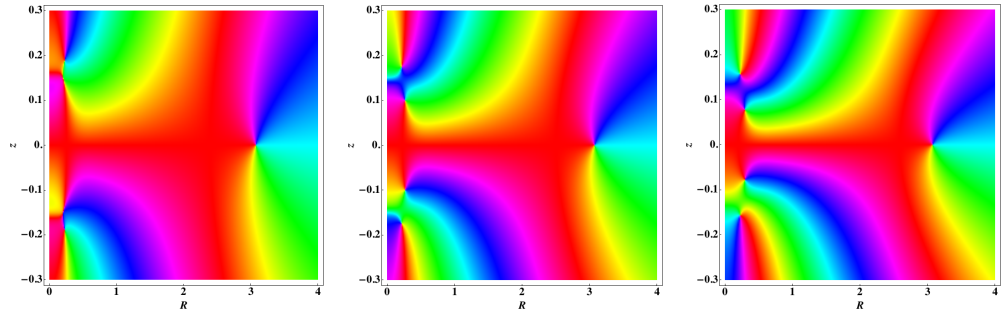

(a) (b) (c)

Figure 4.6: The phase of the (R, z)-plane at $\phi = 0$ for the paraxial function homogenised at different levels. The standard homogenisation, $s = 0$, is shown in (a). Only three zeroes can be seen in this plane despite the rapid phase change at two points. This does not give the five braid strands required to form the cinquefoil knot. The over homogenised functions, (b) and (c) for $s = 1, 2$ respectively, do exhibit five zeroes, which persist for all values of ϕ and the cinquefoil knot is successfully formed.

phase of the three q_i functions, in which this difference in the number of zeroes is clear.

This partitions the paraxial torus knots into two classes, standard and over homogenised knots. The symmetry of the torus knots, $T_{m,n} \cong T_{n,m}$ means that some torus knots, like the cinquefoil, have geometrically different, but still ambient isotopic, forms in both partitions.

The level of homogenisation of the Milnor polynomial can affect the transfer of the nodal set topology to a function satisfying the paraxial equation. The paraxial equation contains derivatives of R and z at different orders to each other. This restricts the power of z that appears in the paraxial polynomial to be half of the power that R appears as. The Milnor polynomial does not restrict the power and hence contributes to the number of zeroes in this way. Increasing the power of w increases the power of R and hence the power z in the created paraxial function. This allows for more information to be carried over from the Milnor map to the paraxial function.

4.7 Discussion

We now summarise the results of this chapter before further discussion:

- We have detailed a construction of complex scalar functions with preimages of zero that are a prescribed knot or link in $\mathbb{R}^3$, based on first constructing braided zeroes where the braid strands follow a lemniscate

trajectory, sections 4.1-4.4. The braid is closed by taking the Milnor map of the braided function to form the function with a knotted/linked nodal set.

- We have introduced three parameters into the construction that have a geometric effect on the curves constructed, a (section 4.2), θ (section 4.5) and s (section 4.6).

- The Conway notation of the knots/links constructed from *squares* of braid words of our construction forms a sequence as the number of strands in the braid word increases, tables 4.3, 4.5 and 4.6. We can use this to predict the next knot or link in the series.

- The coefficients of the Alexander polynomial of the lemniscate knots, section 4.2, for the knots created by squares of a constructed braid word, form a sequence as the number of strands in the braid increases.

- Higher lemniscates $\beta > 2$ give rise to links as well as knots for the squares of the braid words constructed. The Jones polynomial coefficients give rise to a pattern in this case, section 4.3. Unlike the Alexander polynomial where all the coefficients (half of them by symmetry) appear in the predicted sequence, in the case of the Jones polynomial, the sequence appears to limit to the pattern. This gives rise to two different sequences of integers, one starting from either end of the polynomial.

The Lissajous construction creates functions with a knot or link as the preimage of zero. These arise as the closure of periodic braids where the strands follow a generalised lemniscate as their trajectory. The basic braid words are homogeneous braids so the created knots and links are fibred by Stallings [Sta78].

The construction naturally creates a three-parameter subset of all knots. The (integer) dimensions of this this space are given by:

- β the number of loops in the lemniscate of the braid trajectory,

- N the number of strands in the braid,

- n the number of repeats of the basic braid word before closing the braid.

Not every discrete triplet (β, N, n) is a unique knot or link; duplicates can occur. The torus knots in the $\beta = 1$ plane of this space are an example of this: the symmetry of $T_{m,n} \cong T_{n,m}$ means there are two entries for each torus knot and link with possibly more occurring in other planes. These are examples of trivial knots / links on the 1-lemniscate as defined in definition 4.2. Trivial knots and links appear to occur when the number of braid strands n is less than β.

The construction also allows for three natural parameters that affect the geometric shape, giving an ambient isotopy of the knot or link :

- $a \in \mathbb{R}^+$, a parameter that effects the scaling of the curves,
- $\theta \in [0, 2\pi)$, a parameter that positions the $z = 0$ when closing the braid,
- $s \in \mathbb{N}$, the level of homogenisation that can be used to to modify the Milnor polynomial to aid the inheritance of the nodal topology into functions satisfying the paraxial equation.

In chapter 5 we examine the effect of a on the topology of the 6_3 knot and conclude that there is a range of validity, at least for the Milnor map we use, where the desired knot is actually formed. Chapter 6 concludes with a look at s, the level of homogenisation of the complex function, and uses the cinquefoil knot as an example to show how this effects the creation of a function satisfying the paraxial equation and its nodal set.

The traditional tabulations of knots, such as Rolfsen's [Rol76], group the knots by their minimum crossing number. Within these groupings, the knots share no other similarly valued invariants. The Lissajous construction naturally groups the knots / links with similar other invariants together. Notably, the coefficients of knot polynomials can be predicted in the $n = 2$ plane of our knot space as well as their respective Conway notations. Each column for an increasing n gives an increasing number of rotational symmetries to the knot.

This way of tabulating knots has similarities to the work of Jablan [Jab01] and Jablan and Sazdanović [JS07]. Such tabulation orders knots by their Conway notation and patterns such as those given in table 4.4 are also present. Our tabulation from the Lissajous construction includes non-rational knots, for knots and links with $n > 2$, the number of repeats of the underlying basic braid word.

The coefficients of the Alexander polynomial of the 2-lemniscate knots, that are formed from the square of the basic word, follow an obvious pattern shown in table 4.4. More complicated sequences are formed in the Jones polynomial coefficients from the braids following a 3-lemniscate trajectory. This structure to the knots and links not obviously observed when tabulating knots and links by their crossing number alone. In fact, the three-dimensional tabulation we form does not necessarily construct the curves with a form that exhibits their minimum crossing number, for example $\beta = 2, N = 5, n = 2$ the 6_3 knot. This knot has a Lissajous constructed braid word of length eight but a minimum crossing number of six. Our construction does give braid words with a minimal amount of information, taking advantage of the symmetry that the knot inherits from the use of a repeated basic braid word.

This three-dimensional tabulation puts knots and links on an equal level, that is to say that we do not require a one component knot table separate from the multi-component links. We can label any knot or link from our construction with just the position (β, N, n). From our observations we propose that

- The knots and links formed by the closure of the square of a basic braid word from the Lissajous construction exhibit patterns in their respective Conway notations and coefficients of their Alexander and Jones polynomials. Each pattern is specific to the type of lemniscate the braid strands follow, labelled by β. These are the patterns shown in tables 4.3 and 4.4-4.6 and appendix B.

Appendix B shows the knots and links we have constructed and studied using the Lissajous construction.

Lemniscate curves are a special case of Lissajous curves. A Lissajous curve has parametrised form $(\sin \alpha h, \cos \beta h)$ where $\alpha \neq 0$. However, attempts to close these braids using our Milnor maps have failed. One reason for this failure could be our use of $u(\boldsymbol{r})$ and $v(\boldsymbol{r})$. We have considered the 3-sphere of unit radius in our Milnor maps and inverse stereographic projection of equations (2.2) and (2.3). This is the size of the small 3-sphere enclosing the singularity in our function [Mil68]. Within the definitions of u and v, we could explicitly include the radius of the 3-sphere as an additional parameter of the construction.

We could investigate alternative forms of the inverse stereographic projection functions from $\mathbb{R}^3$ to the 3-sphere, for example the functions

$$p(\boldsymbol{r}) = \frac{1}{\sqrt{2}} \left(u(\boldsymbol{r}) + v(\boldsymbol{r}) \right), \tag{4.12}$$

$$q(\boldsymbol{r}) = \frac{1}{\sqrt{2}} \left(u(\boldsymbol{r}) - v(\boldsymbol{r}) \right). \tag{4.13}$$

For the cases we have investigated with these functions, the nodal curve formed is open. If this curve is broken and a closing curve adjoined, then the resulting curve was the desired knot. But by requiring knots to be closed, these "knots" with their infinite open nature, are not considered further by us.

A similarly named class of knots, to the Lissajous construction, are the Lissajous knots [BHJS94]. These are three-dimensional curves that are ambient isotopic to a parametric curve of the form

$$\begin{cases} x &= \cos(\eta_x t + \phi_x) \\ y &= \cos(\eta_y t + \phi_y) \\ z &= \cos(\eta_z t) \end{cases}$$

where $0 \leq t < 2\pi$, $(\eta_x, \eta_y, \eta_z) \in \mathbb{N}^3$ and $\phi_x, \phi_y \in \mathbb{R}$. To avoid self-intersections in the curve the η_i are all co-prime to each other. Obviously this only constructs

knots not multi-component links. Examples of Lissajous knots, with values $(\eta_x, \eta_y, \eta_z, \phi_x, \phi_y)$, are

$$\begin{array}{ll} 5_2 & (2, 3, 7, 0.2, 0.7) \\ 8_{21} & (3, 4, 7, 0.7, 1) \\ 3_1 \# \bar{3}_1 & (3, 5, 7, 0.7, 1) \end{array}$$

where $\bar{3}_1$ is the mirror image of the trefoil knot. Hence fibred, non-fibred and non-prime knots can be Lissajous and there are an infinite number of Lissajous knots [Lam97]. This means that the Lissajous knots and our three-dimensional table of Lissajous constructed knots are in general very different knots. The similarity is in the name of the constructions only.

The Lissajous construction can be used to construct a wide range of knots, forming an infinite family of related knots and links. This family does not include all knots, especially non-fibred knots. It is unknown whether a composite knot can be constructed from the Lissajous construction.

There exist other methods for constructing braids and fibred knots and these could potentially be used to construct complex scalar functions with knotted nodal sets. Similar to our method, at least qualitatively, is the construction of *symmetric fibered links* by Goldmith [Gol75], where fibred knots and links are constructed that have rotational symmetry in S^3. This contrasts to our construction which has a rotational symmetry in $\mathbb{R}^3$. Berger [Ber01a] constructs braids with three strands using Hamiltonian dynamics. This allows for a simple trajectory in an abstract space to describe a complicated braid word. This construction has not lent itself to our method of Milnor mapping functions containing such braids to form closed knots, requiring a trigonometric trajectory for the braids to allow us to use equations (2.2) and (2.3) to close the braid.

We conclude this chapter with a review of some questions that arise from our Lissajous construction.

- What is the full sub-set of knots that are possible to construct with the Lissajous construction? This includes the generalisation from lemniscate trajectory braids to general closed Lissajous figures. We believe that our construction gives at least a subset of the fibred knots and gives rise to homogenous braid words, table 2.3. It may be possible with a Lissajous figure to construct inhomogeneous braid words and it is unclear as to if this would give rise to a non-fibred knot or a braid word of a fibred knot that is not in a homogeneous representation.

- Can it be proved that the coefficients of the Jones/Alexander polynomial form a sequence as the number of braid strands increase when the knot or link is the square of a basic braid word from the Lissajous construction?

The sequences we have observed, sections 4.2 and 4.3, certainly appear robust and continue to form as we increase the number of strands in our construction. Do other knot invariants exhibit similar patters and do these form sequences when increasing the other two parameters of the lemniscate constructed knots, β (equation (4.1)) and n the number of repeats of the basic braid word?

- The basic braid words we construct, when repeated n times, in general have more letters than the minimum crossing number of the knot/link they represent. Do these braid words reveal more topological information about the knot itself? For example, the braid words in proposition 4.1 are significantly longer than the minimum braid representative [Git08]. Can this difference in braid word lengths tell us anything about the knots and links we construct? The braid words we construct do however give a *minimal information* representation, which may have a high number of strands compared to Gittings [Git08], but only needs the basic braid word to be given and the number of times this is repeated.

4.A Figure-8 Laguerre-gaussian Superposition with a and θ

mode (l,p)	Coefficient
$(0,0)$	$-\left(\frac{3\left(-1+a^2\right)\left(1+2w^2\right)\left(-1+12w^6\right)}{4a^2}\right)\mathrm{e}^{\mathrm{i}\theta} + \left(-1+2w^2\right)\left(1+12w^6\right)\mathrm{e}^{3\mathrm{i}\theta}$
$(-2,0)$	$\frac{w^2\left(6a\mathrm{e}^{\mathrm{i}\theta}\left(-1+12w^4\right)-\left(3+a^2\right)\left(1+6w^2+12w^4\right)\right)}{\sqrt{2}a^2}$
$(0,1)$	$\frac{1}{2}\mathrm{e}^{\mathrm{i}\theta}w^2\left(-4\mathrm{e}^{2\mathrm{i}\theta}\left(1-18w^4+48w^6\right)+\frac{3\left(-1+a^2\right)\left(-1+18w^4+48w^6\right)}{a^2}\right)$
$(2,0)$	$-\frac{w^2\left(6a\mathrm{e}^{\mathrm{i}\theta}\left(-1+12w^4\right)-\left(3+a^2\right)\left(1+6w^2+12w^4\right)\right)}{\sqrt{2}a^2}$
$(-4,0)$	$\frac{4}{a^3}\sqrt{6}w^4$
$(-2,1)$	$\frac{\sqrt{6}w^4\left(-24a\mathrm{e}^{\mathrm{i}\theta}w^2+\left(3+a^2\right)\left(1+4w^2\right)\right)}{a^2}$
$(0,2)$	$\frac{1}{a^2}9w^6\mathrm{e}^{2\mathrm{i}\theta}\left(\left(3-7a^2+4\left(3+a^2\right)w^2\right)\cos\theta + \mathrm{i}\left(-3-a^2+4\left(-3+7a^2\right)w^2\right)\sin\theta\right)$
$(2,1)$	$\frac{\sqrt{6}w^4\left(24a\mathrm{e}^{\mathrm{i}\theta}w^2+\left(3+a^2\right)\left(1+4w^2\right)\right)}{a^2}$
$(4,0)$	$-\frac{4\sqrt{6}w^4}{a^3}$
$(-2,2)$	$-\frac{2\sqrt{3}\left(3+a^2-6a\mathrm{e}^{\mathrm{i}\theta}\right)w^6}{a^2}$
$(0,3)$	$3\mathrm{e}^{\mathrm{i}\theta}w^6\left(-4\mathrm{e}^{2\mathrm{i}\theta}\left(-1+8w^2\right)+\frac{3\left(-1+a^2\right)\left(1+8w^2\right)}{a^2}\right)$
$(2,2)$	$\frac{2\sqrt{3}\left(3+a^2+6a\mathrm{e}^{\mathrm{i}\theta}\right)w^6}{a^2}$
$(0,4)$	$\frac{1}{a^2}\left(6w^8\left(\left(3+a^2\right)\cos\theta+\mathrm{i}\left(-3+7a^2\right)\sin\theta\right)\left(\mathrm{e}^{2\mathrm{i}\theta}\right)\right.$

Table 4.7: Laguerre-gaussian mode coefficients for the figure-8 knot with the dependence on a and θ given.

Nodal Lemniscate Knots

5

We now look at several physical PDEs and use our construction to examine whether we can construct our nodal knots in functions satisfying such equations. We continue our approach of constructing the function as an initial value problem based on the $z = 0$ plane. In the case of the Schrödinger equation in the absence of potentials, equivalently we begin with a constructed knot in three dimensions, present at $t = 0$ and evolve time.

We begin with some further examples of paraxial knotting, and use the 6_3 knot as an example of a restricted parameter space of success in both the Milnor polynomial and the paraxial function. The Helmholtz equation is the second equation we attempt to satisfy and we show how our Lissajous constructed nodal knots can be transferred to functions satisfying it. Our concluding example is the three-dimensional Schrödinger equation with various potentials. This gives examples that go beyond our optical motivations within this thesis. Specifically, we try the three-dimensional harmonic oscillator and the hydrogen atom.

5.1 Paraxial Nodal Knots

We now examine some further cases of how the nodal topology of Milnor polynomials, created by the Lissajous construction, can be transferred to that of functions satisfying the paraxial equation. At this stage we also further examine the effect of the geometric parameter a. The knots are readily studied by considering the (R, z)-plane, where the lemniscate is traced out as ϕ varies. The geometry of this twice mapped lemniscate, first in forming the Milnor polynomial and secondly in the creation of the paraxial function, has a profound effect on the nodal knot in paraxial functions.

First, we look at the 6_3 knot. This knot has braid word created from a 2-

lemniscate ($\beta = 2$), with five strands and two repeats. This is the next generalisation of the figure-8 knot family after considering additional repeats of the basic braid word (section 4.2). As with the other paraxial functions, the paraxial function has the highest power of z half that of the Milnor polynomial. The range in z is smaller in the paraxial knot than the Milnor polynomial as well. This combines to give a very different geometric form of the lemniscate the zeroes follow in the (R, z)-plane for the paraxial function.

In braid space, the parameter a does not change the topology of the braid. For all $a > 0$, the braid word formed is identical. Under the braid closure by the Milnor-like map, this parameter controls the success of the Milnor polynomial containing the target knot. We cannot expect a paraxial function to contain this knot if the Milnor polynomial does not, but it is possible that this could happen, especially when close to critical values of a etc.

The (R, z)-plane projections of the curves can be used to rule out if for a given a, the knot has correctly formed. In figure 5.1 we show a series of such planes to illustrate the process of successful knot formation. For values of a too low, $a \lesssim 2$, the knot does not correctly form. Such a case is shown in figure 5.1(a) for when $a = 1$. In this figure additional components can be seen in the Milnor polynomial case.

The case of $a \gtrsim 5.5$ also does not contain the 6_3 knot. The curve of the Milnor case in the (R, z)-plane contains many turning points, which as a increases, forces parts of the curve towards the z-axis. This ultimately intersects and reconnects with the curve because the twisting is symmetric above and below $z = 0$ (in this projection). Additional components are once again formed, destroying the target topology. The nodal set of the paraxial function exhibits this destruction as well.

The 6_3 knot appears to occur for the range of a as above, both in the Milnor- and paraxial- functions. It is possible that for a range of $a \gg 5.5$ the required lemniscate in the (R, z)-plane is once again formed. In a numerical investigation, we have not be able to obtain such a value. It would be surprising if such a value were to exist. In section 5.4 we discuss possible reasons for this restricted range and suggest possible resolutions.

To finish our discussion of nodal knots in paraxial functions, we give the knot 7_7 as an example. This knot is the simplest example of a 3-lemniscate knot and we will check if the mapping $u \to \mathrm{i}u$, discussed in section 4.5, can successfully work paraxially. The obvious difference under this map is the number of zeroes in the $z = 0$ plane. The standard case, $\theta = 0$, gives rise to a complicated constellation of zeroes, consisting of twelve zeroes. The parameter θ determines the location of the axis around which the braid is closed, section 4.5. When $\theta = \frac{\pi}{2}$,

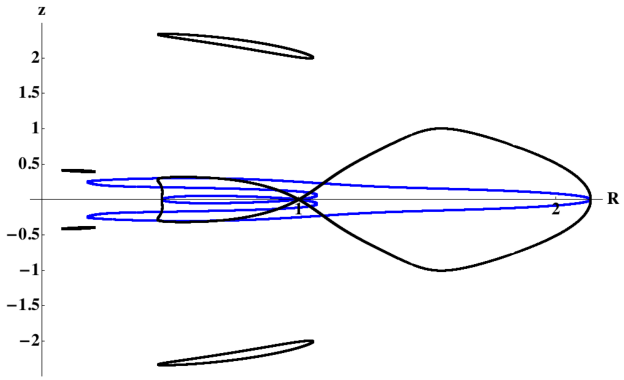

(a)

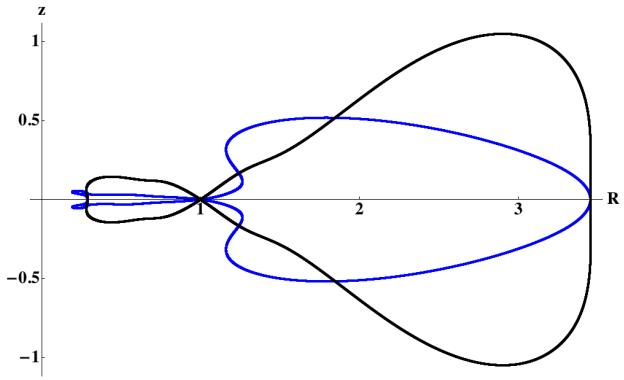

(b)

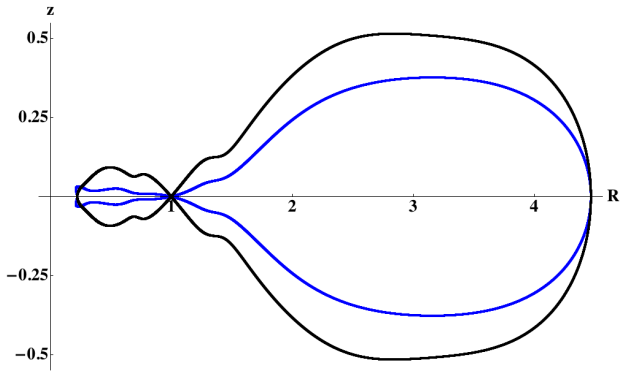

(c)

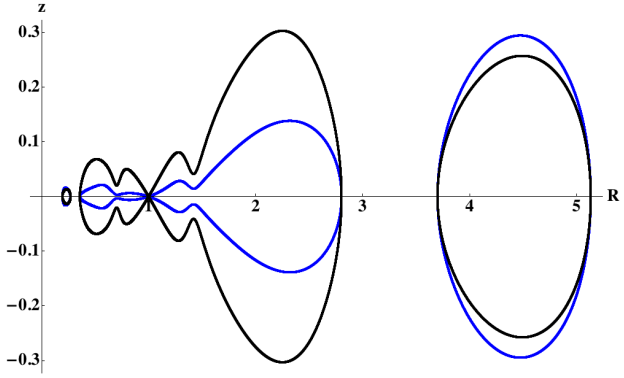

(d)

Figure 5.1: The (R, z)-planes for the 6_3 knot for values of $a = 1, 3, 4.5, 6$ in parts (a) to (d) respectively. The black curve is the Milnor polynomial's nodal set and the blue represents that of the corresponding paraxial polynomial function.

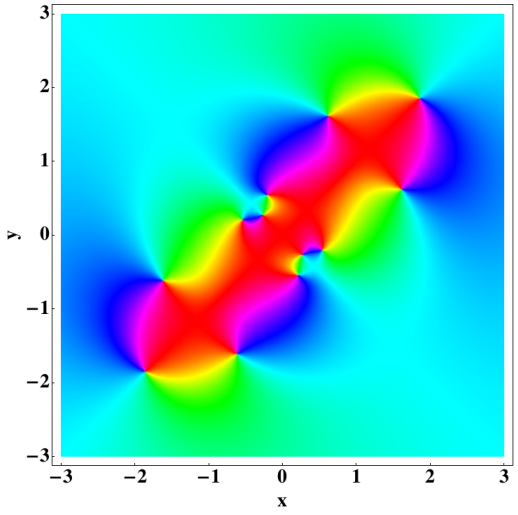

(a)

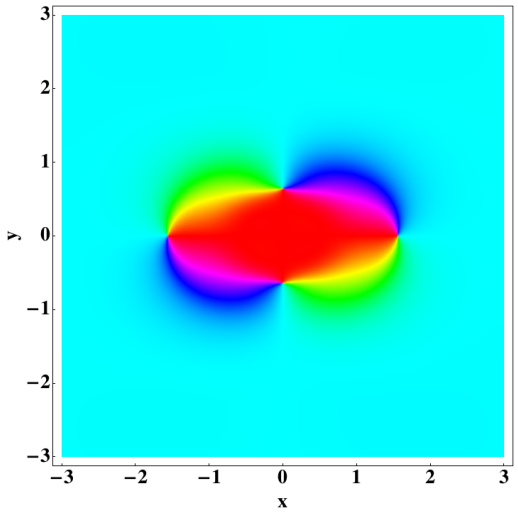

(b)

Figure 5.2: The $z = 0$ plane of 7_7 knot. (a) shows for $\theta = 0$ and (b) shows for $\theta = \frac{\pi}{2}$. The former case contains twelve zeroes in this plane compared to the later exhibiting only four. The full three-dimensional curves for both these cases are shown in figure 5.3.

hence $u \to iu$, this reduces to four. Both $z = 0$ planes are shown in figure 5.2.

This difference manifests itself in the three-dimensional curves of the knot. However, as expected both curves are ambient isotopic to the 7_7 knot. Both curves are shown in figure 5.3. This is an interesting feature of the paraxial equation that both very different forms of the same knot can successfully occur as solutions.

The ability to construct functions satisfying the paraxial equation that contain nodal knots based on our construction appears robust. The parameters in-

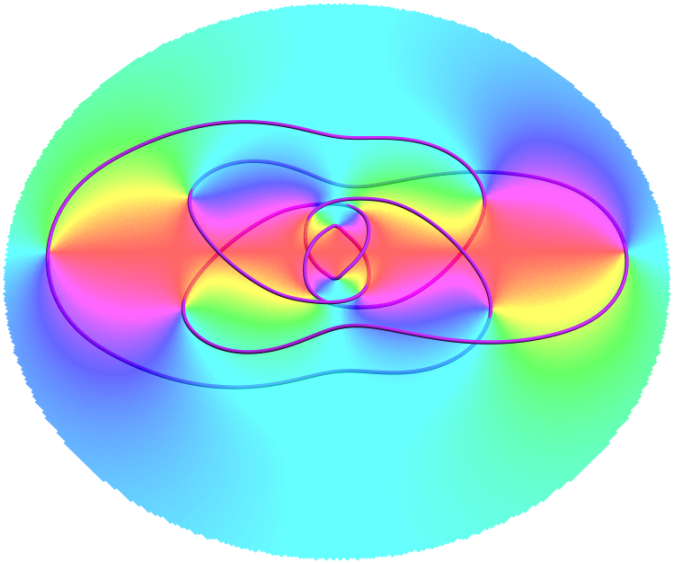

(a)

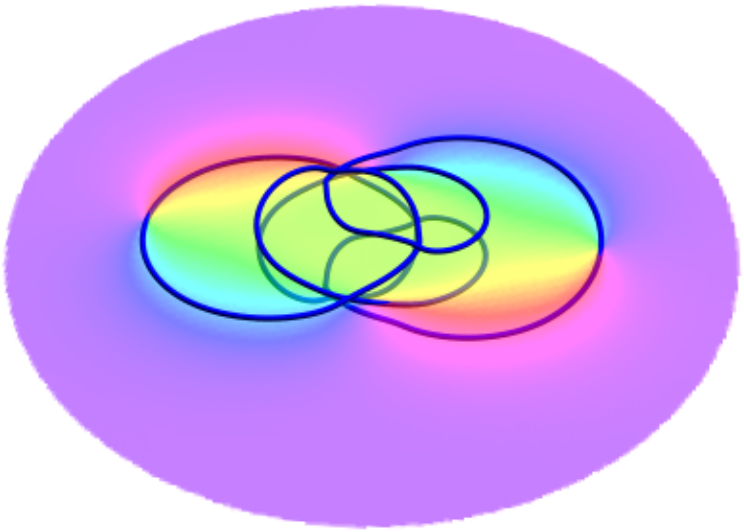

(b)

Figure 5.3: The three-dimensional curves of the 7_7 knot realised as the phase singularities of a paraxial function shown for two values of θ : (a) $\theta = 0$ and (b) $\theta = \frac{\pi}{2}$.

troduced in chapter 4 effect the geometric form the knot takes in a similar way in both the paraxial functions and the Milnor polynomials. It is possible to construct Laguerre-gaussian superpositions for all of the knots that we can construct using the methods of chapter 3. If a polynomial function can be constructed for an appropriate set of our parameters that successfully contains the desired knot, then it is certainly reasonable to attempt a Laguerre-gaussian superposition. The additional vortices that are present in such a superposition will obviously need more careful control for more complex knots than those considered in chapter 3. The parameters such as a and θ in the construction can be used in addition to the superposition's beam waist width w to provide this control.

5.2 Helmholtz Nodal Knots

The paraxial equation is an approximation to the Helmholtz wave equation. It is a natural question to ask that, if a Milnor polynomial's nodal topology can be inherited by a function satisfying the paraxial equation, can the same knot or link exist in a function satisfying the Helmholtz wave equation?

The work of Berry and Dennis [BD01a] has shown that threaded torus knots and links are possible as the phase singularities of a function satisfying the Helmholtz equation. We wish to apply our Lissajous construction to functions satisfying the Helmholtz equation and attempt to construct the wide range of knots and links available to us, as Helmholtz equation nodal sets. Also, we desire that the knotted nodal set is isolated, not threaded or containing additional components.

In this section we construct polynomials that satisfy the Helmholtz equation using the same method of expanding a generating function, as explained for the paraxial case in section 3.2. To construct the Helmholtz polynomials we use the construction from [Den01]. This time the generating function for the expansion is the Bessel beam solution for the Helmholtz equation :

$$\Psi = \mathrm{e}^{\mathrm{i}m\phi}\mathrm{e}^{\mathrm{i}z\sqrt{1-\kappa^2}}J_m(\kappa R). \tag{5.1}$$

This expression has an $\mathrm{e}^{\mathrm{i}z}$ term and hence the coefficients of κ in a Taylor expansion require multiplication of such a factor to satisfy the Helmholtz equation. Without such a factor, a function satisfying the Helmholtz equation of the form $\tilde{\Psi} = \mathrm{e}^{-\mathrm{i}z}\Psi$, satisfies

$$\nabla_\perp^2\tilde{\Psi} + \partial_z^2\tilde{\Psi} + 2\mathrm{i}\tilde{\Psi} = 0, \tag{5.2}$$

the Helmholtz beam equation or reduced Helmholtz equation. With equivalence up to a factor, we do not consider the $\mathrm{e}^{-\mathrm{i}kz}$ factor in our analysis here.

Table 5.1 in appendix 5.A to this chapter lists the first few Helmholtz polynomials. These polynomials require the ϕ and z terms as factors so the full solutions of the Helmholtz equation are

$$\Psi_{m,n}(R,z,\phi) = \mathrm{e}^{-\mathrm{i}kz}\mathrm{e}^{\mathrm{i}n\phi}p_m(R,z), \tag{5.3}$$

where p_m is as in table 5.1 and is of order m in R.

The Helmholtz polynomials are related to the paraxial polynomials of corresponding order. A Helmholtz polynomial, with labels m and n, is expressible in terms of the equivalent paraxial polynomial plus a correction term $H_{m,n}$ which is a non-trivial function :

$$\Psi_{m,n}(R,z,\phi) = \psi_{m,n}(R,z,\phi) + H_{m,n}(R,z,\phi). \tag{5.4}$$

To make Helmholtz nodal knots, the Milnor polynomials are, as before in the paraxial case, constructed and considered at $z = 0$. A unique function is then created, coinciding exactly with the Milnor polynomial's $z = 0$ plane and satisfies the Helmholtz equation. The wave number k now exists as a parameter in such a function which is explored in this section.

We now construct the Helmholtz trefoil knot and use it as our main example of Helmholtz knotting. We begin with the Milnor polynomial of the trefoil knot (with the standard homogenisation) and construct using the Helmholtz polynomials

$$\begin{aligned}\Psi_{\text{trefoil}} \;=\; & \frac{1}{k^5}\mathrm{e}^{-\mathrm{i}kz}\Big(\{1+R^2+8\mathrm{e}^{3\mathrm{i}\phi}R^3+R^4+R^6\} \\ & +\mathrm{i}z\left(-144+8k^2-2k^4+(72k^2-8k^4)R^2-18k^4R^4\right) \\ & +\left(144k-8k^3-72k^3R^2\right)z^2 \\ & +48\mathrm{i}k^2z^3\Big)\end{aligned} \tag{5.5}$$

where the Helmholtz z-dependence shown outside of the curly $\{\bullet\}$ brackets.

The k-dependence of equation (5.5) affects both the topology and the geometric form the nodal curves take. As k tends to zero, the Helmholtz equation becomes the Laplace equation. The Helmholtz polynomials become invalid when $k = 0$, they are not solutions of the Laplace equation and equation (5.5) explicitly shows this, having every term attracting a factor of at least k^{-1}.

For low k, $k < 1.188$, we find that the nodal topology of Ψ_{trefoil} is not the trefoil knot. There are five distinct, unlinked rings that are approximately planar, which loop annihilate themselves as $k \to 0$. As k increases, these disjoint loops are perturbed and connect together to form the trefoil knot. This reconnection

event occurs at a critical value $k_{\text{crit}} \approx 1.188$, a value found numerically. The trefoil knot exists for $k > 1.188$. This process of the knot formation is shown in figure 5.4.

In chapter 4 we discussed the $(5,2)$-form of the cinquefoil. We have shown that the standard homogenisation of the Milnor-like map does not successfully transfer the cinquefoil knot to a paraxial function's nodal set. We next look at what happens to this form of the cinquefoil when the Milnor polynomial is made to satisfy the Helmholtz equation.

The function that satisfies the Helmholtz equation, constructed from the Milnor polynomial of $u^5 - w^3v^2$, is given in the following equation :

$$\begin{aligned}
\Psi_{5,2\text{-cinq}} \;=\; & \frac{1}{k^9}\mathrm{e}^{-\mathrm{i}kz}\Big(\{1 - 5R^2 + 4\mathrm{e}^{2\mathrm{i}\phi}R^2 + 10R^4 + 12\mathrm{e}^{2\mathrm{i}\phi}R^4 - 10R^6 \\
& +12\mathrm{e}^{2\mathrm{i}\phi}R^6 + 5R^8 + 4\mathrm{e}^{2\mathrm{i}\phi}R^8 - R^{10}\} \\
& 2\mathrm{i}\Big(201600 + 14400k^2 + 720k^4 + 40k^6 + 5k^8 \\
& -40k^2(1800 + 144k^2 + 9k^4 + k^6)R^2 \\
& -36k^4(80 - 8k^2 + k^4)\mathrm{e}^{2\mathrm{i}\phi}R^2 + 90k^4(80 + 8k^2 + k^4)R^4 \\
& +96k^6(5 - k^2)\mathrm{e}^{2\mathrm{i}\phi}R^4 \\
& -80k^6(5 + k^2)R^6 - 60k^8\mathrm{e}^{2\mathrm{i}\phi}R^6 + 25k^8R^8\Big)z \\
& 16k\Big(-5(5040 + 360k^2 + 18k^4 + k^6) + 45k^2(200 + 16k^2 + k^4)R^2 \\
& +36k^4(10 - k^2)\mathrm{e}^{2\mathrm{i}\phi}R^2 - 90k^4(10 + k^2)R^4 - 60k^6\mathrm{e}^{2\mathrm{i}\phi}R^4 + 50k^6R^6\Big)z^2 \\
& +480\mathrm{i}k^2\Big(-360 - 24k^2 - k^4 + 8k^2(15 + k^2)R^2 \\
& +4k^4\mathrm{e}^{2\mathrm{i}\phi}R^2 - 10k^4R^4\Big)z^3 \\
& 1920k^3\Big(20 + k^2 - 5R^2\Big)z^4 + 3840\mathrm{i}k^4z^5, \qquad (5.6)
\end{aligned}$$

shown with the z-independent terms in the $\{\bullet\}$ brackets.

Equation (5.6) does, for $k > k_{\text{crit}}$, contain the cinquefoil knot, in the desired $(5,2)$-geometric form, as its nodal set. This curve is shown in figure 5.5 for $k = 4$. A numerical search for the critical value of k finds $k_{\text{crit}} \approx 2.445$. Notice how for this knot, k_{crit} is higher than the corresponding value for the trefoil knot examined in this section. This appears to be a feature of more complicated knots, in terms of a higher number of crossings, braid repeats and β loops in the lemniscate, that their critical value of k for the topology to exist as desired is higher. For values of k that are $k < k_{\text{crit}}$, small loops nucleate and reconnect with the cinquefoil knot. This destroys the topology after the knot has become un-isolated.

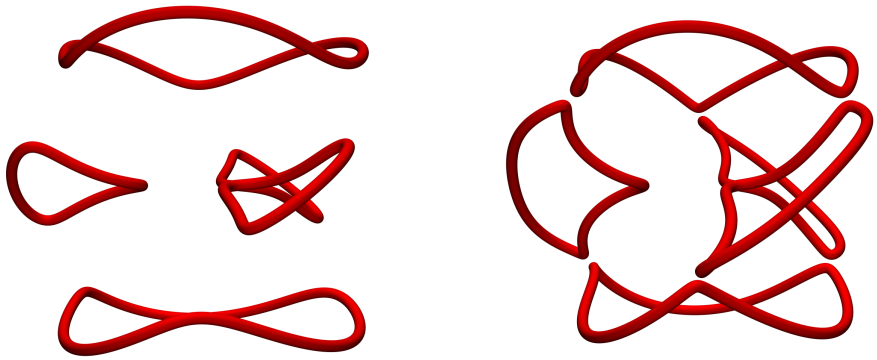

(a)

(b)

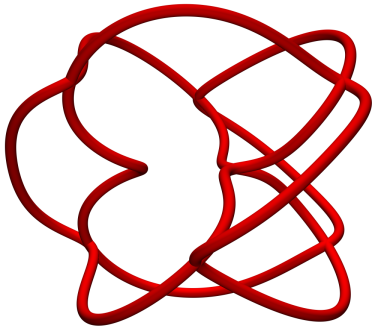

(c)

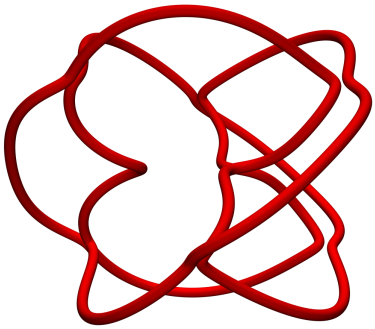

(d)

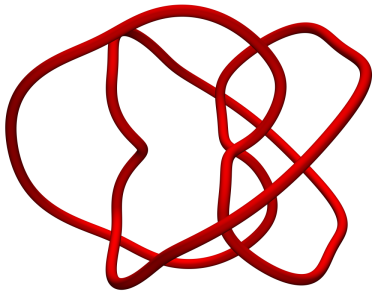

(e)

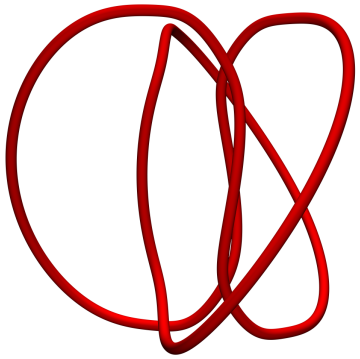

(f)

Figure 5.4: The nodal set of the Helmholtz equation satisfying equation (5.5). For values of $k < 1.188$, which are shown in (a) and (b) for $k = 1.050$ and $k = 1.180$ respectively, the five rings can be seen. (c) shows the zero lines for the value $k = 1.188 \approx k_{\text{crit}}$, in which the reconnection of the nodal lines can be seen. (d), (e), (f) show the nodal set for $k = 1.195, 1.500, 4.000$ respectively. As k increases the trefoil knot persists as the nodal topology. The geometry of the curve becomes simpler when k increases from k_{crit}. All six images are viewed from the same viewpoint, on the y-axis, looking at the origin, with the positive z-direction vertical.

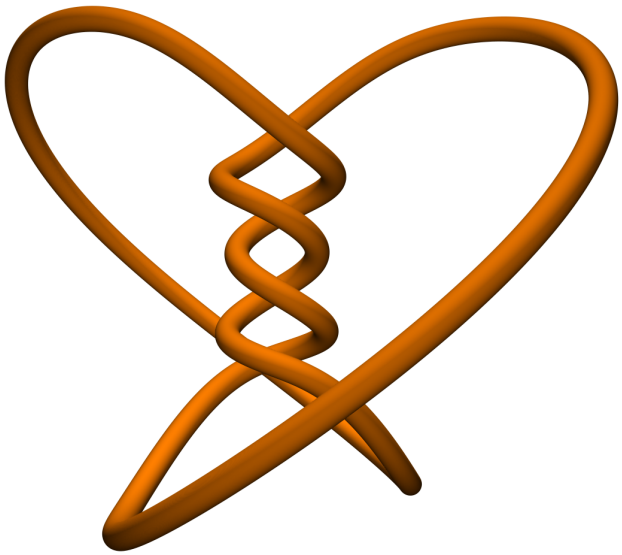

Figure 5.5: The $(5,2)$-form of the cinquefoil knot, realised as the nodal set of equation (5.6), satisfying the Helmholtz equation, with $k = 4$. The z-direction is vertical.

This method of constructing the $(5,2)$-form of the cinquefoil knot is realisable in both paraxial and Helmholtz functions. However in the former case of the paraxial equation there is the need to over-homogenise the Milnor polynomial. Given that the standard homogenised form works for the Helmholtz equation and the paraxial equation is an approximation to the Helmholtz equation, the desired form may exist in the paraxial function, requiring a small perturbation to form the correct knot. If this is the case, then the over-homogenisation provides this perturbation in the paraxial case. In chapter 6, we investigate a mechanism to examine how the nodal curves of a paraxial function can be approximated and the topology estimated. The "Steering of Optical Vortices" is an attempt to quantitively show the difference between a paraxial function's nodal topology and geometry.

We conclude this section with an examination of non-torus fibred knots as the nodal sets of solutions of the Helmholtz equation. The figure-8 knot is shown in figure 5.6. In this figure, we plot the (R,z)-plane for the values of $k = 3,4,5$. At $k = 3$ there are some very tight corners on the curve, like cusps. How these parts of the curve interact affects what topology is formed, and is k-dependent.

The value of k once again plays an important role in the successful transfer of the nodal knot from the Milnor polynomial. For low values of k, the nodal topology of the function is, as with the trefoil knot, several disconnected components. This transformation is shown in figure 5.7. The knot, as k decreases, first forms

a single curve not ambient isotopic to the figure-8 knot, before smaller loops are created.

5.3 Schrödinger Equation Based Systems

We have only considered optical PDEs to attempt an embedding of our nodal topology into. In this section we generalise to physical systems based on the Schrödinger equation. Although we have stated that the paraxial equation is equivalent, up to constants, to the $(2+1)$-dimensional Schrödinger equation with no potentials (section 1.5) we now explore the $(3+1)$-dimensional form of the equation. That is three spatial dimensions and one time dimension. After a brief introduction to the Schrödinger equation, we will consider using our knot construction to build wavefunctions satisfying it, with knotted phase singularities as their nodal sets.

In quantum mechanics, the Schrödinger equation describes how a quantum wave function evolves in time. It relates the time-derivatives of the wavefunction to the Hamiltonian of the system. The Hamiltonian corresponds to the total energy of the quantum system. However, we will be interested in specific Hamiltonians and their solutions. Quantum mechanics textbooks provide a full interpretation and details of the equation's derivation, such as [Mes99].

The Schrödinger equation has the form

$$\mathrm{i}\hbar\frac{\partial\Psi(\boldsymbol{r},t)}{\partial t} = \mathcal{H}\Psi(\boldsymbol{r},t), \tag{5.7}$$

where $\mathcal{H}$ is the Hamiltonian of the system and Ψ, in this section, is a time-dependent quantum wavefunction. The systems we consider here have Hamiltonian of the form

$$\mathcal{H} = -\frac{\hbar^2}{2m}\nabla^2 + V(r), \tag{5.8}$$

where V is a potential and $\mathcal{H}$ is written in operator notation. In the subsequent sections we look at the potential-less system, the 3D isotropic harmonic oscillator and the wavefunctions of the hydrogen atom, describing the specific V in the appropriate section.

The Schrödinger Equation with no Potentials

The functions we have studied so far have been static in three dimensions. The main result of the construction was the existence of a solution with the desired nodal topology. We now consider knotted nodal lines in functions that satisfy an equation where the three spatial dimensions are evolved in a fourth, time, dimension.

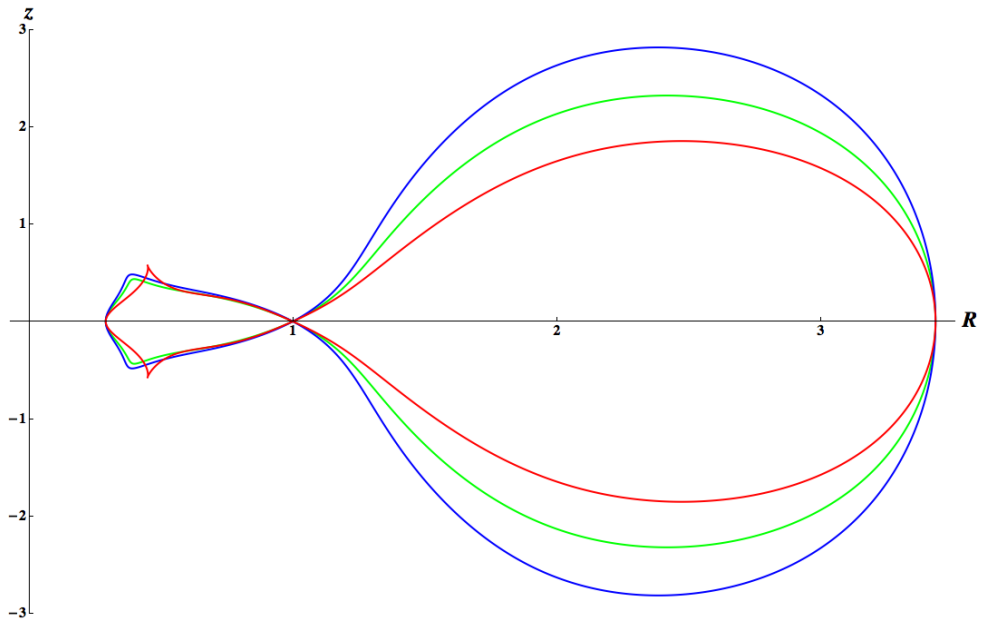

(a)

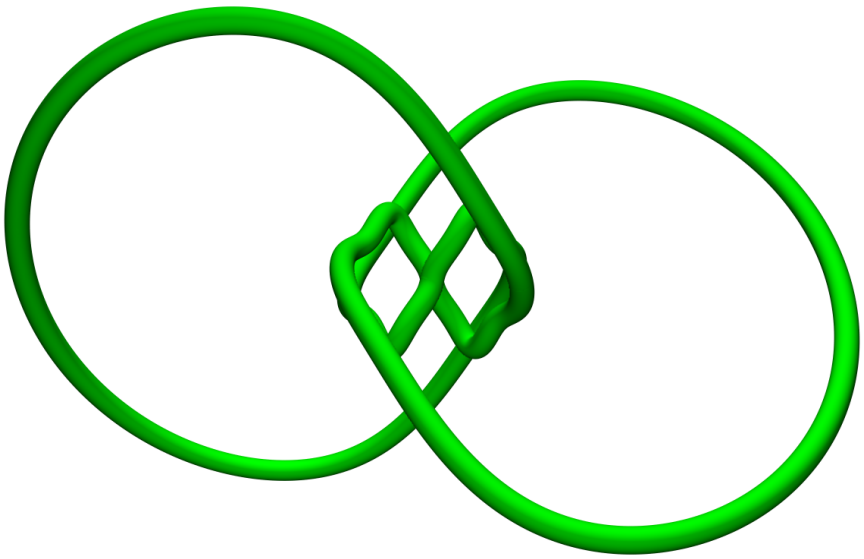

(b)

Figure 5.6: The nodal figure-8 knot in a Helmholtz equation satisfying function. All figures have $a = 2$. (a) The (R, z)-plane of the nodal curve for values $k = 3, 4, 5$ corresponding to the red, green, blue curves respectively. The "cusp" like nature of the curve at $x \approx 0.45$, self-reconnecting for lower values of k, destroying the knot. These cusps manifest into a detailed structure seen in (b), the full three-dimensional curve.

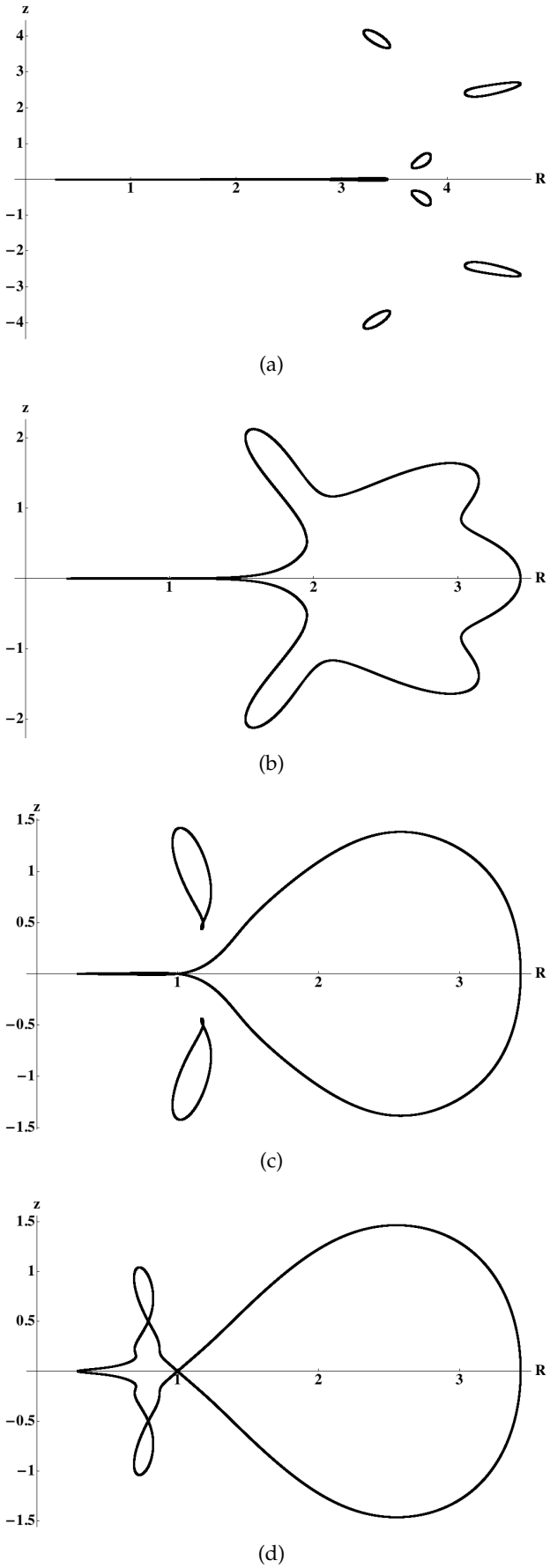

Figure 5.7: (R, z)-planes for the Helmholtz figure-8 knot with low k. (a)-(d) show the projection for values of $k = 0.5, 1, 1.5, 2$ respectively. The required lemniscate is not formed until $k \approx 2$.

The simplest such system is the Schrödinger equation with no potentials. This has Hamiltonian, as an operator,

$$\mathcal{H} = -\nabla^2, \tag{5.9}$$

with the constants normalised to unity. The Schrödinger equation of this form becomes,

$$(\nabla^2 + 2ik\partial_t)\psi = 0, \tag{5.10}$$

where now the Laplacian is in three dimensions, $\nabla^2 = \partial_x^2 + \partial_y^2 + \partial_z^2$, and t represents time. Equation (5.10) is equivalent to the $(3+1)$-dimensional form of the paraxial equation, with the coefficient of the time-derivative set to match the paraxial equation. The paraxial equation used throughout this thesis is the $(2+1)$-dimensional form of the Schrödinger equation where z takes the role of time. We now look at polynomial solutions of this equation in the same way we did for the paraxial equation in section 3.2. The nodal curves are still codimension two because the fourth dimension is interpreted as a parameter describing a dynamic change to the function.

To construct polynomials in Cartesian coordinates, a simple generalisation to three space variables is made to the paraxial Cartesian polynomials. The separation of variables generalises to a trial function of the form $\psi(x,y,z,t) = f(x,t)g(y,t)h(z,t)$. This leads to solutions of the form

$$\psi_{l,m,n}(\boldsymbol{r}) = \tau^{\frac{l+m+n}{2}} H_l\left(\frac{x}{\sqrt{\tau}}\right) H_m\left(\frac{y}{\sqrt{\tau}}\right) H_n\left(\frac{z}{\sqrt{\tau}}\right), \tag{5.11}$$

where $\tau = \frac{-2it}{k}$ and H_i is the i^{th} Hermite polynomial for $i = l, m, n$.

The Laplacian is separable in spherical coordinates (r, θ, ϕ) and we now seek polynomial based solutions of the Schrödinger equation in this coordinate system. Writing the Schrödinger equation this way, it becomes

$$\frac{1}{r^2}\frac{\partial}{\partial r}\left(r^2\frac{\partial\psi}{\partial r}\right) + \frac{1}{r^2\sin\theta}\frac{\partial}{\partial\theta}\left(\sin\theta\frac{\partial\psi}{\partial\theta}\right) + \frac{1}{r^2\sin^2\theta}\frac{\partial^2\psi}{\partial\phi^2} + 2ik\frac{\partial\psi}{\partial t} = 0. \tag{5.12}$$

A separation of variables solution is now constructed with $\psi = F(r,t)G(\theta,\phi)$. Beginning by solving for g we find, after further separating such that $G = H(\theta)I(\phi)$, two differential equations to solve

$$\frac{\mathrm{d}^2 I(\phi)}{\mathrm{d}\phi^2} + m^2 I(\phi) = 0, \tag{5.13}$$

$$\lambda\sin^2\theta + \frac{\sin\theta}{H(\theta)}\frac{\mathrm{d}}{\mathrm{d}\theta}\left(\sin\theta\frac{\mathrm{d}H(\theta)}{\mathrm{d}\theta}\right) - m^2 = 0, \tag{5.14}$$

where λ is the separation constant when solving for F and G, and m is the separation constant for solving for H and I. Equation (5.13) solves to give

$$I(\phi) = \mathrm{e}^{\mathrm{i}m\phi}, \tag{5.15}$$

and to make I periodic we require $m \in \mathbb{Z}$. To solve equation (5.14), a change of variables $\theta \to x = \cos\theta$ is made which transforms it to the general Legendre equation [AS64]

$$(1-x^2)\frac{\partial^2 I(x)}{\partial x^2} - 2x\frac{\partial I(x)}{\partial x} + \left(l(l+1) - \frac{m^2}{1-x^2}\right) = 0, \tag{5.16}$$

which has associated Legendre polynomials $P_l^m(x)$ as its solutions, where $\lambda = l(l+1)$ and $l \in \mathbb{Z}$ ensures that the solution exists. With $x = \cos\theta$, we combine I and H into a single spherical harmonic

$$Y_{l,m}(\theta,\phi) = N_{l,m}\mathrm{e}^{\mathrm{i}m\phi}P_l^m(\cos\theta), \tag{5.17}$$

where $N_{l,m}$ is an l and m dependent normalisation constant. We normalise the solutions, combining all the constants of integration, such that the leading order term in R has a coefficient of one.

The final function to solve for is $F(r,t)$:

$$r^2\frac{\partial^2 F(r,t)}{\partial r^2} + 2r\frac{\partial F(r,t)}{\partial r} - l(l+1)F(r,t) + 2\mathrm{i}kr^2\frac{\partial f(r,t)}{\partial t} = 0. \tag{5.18}$$

We make a similar change of variables as in the case of the paraxial polynomials

$$r \to \rho = r^2 \quad t \to \tau = \tfrac{-2\mathrm{i}t}{k},$$

which allows us to solve the equation

$$4\rho^2\frac{\partial^2 F(\rho,\tau)}{\partial \rho^2} + 6\rho\frac{\partial F(\rho,\tau)}{\partial \rho} - l(l+1)F(\rho,\tau) + 4\rho\frac{\partial F(\rho,\tau)}{\partial \tau} = 0. \tag{5.19}$$

Our ansatz solution is a function of the form

$$F(\rho,\tau) = \tau^p\Phi\left(\frac{\rho}{\tau}\right), \tag{5.20}$$

which upon removing a factor of τ^{p-2}, leaves the equation

$$4X^2\frac{\mathrm{d}^2\Phi(X)}{\mathrm{d}X^2} + 2X(3-2X)\frac{\mathrm{d}\Phi(X)}{\mathrm{d}X} - (l(l+1)+4pX)\Phi(X) = 0, \tag{5.21}$$

to solve, where $X = \frac{\rho}{\tau}$. This is now an ordinary differential equation. Equation (5.21) has two solutions, one involving Laguerre polynomials

$$\Phi(X) = \sqrt{X}L_{p-\frac{l}{2}}^{l+\frac{1}{2}}(X), \tag{5.22}$$

and a confluent hypergeometric function occurring as the second linearly independent solution. We neglect the second solution because for some values of l, it becomes infinite at $X = 0$, although for some values of l and p it becomes a Laguerre polynomial [AS64].

The method for creating functions satisfying the Schrödinger equation is to create the unique function at $t = 0$ that coincides with the Milnor polynomial. The Milnor polynomial has no t-dependence, so at $t = 0$ the full three-dimensional Milnor polynomial is used as the initial condition for the time evolution. A paraxial function could also be used as an initial condition in this case.

We now look at the nodal trefoil knot, from the Milnor polynomial, under Schrödinger time evolution. This has a Schrödinger polynomial, in Cartesian coordinates,

$$\begin{aligned}\psi \;=\; & \{1 - x^2 - 8x^3 - x^4 + x^6 - y^2 + 24xy^2 - 2x^2y^2 + 3x^4y^2 - y^4 + 3x^2y^4 \\ & +y^6 - 5z^2 - 6x^2z^2 + 3x^4z^2 - 6y^2z^2 + 6x^2y^2z^2 + 3y^4z^2 - 5z^4 \\ & +3x^2z^4 + 3y^2z^4 + z^6 \\ & +\mathrm{i}(-24x^2y + 8y^3 - 4z + 4x^4z + 8x^2y^2z + 4y^4z + 8x^2z^3 + 8y^2z^3 + 4z^5)\} \\ & -t(56(x^2z + y^2z + z^3) + 7\mathrm{i}(1 + 2x^2 - 3x^4 + 2y^2 \\ & -6x^2y^2 - 3y^4 + 6z^2 - 6x^2z^2 - 6y^2z^2 - 3z^4) \\ & +35t^2(1 - 3x^2 - 3y^2 - 3z^2 - 4\mathrm{i}z) - 105\mathrm{i}t^3. \end{aligned} \tag{5.23}$$

When $t = 0$, equation (5.23) reduces by construction to the Milnor polynomial. The function evolves with t as a parameter and this changes the nodal set topology under this evolution. For t close to zero, the nodal set is stable and remains as the trefoil knot, in a geometric form similar to that of the $t = 0$ case. As $t \to t_{\text{crit}}$, a critical value, different parts of the curve approach a common point. At the point $t = t_{\text{crit}}$, the nodal curve reconnects with itself. This process destroys the knot and forms a single nodal loop in the function. As t continues to increase, the loop contracts and annihilates itself, leaving the function with no nodal set. This process is illustrated in figure 5.8.

The 3D Harmonic Oscillator

The quantum harmonic oscillator models the wavefunction of a particle trapped in a potential. This is a time-independent system which can evolve with time after the potential is switched off, but we do not consider that case here. We are interested here in determining if knots and links, constructed as in chapter 4, can be realised as phase singularities in superpositions of wavefunctions which satisfy the conditions of the harmonic oscillator.

We derive the equation to solve from the general form of the Schrödinger equation (5.7). We are interested in the 3D harmonic oscillator, with an isotropic potential, which has Hamiltonian as in equation (5.8). The appropriate potential is [Mes99],

$$V(r) = \frac{1}{2}m\omega^2 r^2, \tag{5.24}$$

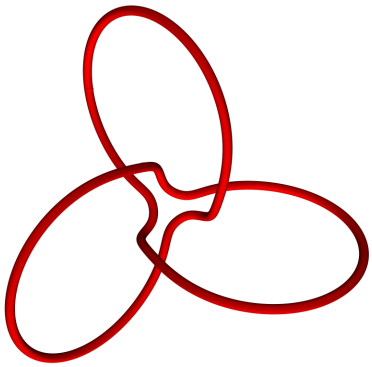

(a)

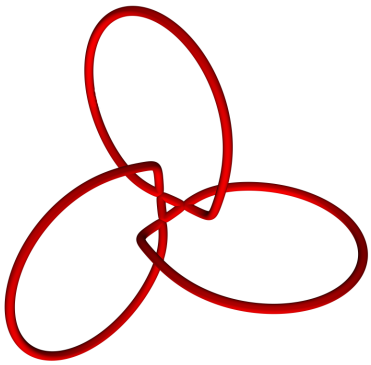

(b)

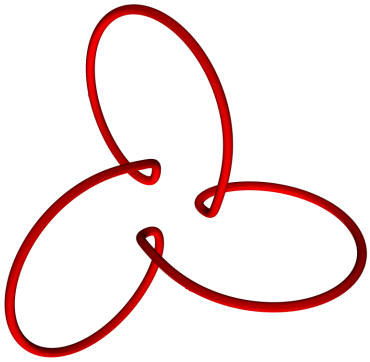

(c)

Figure 5.8: The evolution of the trefoil knot under Schrödinger evolution. (a) Shows the curve at $t = 0.175 < t_{\text{crit}}$ with several parts of the curve converging on the point (x, y, z). (b) At $t = t_{\text{crit}} \approx 0.180$, the self-reconnection takes place and destroys the trefoil knot. (c) Shows $t = 0.185 > t_{\text{crit}}$ where the single unknotted loop has been formed.

where ω is the angular frequency of the system. We desire a solution that is equivalent to being a monochromatic optical wave, to remain consistent with the rest of this thesis. This gives a solution that is time-independent. By letting Ψ be written with the time and spatial variables separated in the form of

$$\Psi(\boldsymbol{r}, t) = \mathrm{e}^{\mathrm{i}Et}\psi(\boldsymbol{r}), \tag{5.25}$$

where E is the energy level of the system, and substituting this into equation (5.7) with the non-differentiating potential, as in equation (5.24), we get

$$-\hbar E\psi(\boldsymbol{r}) = -\frac{\hbar^2}{2m}\nabla^2\psi(\boldsymbol{r}) + \frac{1}{2}m\omega^2 r^2\psi(\boldsymbol{r}), \tag{5.26}$$

after cancelling the common $\mathrm{e}^{\mathrm{i}Et}$ factor from both sides and the zero valued t-derivative of $\psi(\boldsymbol{r})$. We use ψ to represent a time-independent wavefunction throughout the rest of this section. This leads to the 3D harmonic oscillator satisfying the equation

$$\nabla^2\psi - \left(\frac{2m}{\hbar}E + \frac{m^2\omega^2}{\hbar^2}\right)\psi = 0, \tag{5.27}$$

written with the sign of the Laplacian positive to remain consistent with the form of equations used throughout this thesis. It is common in the physics literature for equation (5.27) to be written with the Laplacian being negative.

By neglecting constants, unnormalised solutions of the 3D harmonic oscillator are, in spherical coordinates,

$$\psi(r, \theta, \phi) = r^l \mathrm{e}^{-r^2} L_n^{l+\frac{1}{2}}(2r^2) Y_{l,m}(\theta, \phi). \tag{5.28}$$

We proceed as before and construct the harmonic oscillator solution from the $z = 0$ plane of a Milnor map. In spherical coordinates this equivalent to the $\theta = \frac{\pi}{2}$ plane. When $l - m \equiv 1 \mod 2$, $Y_{l,m}(\frac{\pi}{2}, \phi) = 0$. This restricts our choice of l because $l - m$ must be an even number. Another restriction is given by the order of the Laguerre polynomial being $\frac{1}{2}(n - l)$. This further restricts $n - l$ to be even in order for the polynomial to be defined with integer order.

In order to satisfy the monochromatic criterion, by having solutions for fixed E, this means that all solutions in the superposition must have the same value of n. Let us begin by attempting to construct a harmonic oscillator solution with the trefoil knot as its phase singularity. This requires us to be able to construct all of the terms in the Milnor polynomial

$$1 - r^2 - 8\mathrm{e}^{3\mathrm{i}\phi}r^3 - r^4 + r^6. \tag{5.29}$$

This requires the superposition to have a term with $m = 3$ and hence forces all l to be odd. Our monochromatic criterion then forces us to fix an odd n

to allow $n-l$ to be even. On their own these conditions are not restrictive, however we also require terms with $m=0$. This requires l to be even and hence n even, which cannot simultaneously occur with an odd n. A function that coincides at $z=0$ ($\theta=\frac{\pi}{2}$) with the Milnor polynomial of the trefoil knot cannot be constructed as a solution of the harmonic oscillator. This also means that any Milnor polynomial that requires a mix of odd and even m, cannot be constructed in this fashion.

We now attempt to construct a monochromatic harmonic oscillator solution of a Milnor polynomial that does not mix odd and even m. The simplest such example is the Hopf link, with Milnor polynomial

$$1-2r^2-4\mathrm{e}^{2\mathrm{i}\phi}r^2+r^4. \tag{5.30}$$

By fixing $n=4$ we can construct the following superposition, with "modes" labelled $\psi^n_{l,m}$:

$$\begin{aligned}\psi^{n=4}_{\text{Hopf}} &= \frac{16}{315}\sqrt{\pi}\left(11\psi^4_{4,0}-3\sqrt{5}\psi^4_{2,0}+21\psi^4_{0,0}\right)\\ &\quad -\frac{8}{21}\sqrt{\frac{2\pi}{5}}\left(7\psi^4_{4,2}-\sqrt{3}\psi^4_{2,2}\right).\end{aligned} \tag{5.31}$$

Despite coinciding exactly with the Milnor polynomial at $z=0$, this harmonic oscillator solution does not contain the Hopf link in its phase singularities. The nodal set is a complicated mix of intersecting loops and lines. This is shown in figure 5.9.

It can be seen that the nodal lines that pass through the $z=0$ plane, in the four locations, do not approach the plane from opposite directions. They are mirrored in this plane. This contrasts to those of the Milnor polynomial which mirror in a plane at 45 degrees to the x-axis.

The superposition to obtain the Milnor polynomial, equation (5.30), is not unique. For a different energy level, n, a different superposition can be constructed. The higher the energy, the more redundant terms, at $z=0$, need to be cancelled to coincide with the Milnor polynomial. For example, when $n=6$,

$$\psi^6_{0,0}|_{\theta=\frac{\pi}{2}}=\frac{1}{96\sqrt{\pi}}\left(105-420r^2+336r^4-64r^6\right). \tag{5.32}$$

To be able to construct the required $m=0$ terms, the mode $\psi^6_{6,6}$ is required to cancel the r^6 term. However, this is at the cost of introducing more complicated terms involving θ.

The $n=6$ superposition is

$$\begin{aligned}\psi^{n=6}_{\text{Hopf}} &= \frac{32}{45045}\sqrt{\pi}\left(-92\sqrt{13}\psi^6_{6,0}+39\psi^6_{4,0}-286\sqrt{5}\psi^6_{2,0}+1287\psi^6_{0,0}\right)\\ &\quad +\frac{32}{9009}\sqrt{\frac{2\pi}{15}}\left(16\sqrt{182}\psi^6_{6,2}-156\sqrt{3}\psi^6_{4,2}+143\psi^6_{2,2}\right).\end{aligned} \tag{5.33}$$

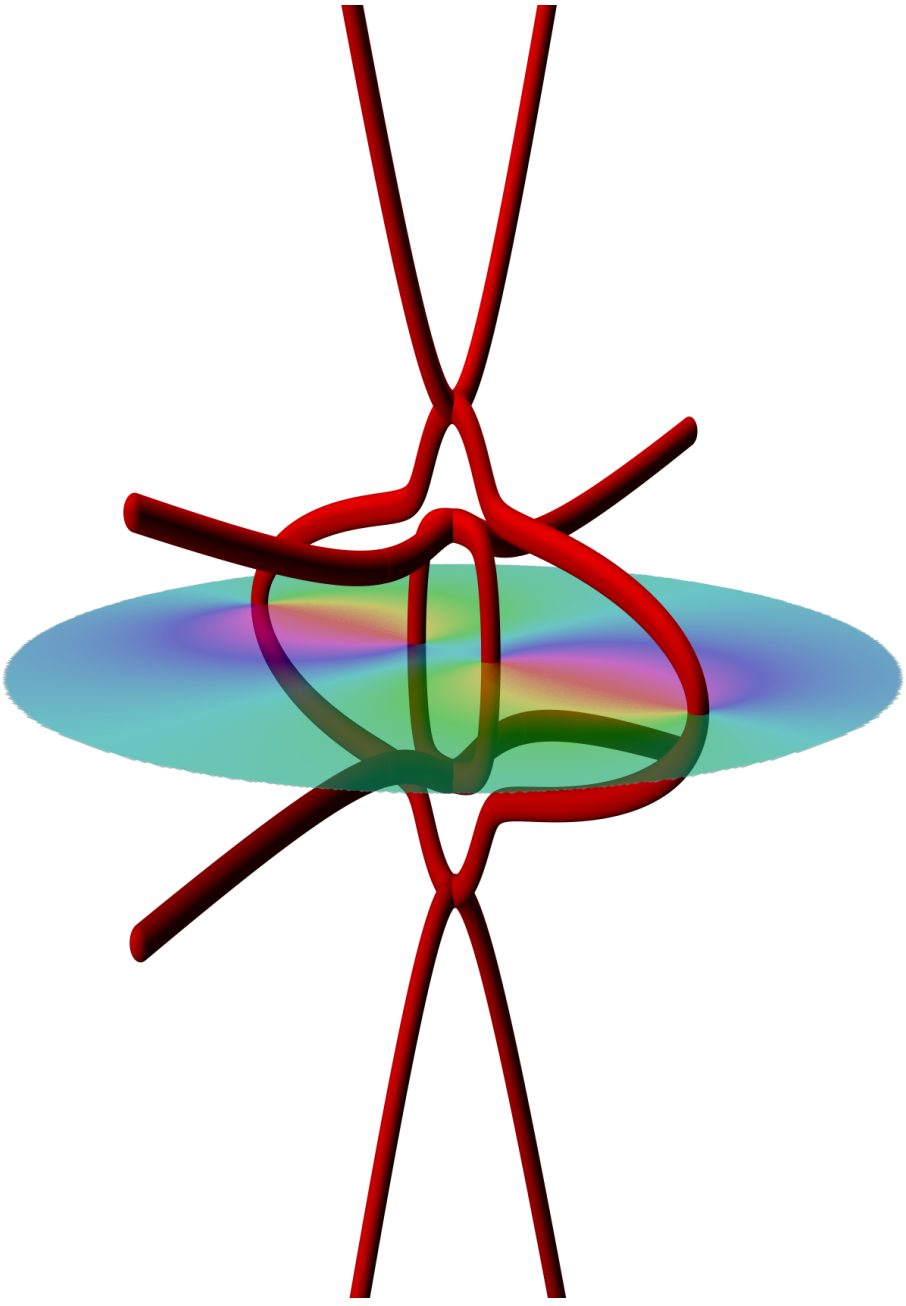

Figure 5.9: The nodal lines of the $n = 4$ harmonic oscillator wavefunction from equation (5.33). Despite coinciding exactly with the Milnor polynomial in the $z = 0$ plane, where its phase is shown as the opaque disk, it is clear that a Hopf link has not formed.

This function, like its lower energy counterpart, does not contain the Hopf link as its nodal set. In addition to the many extra intersecting components, this $n = 6$ superposition does not have the correct symmetry about the $z = 0$ plane. This set of curves is shown in figure 5.10. In this case, the nodal lines exhibit higher order crossings consisting of intersections with four nodal lines.

The fact that odd and even m modes cannot be mixed in our construction, limits the knots and links that we can attempt to construct with these solutions of the harmonic oscillator. This does not prevent us from forming monochromatic solutions that do not mix these terms. However, as we have seen for the Hopf link, the symmetry of the superpositions in the $z = 0$ plane prevents the desired topology being formed. This has to lead to the conclusion that this form of harmonic oscillator solutions will not support knots from our construction by using the $z = 0$ plane information only. We are not concluding that knotted nodal sets are forbidden by the 3D isotropic harmonic oscillator, just they cannot be constructed using the methods of this thesis.

The Hydrogen Atom

Under the right assumptions, hydrogen atom wavefunctions can be constructed that are complex scalar fields in space and stationary in time. The phase singularities of such a complex wave functions and their topology have been studied by Berry [Ber01b]. This work adapts the techniques of [BD01a] and constructs threaded torus knots, explicitly the Hopf link and trefoil knot, as phase singularities of hydrogen atom wavefunctions. We now examine whether the knots and links of our construction can be formed in such wavefunctions.

The hydrogen atom is usually considered with its time-reversal symmetry which means that the stationary state wavefunctions are real. This contrasts to our complex wavefunction approach. Restricting the problem to take advantage of the degeneracies arising from the spherical symmetry of the problem, allows a complex wavefunction solution to arise.

The Schrödinger equation is given a Hamiltonian of the form equation (5.8) where the potential is now given by Coulomb's law :

$$V(\boldsymbol{r}) = -\frac{1}{4\pi\epsilon_0}\frac{e^2}{r}, \tag{5.34}$$

where ϵ_0 is the permittivity of the vacuum, e is the charge of the electron and the atomic nucleus contains only one proton, by definition.

As in the case of the harmonic oscillator, we consider the time-independent "monochromatic" form of the Schrödinger equation. Neglecting the constants, but keeping the correct form, the hydrogen atom wave function ψ, satisfies the

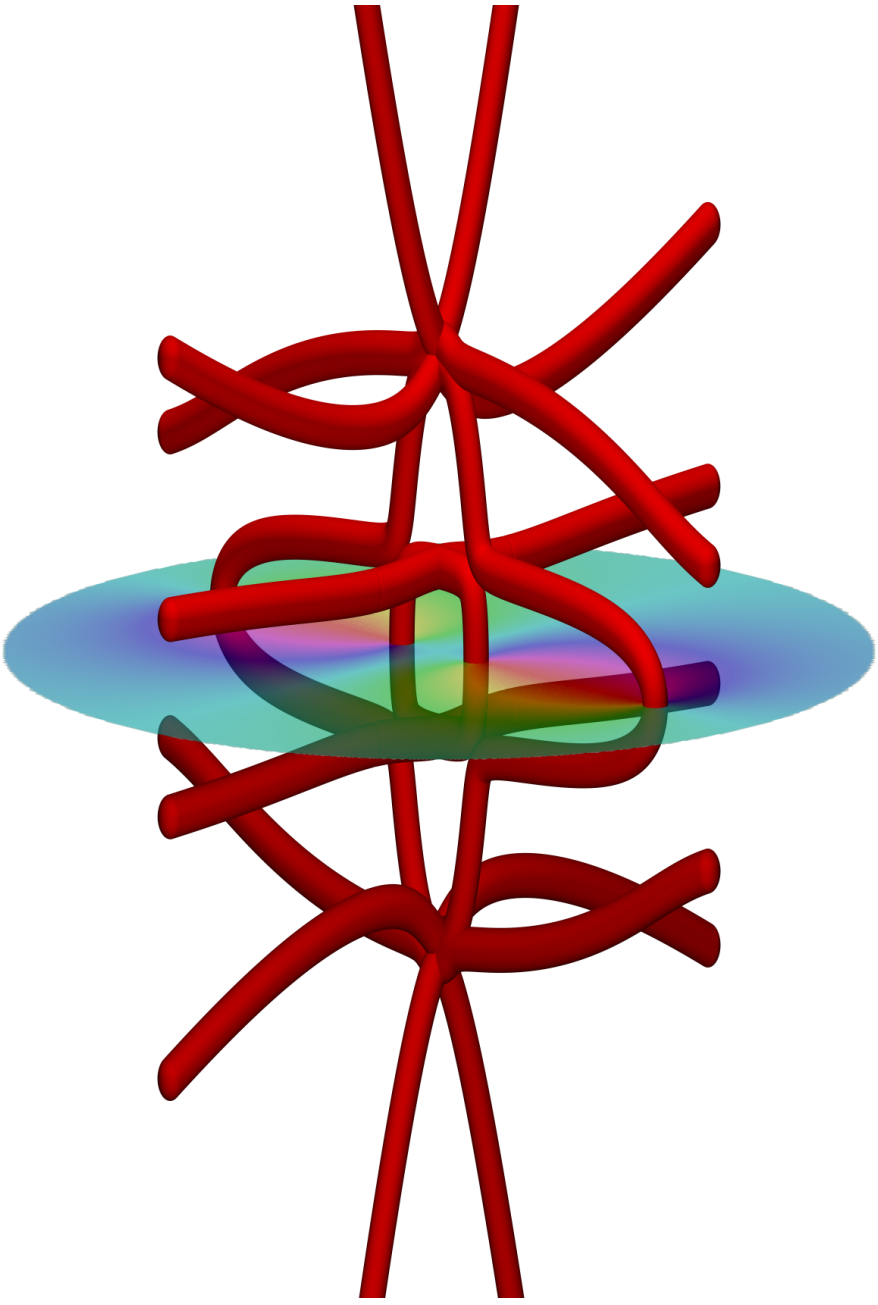

Figure 5.10: The nodal lines of the $n = 6$ harmonic oscillator wavefunction from equation (5.33). Despite coinciding exactly with the Milnor polynomial in the $z = 0$ plane, where its phase is shown as the opaque disk, it is clear that the Hopf link is not formed, like in the $n = 4$ case.

equation

$$\nabla^2\psi + \left(E + \frac{1}{r}\right)\psi = 0, \tag{5.35}$$

which is the Schrödinger equation with a Coulomb potential. This has time-independent solutions, from [Ber01b], of unnormalised form

$$\psi = r^l \mathrm{e}^{-\frac{1}{2}r} L^{2l+1}_{n-l-1}(r) P^m_l(\cos\theta)\mathrm{e}^{\mathrm{i}m\phi}, \tag{5.36}$$

where $l, m, n \in \mathbb{N}$.

The solutions of (5.36) are expressed in spherical coordinates so we need to set $\theta = \frac{\pi}{2}$ to replicate the $z = 0$ plane of our Milnor polynomials. Monochromatic superpositions require all modes to have the same fixed n. This condition arises from the spherical harmonic part, expressed as exponential and Legendre functions in equation (5.36), requires $l - m$ to be even for a non-zero value of ψ in this plane. It is also required that $n - l$ be even for a non-zero solution.

The argument of the Laguerre polynomial in this case is in r not r^2. The fact that we cannot have $n - l$ odd means that the odd powers of r present in low l modes cannot be cancelled by the required odd l modes. For example, the r polynomial part of $\psi^6_{0,0}$ is proportional to

$$r^6 - 42r^5 + 630r^4 - 4200r^3 + 12600r^2 - 15120r + 5040. \tag{5.37}$$

The next non-zero term, with $n = 7$ fixed and $m = 0$ has $l = 2$. Hence, terms of order r^1 cannot be cancelled. This means that we cannot construct superpositions to coincide with our Milnor polynomials with these hydrogen atom wavefunctions.

Despite being a second negative result of this section, we know from [Ber01b] that at least torus knots, though not necessary isolated, are possible in the wavefunction's phase singularities. It is possible that unthreaded and non-torus knots can be constructed in this system. Our construction requiring the coinciding of $z = 0$ planes is not appropriate to these modes of the hydrogen atom, but knots constructed by the Lissajous construction may be possible by other embedding methods.

5.4 Discussion

The results of this chapter can be summarised as :

- We have given further examples of paraxial optical vortex knots, 6_3 and 7_7 in section 5.1. For the 6_3 knot we have shown that the parameter a from equation (4.5) does have a limited range for which the knot is formed both in the Milnor polynomial and paraxial polynomial. Changing the axis

around which the braid is closed has large impact in the $z = 0$ plane for the 7_7 knot.

- We have constructed polynomial solutions to the Helmholtz equation, section 5.2. We have been able to construct knotted nodal lines in functions satisfying the Helmholtz equation. This introduces an additional parameter into the function, k on which the topology depends. The case $k = 0$ means the Helmholtz equation becomes Laplace's equation and our solutions breakdown as k approaches zero.

- The Schrödinger equation has been less successful for constructing nodal knots, section 5.3. When no potentials are present, our constructed knots are unstable to evolving time. The harmonic oscillator does not appear to support our nodal knots when evolved from a $z = 0$ plane and hydrogen atom model solutions cannot be used as a basis for the Milnor polynomials at $z = 0$.

We have been able to generate functions satisfying the paraxial equation with knots from the Lisssajous construction. Although the parameter a plays a crucial role in the successful formation of the desired knot, outside the successful range other parameters could play a role in the process. Until now we have not varied the radius of the 3-sphere in the Milnor-like mapping when forming the Milnor polynomials and this is discussed in section 4.7.

Throughout this thesis we have referred to the "geometric form" of the knot. Although it is often trivial to compare differences pictorially, it is more difficult to quantify these differences. A geometric measure of a curve is the writhe.

Definition 5.1 (Writhe, for example [DH05])**.** *The writhe, Wr, of a parameterised closed curve $\gamma(s)$, is*

$$Wr = \frac{1}{4\pi}\int_\gamma \mathrm{d}s \int_\gamma \mathrm{d}s' \frac{(\gamma'(s)\times\gamma'(s'))\cdot(\gamma(s)-\gamma(s'))}{|\gamma(s)-\gamma(s')|^3}, \tag{5.38}$$

which is the average crossing number over all possible viewing directions.

Future comparisons between knots from our construction and other forms of the same knot, could be carried out by comparing the writhe of the curves. Within the context of knot theory, the concept of writhe has been used to describe ideal knots. Ideal knots were introduced by Katritch et al [KBM$^+$96].

Definition 5.2 (Ideal Knot [KBM$^+$96])**.** *Let K be a knotted curve constructed from a solid cylindrical tube of length L and constant diameter D. K is said to be in the particular geometric form called ideal if the ratio L/D is a global minimum.*

Are the knots we construct in ideal form? Or at some other local minimum of L/D? The link between writhe and ideal knots is studied by Cerf and Stasiak [CS00]. By visual inspection, using the images in [SKK98], it can be seen that the knots we have constructed are not ideal.

The measure of writhe could be used to predict when the nodal curve of the Milnor polynomial will fail to form the target topology as the parameters of the Lissajous construction are varied. The writhe of a knot is used by Flammini and Stasiak [FS07] to create a tabulation and classification of knots. Other geometric measures exist, such as the energy of the knot [O'H91], which could also be investigated near the critical values of the Lissajous construction.

The Helmholtz equation was our first example away from the paraxial equation. When the wave number k is sufficiently high, then for the cases studied, the desired nodal knot exists as a solution of the Helmholtz equation. We expect this to be the case for all of the knots and links that we can construct with the Lissajous construction. Although the Helmholtz equation is homogeneous, it is second order in all three axial directions, our solutions choose a propagation direction z. This gives a similarity to the paraxial solutions where the propagation direction is only first order compared to the second order transverse derivatives.

The additional terms in the Helmholtz polynomials, compared to the paraxial polynomials, correspond to the additional correction terms that the paraxial approximation does not consider. The square root in equation (5.1) is expanded to second order only in the paraxial approximation. The Helmholtz equation is the exact propagation of this term. In Berry and Klein [BK96], another form of propagator is considered. They give additional terms in the expansion, allowing for a better approximation to the actual propagation. Should a knot that we can construct fail for reasonable values of available parameters, in either the paraxial or Helmholtz equation, then these post-paraxial terms could be used to construct fields that coincide with the $z = 0$ plane of our Milnor polynomials.

The Schrödinger equation models a variety of quantum mechanical systems. We have considered three possible Hamiltonians, two of which give rise to static solutions. When no potentials are present we are able to study the evolution of nodal knots in time. For a short time, the nodal topology is stable and is only perturbing a small amount, equivalent to a small isotopy of the curve. As time continues to progress, the small isotopy becomes a significant deviation from the $t = 0$ curve. This causes self-reconnections and eventually the rings formed annihilate themselves, leaving a function containing no zero structure. Similar results are found by Bialynicki-Birula et al [BBBBS00], looking at constructing exact solutions, different to our method, by considering local properties of the wavefield close to the vortex lines. One case considered is the time-evolution of

a vortex loop in a trap potential, similar to our static harmonic oscillator solutions. The loop breaks and forms a parabola-like curve before reconnecting into a loop. We could expect a similar behaviour under time-evolution of our vortex knots if a successful embedding could be achieved into the harmonic oscillator.

It is possible that a static nodal knot is possible for other potentials $V(\boldsymbol{r})$ in equation (5.8). Solutions that give rise to a Laguerre polynomial of an odd power of r will, in general, fail because of the inability to subtract odd powers of r in the $z = 0$ plane. Other potentials of the form r^n could give rise to solutions that do support our knot construction.

It is an interesting question to ask what further physical, and non-physical, partial differential equations, our construction can be applied to. We have acknowledged optical vortices in non-linear paraxial propagation in section 1.7, however these vortex knots cannot be controlled by a construction similar to ours. Wavefunctions that contain a vortex structure, satisfying a non-linear Schrödinger equation, have been considered by Bialynicki-Birula et al [BBBB01] and Nazarenko and West [NW03] studying the properties of vortex line reconnections under non-linear Schrödinger evolution. This has applications in the study of the Gross-Pitaevskii equation

$$\mathrm{i}\hbar\frac{\partial\Psi(\boldsymbol{r},t)}{\partial t} = \left(-\frac{\hbar^2}{2m}\nabla^2 + V(\boldsymbol{r}) + K|\Psi(\boldsymbol{r},t)|^2\right)\Psi(\boldsymbol{r},t), \tag{5.39}$$

which models Bose-Einstein condensates (BECs) [Leg06], where V is a trapping potential and K a constant dependent on the atoms being condensated. The vortex structure of BECs has been studied by Ruostekoski and Dutton [RD05] and the effects of time-evolution on vortex rings. A knotted vortex line in a BEC provides a challenging theoretical and experimental project.

A further equation to consider is the Dirac equation. This equation describes relativistically the wavefunction of a spin $\frac{1}{2}$ particle such as an election [Mes99]. The Dirac equation, in three (Cartesian) space dimensions plus one time dimension, is

$$\mathrm{i}\hbar\frac{\partial\Psi(\boldsymbol{r},t)}{\partial t} = \boldsymbol{\beta}mc^2\Psi(\boldsymbol{r},t) - \mathrm{i}\hbar c\left(\boldsymbol{\alpha}_1\frac{\partial\Psi(\boldsymbol{r},t)}{\partial x} + \boldsymbol{\alpha}_2\frac{\partial\Psi(\boldsymbol{r},t)}{\partial y} + \boldsymbol{\alpha}_3\frac{\partial\Psi(\boldsymbol{r},t)}{\partial z}\right), \tag{5.40}$$

where $\boldsymbol{\alpha}_i$ and $\boldsymbol{\beta}$ are the Dirac 4×4 matrices. Non-trivial topology of the nodal set of a solution of the Dirac equation based on our Lissajous construction would certainly be an exciting theoretical insight.

Finally for this chapter, we present some ideas for future investigations of physical systems that could have knotted lines constructed from the Lissajous construction.

- Our work has been concerned with solving linear differential equations. Vortex knots in non-linear fields, as in the example in figure 1.8, do not form from a direct mathematical knot construction. The knots of the Lissajous construction can be applied to solutions of non-linear equations and propagated, with the hope that the vortex structure is stable with respect to the nonlinearity.

- Is there a significance to the geometric form of the knots as we construct them? Are they the stationary values of a functional from the set of knots in the same way being ideal or having minimum energy can be defined?

- We have only worked with complex scalar fields. Even within optics there are a range of types of functions that we have not worked with. Can our construction be applied to a vector field or fluid flows? Vector field singularities exist optically as L and C lines; lines where the polarisation ellipse is linear or circular respectively [Nye99]. Is it possible to make our knots in the L and C lines? The Riemann-Silberstein vector [BBBB03], defined as $\boldsymbol{V} = \mathrm{Re}\,\boldsymbol{E}(t) + \mathrm{i}\,\mathrm{Re}\,\boldsymbol{H}(t)$ (notation as in section 1.5) gives access to a relativistically invariant vector. Both the real and imaginary parts of $\boldsymbol{V}\cdot\boldsymbol{V}$ are the same for all relativistic observers [DOP09], in all inertial frames. Singularities in this vector field $\boldsymbol{V}$, the Riemann-Silberstein vortices, are relativistic invariant singularities of the optical field [DOP09] and if we could extend our construction to these singular structures, relativistically invariant knots would be formed.

5.A Helmholtz Polynomials

$m = 0$	1
$m = 1$	$R^2 - \frac{2\mathrm{i}}{k}(n+1)z$
$m = 2$	$R^4 - \frac{4\mathrm{i}}{k^3}\left((2+3n+n^2) - k^2R^2(2+n)\right)z - \frac{4}{k^2}\left(2+3n+n^2\right)z^2$
$m = 3$	$R^6 - \frac{6\mathrm{i}}{k^5}(3+n)\left(4(1+n)(2+n) - 2k^2(2+n)R^2 + k^4R^4\right)z$ $+\frac{12}{k^4}(2+n)(3+n)\left(-2-2n+k^2R^2\right)z^2 + \frac{8\mathrm{i}}{k^3}(1+n)(2+n)(3+n)z^3$

Table 5.1: The first four cylindrical Helmholtz polynomials

Table 5.1 shows the Helmholtz polynomials, introduced in section 5.2. For each m listed, the Helmholtz polynomial $p_{m,n,k}(R,z,\phi)$ satisfies the Helmholtz equation when

$$\Psi(R,z,\phi,k) = \mathrm{e}^{\mathrm{i}kz}R^n\mathrm{e}^{\mathrm{i}n\phi}p_{m,n,k}(R,z,\phi). \tag{5.41}$$

Steering of Optical Vortices

6

A full three-dimensional function that describes an optical vortex curve is in general difficult to acquire exactly from an optical field. We now construct a scheme to give an approximation for the loci of the vortex lines. This is based on the function describing the $z = 0$ plane and evaluating derivatives of the field there. This will take the idea of two-dimensional functions, using the lexicon of point particle dynamics and their derivatives, to construct a Taylor expansion for the actual three-dimensional vortex curve. Using just the values of the derivatives, we investigate if changes in their directions can be used to predict changes in the overall topology of the vortex lines. We finish with the curious $(5,2)$-form of the cinquefoil knot. This knot, in this geometric form, has been shown to be constructible paraxially from the Lissajous construction but only with an over-homogenised function.

6.1 2D Dynamics vs 3D Geometry

The knotted nodal lines of the previous chapters were considered as purely topological features. We did not describe or give functions for the exact space curve. The exact function of a nodal line in three dimensions is in general complicated, if it is at all available analytically. We now seek to approximate such a function with a Taylor-like series in z, the propagation direction.

Until now, we have thought of the vortex curves as purely three-dimensional objects. Optical vortices can also be thought as zero points in a plane, evolving like point particles in progression from plane to plane. We now show the link between these two complementary pictures of the optical vortex curves.

Optical vortex curves are the pre-images of zero of a wavefunction ψ. The set $\psi^{-1}(0)$ is generically a one-dimensional manifold that can consist of more than one component. Each component is realised as a parametrised curve, $\boldsymbol{Q}(z)$

where $\boldsymbol{Q}(x(z), y(z))$ gives the x- and y-positions as a function of z.

In the plane perpendicular to the beam's propagation direction, the (x, y)-plane, the vortices are points. These points have a motion in the plane that is parametrised by propagation distance. A smooth curve in a transverse plane is formed as the projection of the three-dimensional curve. The two-dimensional motion we refer to as the *dynamical* picture and when referring to the three-dimensional curve, the *geometric* picture.

The derivatives of the particle-like motion can be considered as if the parameter was time, not propagation distance. By considering the motion of the zeroes as points in the plane, we can use the language of dynamics to describe the motion : velocity ($\dot{\boldsymbol{Q}} = \boldsymbol{V}$), acceleration ($\ddot{\boldsymbol{Q}} = \boldsymbol{A}$), etc...where $\dot{\bullet} = \frac{\partial \bullet}{\partial z}$. These derivatives of $\boldsymbol{Q}$ with respect to z are used to build the series expansion for the nodal curves,

$$\boldsymbol{Q}(x(z), y(z)) = \boldsymbol{Q}_0 + \boldsymbol{V}z + \boldsymbol{A}\frac{z^2}{2} + \boldsymbol{J}\frac{z^3}{6} + \ldots, \tag{6.1}$$

where $\boldsymbol{Q}_0$ is the location of the nodal point at $z = 0$ and $\boldsymbol{J}$ is the jerk, the third time derivative of motion, in this case third z derivative[1]. We now consider how to these derivatives can be calculated in general.

Velocity

The first derivative of motion is velocity, $\boldsymbol{V}$. We now derive the velocity of a nodal point in the plane transverse to the beam propagation and arrive at a similar form as given by Berry and Dennis [BD00], although the context there is time-dependent fields, we replace the time dependence with the z-dependence to remain in our context of paraxial monochromatic waves. Velocity is a two-dimensional vector, in the (x, y)-plane defined at a vortex point.

We introduce the following notation for this chapter. We use numeric subscripts to represent components of vectors : a two-dimensional vector $\boldsymbol{Q}$ has components Q_1 and Q_2 corresponding to the x and y components respectively. The wedge product of two, two-dimensional vectors, $\boldsymbol{A}$ and $\boldsymbol{B}$ is defined as

$$\begin{pmatrix} a_1 \\ a_2 \end{pmatrix} \wedge \begin{pmatrix} b_1 \\ b_2 \end{pmatrix} = a_1 b_2 - a_2 b_1. \tag{6.2}$$

We also define the perpendicular to a two dimensional vector as

$$\boldsymbol{A}^{\perp} = \begin{pmatrix} 0 & -1 \\ 1 & 0 \end{pmatrix} \boldsymbol{A}. \tag{6.3}$$

[1]The fourth, fifth and sixth time derivatives are often referred to as the snap, crackle and pop respectively.

The complex optical field ψ can be written as $\psi = \xi + \mathrm{i}\eta$. An optical vortex occurs where $\xi = 0$ and $\eta = 0$. It is this zero contour in ψ we wish to follow. Taking the total derivative at a zero gives the direction of this contour. This gives

$$\mathrm{D}\psi|_{\text{vortex}} = 0. \tag{6.4}$$

This could be taken with respect to any parameter

$$\frac{\partial \boldsymbol{Q}}{\partial \sigma} \cdot \nabla \psi + \frac{\partial z}{\partial \sigma} \psi_z. \tag{6.5}$$

We choose to let the parameter σ be the propagation direction z and hence

$$\psi_z + (\boldsymbol{V} \cdot \nabla_\perp)\psi = 0, \tag{6.6}$$

the velocity here being formed of

$$\dot{\boldsymbol{Q}}(x(z), y(z)) = \boldsymbol{V}(x(z), y(z)) = \begin{pmatrix} \frac{\mathrm{d}x(z)}{\mathrm{d}z} \\ \frac{\mathrm{d}y(z)}{\mathrm{d}z} \end{pmatrix}. \tag{6.7}$$

This allows us to write

$$-\psi_z = \begin{pmatrix} \psi_x \\ \psi_y \end{pmatrix} \cdot \boldsymbol{V}, \tag{6.8}$$

and rearranging, considering the real and imaginary parts gives

$$\boldsymbol{V} = \frac{-1}{\xi_x \eta_y - \eta_x \xi_y} \begin{pmatrix} \eta_y & -\xi_y \\ -\eta_x & \xi_x \end{pmatrix} \begin{pmatrix} \xi_z \\ \eta_z \end{pmatrix}, \tag{6.9}$$

provided $\xi_x \eta_y - \eta_x \xi_y \neq 0$. Finally we take the form

$$\boldsymbol{V} = \frac{(\dot{\psi}^* \nabla_\perp \psi - \dot{\psi} \nabla_\perp \psi^*)^\perp}{\nabla_\perp \psi^* \wedge \nabla_\perp \psi}, \tag{6.10}$$

$$= \frac{2\mathrm{i}\,\mathrm{Im}(\dot{\psi}^* \nabla_\perp \psi)^\perp}{\nabla_\perp \psi^* \wedge \nabla_\perp \psi}, \tag{6.11}$$

which is a ratio of two purely imaginary quantities and gives a real value. This vector is the projection of the three-dimensional tangent vector into the transverse plane.

Acceleration

To build a series expansion we require the higher derivatives of the function $\boldsymbol{Q}$ and hence of the velocity. We can write for a general optical field, $\psi(\boldsymbol{r})$, the vortex position function $\boldsymbol{Q}(z)$, where

$$\psi(\boldsymbol{Q}(z), z)) = 0, \tag{6.12}$$

is used to define the function $\boldsymbol{Q}$. We can define a general function $\boldsymbol{F}(\psi(\boldsymbol{Q}, z))$ which describes the transverse motion, parametrised by z, of any local property of the field ψ. $\boldsymbol{Q}$ in such a general case is the locus of that point. The local property we use is the velocity or acceleration of an optical vortex but other properties, such as the location of a phase saddle point, could also be used. The rate of change with respect to z of such a quantity is then

$$\frac{\mathrm{d}\boldsymbol{F}}{\mathrm{d}z} = \frac{\partial \boldsymbol{F}}{\partial z} + \left(\frac{\partial \boldsymbol{Q}}{\partial z} \cdot \nabla_{\perp}\right) \boldsymbol{F}, \tag{6.13}$$

which can be written as

$$\mathrm{D}\boldsymbol{F} = \frac{\partial F}{\partial z} + (\boldsymbol{V} \cdot \nabla_{\perp})\, \boldsymbol{F}, \tag{6.14}$$

which is the convective derivative of $\boldsymbol{F}$, and $\boldsymbol{V}$ is the velocity of the quantity in question. For our $\boldsymbol{Q}$ representing the locus of the vortex we have

$$\boldsymbol{A} = \frac{\partial \boldsymbol{V}}{\partial z} + (\boldsymbol{V} \cdot \nabla_{\perp})\boldsymbol{V}. \tag{6.15}$$

This means that the jerk of the vortex motion is the convective derivative of its acceleration

$$\boldsymbol{J} = \frac{\partial \boldsymbol{A}}{\partial z} + (\boldsymbol{V} \cdot \nabla_{\perp})\boldsymbol{A} \tag{6.16}$$

and similarly for all higher derivatives.

6.2 Curvature and Torsion of Nodal Lines

The two-dimensional vectors, $\boldsymbol{V}$, $\boldsymbol{A}$, $\boldsymbol{J}$ etc. also allow us to obtain various three-dimensional quantities describing the nodal curve. Spaces curves, curves in three dimensions, like our optical vortex lines can be defined by a set of framing vectors and their associated scalar quantities. We shall now assume that our nodal space curves are differentiable. The notation for this section is general.

A generic three-dimensional space curve $\boldsymbol{\gamma}(s)$, parameterised by s, has speed $|\boldsymbol{\gamma}'(s)| = \sqrt{\boldsymbol{\gamma}'(s) \cdot \boldsymbol{\gamma}'(s)}$. A curve with unit speed everywhere is said to have arc-length parametrisation [Str50]. Here we only consider this class of curves. We denote derivatives with respect to s as

$$\boldsymbol{\gamma}' = \frac{\mathrm{d}\boldsymbol{\gamma}}{\mathrm{d}s}. \tag{6.17}$$

The first derivative of $\boldsymbol{\gamma}$ is the tangent to the curve, $\boldsymbol{\gamma}' = \boldsymbol{t}$, and is a unit vector because of the arc-length parametrisation. Orthogonal to the tangent vector is the normal vector $\boldsymbol{n} = \boldsymbol{\gamma}''/|\boldsymbol{\gamma}''|$. A third vector, completing an orthonormal triad of vectors is the binormal, $\boldsymbol{b} = \boldsymbol{n} \times \boldsymbol{t}$. These three vectors, $\{\boldsymbol{t}, \boldsymbol{n}, \boldsymbol{b}\}$, form the *Frenet frame* for the curve and are defined at all points where $\kappa \neq 0$.

Associated with these vectors are two scalar quantities, the curvature κ and the torsion τ. The curvature is a measure of how much the curve deviates from being a straight line. A curve with zero curvature is locally straight, while a large curvature represents a curve with a small radius of curvature. The torsion is a measure of how flat the curve is. When $\tau = 0$ the curve is locally planar and as the torsion increases the curve bends more out of the plane. The curvature and torsion have definitions [Str50]

$$\kappa = \frac{|\boldsymbol{\gamma}' \times \boldsymbol{\gamma}''|}{|\boldsymbol{\gamma}'|^3}, \tag{6.18}$$

$$\tau = \frac{\boldsymbol{\gamma}' \times \boldsymbol{\gamma}'' \cdot \boldsymbol{\gamma}'''}{|\boldsymbol{\gamma}' \times \boldsymbol{\gamma}''|^2}, \tag{6.19}$$

respectively. The *fundamental theorem of space curves* states that given κ and τ as functions of s, the curve $\boldsymbol{\gamma}$ is defined uniquely up to translation and rotation.

The Frenet frame vectors are linked by their derivatives and the curvature and torsion at each point by the Frenet-Serret formula [Str50],

$$\begin{pmatrix} \boldsymbol{t}' \\ \boldsymbol{n}' \\ \boldsymbol{b}' \end{pmatrix} = \begin{pmatrix} 0 & \kappa & 0 \\ -\kappa & 0 & \tau \\ 0 & -\tau & 0 \end{pmatrix} \begin{pmatrix} \boldsymbol{t} \\ \boldsymbol{n} \\ \boldsymbol{b} \end{pmatrix}. \tag{6.20}$$

This framing becomes undefined at inflection points where the normal vector cannot be assigned a unique direction .

We now use the connection between the transverse motion of the optical vortices and the differential geometric quantities defined above to move between the 2D and 3D descriptions. This allows for a curve representing the vortex trajectory $\boldsymbol{\gamma}(s) = (x(s), y(s), z(s))$, with $z'(s) = \frac{\mathrm{dz}}{\mathrm{ds}} = w$. This w is not a beam waist width and for this chapter takes this definition. The velocity can therefore be written in terms of the arc-length derivatives and the chain rule

$$\boldsymbol{V} = (\dot{x}(z), \dot{y}(z)) = \frac{1}{w}(x'(s), y'(s)). \tag{6.21}$$

With the z-direction in three dimensions being considered as time, we form

$$\dot{\boldsymbol{\Gamma}} = w(\dot{x}(t), \dot{y}(t)) = w(V_1, V_2), \tag{6.22}$$

where $\boldsymbol{\Gamma}$ is the $(2+1)$-dimensional trajectory of the vortex in the transverse plane. The higher derivatives of $\boldsymbol{\Gamma}$ are formed as

$$\begin{pmatrix} \boldsymbol{\Gamma}' \\ \boldsymbol{\Gamma}'' \\ \boldsymbol{\Gamma}''' \end{pmatrix} = \begin{pmatrix} w & 0 & 0 \\ w\dot{w} & w^2 & 0 \\ w\dot{w}^2 + w^2\ddot{w} & 3w^2\dot{w} & w^3 \end{pmatrix} \begin{pmatrix} \boldsymbol{V} \\ \boldsymbol{A} \\ \boldsymbol{J} \end{pmatrix}. \tag{6.23}$$

The inverse of these relations gives the two-dimensional motion in terms of the derivatives of the projected three-dimensional motion

$$\begin{pmatrix} \boldsymbol{V} \\ \boldsymbol{A} \\ \boldsymbol{J} \end{pmatrix} = \begin{pmatrix} w^{-1} & 0 & 0 \\ -\dot{w}w^{-2} & w^{-2} & 0 \\ \Lambda & -3\dot{w}w^{-3} & w^{-3} \end{pmatrix} \begin{pmatrix} \boldsymbol{\Gamma}' \\ \boldsymbol{\Gamma}'' \\ \boldsymbol{\Gamma}''' \end{pmatrix}, \tag{6.24}$$

where $\Lambda = w^{-6}(2w^3\dot{w}^2 - w^4\ddot{w})$.

With the higher s-derivatives of the three-dimensional curve written in terms of the transverse motion of the vortex, equation (6.23), we can define the curvature and the torsion of the curve as it passes through our initial plane. From equations (6.18) and (6.19) we derive using velocity, acceleration and jerk,

$$\kappa^2 = \frac{\boldsymbol{A}^2 + (\boldsymbol{V} \wedge \boldsymbol{A})^2}{(1 + \boldsymbol{V}^2)^3}, \tag{6.25}$$

and

$$\tau = \frac{(\boldsymbol{A} \wedge \boldsymbol{J})(1 + \boldsymbol{V}^2)^3}{\boldsymbol{A}^2 + (\boldsymbol{V} \wedge \boldsymbol{A})^2}. \tag{6.26}$$

6.3 Paraxially Evolving Dynamics

Our interest here is in functions specified at an initial plane, $z = 0$, that satisfy the paraxial equation on propagation with their z-dependence restored. We can modify the initial plane that in general affects the propagation and hence the value of the z-derivatives in the expressions for $\boldsymbol{V}$, $\boldsymbol{A}$, $\boldsymbol{J}$... The paraxial equation (1.19) of page 14, can be rearranged to write the z-derivative in terms of the transverse Laplacian:

$$\partial_z \psi = \frac{\mathrm{i}}{2k} \nabla_\perp^2 \psi. \tag{6.27}$$

The evolution in z of a given (x, y)-transverse plane means we can consider the propagation of an optical field in this case, as an initial value problem. This means that for a given transverse plane, we will choose the $z = 0$ plane for simplicity, we can have a function in only x and y and still be able to evaluate the z-derivatives. This weighted Laplacian, equation (6.27), is substituted for all occurrences of $\partial_z \psi$, but only after all z-derivatives are taken for the specific kinematic quantity. We also require that when the conjugate ψ^* is differentiated the conjugate paraxial equation is used in its substitution:

$$\partial_z \psi^* = \frac{-\mathrm{i}}{2k} \nabla_\perp^2 \psi^*. \tag{6.28}$$

This means that we can express the velocity of an optical vortex in a given $z = 0$ plane constellation in terms of the transverse Laplacian. The paraxial

equation allows us to consider the propagation of the vortices as an initial value problem. We can re-write equation (6.10), the velocity of a vortex in a paraxial beam as

$$\boldsymbol{V} = \mathrm{Im}\,\frac{\mathrm{i}}{2k}\frac{\left((\nabla_\perp^2\psi^*)\nabla_\perp\psi - ((\nabla_\perp^2\psi)\nabla_\perp\psi^*\right)^\perp}{(\nabla_\perp\psi^*\wedge\nabla_\perp\psi)}. \tag{6.29}$$

This is not the same as taking the z-derivative of the velocity; this substitution is only made after all necessary arithmetic is complete. This means that a non-paraxial acceleration expression is first arrived at with terms of the form $\partial_z^2\psi$ which does not become $\partial_z\frac{\mathrm{i}}{2k}\nabla_\perp^2\psi$. The second z-derivative is substituted with $\frac{-1}{4k^2}\nabla_\perp^2(\nabla_\perp^2\psi) = \frac{-1}{4k^2}(\partial_x^4 + 2\partial_x^2\partial_y^2 + \partial_y^4)\psi$, the transverse biharmonic operator. When evaluating the higher derivatives of $\boldsymbol{Q}$, for a ψ propagating under the paraxial equation, the higher z-derivatives required are substituted such that ∂_z^n becomes the Laplacian applied n times: $(\frac{\mathrm{i}}{2k})^n\nabla_\perp^2(\nabla_\perp^2(\ldots$

6.4 Paraxial Steering Examples

To illustrate this method we now give some examples of increasing complexity. The simplest example is a vortex constellation consisting of isotropic vortices, all of the same sign, embedded in a Gaussian beam. This is the first example of Indebetouw [Ind93].

Indebetouw shows that such an initial configuration propagates very simply. The vortex constellation is invariant except for the beam spread and a rotation of $\frac{\pi}{2}$ into the far-field. This constellation is factorisable in the $z = 0$ plane. This remains the case after applying the paraxial propagator to obtain the z-dependent form. The resulting function, up to a common Gaussian factor and non-zero z-dependent term, remains factorised upon propagation.

This concept is extended to complex analytic functions, not just polynomials by Abramochkin and Volostnikov [AV96], the so-called *spiral-type* beams. The zeroes of the analytic function are used to construct arbitary patterns in the intensity of the beam. The zeroes all being of the same sign propagate distinctly and the whole beam structure remains constant, up to rotation and scaling.

We compute the velocities and accelerations of the vortices in the field

$$\psi|_{z=0} = \mathrm{e}^{-(x^2+y^2)/w}(x+1+\mathrm{i}y)(x-1+\mathrm{i}y)(x+\mathrm{i}(y+1))(x+\mathrm{i}(y-1)), \tag{6.30}$$

which has four positive unit charge vortices located at $(\pm1, 0)$ and $(0, \pm1)$. We find that the velocities are all tangential to the unit circle pointing in an anticlockwise sense. The accelerations are all zero. This is shown in figure 6.1.

Although the accelerations work out to be zero in this case, this does match the exact forms of the vortex curves Indebetouw gives. Expanding the terms of

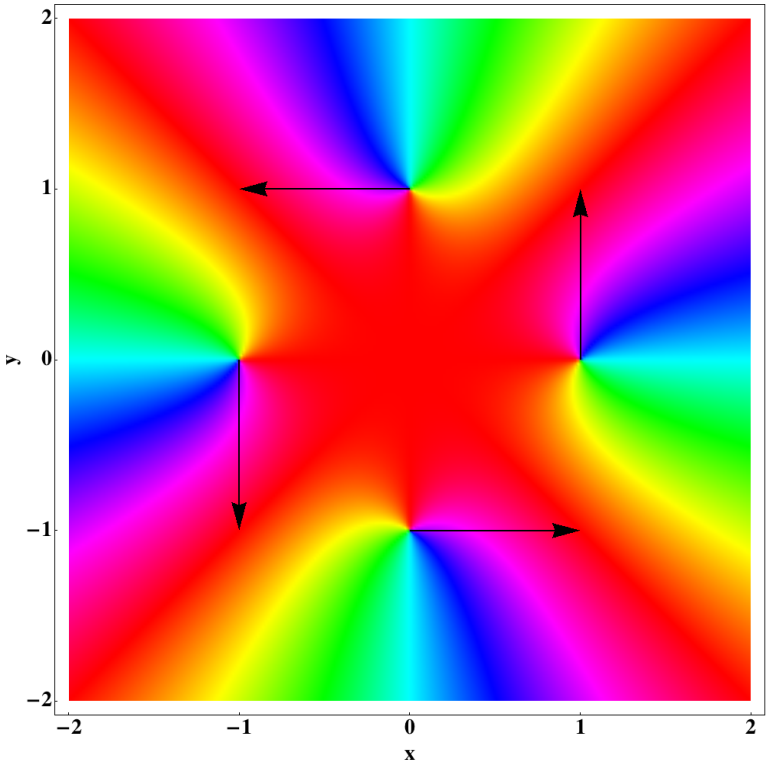

Figure 6.1: The phase of $z = 0$ of the function in equation (6.30). The velocity directions are shown with the black arrows. They can be seen to point anti-clockwise, as tangents to the circle passing though all four vortices.

Indebetow's solution [Ind93, eq. 27a,b] that contain zeroes, shows there are no second order or higher terms

$$Re^{i\phi} - R_i\sqrt{1+z^2}e^{i(\phi_i - \arctan z)} \approx Re^{i\phi} - R_i e^{i\phi_i} + (iR_i e^{i\phi_k})z, \qquad (6.31)$$

written in cylindrical coordinates where (R_i, ϕ_i) gives the vortex location. We have set the Rayleigh range [Sie86] to be unity in equation (6.31). The vortex trajectories are straight lines and indeed zero acceleration is a correct result. Despite the simple trajectories, they remain consistent with the work of Indebetouw. The vortex lines can be computed exactly in this case. This is one of only a few examples where the vortex curve can be explicitly calculated. Our next examples contain vortices of both signs and hence more complicated interactions occur between them.

Initial planes with vortices of opposite sign present give rise to a different set of vortex trajectories. Pairs of oppositely signed vortices can come together to annihilate each other. Along the full three-dimensional curve, this represents a point where the vortex curve tangent becomes perpendicular to the z propagation direction, at a hairpin or inflection point as in figure 1.4, page 8. A

Vortex	Velocity	Acceleration
$(-a, 0)$	$(0, \frac{2a}{w^2} - \frac{1}{a})$	$(\frac{1}{a^3}(1 - \frac{4a^2}{w^2}), 0)$
$(a, 0)$	$(0, \frac{2a}{w^2} - \frac{1}{a})$	$(-\frac{1}{a^3}(1 - \frac{4a^2}{w^2}), 0)$

Table 6.1: The values of velocity and acceleration for the vortex dipole, with vortices at initial positions $(\pm a, 0)$. The field is given by equation (6.32) where w is the waist width of the Gaussian at $z = 0$.

well-studied case is that of an initial constellation consisting of a single positive and a single negative vortex, a *vortex dipole*. Both Indebetouw [Ind93] and Roux [Rou04] have studied the vortex dipole and given conditions on whether, when embedded in a Gaussian beam, the pair will annihilate or not.

We place the zeroes, symmetrically on the x-axis and calculate the derivatives and compare to the known curves. The system is simple enough that the exact nodal curve can be computed and compared to our Taylor expansion. Consider a positive isotropic vortex at $x = +a$ and a negative isotropic vortex at $x = -a$. This is embedded in a Gaussian and gives, at $z = 0$,

$$\psi = \mathrm{e}^{-\frac{x^2+y^2}{w^2}}(x - a + \mathrm{i}y)(x + a - \mathrm{i}y). \tag{6.32}$$

This gives velocities and accelerations shown in table 6.1.

The vortices in the dipole have the same velocities in the y-direction and have accelerations with the same magnitude but opposite directions. The acceleration directions are particularly sensitive to the beam waist width w. At a critical value, $w > 2a$, the sign of the acceleration changes. This means that either the accelerations are pointing away from the beam centre, when the beam is narrow, or point towards the beam centre when the beam is wide. This can be extrapolated into the vortices either moving away from each other, or towards each other and annihilating.

The two cases of vortex behaviour matches the analysis of Indebetouw and Roux. Indebetouw also shows that $w = 2a$ is the transition between the two cases of vortex annihilation or not. Roux's work gives the same conclusions.

Optical vortices are not always desirable in a beam and need to be removed. This is the emphasis of Chen and Roux [CR08], studying the vortex dipole, the aim of their work is to reduce the propagation distance to dipole annihilation, whilst maintaining the background intensity as much as possible. We now examine if the vortex steering derivatives can be used to justify their observed "accelerated vortex dipole annihilation."

Our example is a vortex dipole in a Gaussian beam of width one. The vortices are located at $(\pm\frac{1}{2}, 0)$ in the $z = 0$ plane. This can be constructed as a superposition of Laguerre-gaussian modes and propagated. The Roux and Chen

	Vortex location	Velocity	Acceleration
Standard dipole	$(0.5, 0)$ $(-0.5, 0)$	$(0, 1.72)$ $(0, 1.71)$	$(-7.99, 0)$ $(7.99, 0)$
Accelerated dipole	$(0.5, 0)$ $(-0.5, 0)$	$(-2.43, -8.24)$ $(2.43, -8.24)$	$(-683.16, 451.42)$ $(683.16, 451.42)$

Table 6.2: A comparison between the steering values of a vortex dipole and its accelerated version using the scheme of [CR08].

Vortex location	Velocity	Acceleration
$(0.4559, 0)$	$(0, -0.5784)$	$(-1.2120, 0)$
$(2.1936, 0)$	$(0, 3.2581)$	$(-11.8481, 0)$
$(-0.2279, 0.3948)$	$(0.5009, 0.2892)$	$(0.6060, -1.0496)$
$(-1.0968, 1.8997)$	$(-2.8216, -1.6291)$	$(5.9240, -10.2607)$
$(-0.2279, -0.3948)$	$(-0.5009, 0.2892)$	$(0.6050, 1.0496)$
$(-1.0968, -1.8997)$	$(2.8216, -1.6291)$	$(5.9240, 10.2607)$

Table 6.3: The steering derivative values for the trefoil knot. The values for $\boldsymbol{V}$ and $\boldsymbol{A}$ are given for the six vortices in the $z = 0$ plane of the paraxial polynomial function.

method needs the background phase, $\exp(\mathrm{i}\Phi)$, at a small distance beyond the annihilation point in the unmodified beam. Translating this function to the center of the dipole, in this example the origin, the modified beam, ψ' is defined as

$$\psi' = \psi \mathrm{e}^{\mathrm{i}\Phi'}, \tag{6.33}$$

where Φ' is the translated background phase function. We find the velocity and acceleration of the vortices at $z = 0$ is substantially different as shown in table 6.2. This method of Chen and Roux is therefore detectable by our steering method and steering concludes the vortex propagation is very different to the un-accelerated vortex dipole of above.

Our final example is from our knot construction. The Hopf link is studied in the next section, so we look at the trefoil knot here. The values of the velocity and acceleration for the $(2, 3)$-form of the trefoil knot are shown in table 6.3. We use the paraxial polynomial of the trefoil, equation (3.25), to obtain the three-dimensional curve. Figure 6.2 shows the directions and a comparison between the steering Taylor expansion and the actual nodal curves.

The directions of the velocity and acceleration are consistent with how the vortices move in the transverse plane. The comparison of the approximation and real curves shows that for the outer three vortices the approximation is very good for a long distance. For the inner three vortices, the fit is not as good. It is possible that the main geometric features of the curve there are dominated by

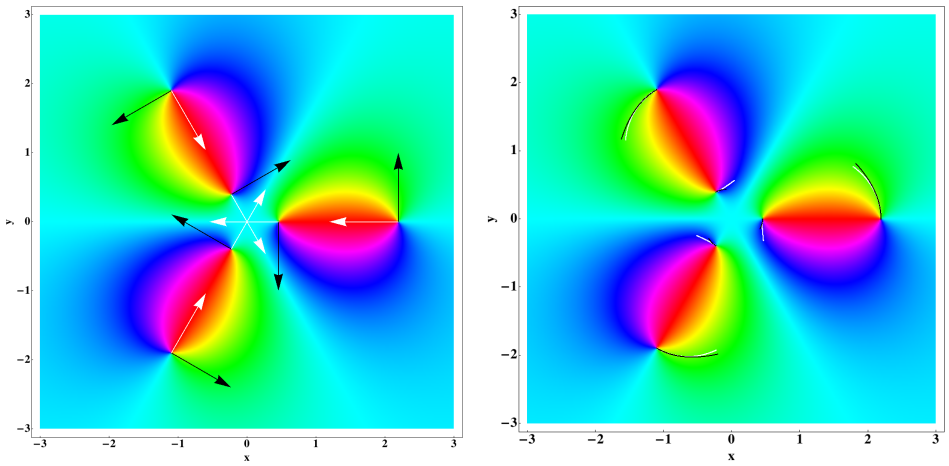

(a) (b)

Figure 6.2: Plots to show the steering of the trefoil knot. Both plots show the phase of the polynomial trefoil knot in the $z - 0$ plane. (a) The velocity and acceleration directions, the black and white arrows respectively, at each of the six vortices in the $z = 0$ plane. (b) The curves from both the Taylor expansion with the steering derivatives, black lines, and the actual curve shown in white. Both curves are the projection into the $z = 0$ plane.

effects due to higher order terms which we have not included in our Taylor expansion. This is a general issue for the two term Taylor expansion we construct. The next section examines how this manifests itself in the simpler curves of the Hopf link.

6.5 Steering of Vortex Topology

The vortex topology in paraxial beams has been seen in previous sections to be robust to perturbations to our constructed optical fields containing knotted nodal sets. These effects can come from parameters such as a in equation (4.5) or from an experimental optimisation algorithm, section 3.5. Here we study how the directions of velocity and acceleration describe, not only the curve geometry, but also their limitations when other events occur in propagation. These topology changing events can be explored in the superposition space of the Hopf link.

From the Lissajous construction the Hopf link has the form, equation (3.24), at $z = 0$,

$$\psi = (1 + A)R^4 - 2(1 + B)R^2 + (1 + C) - 4R^2 e^{2i\phi}, \tag{6.34}$$

where A, B, C are parameters in superposition space such that $A = B = C = 0$ gives the unperturbed function, the origin of superposition space. We choose

this three-dimensional space rather than introduce a fourth parameter multiplying the exponential term because this term does not contribute to the z-dependence acquired by paraxial propagation.

We enforce the $z = 0$ plane to have a similar vortex constellation to that of the $A = B = C = 0$ case, namely only four real zeroes existing on the $y = 0$ line symmetrically. The imaginary part of equation (6.34) is proportional to xy, hence the zeroes of ψ lie on $x = 0$ or $y = 0$. Equation (6.34) has a real part that can be split into two Cartesian expressions to solve for the nodal points at $y = 0$ and $x = 0$ respectively :

$$(1 + A)x^4 - 2(B + 3)x^2 + (1 + C) = 0, \tag{6.35}$$

$$(1 + A)y^4 - 2(B - 1)y^2 + (1 + C) = 0. \tag{6.36}$$

This means that we require four unique real solutions in x, and all solutions in y to have a non-zero imaginary part. This gives a set of complicated conditions on the valid (A, B, C)-space. Solving for x leads to a simple set of conditions, all three of which much be true :

$$(B + 3)^2 - (A + 1)(C + 1) > 0, \tag{6.37}$$

$$\frac{(B + 3) \pm \sqrt{(B + 3)^2 - (A + 1)(C + 1)}}{(A + 1)} > 0, \tag{6.38}$$

the first arising from $x^2 > 0$ and the second ensures that there are four solutions. Similar conditions are placed on the region of validity by solving for y, however these are a series of logical OR expressions, either one of which must be true:

$$(B - 1)^2 - (A + 1)(C + 1) \leq 0, \tag{6.39}$$

$$\frac{(B - 1) \pm \sqrt{(B - 1)^2 - (A + 1)(C + 1)}}{(A + 1)} < 0. \tag{6.40}$$

In this region, there are four vortices on the x-axis, at $z = 0$. We label these x_i where $i = 1, 2, 3, 4$, and the labelling is ordered such that $x_1 < x_2 < x_3 < x_4$. The symmetry requires that $x_1 = -x_4$ and $x_2 = -x_3$.

Despite this restriction, a rich structure exists topologically within this superposition space. The directions of velocity and acceleration are now compared within this region. The velocities and accelerations of the vortices in the Hopf link are given by

$$\boldsymbol{V} = \left(0, -\frac{1 + B - 2(1 + A)x^2}{2x}\right), \tag{6.41}$$

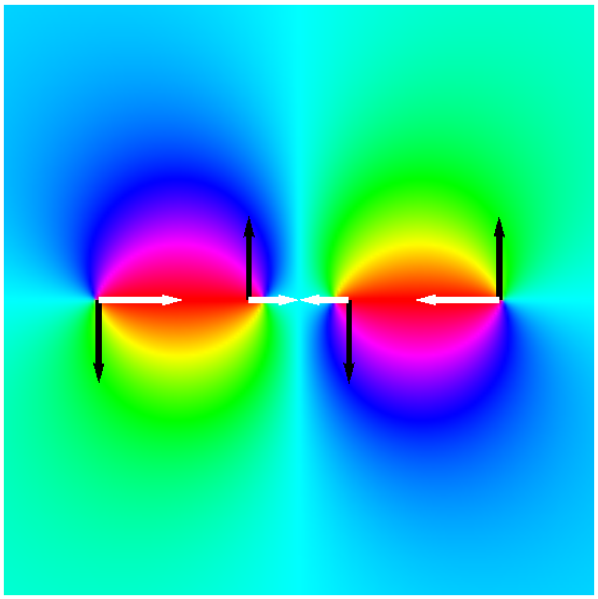

Figure 6.3: The phase of the $z = 0$ for ψ as in equation (6.34) with $A = B = C = 0$, with the vortices lying on the $y = 0$ line symmetric about the origin. The velocity directions are shown by the black arrows, pointing alternately in the $-y$ and the $+y$ directions. The acceleration directions are shown by the white arrows, parallel to the x-direction.

Velocity $\boldsymbol{V}$	$(0,-1)$	$(0,1)$	$(0,-1)$	$(0,1)$
Acceleration $\boldsymbol{A}$	$(-1,0)$	$(-1,0)$	$(1,0)$	$(1,0)$
x position (ordered)	x_1	x_2	x_3	x_4

Table 6.4: The values of velocity and acceleration have directions as in this table for the case $A = B = C = 0$, as shown in figure 6.3. The x-positions are orders such that $x_i < x_{i+1}$.

and

$$\boldsymbol{A} = \left(\frac{(B^2-1)^2 - (1+A)(-19+B(2+5B))x^2 + 8B(1+A)^2x^4 - 4(1+A)^3x^6}{4x^3\left(-3-B+(1+A)x^2\right)}, 0 \right), \tag{6.42}$$

where $x = x_i$ for $i = 1, 2, 3, 4$.

The velocity and acceleration directions are shown in figure 6.3 for the origin of superposition space. These directions are those that we compare to those explicitly shown in table 6.4. Within this region of matching steering directions, a number of topological and geometric features can be acquired by the nodal curves. The number of zeroes in a transverse plane at a given z value can be used

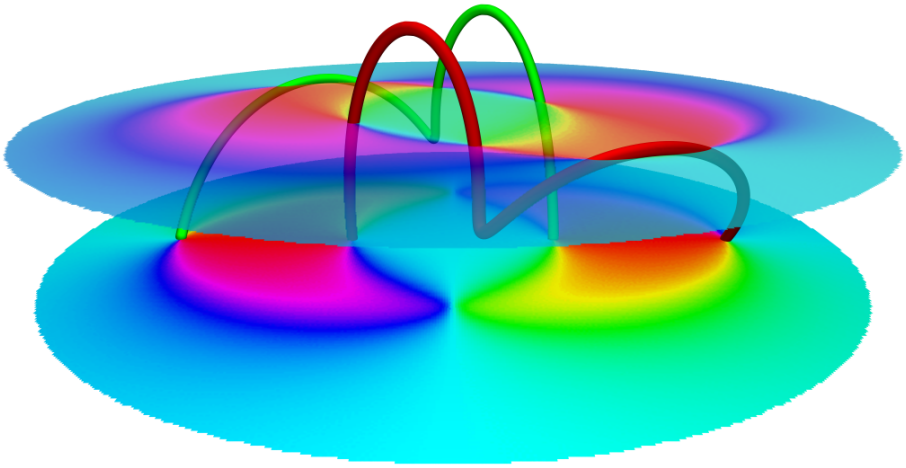

Figure 6.4: Two vortex curves exhibiting complex geometry. The lower plane is $z = 0$ and contains four vortices similar to the superposition space origin. In propagation, two pairs of vortices nucleate and reconnect with the vortices from the $z = 0$ plane. This nucleation occurs just before the upper plane, which shows eight zeroes, four for each of the two components. This gives the curve two additional turning points above $z = 0$ (as well as below). These curves are from $A = 2$, $B = 8$, $C = 16$ in equation (6.34).

to identify the specific features of the full three-dimensional curves. A Hopf link formed at the origin of superposition space contains four zeroes in every z-plane, except at the values of z where the vortices nucleate, corresponding to the tangent of the three-dimensional curve lying in the plane perpendicular to the z-direction. Vortex nucleation and annihilation, in two dimensions, is characterised by $w = \nabla_\perp \xi \wedge \nabla_\perp \eta = 0$ at the point of creation / death where the wedge product is as defined in equation (6.2).

Away from the origin in superposition space, the nodal curve's topology can remain fixed, as a Hopf link, but for a given range of z, the number of zeroes is greater than four. This means that additional vortices have nucleated in a plane $z > 0$. These cases we refer to as having *complex geometry* but they still form an isolated Hopf link. We illustrate such a case in figure 6.4. At the nucleation points in two dimensions, just turning points of the three-dimensional curve, a new Taylor series could be constructed from derivatives recalculated at these points. In cases where there are more than four vortices in the plane, this could

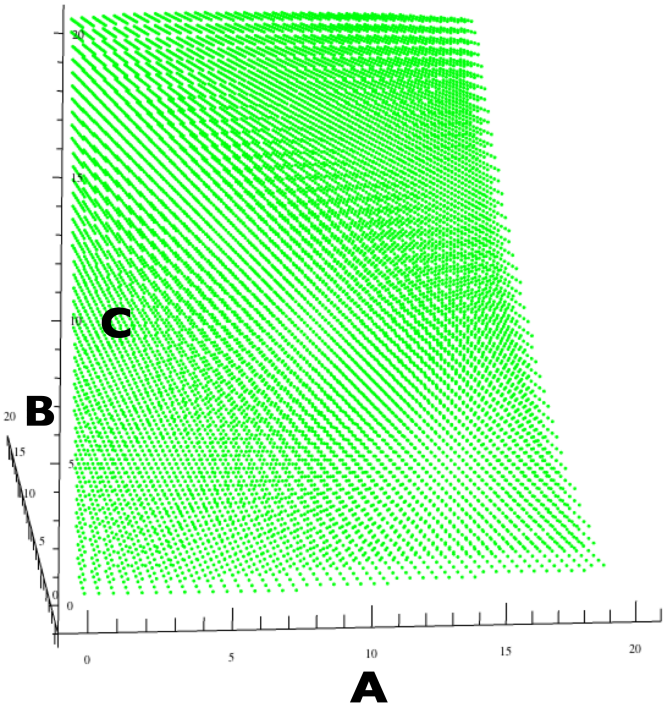

Figure 6.5: The permitted region of (A, B, C)-space, defined by equations (6.35) and (6.36) allowing four vortices to occur on the x-axis. Within this region, equation (6.34) has, at $z = 0$, only four vortices exist and they lie on the x-axis.

also mean that the linked vortex topology has been destroyed, in which case the linked topology becomes unisolated, intersected by other vortex lines or an unknown topology.

We now numerically investigate (A, B, C)-space (superposition space) to examine if the steering directions can predict the breakdown of simple geometry, or a change of topology. It is the restricted subset of superposition space that matches the vortex constellation with four vortices symmetrically on the x-axis, as in the case of figure 6.3. We shall refer to this as the *permitted region* of superposition space. Matching the conditions of equations (6.37)-(6.40), this allows for the permitted region to be plotted in figure 6.5. To numerically investigate this space, we work in the region $0 \leq a, b, c \leq 20$ and increase in steps of $\frac{1}{2}$. This gives rise in the permitted region, to 13269 points to consider.

The first check with the permitted region is to test the directions of the steering velocity and acceleration. These are tested and compared to the values in table 6.4. We desire to determine if, when in the permitted region, the steering directions are a good indicator of whether the Hopf link forms or not. Figure 6.6 shows the cases of the steering directions matching the desired values and re-

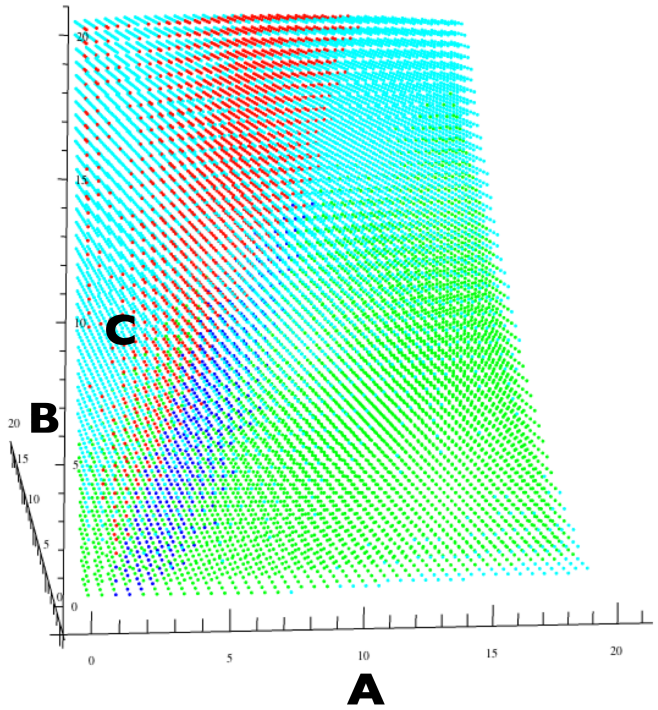

Figure 6.6: Within the permitted region, the directions of velocity and acceleration of the vortices at $z = 0$ are compared to the correct case. The colouring is: green is both velocity and acceleration are in the correct direction, blue is just velocity correct, cyan is just acceleration correct and red is where both vectors point in the wrong direction.

ferred to herein as the *correct values*.

Where the steering derivatives are in the correct directions, we can examine the topology of the nodal curves formed on propagation. A three-dimensional vortex tracking, appendix A, can be used to aid the determining of the topology, however this is expensive computationally. The polynomial nature of the equation (6.34) means that numerical integrals on this function are fast to compute. We also employ a numerical algorithm to determine the number of zeroes in a given (x, y)-plane to determine the geometry type - simple or complex.

To determine if the vortex loops are linked, we calculate the integrated phase change around a closed contour :

$$I = \oint_C \partial\chi \mathrm{d}\chi, \tag{6.43}$$

where C is the closed contour. This contour must pass through the inside of both vortex loops. This has the value of $2\pi Lk$, where Lk is the linking number of the contour with the vortex curves. This contour needs to be chosen such that it

does not intersect any of the vortex lines.

The obvious contour consists of an infinite line on the z-axis closed with a semi-circular path. The phase is defined as $\chi = \arg(\operatorname{Im}\psi / \operatorname{Re}\psi)$. This choice of contour has a singularity in the semi-circular part of the curve. The contour we choose is a rectangular curve, chosen such that equation (6.43) becomes

$$\begin{aligned} I &= \int_{-z_{max}}^{z_{max}} \left.\frac{\partial\chi}{\partial z}\right|_{\substack{x=0\\y=0}} \mathrm{d}z + \int_{0}^{100} \left.\frac{\partial\chi}{\partial x}\right|_{\substack{y=0\\z=z_{max}}} \mathrm{d}x \\ &\quad + \int_{z_{max}}^{-z_{max}} \left.\frac{\partial\chi}{\partial z}\right|_{\substack{x=100\\y=0}} \mathrm{d}z + \int_{100}^{0} \left.\frac{\partial\chi}{\partial x}\right|_{\substack{y=0\\z=-z_{max}}} \mathrm{d}x. \end{aligned} \tag{6.44}$$

When $\frac{I}{2\pi} = \pm 2$, then the contour is linked with both loops. We are assuming there are no large sections of the vortex loops that look locally like that of a crossing that can be removed by a Reidemeister move type one, see figure 2.2. This set of integrals is also evaluated exchanging x with y to provide a check that the value is well-behaved.

The value z_{max} needs to be chosen carefully. A vortex topology that is supported by our paraxial Hopf link function, is two unlinked loops, that pass though the $z = 0$ plane at the four points on the x-axis, but with an additional pair of loops that are approximately planar (transversely), beyond (and below) the hairpins of the aforementioned loops. This topology is illustrated in figure 6.7. The method of vortex steering does not directly have information of these planar loops and hence we do not check to see if the global topology is two unlinked loops or a set of four unlinked loops. What is important is to ensure the contour chosen in equation (6.44) does not pass through these loops or intersect with them.

We count the number of zeroes in a given (x, y)-plane. Normally, this is four. If the number is greater than four, then this represents complex geometry due to additional nucleation events occurring. This can also represent additional vortex components being formed, although this has not been observed with the range of parameters this investigation is taken over. We step though z in steps of $\frac{1}{500}$. Once a z-plane with no zeroes in is found, we step forward a further three planes checking these also contain no zeroes. This third plane above the vortex loops, which by symmetry have the same extent in $-z$, is taken as the value z_{max}. If additional components are in this "neutral zone" then the process will fail. Within the permitted region, and with our discretisation of it, no such cases were observed, which would manifest in the contour integral returning an unexpected value.

Despite the several steps and logic required, this method presents a improvement in computation time compared to a full three-dimensional vortex

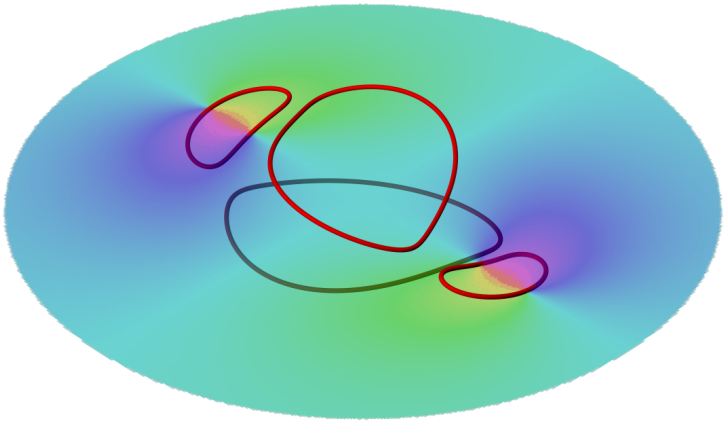

Figure 6.7: Four unlinked loops. The two loops passing through the $z = 0$ plane, the opaque disk coloured by phase, are unlinked. Two additional loops, at higher and lower values of z exist. It is these additional loops that the steering directions do not give any information about and must be avoided by the contour used in the integration to detect linked vortex loops.

line tracking, such as what we describe in appendix A. At no point in this method do we need to know which zero points belong to a particular component of the link. This may not be the case for more complicated knots and links undergoing a similar analysis, or when considering Gaussian beam superpositions. Outside of the permitted region, this analysis of simple vs complex geometry and linked vs unlinked can be carried out, but with additional vortices in the $z = 0$ plane means the number of topologies that exist increases. An example is a pair of rings that intersect each other.

We now present the results of this investigation in the range specified. The data we compare is whether linked vortex loops are formed on propagation for given (A, B, C) in the permitted region, and the geometry type, simple or complex. It turns out that within our data set, no unlinked vortex loops exhibiting complex geometry were observed, although for the small subset further tested, the vortex topology was the four loops as in figure 6.7. Table 6.5 gives the observed values for these phenomenon, separated by whether the steering derivative directions match the correct values.

Within our data set the majority of the points, 64.6%, do not have the correct steering directions. Yet within these cases, there are still a large number of

	$\boldsymbol{V}$ and $\boldsymbol{A}$ correct	$\boldsymbol{V}$ and $\boldsymbol{A}$ incorrect
Linked (Simple)	3090	4553
Linked (Complex)	1323	1518
Unlinked	290	2495
Total	4703	8566

Table 6.5: The results of the topology and geometry tests within the permitted region of (A, B, C)-space, sorted by whether the vortices satisfy the correct steering direction in the $z = 0$ plane. Figures 6.8 and 6.9 illustrate these results.

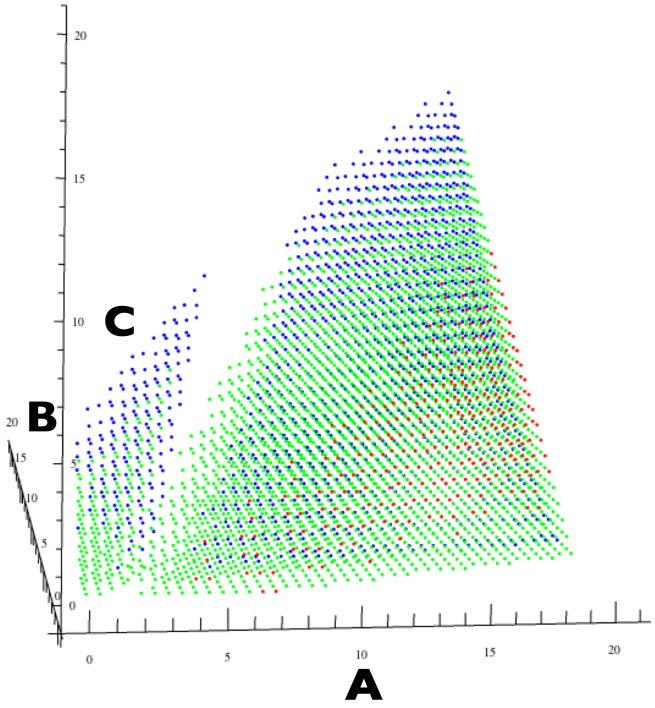

Figure 6.8: The points in the permitted region that do satisfy the correct steering directions, coloured by topology and geometry type. The green points are simple links, blue points correspond to complex links and the red points are the unlinked loops.

simply linked cases. From figure 6.6, the cases of the steering directions being correct tend to be below a critical strip, the red region. There is a transitional zone of where only one of the velocity or accelerations are incorrect.

The results do not show a clear majority of simple links only occurring with the correct steering directions, only 23.3% of our data set. This does show that the topology the vortices form depends on more than the velocity and acceleration directions. When the steering directions are correct, 94% of these cases are

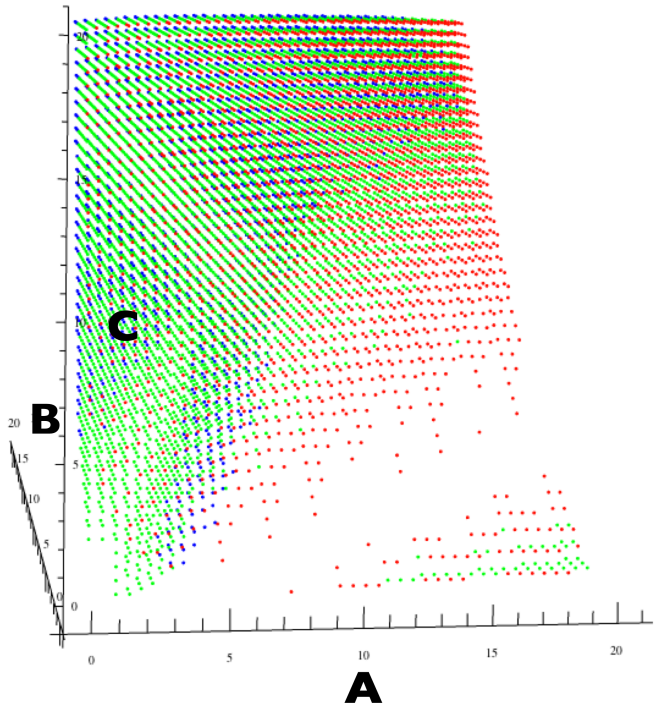

Figure 6.9: The points in the permitted region that do not satisfy the correct steering directions, coloured by topology and geometry type. The green points are simple links, blue points correspond to complex links and the red points are the unlinked loops.

linked. This is a success for the steering method. Of the cases where the steering directions are incorrect, 46% of the results are not simple links. This result shows that additional vortices created away from the $z = 0$ plane can have a strong influence on the three-dimensional vortex curves propagating from the $z = 0$ plane.

Outside the permitted region we have studied, other topologies are possible. This is a similar situation to the Laguerre-gaussian superposition of the Hopf link, with the beam width as a parameter, section 3.4. Although that function is more complicated than we studied here, it showed how unexpected topological events, such as loop nucleation, can occur as intermediate steps between two distinct topologies. Due to the possibility of further creation points on propagation, using a change in steering directions as measure of topology is not a good method. The geometric changes that the vortex curves undergo, from simple to complex, also provide a challenge to this measure. However, when a three-dimensional curve $\boldsymbol{Q}$ is constructed with just $\boldsymbol{V}$ and $\boldsymbol{A}$, a difference in z values

for the actual and predicted annihilation event can occur, with even the (x, y)-locations being different. These differences are an indicator of additional vortex creations.

6.6 Steering of the Cinquefoil Knot

We have mentioned several times, the curiosity of the $(5, 2)$-form of the cinquefoil knot and how, under standard homogenisation, it fails to transfer to a paraxial function. Yet for over-homogenisation, and under the Helmholtz equation, the correct knot does form. To finish our discussion of vortex steering, we look at if the steering method can explain this phenomena in the paraxial equation.

The various homogenisations of the cinquefoil knot are

$$q_0 = u^5 - v^2w^3 \tag{6.45}$$

$$q_1 = wu^5 - v^2w^4 \tag{6.46}$$

$$q_2 = w^2u^5 - v^2w^5, \tag{6.47}$$

also given in chapter 4, and we label the paraxial functions ψ_s where $s = 0, 1, 2$ is the level of homogenisation. These all have four zeroes at $z = 0$ at the same locations, additional factors of $1 + R^2 + z^2$ do not introduce any additional zeroes. The locations are given, to three decimal places, as part of table 6.6. We now compare the values of velocity and acceleration for the three levels of homogenisation.

The velocities and accelerations are in the same direction for all three functions. These are given in table 6.6 and shown in figure 6.10. The magnitudes of both $\boldsymbol{V}$ and $\boldsymbol{A}$ increase with additional homogenisation.

From the calculated steering derivatives, we can construct the Taylor series for each s and compare it to the actual nodal curve of the Milnor polynomials. These are plotted in figure 6.11. It is apparent that there is not a big difference between the three curves. The actual curve, shown as the dotted curve, is close to all three constructed curves initially but diverges quickly as z increases. However, the differences are even smaller for the outer vortices that start on the x-axis.

The curve for the $s = 2$ paraxial function does ultimately have the smallest radius of curvature, which is what the actual real curve possesses. Due to these small differences, we reserve making a quantitative statement regarding over-homogenisation and steering. There is however a definite qualitative observation that can be made. Projected into a transverse plane, the required curve to form the $(5, 2)$-form of the cinquefoil knot is tight and must wind around the origin completely. This compares to the similar, geometrically, $(3, 2)$-form of

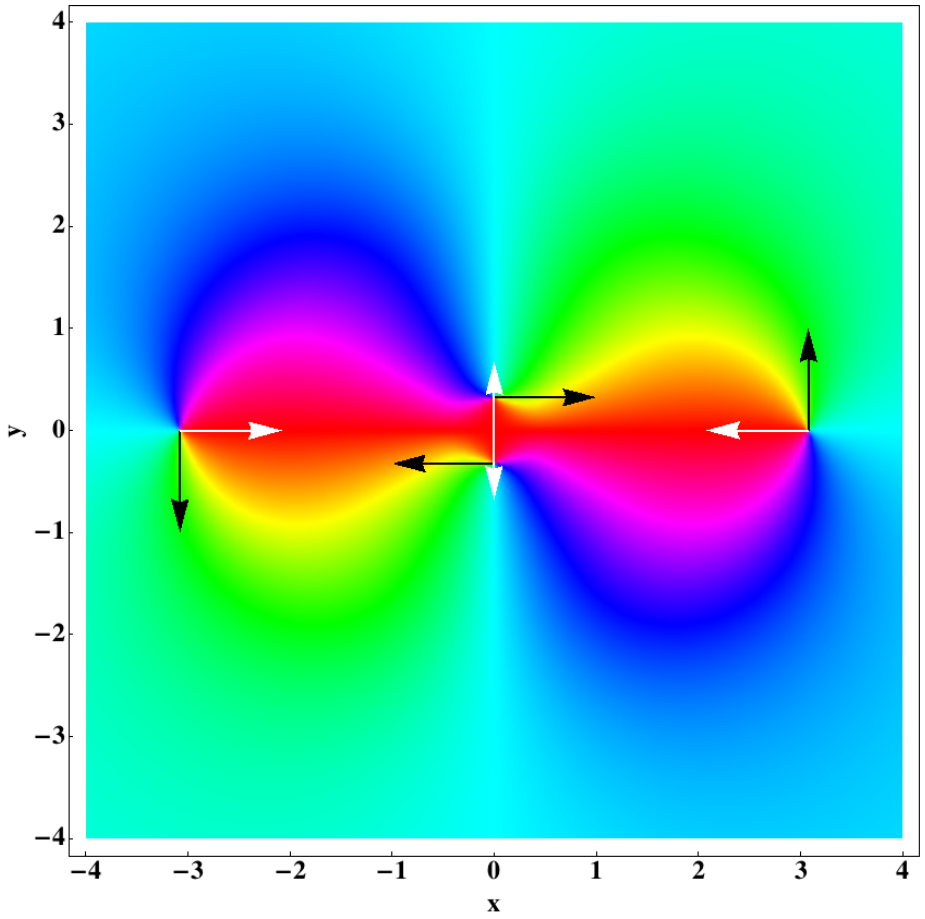

Figure 6.10: The phase of the $z = 0$ plane of the $(5,2)$-form of the cinquefoil knot, shown with the directions of the velocities (black arrows) and accelerations (white arrows). The directions are the same for the homogenisation levels $s = 0, 1, 2$.

Vortex location	$(3.075, 0)$	$(-3.075, 0)$	$(0, 0.325)$	$(0, -0.325)$
$s = 0 : \boldsymbol{V}$	$(0, 5.709)$	$(0, -5.709)$	$(3.774, 0)$	$(-3.774, 0)$
$\boldsymbol{A}$	$(-21.119, 0)$	$(21.119, 0)$	$(0, -50.812)$	$(0, 50.812)$
$s = 1 : \boldsymbol{V}$	$(0, 6.813)$	$(0, -6.813)$	$(4.878, 0)$	$(-4.878, 0)$
$\boldsymbol{A}$	$(-30.197, 0)$	$(30.197, 0)$	$(0, -80.262)$	$(0, 80.262)$
$s = 2 : \boldsymbol{V}$	$(0, 7.918)$	$(0, -7.918)$	$(5.983, 0)$	$(-5.983, 0)$
$\boldsymbol{A}$	$(-40.878, 0)$	$(40.878, 0)$	$(0, -133.817)$	$(0, 133.817)$

Table 6.6: A comparison between the velocities $\boldsymbol{V}$ and accelerations $\boldsymbol{A}$ for the four vortices in the $z = 0$ plane of the $(5,2)$-form of the cinquefoil knot, shown for three levels of homogenisation $s = 0, 1, 2$.

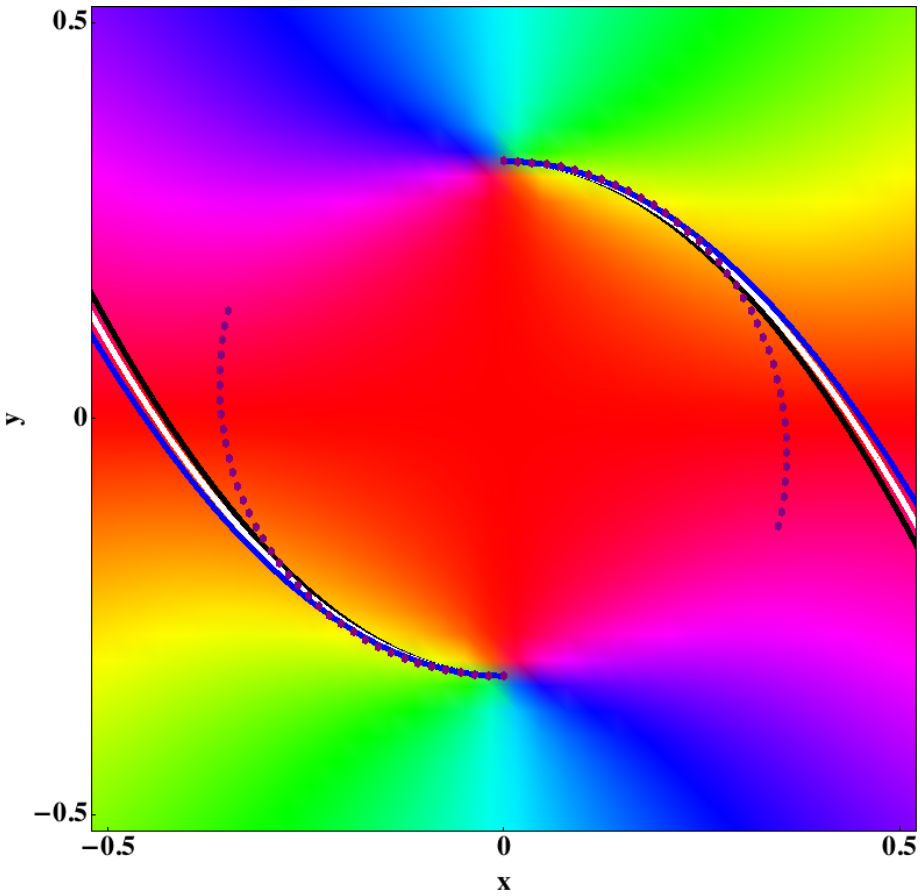

Figure 6.11: A comparison between the steering predictions for various levels of homogenisation to that of the actual standard homogenised nodal curve. The plot is a zoom in around the two zeroes that occur on the y-axis. The curves from the steering Taylor expansion for $s = 0, 1, 2$ are given in blue, white and black respectively. The dotted curve is the actual nodal curve of the standard homogenised curve under paraxial propagation.

the trefoil knot requiring only a half turn. A zero following a tighter curve has the potential to make these extra winds before interacting with the appropriate outer zero, which takes a much shallower curve. The higher levels of homogenisations produce nodal curves with these tighter curving inner vortices given by the steering derivatives. Analysis of these curves with higher derivatives may provide more insight into why the standard homogenisation does not paraxially form the expected knot.

Creating a steering-method based Taylor expansion with more terms is expected to provide more insight into the behaviour of the vortex lines in paraxial functions. The inclusion of the jerk, and higher derivatives, should allow for the effects of additionally created vortices away from the $z = 0$ plane to be taken

into account. We have found that usable forms of these higher derivatives have been difficult to construct and verify.

6.7 Discussion

The main results of this chapter are

- We have constructed a method for describing the three-dimensional optical vortex curve based on the derivatives evaluated at the vortex points in the $z = 0$ plane. This works for paraxially propagating fields because the propagation is an initial value problem from the $z = 0$ plane. This method has been shown to be consistent with known cases of vortex propagation (section 6.4).

- We have used steering to understand if it can be used to detect whether a vortex constellation known to propagate to a Hopf link still forms this topology when parameters are varied in the $z = 0$ plane. For the cases where the directions of velocity and acceleration are as in the prescribed case, 96% of the values tested did form a Hopf link. This is a successful application of vortex steering.

- We applied the steering method to the cinquefoil knot to determine how the level of homogenisation (section 4.6) affects the vortex topology. However, the curves formed by the Taylor expansion for the three levels investigated did not vary by a quantitative amount. We conclude that steering does not help us understand why paraxial polynomial functions need the homogenisation level varied to successfully contain certain knots as their nodal set, when constructed from the corresponding Milnor polynomial.

Throughout this thesis we have constructed functions, that satisfy the paraxial equation, with knotted vortex topology. Despite the correct topology being present in the nodal set of the Milnor polynomial, not every case initially succeeds when the equivalent paraxial function is constructed. Yet additional parameters, such as the homogenisation level, or moving to the Helmholtz equation, make the construction work. Furthermore, in cases when the desired knot is formed paraxially, it is not clear why as an initial value problem the $z = 0$ plane holds all the required information to give a working z-dependence.

We are not in a position to prove whether a specific case will succeed paraxially, or ultimately what nodal knots can exist, isolated, as nodal sets of solutions of the paraxial equation. Vortex steering is a method that justifies that it is reasonable to expect a given vortex constellation to propagate into the curve we

desire. The steering derivatives give the same results and predictions as several known vortex propagation works, see section 6.4. Also we used the trefoil knot as an example of how the predicted curves match closely, initially, the actual curves formed.

Steering has its limitations. These have been shown in section 6.5. When a vortex under paraxial propagation has a hairpin bend or inflection point in the cases of complex geometry, the steering derivatives fail to pick this up. This is due to, in the $(2+1)$-dimensional dynamical picture, additional vortices being created and annihilated. In these cases, it is possible that the desired vortex knot or link is formed, but in a more complicated fashion than anticipated.

The case of all the vortices in $z = 0$ plane of Indebetouw [Ind93] appears to be the only case of a function we have studied being factorisable in the $z = 0$ plane and remaining factorisable on propagation. Furthermore, the zeroes of each factor correspond to the individual zero lines that remain distinct on propagation. We have an observation of how the polynomial function at $z = 0$ of the Hopf link, equation (6.34), factors (when $A = B = C = 0$ corresponding also to both the Milnor and paraxial polynomials). If the quartic equation (6.34) factorises into two irreducible quadratics, A and B, with zeroes A_1, A_2 and B_1 and B_2 respectively, then on paraxial propagation, the locus of A_1 will annihilate with that of A_2, similarly for B_1 and B_2. The zeroes of each factor appear to only annihilate with a zero from the same irreducible factor. In the cases of this chapter where the vortex topology is the four unlinked loops, the function does not factorise at $z = 0$, remaining an irreducible quartic expression. This is not inconsistent with the quadratic factors observation.

The zeroes of sets of polynomials are varieties. In our work, this is a set of two polynomials: one for the real part and one for the imaginary part. Understanding the geometry, and how varieties transform when the governing polynomial's coefficients are varied, is a part of the subject of algebraic geometry [Has07]. Framing our questions in the language of algebraic geometry, on factors (above) or with a parameter such as Gaussian width (section 3.4), could prove enlightening.

We have only used the velocity and acceleration in our analysis of steering. The higher derivatives are, in general, extremely difficult to compute paraxially. With access to these higher derivatives, a more accurate curve $\boldsymbol{Q}(z)$ can be constructed. This would provide more insight into the case of the $(5,2)$-form of the cinquefoil, section 6.6. It is surprising that there is not a more profound difference between the steering curves for the levels of homogenisation studied. We would anticipate that including the jerk, at least, into this calculation would begin to differentiate between the three cases.

Our final set of questions, based on this chapter are:

- Would a similar analysis as we performed for the Hopf link (section 6.5) carried out on other knots or links, yield similar results? We have not explored fully the superposition space of other knots. More complicated knots require a higher dimensional superposition space, the trefoil four-dimensional, which means it is more difficult to study.

- Does the Taylor series we construct have a finite radius of convergence? Such a radius would coincide with an annihilation event/hairpin or inflection point on the curve. This distance could be used to predict the propagation distance to these events on the curve.

- Can the Taylor series we construct for the vortex curves be used to prove why we can construct our knots in functions satisfying the paraxial equation? The nodal lines in Milnor polynomial have prescribed directions in the $z = 0$ plane. We have seen at least with the Hopf link, that when the directions match in both the Milnor and paraxial cases, then this is a good indicator that the link will form. We have the counter-example of the $(5, 2)$-form of the cinquefoil knot. The inclusion of the higher derivatives beyond acceleration might lead to an answer to this question.

Tracking Three Dimensional Nodal Lines

In this thesis, we have presented three-dimensional figures representing the nodal lines we have studied. Several of the methods and calculations performed require us to know, at least point-wise, a set of three-dimensional positions on the line. Here we describe the method used to determine the three-dimensional nodal line locations.

A.1 Locating Nodal Points in 2D

We begin by describing the technique used to find the points at which a planar complex scalar function is zero and extend this to three dimensions in the next section.

A complex function is zero when both the real part and imaginary are zero. This occurs in two dimensions at the intersection of the contours $\mathrm{Re}\, f = 0$ and $\mathrm{Im}\, f = 0$. Either side of such a contour the real (respectively imaginary) part of the value of the function has opposite sign. It is this fact of the intermediate value theorem that we use to locate the zeroes' locations.

A choice is required as to where to sample the continuous function to use the above facts. The continuous function is sampled on a square lattice, with side length $\mathrm{d}x$, with an additional point at the centre. This splits the square into four triangles, each of which have an edge on square's edge and a vertex at the square's centre. We shall test to determine if a zero is present in one of these four triangles. Between each pair of adjacent vertices of a triangle. the sign of the real and imaginary parts of the function at those points is tested to determine if there is a change. If both the real part and imaginary part change sign on one, not necessary the same, edge then the triangle may contain a zero of the function.

This information cannot alone determine if both contours intersect creating

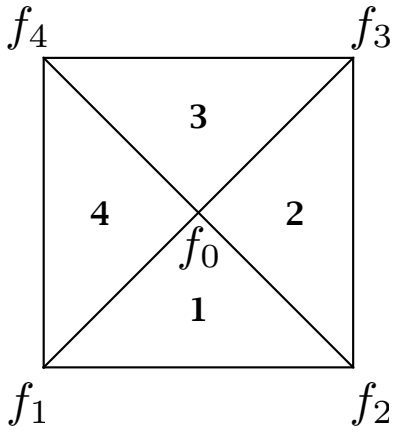

Figure A.1: The square lattice we sample the data on is split into four triangles. The centre point is labelled f_0 and is the average value of the four corner values.

a zero. We use the value of the function at the vertices of the triangle to create an affine transformation,

$$A\boldsymbol{w} + \boldsymbol{t} = \boldsymbol{z}, \tag{A.1}$$

to an arbitrary triangle in the complex plane, where A is a 2×2 matrix, and the vector components are the real and imaginary parts of the point in the respective Argand planes. The actual function values lie in the z-plane and the triangle formed from the affine map lies in the w-plane. This affine mapping allows us to numerically approximate the position of a zero point as well as determining if a zero is present inside the z-plane triangle.

We test whether the pre-image of zero under this map is contained in the equivalent triangle in the w-plane. The matrix A and vector $\boldsymbol{t}$ can be determined uniquely by choosing an appropriate triangle in the w-plane. The choice we make is to position the vertices at 0, 1 and i. The z-plane vertices are the square centre point, f_0, and the two corresponding vertices on the edge, f_1 and f_2 and write

$$\boldsymbol{f}_i = \begin{pmatrix} \operatorname{Re} f_i \\ \operatorname{Im} f_i \end{pmatrix}. \tag{A.2}$$

We set

$$A\mathbf{o} + \boldsymbol{t} = \boldsymbol{f}_0, \tag{A.3}$$

giving $\boldsymbol{t} = \boldsymbol{f}_0$. The elements a_{11} and a_{21} become the real and imaginary parts of f_1 respectively and a_{12} and a_{22} similarly from f_2.

The pre-image of zero is therefore

$$\boldsymbol{w}_0 = -A^{-1}\boldsymbol{f}_0. \tag{A.4}$$

The final check is to determine if $\boldsymbol{w}_0$ lies inside the triangle $(0, 1, \mathrm{i})$. The location is tested to see if it is present in the upper half plane, the right half plane and

finally tested with $\operatorname{Re} \boldsymbol{w}_0 + \operatorname{Im} \boldsymbol{w}_0 < 0$. This ordering and method allows an algorithm to exit at two stages to save computing time. A $\boldsymbol{w}_0$ failing any of these conditions is rejected and no nodal point exists inside the z-plane triangle. Matrices A with $\det A = 0$ are tested for and the triangle is rejected if this occurs.

For triangles successfully determined to contain a nodal point, the location $\boldsymbol{z}_0$ within the original test square is required. The position within the z-plane square is located by a combination of scaling, rotating and translating the position $\boldsymbol{w}_0$. The hypotenuse of the triangle in the w plane is of length $\sqrt{2}$ and needs scaling to the length $\mathrm{d}x$ of the square edge length. The w-plane is rotated by $\pi/4$ then the appropriate factor of $\pi/2$ to orientate the triangle correctly, followed by a final translation of $(\mathrm{d}x/2, \mathrm{d}x/2) + \boldsymbol{f}_1$. The origin of the w-plane is mapped to the centre of the square, $\boldsymbol{f}_0$. The value $\boldsymbol{z}_0$ is used as the approximation of the location of the zero in the square.

This method of testing if a zero lies inside a square is chosen over the following discretation of the contour integral,

$$\arg f_1 f_2^* + \arg f_2 f_3^* + \arg f_3 f_4^* + \arg f_4 f_1^* \tag{A.5}$$

which takes the value 2π when a zero (of multiplicity one) is contained inside the square. Although this can be be generalised to test round triangles, computationally this method is expensive in time.

A.2 3D Extension

The three-dimensional nodal lines are tracked by considering a cubic lattice for the function to be sampled on. Additionally, the face centre points are also calculated when required. Each face of the cube is tested for a zero passing through it as if it were a two-dimensional plane using the above method. To avoid double counting, only three faces of each cube need to checked. These are the faces that share a common vertex nearest to the origin (assuming a translation so that the origin of the sampled volume lies in such a fashion). For a line to pass through a cube, the overall charge on the six faces must be neutral.

The topological charge of the zero determines the direction the nodal line is passes through the face: a positive zero gives the line entering the cube; a negative zero represents a line leaving the cube.

We join each line segment by following the line into a cube though a positive zero. In order to form the whole line, we consider two types of curve, those that start on a face of the volume, boundary lines, and the closed loops contained within the volume. The lattice locations in $\mathbb{Z}^3$ are used to form the first of two lists that represent each line. From this integer list, a second list is created retro-

spectively with the $\mathbb{R}^3$ locations of the entry points into the cube. Each exit point corresponds to an entry point in another cube hence only one vector is required to be returned for each cube along the line.

The coordinates of the lines are stored in two ways. The first is the lattice location in $\mathbb{Z}^3$. For many calculations, such as determining the topology, some scaling properties, this is sufficient. The second list contains the positions in $\mathbb{R}^3$ and can be used for fine three-dimensional drawing and calculating fractal properties.

In both the two- and three-dimensional cases, it is possible that more than one vortex line passes through the square face, and there is even the possibility that a vortex loop is entirely contained with a sample cube. Obviously the sample size can be increased to try and locate such features but at the expense of computation time and increased amount of output data. When two lines pass through a cube, the cube can be further split into tetrahedrons with a common point at the cube centre. Both lines can then be traced through the additional triangular faces.

Tables of Knots and Links Constructed

B

These tables show the knots that the Lissajous construction creates for values of β up to five. The tables have as rows the number of strands in the basic braid word and columns representing the number of repeats. The format for each cell of the tables is :

Rolfsen / Hoste Notation Common Name Conway Notation

The Conway notation is given for the knots and links when $n = 2$.
The following tables are given :

- Table B.1 $\beta = 1$
- Table B.2 $\beta = 2$ and B.3 for the $n = 2$ row.
- Table B.4 $\beta = 3$
- Table B.5 $\beta = 4$
- Table B.6 $\beta = 5$

We give some notes on two unidentified links in table B.6 here. The link formed by $\beta = 5, n = 2$, strands= 6, has braid word $(135\bar{2}\bar{4})^2$ which computing the Jones polynomial using [BNM10], we get

$$V(q) = -q^{\frac{7}{2}}(1 - 3q + 6q^2 - 9q^3 + 11q^4 - 12q^5 + 11q^6 - 8q^7 + 6q^8 - 2q^9 + q^{10}), \tag{B.1}$$

which is up to factors of q, is the Jones polynomial given by [BNM10] for $L10a87$. Other invariants do not match which may be due to choices of orientation.

The second unidentified value is for $\beta = 5, n = 2$, strands= 8, which has braid word $(1\bar{3}\bar{5}7\bar{2}4\bar{6})^2$. This is a two component link and should have a minimum crossing number of twelve but the unavailability of data for such links and no Conway notation being found means we cannot confirm the minimum crossing number.

	$n = 2$	3	4	5
Strands =2	$L2a1$ Hopf [2]	3_1 Trefoil [3]	$L4a1$ 2 Twist Link [4]	5_1 Cinquefoil [5]
3	3_1 Trefoil [3]	$T_{3,3}$ Link	$T_{3,4}$ 8_{19}	$T_{3,5}$ 10_{124}
4	$T_{2,4}$ 2 Twist Link [4]	$T_{3,4}$ 8_{19}	$T_{4,4}$ Link	$T_{4,5}$
5	5_1 Cinquefoil [5]	$T_{3,5}$ 10_{124}	$T_{4,5}$	$T_{5,5}$ Link

Table B.1: The torus knots or 1-lemniscate knots and links.

	$n = 2$
Strands =3	4_1 Figure-8 [2 2]
5	6_3 [2 1 1 2]
7	8_9 [3 1 1 3]
9	10_{17} [4 1 1 4]
11	$12a1273$ [5 1 1 5]
11	$K14a19298$ [6 1 1 6]

Table B.2: The 2-lemniscate knots with $n = 2$.

$n = 2$	3	4	5	6
4_1 Figure-8	$L6a4$ Borromean Rings	8_{18} Turk's Head	10_{123}	 A Brunnian Link

Table B.3: The 2-lemniscate knots with three strands, shown with increasing n, the number of repeats of the basic braid word $1\bar{2}$.

	$n = 2$
Strands = 4	$L6a1$ [2 2 2]
5	7_7 [2 1 1 1 2]
7	9_{31} [2 1 1 1 1 1 2]
8	$L10a91$ [2 1 1 2 1 1 2]
10	A 12 crossing two component link [3 1 1 2 1 1 3]
11	$K13a4296$ [3 1 1 3 1 1 3]
13	$K15a75986$ [4 1 1 3 1 1 4]

Table B.4: The 3-lemniscate knots and links with $n = 2$.

	$n = 2$
Strands = 3	4_1 Figure-8 Knot [2 2]
5	8_{12} [2 2 2 2]
7	10_{45} [2 1 1 1 1 1 1 2]
9	$K12a499$ [2 1 1 1 1 1 1 1 1 2]
11	$K14a10074$ [2 1 1 2 1 1 2 1 1 2]
13	A 16 crossing Knot [3 1 1 2 1 1 2 1 1 3]
15	An 18 crossing knot [3 1 1 3 1 1 3 1 1 3]

Table B.5: The 4-lemniscate knots with $n = 2$.

	$n = 2$
Strands =2	$L2a1$ Hopf Link [2]
3	3_1 Trefoil [3]
4	$L6a1$ [2 2 2]
6	Unidentified (See page 179)
7	$K11a121$ [2 2 1 1 1 2 2]
8	Unidentified (See page 180)
9	$K13a1739$ [2 1 1 1 1 1 1 1 1 2]
11	$K15a5180$ [2 1 1 1 1 1 1 1 1 1 1 2]
12	A 16 crossing 2 component link [2 1 1 1 1 1 2 1 1 1 1 1 2]
13	A 17 crossing Knot [2 1 1 2 1 1 1 1 1 2 1 1 2]
14	An 18 crossing 2 component link [2 1 1 2 1 1 2 1 1 2 1 1 2]
16	A 20 crossing 2 component link [3 1 1 2 1 1 2 1 1 2 1 1 3]

Table B.6: The 5-lemniscate knots with $n = 2$. The Conway notation is shown through to sixteen strands to show the pattern in this notation being formed.

Bibliography

[AB27] J W Alexander and G B Briggs, *On types of knotted curves*, Annals of Mathematics. Second Series **28** (1926/27), no. 1-4, 562–586.

[Ada94] C Adams, *The knot book*, W. H. Freeman and Company, 1994, An elementary introduction to the mathematical theory of knots.

[AK81] S Akbulut and H King, *All knots are algebraic*, Commentarii Mathematici Helvetici **56** (1981), no. 3, 339–351.

[Ale23] J W Alexander, *A lemma on systems of knotted curves*, Proceedings of the National Academy of Science **9** (1923), no. 3, 93–95.

[Ale28] ———, *Topological invariants of knots and links*, Transactions of the American Mathematical Society **30** (1928), no. 2, 275–306.

[AS64] M Abramowitz and I A Stegun, *Handbook of mathematical functions with formulas, graphs, and mathematical tables*, National Bureau of Standards Applied Mathematics Series, vol. 55, For sale by the Superintendent of Documents, U.S. Government Printing Office, Washington, D.C., 1964.

[AV96] E Abramochkin and V Volostnikov, *Spiral-type beams: Optical and quantum aspects*, Optics Communications **125** (1996), no. 4–6, 302–323.

[BBBB01] I Bialynicki-Birula and Z Bialynicka-Birula, *Motion of vortex lines in nonlinear wave mechanics*, Physical Review A **65** (2001), no. 1.

[BBBB03] I Bialynicki-Birula and Z Bialynicki-Birula, *Vortex lines of the electromagnetic field*, Physical Review A **67** (2003), no. 6.

[BBBBS00] I Bialynicki-Birula, Z Bialynicka-Birula, and C Sliwa, *Motion of vortex lines in quantum mechanics*, Physical Review A **61** (2000), no. 3.

[BD00] M V Berry and M R Dennis, *Phase singularities in isotropic random waves*, The Royal Society of London. Proceedings. Series A. Mathematical, Physical and Engineering Sciences **456** (2000), no. 2001, 2059–2079.

[BD01a] ———, *Knotted and linked phase singularities in monochromatic waves*, The Royal Society of London. Proceedings. Series A. Mathematical, Physical and Engineering Sciences **457** (2001), no. 2013, 2251–2263.

[BD01b] ———, *Knotting and unknotting of phase singularities: Helmholtz waves, paraxial waves and waves in* $2+1$ *spacetime*, Journal of Physics A. Mathematical and General **34** (2001), no. 42, 8877–8888.

[BD01c] ———, *Polarization singularities in isotropic random vector waves*, Proceedings of the Royal Society of London A. Mathematical, Physical and Engineering Sciences **457** (2001), no. 2005, 141–156.

[BDL04] M V Berry, M R Dennis, and R L Lee, *Polarization singularites in the clear sky*, New Journal of Physics **6** (2004).

[Ber78] M V Berry, *Disruption of wavefronts : statistics of dislocations in incoherent Gaussian random waves*, Journal of Physics A: Mathematical and General **11** (1978), no. 1, 27–37.

[Ber98] ———, *Wave dislocation reactions in non-paraxial Gaussian beams*, Journal of Modern Optics **45** (1998), no. 9, 1845–1858.

[Ber00] ———, *Making waves in physics*, Nature **403** (2000), 21–26.

[Ber01a] M A Berger, *Hamiltonian dynamics generated by Vassiliev invariants*, Journal of Physics A. Mathematical and General **34** (2001), no. 7, 1363–1374.

[Ber01b] M V Berry, *Knotted zeros in the quantum states of hydrogen*, Foundations of Physics **31** (2001), no. 4, 659–667.

[BHJS94] M G V Bogle, J E Hearst, V F R Jones, and L Stoilov, *Lissajous knots*, Journal of Knot Theory and its Ramifications **3** (1994), no. 2, 121–140.

[Bir74] J S Birman, *Braids, links and mapping class groups*, Princeton University Press, 1974.

[BK96] M V Berry and S Klein, *Integer, fractional and fractal Talbot effects*, Journal of Modern Optics **43** (1996), no. 10, 2139–2164.

[BL52] W Braunbek and G Laukien, *Einzelheiten zur halbebenen-beugung*, Optik **9** (1952), no. 4, 174–179.

[BNM10] D Bar-Natan and S Morrison, *Knot atlas*, `http://katlas.math.toronto.edu` 29 September, 2010.

[Bra28] K Brauner, *Zur geometry der funktionen zweier komplex veränderlichen*, Abhandlungen aus dem Mathematischen Seminar der Hamburgischen Universität **6** (1928), no. 3 and 4, 8–54.

[BRS01] C F Barenghi, R L Ricca, and D C Samuels, *How tangled is a tangle?*, Physica D **157** (2001), no. 3, 197–206.

[BW59] M Born and E Wolf, *Principles of optics*, Pergamon Press Inc., 1959.

[BZ85] G Burde and H Zieschang, *Knots*, Walter de Gruyter and Co., 1985.

[Can84] J R Cannon, *The one-dimensional heat equation*, Encyclopedia of Mathematics and its Applications, vol. 23, Addison-Wesley, 1984.

[CF63] R H Crowell and R H Fox, *Introduction to knot theory*, Ginn and Company, 1963.

[CGR89] P Coullet, L Gil, and F Rocca, *Optical vortices*, Optics Communications **73** (1989), no. 5, 403–408.

[CL10] J C Cha and C Livingston, *KnotInfo : Table of knot invariants*, `http://www.indiana.edu/~knotinfo` 29 September, 2010.

[Con70] J H Conway, *An enumeration of knots and links, and some of their algebraic properties*, Computational Problems in Abstract Algebra (Proc. Conf., Oxford, 1967), Pergamon, 1970, pp. 329–358.

[CR08] M Chen and F S Roux, *Accelerating the annihilation of an optical vortex dipole in a Gaussian beam*, Journal of Optical Society of America A **25** (2008), no. 6, 1084–1090.

[CS00] C Cerf and A Stasiak, *A topological invariant to predict the three-dimesional writhe of ideal configurations of knots and links*, Proceedings of the National Academy of Sciences **8** (2000), 3795–3798.

[DBDK10] A S Desyatnikov, D Buccoliero, M R Dennis, and Y S Kivshar, *Suppression of collapse for spiraling elliptic solitons*, Physical Review Letters **104** (2010).

[DDM+03] A Dobay, J Dubochet, K Millett, P Sottas, and A Stasiak, *Scaling behaviour of random knots*, Proceedings of the National Academy of Sciences **100** (2003), no. 10, 5611–5615.

[Den01] M R Dennis, *Topological singularites in wave fields*, Ph.D. thesis, University of Bristol, 2001.

[Den03] ———, *Braided nodal lines in wave superpositions*, New Journal of Physics **5** (2003).

[Den09] ———, *On the Burgers vector of a wave dislocation*, Journal of Optics A **11** (2009).

[DH05] M R Dennis and J Hannay, *Geometry of Călugăreanu's theorem*, Proceedings of The Royal Society of London. Series A. Mathematical, Physical and Engineering Sciences **461** (2005), 3245–3254.

[Dia93] Y Diao, *Minimal knotted polygons on the cubic lattice*, Journal of Knot Theory and its Ramifications **2** (1993), no. 4, 413–425.

[Dir31] P A M Dirac, *Quantised singularities in the electromagnetic field*, Proceedings of the Royal Society of London A - Containing papers of a mathematical and physical character **133** (1931), 60–72.

[DKJ+10] M R Dennis, R P King, B Jack, K O'Holleran, and M J Padgett, *Isolated optical vortex knots*, Nature Physics **6** (2010), 118–121.

[DKT05] A S Desyatnikov, Y S Kivshar, and L Torner, *Optical vortices and vortex solitons*, Progress in Optics **47** (2005), 291–391.

[DOP09] M R Dennis, K O'Holleran, and M Padgett, *Singular optics: Optical vortices and polarization singularities*, Progress in Optics (2009), 293–363.

[DT83] C H Dowker and M B Thistlethwaite, *Classification of knot projections*, Topology and its Applications **16** (1983), no. 1, 19–31.

[Dur87] J Durnin, *Exact solutions for nondiffracting beams. I. The scalar theory*, Journal of Optical Society of America A **4** (1987), no. 4, 651–654.

[EP02] C Ernst and M Phipps, *A minimal link on the cubic lattice*, Journal of Knot Theory and its Ramifications **11** (2002), no. 2, 165–172.

[Fal03] K Falconer, *Fractal geometry : Mathematical foundations and applications*, second ed., John Wiley & Sons Inc., 2003.

[FODP08] F Flossmann, K O'Holleran, M R Dennis, and M J Padgett, *Polarization singularities in 2D and 3D speckle fields*, Physical Review Letters **100** (2008).

[Fox49] R H Fox, *A remarkable simple closed curve*, Annals of Mathematics. Second Series **50** (1949), 264–265.

[Fox53] ———, *Free differential calculus. I. Derivation in the free group ring*, Annals of Mathematics **57** (1953), no. 3, 547–560.

[Fox62] ———, *A quick trip through knot theory*, Topology of 3-manifolds and related topics (Proc. The Univ. of Georgia Institute, 1961), Prentice-Hall, 1962, pp. 120–167.

[FPS05] G Foo, D Palacios, and G Swartzlander, *Optical vortex coronagraph*, Optics Letters **30** (2005), no. 24, 3308–3310.

[Fre00] I Freund, *Optical vortex trajectories*, Optics Communications **181** (2000), 19–33.

[FS07] A Flammini and A Stasiak, *Natural classification of knots*, Proceedings of the Royal Society A. Mathematical, Physical and Engineering Sciences **463** (2007), 569–582.

[FYH+85] P Freyd, D Yetter, J Hoste, W Lickorish, K Millett, and A Ocneanu, *A new polynomial invariant of knots and links*, Bulletin of the American Mathematical Society **12** (1985), no. 2, 239–246.

[Git08] T Gittings, *Minimum braids : A complete invariants of knots and links*, arXiv : math.GT/0401051 (2008).

[GK94] A Y Grosberg and A R Khokhlov, *Statistical Physics of Macromolecules*, American Institute of Physics Press, 1994.

[GK97] J R Goldman and L H Kauffman, *Rational tangles*, Advances in Applied Mathematics **18** (1997), 300–332.

[Gol75] D L Goldsmith, *Symmetric fibered links*, Knots, groups, and 3-manifolds (Papers dedicated to the memory of R. H. Fox), Princeton Univ. Press, 1975, pp. 3–23. Ann. of Math. Studies, No. 84.

[Goo07] J W Goodman, *Speckle phenomena in optics : Theory and applications*, Roberts and Company, 2007.

[GR00] I S Gradshteyn and I M Ryzhik, *Tables of integrals, series and products*, 6th ed., Academic Press, 2000.

[Har79] R Hartley, *On two-bridge knots polynomials*, Journal of the Australian Mathematical Society **28** (1979), 241–249.

[Has07] B Hassett, *Introduction to Algebraic Geometry*, Cambridge University Press, 2007.

[HS95] M Hindmarsh and K Strobl, *Statistical properties of strings*, Nuclear Physics B **437** (1995), no. 2, 471–488.

[HTW98] J Hoste, M B Thistlethwaite, and J Weeks, *The first 1701936 knots*, The Mathematical Intelligencer **20** (1998), no. 4, 33–48.

[IB08] W T M Irvine and D Bouwmeester, *Linked and knotted beams of light*, Nature Physics **4** (2008), no. 9, 716–720.

[Ind93] G Indebetouw, *Optical vortices and their propagation*, Journal of Modern Optics **40** (1993), no. 1, 73–87.

[Jab99] S V Jablan, *Are Borromean links so rare?*, Proceedings of the 2nd International Katachi U Symmetry Symposium, Part 1 (Tsukuba, 1999), vol. 14, 1999, pp. 269–277.

[Jab01] ———, *New knot tables*, Univerzitet u Nišu. Prirodno-Matematički Fakultet. Filomat (2001), no. 15, 141–152.

[Jac62] J D Jackson, *Classical electrodynamics*, John Wiley and Sons, Inc., 1962.

[Jon85] V R F Jones, *A polynomial invariant for knots via von neumann algebras*, Bulletin of the American Mathematical Society **12** (1985), no. 1, 103–111.

[JS07] S Jablan and R Sazdanović, *LinKnot*, Series on Knots and Everything, vol. 21, World Scientific Publishing Co. Pte. Ltd., 2007.

[KBM+96] V Katritch, J Bednar, D Michoud, R G Scharein, J Dubochet, and A Stasiak, *Geometry and physics of knots*, Nature **384** (1996), 142–145.

[Lam97] C Lamm, *There are infinitely many Lissajous knots*, Manuscripts Mathematica **93** (1997), 29–37.

[Law72] J D Lawrence, *A catalog of special plane curves*, Dover Publications, Inc, 1972.

[LDCP04] J Leach, M R Dennis, J Courtial, and M J Padgett, *Knotted threads of darkness*, Nature (2004), 165.

[LDCP05] ———, *Vortex knots in light*, New Journal of Physics **7** (2005).

[Leg06] A J Leggett, *Quantum liquids : Bose condensation and cooper pairing in condensed-matter systems*, Oxford University Press, 2006.

[Lic97] W B R Lickorish, *An introduction to knot theory*, Springer, 1997.

[Lit90] C N Little, *Alternate ± knots of order eleven*, Transactions of the Royal Society of Edinburgh **36** (1890), 253–255.

[Lit00] ———, *Non-alternate ± knots*, Transactions of the Royal Society of Edinburgh **39** (1900), 771–778.

[LLM75] M Lax, W H Louisell, and W B McKnight, *From Maxwell to paraxial wave optics*, Physical Review A **11** (1975), no. 4.

[Loo71] E Looijenga, *A note on polynomial isolated singularities*, Nederl. Akad. Wetensch. Proc. Ser. A **74** Indagationes Mathematicae **33** (1971), 418–421.

[Man04] V Manturov, *Knot theory*, Chapman and Hall/CRC, 2004.

[MD01] J Masajada and B Dubik, *Optical vortex generation by three plane wave interference*, Optics Communications **198** (2001), 21–27.

[Mes99] A Messiah, *Quantum mechanics*, Dover, 1999.

[Mil68] J Milnor, *Singular points of complex hypersurfaces*, Princton University Press, 1968.

[MTWT01] G Molina-Terriza, E M Wright, and L Torner, *Propagation and control of noncanonical optical vortices*, Optics Letters **26** (2001), no. 3, 163–165.

[NB74] J Nye and M V Berry, *Dislocations in wave trains*, Proceedings of the Royal Society of London A. Mathematical, Physical and Engineering Sciences **336** (1974), no. 1605, 165–190.

[NH87] J F Nye and J V Hajnal, *The wave structure of monochromatic electromagnetic radiation*, Proceedings of the Royal Society of London A. Mathematical, Physical and Engineering Sciences **409** (1987), 21–36.

[NW03] S Nazarenko and R West, *Analytical solution for nonlinear schrödinger vortex reconnection*, Journal of Low Temperature Physics **132** (2003), no. 1–2, 1–10.

[Nye98] J F Nye, *Unfoldings of higher-order wave dislocations*, Journal of Optical Society of America A **15** (1998), no. 5, 1132–1138.

[Nye99] ———, *Natural focusing and fine structure of light*, Institute of Physics Publishing, 1999.

[ODFP08] K O'Holleran, M R Dennis, F Flossmann, and M J Padgett, *Fractality of light's darkness*, Physical Review Letters **100** (2008), no. 5.

[ODP00] K O'Holleran, M R Dennis, and M J Padgett, *Topology of light's darkness*, Physical Review Letters **102** (2000).

[OEI10] OEIS, *The online encyclopaedia of integer sequences*, `http://oeis.org/classic/index.html` 29 September, 2010.

[OFDP09] K O'Holleran, F Flossmann, M R Dennis, and M J Padgett, *Methodology for imaging the 3D structure of singularities in scalar and vector optical fields*, Journal of Optics A **11** (2009).

[O'H91] J O'Hara, *Energy of a knot*, Topology **10** (1991), no. 2, 241–247.

[O'H08] K O'Holleran, *Fractality and topology of optical singularities*, Ph.D. thesis, University of Glasgow, 2008.

[OPD06] K O'Holleran, M J Padgett, and M R Dennis, *Topology of optical vortex lines formed by the interference of three, four and five plane waves*, Optics Express **14** (2006), 3039–3044.

[OW07] E Orlandini and S G Whittington, *Statistical topology of closed curves: Some applications in polymer physics*, Reviews of Modern Physics **79** (2007), no. 2, 611–642.

[Per74] K A Perko, *Classification of knots*, Proceedings of the American Mathematical Society **45** (1974), no. 2, 262–266.

[Per82] B Perron, *Le nœud "huit" est algébrique réel*, Inventiones Mathematicae **65** (1982), 441–451.

[PŠ08] P Poláčik and V Šverák, *Zeros of complex caloric functions and singularities of complex viscous burgers equation*, Journal für die Reine und Angewandte Mathematik. [Crelle's Journal] **616** (2008), 205–217.

[PT87] J H Przytycki and P Traczyk, *Conway algebras and skein equivalence of links*, Proceedings of the American Mathematical Society **100** (1987), no. 4, 744–748.

[PW92] T Poston and A T Winfree, *Complex singularities and excitable media*, Unpublished, 1992.

[Rañ89] A F Rañada, *A topological theory of the electromagnetic field*, Letters in mathematical physics **18** (1989), 97–106.

[RD05] J Ruostekoski and Z Dutton, *Engineering vortex rings and systems for controlled studies of vortex interactions in Bose-Einstein condensates*, Physical Review A **72** (2005), no. 6.

[Rea53] W T Read, *Dislocations in crystals*, McGraw-Hill Education, 1953.

[Rei26] K Reidemeister, *Elementare begründung der knotentheorie*, Abhandlungen aus dem Mathematischen Seminar der Hamburgischen Universität **5** (1926), 24–32.

[RF04] S Rankin and O Flint, *Enumerating the prime alternating knots*, Journal of Knot Theory and its Ramifications **13** (2004), no. 1, 151–173.

[RFS04a] S Rankin, O Flint, and J Schermann, *Enumerating the prime alternating knots, part 1*, Journal of Knot Theory and its Ramifications **13** (2004), no. 1, 57–100.

[RFS04b] ———, *Enumerating the prime alternating knots, part 2*, Journal of Knot Theory and its Ramifications **13** (2004), no. 1, 101–149.

[Rol76] D Rolfsen, *Knots and links*, Publish or Perish, 1976.

[Rou04] F S Roux, *Canonical vortex dipole dynamics*, Journal of the Optical Society of America B **21** (2004), no. 3, 655–663.

[RS07] D M Raymer and D E Smith, *Spontaneous knotting of an agitated string*, Proceedings of the National Academy of Sciences **104** (2007), no. 42, 16432–16437.

[Rud87] L Rudolph, *Isolated critical-points of mappings from $\mathbb{R}^4$ to $\mathbb{R}^2$ and a natural splitting of the Milnor number of classical fibred link : 1. Basic theory and examples*, Commentarii Mathematici Helvetici **62** (1987), no. 4, 630–645.

[SAM93] D Stauffer, A Aharony, and B B Mandelbrot, *Self-similarity and covered neighbourhoods of fractals: A random walk test*, Physica A **196** (1993), 1–5.

[ŞBY04] H Şimşek, M Bayram, and U Yavuz, *A computer program to calculate Alexander polynomial from braids presentation of the given knot*, Applied Mathematics and Computation **153** (2004), no. 1, 199–204.

[SFAM+08] G A Swartzlander, E L Ford, R S Abdul-Malik, L M Close, M A Peters, D M Palacios, and D W Wilson, *Astronomical demonstration of an optical vortex coronagraph*, Optics Express **16** (2008), no. 14, 10200–10207.

[Sie86] A E Siegman, *Lasers*, University Science Books, 1986.

[SKK98] A Stasiak, V Katritch, and L H Kauffman, *Ideal knots*, World Scientific, 1998.

[SS96] Y Y Schechner and J Shamir, *Parameterization and orbital angular momentum of anisotropic dislocations*, Journal of the Optical Society of America A **27** (1996), no. 9, 967–973.

[Sta78] J Stallings, *Constructions of fibred knots and links*, Algebraic and geometric topology (Proc. Sympos. Pure Math., Stanford Univ., Stanford, Calif., 1976), Part 2, Proc. Sympos. Pure Math., XXXII, Amer. Math. Soc., 1978, pp. 55–60.

[Str50] D J Struik, *Lectures on Classical Differential Geometry*, 2nd ed., Addison-Wesley Press, Inc., 1950.

[Sum90] D W Sumners, *Untangling DNA*, The Mathematical Intelligencer **12** (1990), no. 3, 71–80.

[SV01] M S Soskin and M Vasnetsov, *Singular Optics*, Progress in Optics **42** (2001), 219–276.

[SW03] P M Sutcliffe and A T Winfree, *Stability of knots in excitable media*, Physical Review E **68** (2003), no. 1.

[Tai77] P G Tait, *On knots 1*, Transactions of the Royal Society of Edinburgh **28** (1877), 145–190.

[Tai83a] _____, *On knots 2*, Transactions of the Royal Society of Edinburgh **32** (1883), 327–342.

[Tai83b] _____, *On knots 3*, Transactions of the Royal Society of Edinburgh **32** (1883), 493–506.

[Tho67] W Thomson, *On vortex atoms*, Proceedings of the Royal Society of Edinburgh, Reprinted in Phil. Mag. Vol. XXXIV, 1867, pp. 15-24 **6** (1867), 94–105.

[Vas90] V A Vassiliev, *Cohomology of knot spaces*, Advances in Soviet Mathematics **1** (1990), 23–70.

[VV84] T Vachaspati and A Vilenkin, *Formation and evolution of cosmic strings*, Physical Review D **30** (1984), no. 10, 2036–2045.

[WH05] V Westphal and S W Hell, *Nanoscale resolution in the focal plane of an optical microscope*, Physical Review Letters **94** (2005).

[Whe36] W Whewell, *Researches on the tides - sixth series. on the results of an extensive system of tide observations made on the coasts of Europe and America in June 1835*, Philosophical Transactions of the Royal Society of London **26** (1836), no. 3, 289–341.

[Win87] A T Winfree, *When time breaks down*, Princeton University Press, 1987.

[Wol50] H Wolter, *Zur frage des litchtweges bei totalreflexion*, Zeitschrift fur Naturforschung Section A **5** (1950), no. 5, 276–283.

[Wol09] _____, *Concering the path of light upon total refection, translated by U T schwarz and M R dennis*, Journal of Optics A **11** (2009), no. 9.